UNIVERSITY of TASMANIA

AMC
AUSTRALIAN MARITIME COLLEGE

Unsteady loading on hydrofoils due to turbulence and cavitation

Samuel M. Smith
Bachelor of Engineering - Naval Architecture (First Class Honours)
National Centre for Maritime Engineering and Hydrodynamics
Australian Maritime College, University of Tasmania

Submitted in fulfilment of the requirements
for the degree of Doctor Of Philosophy,
University of Tasmania

January, 2020

Declarations

Authority of Access

The publishers of the papers comprising Chapters 2-4 hold the copyright for that content, and access to the material should be sought from the respective journals. The remaining non-published content of this thesis may be made available for loan and limited copying and communication in accordance with the Copyright Act 1968.

Statement of Originality

This thesis contains no material which has been accepted for a degree or diploma by the University or any other institution, except by way of background information and as duly acknowledged in the text, and to best of my knowledge and belief no material previously published or written by another person except where due acknowledgement is made in the text of the thesis, nor does the thesis contain any material that infringes copyright.

Signed: _____ Date: 3rd of October, 2020

Mr Samuel Smith
National Centre for Maritime Engineering and Hydrodynamics
Australian Maritime College, University of Tasmania

Statement of Co-Authorship

The following people and institutions contributed to the publication of work undertaken as part of this thesis:

Candidate	Mr Samuel Smith	University of Tasmania
Author 1	Prof. Paul Brandner	University of Tasmania
Author 2	Dr. Bryce Pearce	University of Tasmania
Author 3	Dr. James Venning	University of Tasmania
Author 4	Dr. David Clarke	DST Group, Australia
Author 5	Prof. Yin Lu Young	University of Michigan
Author 6	Dr. Danielle Moreau	University of New South Wales
Author 7	Dr. Dean Giosio	University of Tasmania
Author 8	Dr. Yunpeng Xue	University of Tasmania

Contribution of work by co-authors for each paper:

Paper 1: Located in Chapter 2

This chapter is under review for publication in *Journal of Fluids and Structures* titled:

Steady and unsteady loading on a hydrofoil immersed in a turbulent boundary layer

The contributing authors are:

Smith, S. M., Brandner, Pearce, B. W., P. A., Venning, J. A., Moreau, D. J. and Clarke, D. B.

Contributions:

Conceived experiment design: *Candidate, Author 1 & Author 2*

Performed experiments: *Candidate*

Data analysis: *Candidate, Author 1, Author 2, Author 3, Author 4 & Author 6*

Manuscript preparation: *Candidate, Author 1, Author 2, Author 3, Author 4 & Author 6*

Paper 2: Located in Chapter 3

This chapter has been published in the *Journal of Fluid Mechanics* titled:

The influence of fluid-structure interaction on cloud cavitation about a stiff hydrofoil. Part 1.

The contributing authors are:

Smith, S. M., Venning, J. A., Pearce, B. W., Young, Y. L. and Brandner, P. A.

Contributions:

Conceived experiment design: *Candidate, Author 1 & Author 2*
Performed experiments: *Candidate, Author 1, Author 2 & Author 3*
Data analysis: *Candidate, Author 1, Author 2, Author 3 & Author 5*
Manuscript preparation: *Candidate, Author 1, Author 2, Author 3 & Author 5*

Paper 3: Located in Chapter 4

This chapter has been published in the *Journal of Fluid Mechanics* titled:

The influence of fluid-structure interaction on cloud cavitation about a flexible hydrofoil. Part 2.

The contributing authors are:

Smith, S. M., Venning, J. A., Pearce, B. W., Young, Y. L. and Brandner, P. A.

Contributions:

Conceived experiment design: *Candidate, Author 1 & Author 2*
Performed experiments: *Candidate, Author 1, Author 2 & Author 3*
Data analysis: *Candidate, Author 1, Author 2, Author 3 & Author 5*
Manuscript preparation: *Candidate, Author 1, Author 2, Author 3 & Author 5*

Paper 4: Located in Appendix A

This conference paper was presented at the *20th Australasian Fluid Mechanics Conference* titled:

Steady and Unsteady loads acting on a hydrofoil immersed in a turbulent boundary layer

The contributing authors are:

Smith, S. M., Brandner, Pearce, B. W., P. A., Venning, J. A., Moreau, D. J. and Clarke, D. B.

Contributions:

Conceived experiment design: *Candidate, Author 1 & Author 2*

Performed experiments: *Candidate*

Data analysis: *Candidate, Author 1, Author 2, Author 3, Author 4 & Author 6*

Manuscript preparation: *Candidate, Author 1, Author 2, Author 3, Author 4, Author 6 & Author 8*

Paper 5: Located in Appendix B

This conference paper was presented at the *17th International Symposium on Transport Phenomena and Dynamics on Rotating Machinery (ISROMAC 2017)* titled:

Cloud cavitation behaviour on a hydrofoil due to fluid-structure interaction.

The contributing authors are:

Smith, S. M., Venning, J. A., Giosio, D. R., Brandner, P. A, Pearce, B. W. and Young, Y. L.

Contributions:

Conceived experiment design: *Candidate, Author 1 & Author 2*

Performed experiments: *Candidate, Author 1, Author 2, Author 3 & Author 7*

Data analysis: *Candidate, Author 1, Author 2, Author 3 & Author 7*

Manuscript preparation: *Candidate, Author 1, Author 2, Author 3, Author 5 & Author 7*

Paper 6: Located in Appendix C

This article was published in the *ASME Journal of Fluids Engineering* titled:

Cloud cavitation behaviour on a hydrofoil due to fluid-structure interaction.

The contributing authors are:

Smith, S. M., Venning, J. A., Giosio, D. R., Brandner, P. A, Pearce, B. W. and Young, Y. L.

Contributions:

Conceived experiment design: *Candidate, Author 1 & Author 2*

Performed experiments: *Candidate, Author 1, Author 2, Author 3 & Author 7*

Data analysis: *Candidate, Author 1, Author 2, Author 3 & Author 7*

Manuscript preparation: *Candidate, Author 1, Author 2, Author 3, Author 5 & Author 7*

Paper 7: Located in Appendix D

This conference paper was presented at the *10th International Symposium on Cavitation (CAV2018)* titled:

The influence of fluid-structure interaction on cloud cavitation about a hydrofoil.

The contributing authors are:

Smith, S. M., Venning, J. A., Brandner, P. A, Pearce, B. W., Giosio, D. R. and Young, Y. L.

Contributions:

Conceived experiment design: *Candidate, Author 1 & Author 2*

Performed experiments: *Candidate, Author 1, Author 2, Author 3 & Author 7*

Data analysis: *Candidate, Author 1, Author 2, Author 3 & Author 7*

Manuscript preparation: *Candidate, Author 1, Author 2, Author 3, Author 5 & Author 7*

We, the undersigned, endorse the above stated contribution of work undertaken for each of the published (or submitted) peer-reviewed manuscripts contributing to this thesis:

Signed: _____ Date: 24th of February, 2020

Mr Samuel Smith
Candidate
National Centre for Maritime Engineering and Hydrodynamics
Australian Maritime College, University of Tasmania

Signed: _____ Date: 24th of February, 2020

Prof Paul Brandner
Primary Supervisor
National Centre for Maritime Engineering and Hydrodynamics
Australian Maritime College, University of Tasmania

Signed: _____ Date: 25th of March, 2020

Dr Vikram Garaniya
Acting Director
National Centre for Maritime Engineering and Hydrodynamics
Australian Maritime College, University of Tasmania

Acknowledgements

The privilege of undertaking this doctorate would not have been possible without the generous support from many individuals. Firstly, I would like to express my sincere gratitude to my supervisors Prof. Paul Brandner, Dr. Bryce Pearce, Dr. James Venning and Dr. David Clarke for their continuous support of my research. This would not be possible if it was not for their patience, motivation, and immense knowledge they have passed on to me. I would like to also acknowledge the other members of the Cavitation Research Laboratory, Robert Wrigley, Steven Kent, Patrick Russell and Luka Barbaca for their essential help with setting up and carrying out the experiments as well as data processing and analysis. Working with the team at the Cavitation Research Laboratory and being apart of a group that share my passion for research made my candidature very enjoyable. It was both a privilege and a truly rewarding experience working in such a prestigious institution that they have worked so hard to develop and maintain.

I would like to express my gratitude to Prof. Jonathan Binns for the support and supervision you provided as my undergraduate thesis supervisor and as director of the Research Training Centre of Naval Design and Manufacturing (RTCNDM). The knowledge and advice you continue to pass on is something I highly value. I would also like to thank my research collaborators Prof. Yin Lu Young from the University of Michigan and Dr. Danielle Moreau from the University of New South Wales. The knowledge and experience you brought to the project was invaluable and raised the quality and impact the research is having. The willingness and patience to teach me new concepts and expand my knowledge is a testament to their exceptional character and intellect.

I am deeply indebted to my wonderful family that have provided me amazing support throughout the 7 years I have spent at the Australian Maritime College completing my Naval Architecture degree and doctorate. To my beautiful mother, Robyn Smith, thank you for always being there for me and being the glue that keeps our amazing family together. To my phenomenal father, Michael Smith, thank you for all the advice you have given me throughout my life, you have been a role model for me my entire life teaching me the importance of morals, resilience and a strong work ethic. To my wonderful sisters,

you may not understand what I do but I cannot thank you enough for the happiness and laughter you bring to our family. If it were not for the support, opportunities, knowledge and joy each of you have provided me throughout my life I would not be where I am today. I would also like to acknowledge Dr. Arno Dubois for his friendship and support throughout our time together at AMC, you made my time in Tasmania that much more enjoyable both inside and outside of work.

I would like to thank the RCTNDM for the opportunity to undertake this Ph.D, the program is truly special with the resources and opportunities it has provided me. Additionally, I would like to thank the main sponsors of this research: The Australian Defence Department - Defence Science and Technology Group (DST-G), ASC Pty Ltd and the U.S Office of Naval Research.

Abstract

There is an increasing demand in the operational requirements of a submarine for quieter, stealthier designs. For ships and submarines, constraints relating to control, serviceability and efficiency dictate that propulsion and control equipment be compact and located at the stern of the vessel. This equipment is then exposed to the turbulent flow about the vessel afterbody. At the stern, the hull boundary layer and embedded wakes have had the full vessel length to develop and may be further thickened due to afterbody adverse pressure gradients. Consequently, control surfaces and propulsion devices may be partially or fully immersed within the afterbody flow and be subject to unsteady loading and hence be a source of vibration and noise production. For these effects to be minimized, insight into the flow physics and excitation spectra are required. Such information would enable more rigorous analysis and design for optimisation of control surface and propeller structural response.

To further understand the flow physics, an experimental investigation was undertaken to analyze the steady and unsteady loads acting on a hydrofoil immersed in a turbulent boundary layer. Measurements were performed in a cavitation tunnel in which the hydrofoil was mounted from the test section ceiling, via a 6-component force balance. The turbulent boundary layer was artificially thickened via an array of transverse jets located upstream of the test section. The effect of boundary layer thickness was investigated, in which various thicknesses were generated to allow partial or full immersion of two hydrofoils of different aspect ratios. The effect of varying incidence and Reynolds number on the hydrodynamic loading was also investigated. Steady forces were found to be significantly affected by the relative scale of the boundary layer, particularly in the stall region. Identification of a broad peak in the unsteady force spectra, was made at a constant reduced frequency of 0.2. The amplitude of this peak was found to be dependant on boundary layer immersion and Reynolds number. Furthermore, a low-frequency stall component, superimposed over the existing broadband excitation of the boundary layer turbulence, was apparent in the spectra past stall.

Flow-induced vibrations occur when the motion of a structure is coupled with flow instabilities, resulting in amplification of vibrations and forces. This phenomenon is gaining importance as advances in material technology and ever-increasing optimisation have

caused structures to be lighter, more flexible, and thus more susceptible to vibration. Flow induced vibration phenomena influence the performance of vast range of aerodynamic and hydrodynamic objects and are therefore significant in geometrical and structural design. Cavitation about a hydrofoil involves a range of complex dynamical phenomena including mass transfer via phase change and diffusion, shockwaves, large and small-scale instabilities and turbulence. These phenomena have the potential to cause significant and destructive vibrations. Understanding these fluid-structure interaction (FSI) phenomena is of interest as flow over a lifting body can significantly alter the performance of maritime propulsion and control systems.

The physics associated with various cavitation regimes about a hydrofoil are investigated in a variable-pressure water tunnel using high-speed photography and synchronized force measurements. Experiments were conducted on both a relatively stiff stainless steel and a flexible composite hydrofoil at $Re = 0.8 \times 10^6$ for cavitation numbers, σ, ranging from 0.2 to 1.2. The flexible composite hydrofoil was manufactured as a carbon/glass-epoxy hybrid structure with a lay-up sequence selected principally to consider spanwise bending deformations with no material-induced bend-twist coupling. The hydrofoils experienced a variety of cavitation regimes including sheet, cloud and super-cavitation. The NACA0009 model of tapered planform was vertically mounted in a cantilevered configuration to a six-component force balance at an incidence, α, of 6° to the oncoming flow. Tip deformations and cavitation behaviour were recorded with synchronized force measurements utilizing two high-speed cameras mounted underneath and to the side of the test section.

Break-up and shedding of an attached cavity was found to be due to either interfacial instabilities, re-entrant jet formation, shockwave propagation or a complex coupled mechanism, depending on σ. Three primary shedding modes, designated as Types I, IIa and IIb, are identified to occur on both hydrofoils. The Types IIa & IIb re-entrant jet driven oscillations exhibiting a linear dependence on σ, decreasing in frequency with decreasing σ due to growth in the cavity length. For the stiff hydrofoil, Type IIa shedding is observed to occur for $0.4 \leq \sigma \leq 1.0$ with Type IIb shedding occuring for $0.7 \leq \sigma \leq 0.9$. Shockwave-driven Type I shedding occurs for lower σ values (0.3-0.6) with the oscillation frequency being practically independent of σ. The Type IIa oscillations locked in to the first sub-harmonic of the stainless steel hydrofoil's first bending mode in water which has been modulated due to the reduced added mass of the vapour cavity.

The flexibility of the composite hydrofoil increased the FSI between the complex cavitation physics and structural deformations causing changes in the phenomena observed. Hydrodynamic bend-twist coupling is seen to result in nose-up twist deformations causing frequency modulation from the increase in cavity length. The lock-in phenomenon driven by re-entrant jet shedding observed on the stiff hydrofoil is also evident on the flexible hydrofoil at $0.70 \leq \sigma \leq 0.75$, but occurs between different modes compared to the stiff

hydrofoil. Flexibility is observed to accelerate cavitation regime transition with reducing σ. This is seen with the rapid growth and influence the shockwave instability has on the forces, deflections and cavitation behaviour on the flexible hydrofoil, suggesting structural behaviour plays a significant role in modifying cavity physics. The reduced stiffness causes secondary lock-in of the flexible hydrofoil's one-quarter sub-harmonic, $f_n/4$, at $\sigma = 0.4$. This leads to the most severe deflections observed in the conditions tested along with a shift in phase between normal force and tip deflection.

Contents

List of Figures

List of Tables

Abbreviations

AMC	Australian Maritime College
CRL	Cavitation Research Laboratory
FSI	Fluid-Structure Interaction
FST	Freestream Turbulence
IOP	Incoherent Output Power
LSB	Laminar Separation Bubble
PIV	Particle Imaging Velocimetry
SPOD	Spectral Proper Orthogonal Decomposition
TKE	Turbulent Kinetic Energy

Chapter 1

General Introduction

The pursuit of predicting and understanding the unsteady loading on a lifting surface has been a longstanding issue, garnering attention not just due to the complexity of the problem, but the role these components play in determining the performance of vehicular motion. Lifting surfaces are utilized on a wide range of vehicles, such as ships, cars and planes, as well as various pieces of machinery, including jet engines, wind turbines and pumps. The ability of these lifting surfaces to handle unsteady loads from a variety of sources is a key performance factor of the surface itself, as well as the assembly it is a component of. On marine vessels, lifting surfaces, or hydrofoils, are used as the primary mechanisms for control and propulsion in the form of rudders and propellers, respectively. These hydrofoils are exposed to various sources of unsteady loading including the hull turbulent boundary layer and embedded wakes, and cavitation. The induced unsteady loading can lead to vibration, noise production, erosion and reduced hydrodynamic efficiency, adversely effecting the performance of the vessel. With an ability to accurately predict the unsteady loading on a hydrofoil, designs can then be optimized in mitigating the adverse effects.

This thesis is organized into two distinct sub-topics consisting of *Unsteady loading due to boundary layer immersion* and *Influence of fluid-structure interaction on cloud cavitation about a flexible hydrofoil*. These sub-topics are reviewed individually in the following sections to aid clarity.

1.1 Unsteady loading due to boundary layer immersion

There is an increasing demand in the operational requirements of a submarine for quieter, stealthier designs. For ships and submarines, constraints relating to control,

serviceability and efficiency dictate that propulsion and control equipment be compact and located at the stern of the vessel. This equipment is then exposed to the turbulent flow about the vessel afterbody. At the stern, the hull boundary layer and embedded wakes have had the full vessel length to develop and may be further thickened due to afterbody adverse pressure gradients. Consequently, control surfaces and propulsion devices may be partially or fully immersed within the afterbody flow and be subject to unsteady loading and hence be a source of vibration and noise production. For these effects to be minimized, insight into the flow physics and excitation spectra are required. Such information would enable more rigorous analysis and design for optimisation of control surface and propeller structural response.

Much of the previous work investigating the unsteady loading on control surfaces has been motivated by aeronautical applications, receiving considerable attention since the initial work by Theodorsen (1935). Further developments were made by von Kármán and Sears (1938) whose work paved the way for Sears (1941) who, instead of treating the problem as an oscillating plate in uniform flow, treated it as rigid aerofoil encountering vortical sinusoidal gusts. Motivated by the lack of experimental studies (e.g. Jackson et al. (1973); McKeough and Graham (1980)) to compliment the extensive range of analytical models, Mish and Devenport (2006a,b) conducted experimental and numerical investigations, observing a reduction in the surface pressure spectral level at low reduced frequencies as the incidence was increased. Reduced frequency is given by $f' = fc/U_\infty$, where c denotes the hydrofoil chord and U_∞ denotes the free-stream velocity. The opposite effect was observed at higher f', with the cross over occurring at $f' = 5$ for all incidences, attributing the low f' reduction in loading spectra to distortion of the oncoming flow by the mean velocity field.

Free-stream turbulence (FST) intensity has been shown to have quantitative and qualitative effects on the performance characteristics on a lifting surface (Hoffmann, 1991; Huang and Lee, 1999; Devinant et al., 2002). When exposed to an adverse pressure gradient, Hoffmann and Kassir (1988) observed a higher resistance to separation due to increased momentum transmission from the free stream to the boundary layer. This momentum or turbulent kinetic energy (TKE) transfer encourages shear layer transition resulting in a resistance to separation. With aerofoil performance shown to be significantly affected, not just by intensity level, but by the integral length scales as well, the embedded turbulence of a boundary layer poses an extra degree of complexity due to the various length scales involved (Smits et al., 2011).

Recent experiments by Lysak (2011) and Lysak et al. (2016) have obtained loading spectra from hydrofoils of various thickness encountering grid turbulence that closely resemble theoretical predictions. Comparing the experimental results with their adaptation of vortex lift theory (Howe, 2001), Lysak et al. (2013) accurately predicted the high frequency reduction in the loading spectra as thickness increases. In experiments conducted

by Khoo et al. (2015), the unsteady loading on a NACA0012 hydrofoil was measured where a significant increase in the loading spectra is observed, particularly at low frequencies, when transitioning to stall. In addition, the resolvable frequency range was limited due to the inherent dynamic response from the coupled force balance/hydrofoil system, similar to that experienced by Lysak et al. (2016). Despite this extensive theoretical, numerical and experimental activity on the unsteady loading on a lifting surface encountering grid turbulence, there is a paucity of published material on the related topic of encountering structured turbulence, such as a boundary layer.

The objectives of the present research are as follows:

- Gain insight into the steady and unsteady loads acting on a generic hydrofoil immersed in a turbulent boundary layer.
- Gain insight into the flow structures involved with a hydrofoil immersed in a turbulent boundary layer.
- Understand how varying incidence, boundary layer thickness and Reynolds number affect these loads.

The research questions answered by this research are:

- What are the steady and unsteady loads on a generic hydrofoil immersed in a turbulent boundary layer?
- How does the boundary layer thickness as a proportion of span influence steady and unsteady loads?
- What is the spectral content of the unsteady loads on a hydrofoil immersed in a turbulent boundary layer?
- How does the roll off of the normal force spectra change with level of boundary layer immersion?
- How does the influence of boundary layer immersion on the normal force change with Reynolds number?

1.2 Influence of FSI on cloud cavitation about a flexible hydrofoil

Due to their high stiffness and resistance to both corrosion fatigue and cavitation erosion, marine propulsors and control surfaces are typically manufactured from metallic alloys. However, due to high machining costs and poor acoustic damping properties

of metallic alloys (Mouritz et al., 2001), alternate materials have recently begun to be consider (Young, 2008). With the high-strength-to-weight and stiffness-to-weight ratios, composite materials allow the manufacturing of lightweight flexible propellers that improve hydrodynamic performance and increase cavitation inception speeds through passive load-dependent shape adaptation (Young et al., 2016, 2017). This flexibility also introduces complex FSI phenomena, particularly in cavitating conditions that are not fully understood and need to be investigated.

Experimental studies investigating the influence of cavitation on flexible (i.e. compliant) hydrofoil's has previously been conducted by Kaplan and Lehman (1966); Brennen et al. (1980); Ausoni et al. (2007); Ducoin et al. (2012b) with the earliest of these studies first observing modest vibration amplitudes due to cavitation about a hydrofoil. Examining the coupling between the hydro-elasticity and the trailing-edge vortex cavitation, Ausoni et al. (2005, 2007) observed that not only does the cavitation influence the structural vibrations, but that the reverse situation is also true. The unsteady two-phase flow has a greater effect on the spectral content of a compliant hydrofoil compared to a relatively stiff one, causing frequency modulation (Akcabay and Young, 2015), broadening of the frequency content (Akcabay et al., 2014) and leading to phenomena such as lock-in that leads to significant amplification of vibrations (Kato et al., 2006; Akcabay and Young, 2015).

Cloud cavitation was first extensively investigated by Knapp (1955) where the detachment of a vapour cloud from an attached cavity due to a re-entrant jet was observed. Since then, several mechanisms have been identified as potential instabilities causing periodic shedding, depending on the flow conditions. These include growth of interfacial instabilities such as Kelvin-Helmholtz waves (Brennen, 1969; Avellan et al., 1988; Brandner et al., 2010), re-entrant jet formation (Furness and Hutton, 1975; Le et al., 1993; Kawanami et al., 1997; Stutz and Reboud, 1997; Pham et al., 1999; Callenaere et al., 2001; Laberteaux and Ceccio, 2001a,b; Smith et al., 2017, 2018, 2019), and condensation shock propagation (Jakobsen, 1964; Reisman et al., 1998; Ceccio, 2015; Ganesh et al., 2016; Smith et al., 2018). In certain conditions, multiple instabilities can be present simultaneously with Ganesh et al. (2016) showing both bubbly shock propagation and re-entrant jet flow from measurements of the void fraction field with X-ray densiotmetry. In addition, Brandner et al. (2010), and more recently de Graaf et al. (2017), using high-speed photography observed all three mechanisms either occurring in isolation or as a complex, coupled mechanism in cloud cavitation about a sphere. Furthermore, experiments on a NACA0015 hydrofoil revealed complex multi-stage shedding cycles involving both re-entrant jet and shockwave instabilities (Venning et al., 2017, 2018b).

To reduce the complexity of the cavitation dynamics in three-dimensional (3D) flows, a large number of past studies have focused on two-dimensional (2D) configurations. However, even in the 2D case, the resulting shedding physics still exhibit significant 3D

characteristics, as observed by Kubota et al. (1989); De Lange and De Bruin (1998); Kawanami et al. (1998), resulting in spanwise variations in the cloud cavitation. Furthermore, Kawanami et al. (1998) showed that cloud cavitation can have a spanwise spatial periodicity on a 2D hydrofoil where periodic shedding occurs at multiple locations along the span, depending on the streamwise length of the cavity. This is also observed by Prothin et al. (2016) and Smith et al. (2018, 2019) showing multiple stable shedding locations along a finite-span hydrofoil, highlighting the role of compatibility between the cavity length and the span first noted by Kawanami et al. (1998). In both 2D and 3D flows, incompatible cavity lengths are seen to result in incoherent shedding along the span (Kawanami et al., 1998; Kjeldsen et al., 2000; Smith et al., 2018; Harwood et al., 2019). The formation of stable shedding sites is seen to be reinforced by the spanwise component of the shedding mechanisms, such as re-entrant jets, as they prevent other instabilities from interfering in the local shedding process (De Lange and De Bruin, 1998).

The objectives of the present research are as follows:

- Gain insight into the physics involved with the fluid-structure interaction of cloud cavitation about a flexible hydrofoil.
- Obtain qualitative measurements of the forces, deformations and cavitation behaviour of a hydrofoil experiencing cloud cavitation.
- Understand how the induced deformations alter the cavitation behaviour about a hydrofoil.

The research questions answered by this research are:

- How does fluid-structure interaction change the cloud cavitation about a flexible hydrofoil?
- How does the cavitation behaviour about a flexible hydrofoil change with cavitation number?
- What is the spectral content of the unsteady loads on a flexible hydrofoil experiencing cavitation at various cavitation numbers?
- How do the hydrofoil deformations alter cavitation behaviour and the loads it experiences?

1.3 Thesis content overview

The individual chapters presented in this thesis are written in journal article form and are either published, or submitted. The publishing details for each article are given at

Hydrofoil	Material	Span (mm)	Root chord (mm)	Tip chord (mm)	Chapter
1	Aluminium Alloy	120	120	80	2
2	Aluminium Alloy	240	120	80	2
3	Stainless Steel	300	120	60	3
4	Carbon Fibre	300	120	60	4

Table 1.1: Summary of the hydrofoils used in the various experiments including geometric and material properties.

the start of each chapter. An outline of the chapters, and their contribution to research objectives, is given below:

In chapter 2, the experimental investigation of a hydrofoil immersed to varying degrees in a boundary layer is presented. The influence of boundary layer immersion on the steady and unsteady normal force for a range of incidences and Reynolds numbers is determined. Analysis of the steady force characteristics and spectral content is presented with possible interrelations with underlying fluid physics discussed.

In chapter 3, the influence of FSI on cloud cavitation about a stiff hydrofoil was investigated. Experimental results using high-speed photography and a force balance to obtain synchronized force, deformation and cavitation behaviour measurements are presented. The results are used to establish a nominally rigid reference that can used in a comparative approach with the flexible hydrofoil results presented in chapter 4. Differences between the results of the stiff and flexible hydrofoil can be attributed to the influence of FSI.

In chapter 4, the influence of FSI on cloud cavitation about a flexible hydrofoil is investigated. Experimental results using the same techniques and conditions used for the stiff hydrofoil are presented for the flexible hydrofoil. Results are compared with those from the stiff hydrofoil with key differences identified and analyzed.

Chapter 2

Steady and unsteady loading on a hydrofoil immersed in a turbulent boundary layer

This chapter is presented in article form, and is currently under review for publication in the *Journal of Fluids and Structures*.

The citation for the paper is:

Smith, S. M., Brandner, Pearce, B. W., P. A., Venning, J. A., Moreau, D. J. and Clarke, D. B. (2020) Steady and unsteady loading on a hydrofoil immersed in a turbulent boundary layer. *Journal of Fluids and Structures* - Under review.

2.1 Abstract

The steady and unsteady loads acting on a hydrofoil immersed in a turbulent boundary layer have been investigated. Measurements were performed in a cavitation tunnel in which the hydrofoil was mounted from the test section ceiling, via a 6-component force balance. Two NACA0012 hydrofoil models with trapezoidal planforms and aspect ratios of 2.4 and 1.2 were examined. The ceiling turbulent boundary layer was artificially thickened via an array of transverse jets located upstream of the test section. Thickening the ceiling boundary layer allowed for varying levels of hydrofoil immersion (nominally up to 100%) to be studied. In addition to the level of immersion, the effect of varying incidence and Reynolds number on the hydrodynamic loading normal to the chord was also investigated. Steady forces were found to be significantly affected by the relative scale of the boundary layer, particularly in the stall region. A broadband peak in the unsteady

normal force spectra was observed at a constant reduced frequency of 0.2. The relative peak amplitude was found to be dependent on the boundary layer thickness to hydrofoil span ratio and Reynolds number. As the incidence is increased past stall, a low-frequency power increase was observed which was superimposed over the existing broadband excitation induced by the ceiling boundary layer.

2.2 Introduction

Control surfaces for marine vessels are typically located at the stern, where the boundary layer has had the full vessel length to develop and thicken. In addition, the boundary layer may be further thickened with the occurrence of flow separation due to the adverse pressure gradient present at the aft end of a vessel (Alin et al., 2010). As control surfaces are generally compact compared to overall length scales, they may be substantially immersed within the turbulent flow about the vessel stern. Hence, these control surfaces are subject to unsteady loading and become a source of vibration and radiated noise. To minimize these effects, insight into the flow physics and excitation spectra are required. This would enable a more rigorous analysis and design for control surface optimisation including the structural response.

Much of the previous work into understanding and predicting the unsteady loading on lifting or control surfaces has been motivated by aeronautical applications involving the prediction of radiated noise and undesirable structural responses (e.g. buffeting). The problem of unsteady aerofoil loading has received considerable attention since the initial work by Theodorsen (1935) who simplified the problem to an oscillating flat plate encountering an oncoming uniform flow. This work was developed further by von Kármán and Sears (1938) using basic concepts of circulation theory to establish a unified treatment of unsteady aerofoil theory. This work set the basis for Sears (1941) who treated the problem as a rigid aerofoil encountering vortical sinusoidal gusts. Using linearized inviscid theory, Sears (1941) derived the well-known expression for the lift function, known as the Sears function, which would eventually serve as the foundation to a significant body of future work in which key advancements have been made (Atassi, 1984).

In an attempt to validate the results from prediction models, early experiments were conducted by Lamson (1956) and Hakkinen and Richardson Jr (1957). Issues arose with obtaining conclusive results as the experimental data exhibited excessive scatter attributed to the turbulence scales present being too small to cause sufficient fluctuations in the unsteady loading. This remained an issue for many years, until Jackson et al. (1973) successfully measured the lift on a finite wing in grid turbulence. It was observed that the lift drops off faster than that predicted by Sears 2D strip theory at the high end of

the spectrum which was attributed to the increasing importance of viscous and boundary layer displacement effects at higher frequencies (Li et al., 2018).

In order to calculate the rapidly changing turbulent flow due to large scale velocity gradients and foil interaction, Goldstein and Atassi (1976) and Atassi (1984) implemented Rapid Distortion Theory (RDT). This would take into account the effect of gust distortion, proving to be important in experiments conducted by McKeough and Graham (1980) as RDT predicts that the vertical velocity variance increases with turbulent flow progressing along a body. The results revealed that mean incidence only has significant effect on the loading spectra at low frequencies. Prediction models continued to develop with the introduction of vortex lift theory by Howe (2001, 2002) which took into account various forms of unsteady flow. The effect of aerofoil geometry such as thickness and camber, as well as incidence, became of key interest with significant advancements made by Reba and Kerschen (1996) and Glegg and Devenport (2009). Despite the extensive development of theoretical models there are relatively few complimentary experimental studies, such as those by Jackson et al. (1973) and McKeough and Graham (1980), to validate the analytical predictions. Mish and Devenport (2006a,b) note this as a motivation for their extensive wind tunnel experiments additional to numerical studies.

The experimental investigations by Mish and Devenport (2006a) involved a two dimensional NACA0015 aerofoil immersed in grid-generated turbulence with lift spectra derived from surface pressure measurements via an array of 96 microphones distributed along the chord and span. Experiments were conducted at a Reynolds number (Re) of 1.17×10^6 for incidences ranging from 0° to 20° where they observed a reduction in the surface pressure spectral level at low reduced frequencies, $f' = fc/U$, as the incidence was increased. The opposite effect was observed at higher f', with the cross over occurring at $f' = 5$ for all incidences. These results were in contrast to the earlier experimental observations made by McKeough and Graham (1980) and theoretical formulations by Atassi (1984) and Reba and Kerschen (1996). Mish and Devenport (2006b) attributed the low f' reduction in loading spectra to distortion of the oncoming flow by the mean velocity field. It was also noted that this effect was only significant when the relative scale of the inflow turbulence to aerofoil chord is sufficiently small ($< 13\%$).

The influence of free stream turbulence (FST) intensity on the performance characteristics on a lifting surface has been extensively investigated and shown to have significant quantitative and qualitative effects (Hoffmann, 1991; Huang and Lee, 1999; Devinant et al., 2002). Experiments conducted by Hancock and Bradshaw (1983) showed an increase in skin friction of a flat plate boundary layer when encountering increased FST. When exposed to an adverse pressure gradient, Hoffmann and Kassir (1988) observed a higher resistance to separation due to increased momentum transmission from the free stream to the boundary layer. This resistance to separation is seen on aerofoils encountering FST intensities varying from 0.25% and 16.00% (Hoffmann, 1991; Devinant et al.,

2002; Wang et al., 2014). This momentum or turbulent kinetic energy (TKE) transfer encourages shear layer transition along with a reduction in the integral length scale to boundary layer thickness ratio, thus resulting in a resistance to separation. With aerofoil performance shown to be significantly affected, not just by intensity level, but by the integral length scales as well, the embedded turbulence of a boundary layer poses an extra degree of complexity due to the various length scales involved (Smits et al., 2011).

It has been shown by Swalwell et al. (2001) that the separation and re-attachement of an aerofoil boundary layer is significantly influenced by the Re and FST of the oncoming flow. Hence, the degree of intensity and Re of the flow can either cause or prevent the formation of a separation bubble (Li et al., 2011; Samson and Sarkar, 2016), and is also a known source of vortex shedding, and therefore unsteady loading (Mayda et al., 2002). Additionally, Devinant et al. (2002) showed that variations in the aerodynamic properties due to changes in Re of wind turbine blades, such as lift, drag, pitching moment and pressure distribution, were reduced when encountering high levels of FST intensity ($I > 12\%$). A turbulence intensity threshold identified by Huang and Lee (1999) shows that increases in turbulence intensity past 0.45% has minimal effect to the flow regime.

In a maritime context, insight into the flow phenomena and dynamic response involved with flow-induced vibrations of a hydrofoil due to unsteady loading is of significant interest. Ducoin et al. (2012a) experimentally characterized the laminar to turbulent transition induced vibrations on a hydrofoil. With further investigation, Ducoin et al. (2012b) also observed vortex shedding from the laminar separation bubble as well as dual frequency vortex shedding from the leading edge to cause vibration. One critical aspect noted in these investigations, and highlighted in the work by Zarruk et al. (2014), is the natural frequency of a hydrofoil. In the situation where a flow-induced vibration frequency coincides with the natural frequency, the resulting amplification in tip deflections (resonance) may result in undesirable through to critical conditions.

Recent experiments by Lysak (2011) and Lysak et al. (2016) have obtained loading spectra from hydrofoils of various thickness encountering grid turbulence that closely resemble theoretical predictions. Comparing the experimental results with their adaptation of vortex lift theory (Howe, 2001), Lysak et al. (2013) accurately predicted the high-frequency reduction in the loading spectra as thickness increases. Suggestions for future work by Lysak (2011) highlight the importance to further investigate the effect of incidence and camber on the loading spectra as well as overcoming background vibration contamination to analyze higher frequencies. The importance of these suggestions is highlighted in work by Khoo et al. (2015) who measured the unsteady loading on a NACA0012 hydrofoil where a significant increase in the loading spectra is observed, particularly at low frequencies, when transitioning to stall. In addition, the resolvable frequency range was limited due to the inherent dynamic response from the coupled force balance/hydrofoil system, similar to that experienced by Lysak et al. (2016). Despite this extensive theo-

retical, numerical and experimental activity on the unsteady loading on a lifting surface encountering grid turbulence, there is a paucity of published material on the related topic of encountering structured turbulence, such as a boundary layer.

The present study aims to provide additional insights into the physics determining the loading of a hydrofoil encountering the structured turbulence of an oncoming boundary layer. Forces, both steady and unsteady, are obtained for a range of Reynolds numbers (Re), incidence (α) and boundary layer thicknesses (δ). Immersion of the hydrofoil span in the boundary layer is adjusted from around $\frac{1}{8}$ to the full span. These results provide design guidance for the development of high-performance appendages encountering a boundary layer. Additionally, the data obtained will aid in determining the frequency response necessary from an improved force balance and model design for future unsteady force measurements.

2.3 Experimental Overview

2.3.1 Experimental Setup

Measurements were carried out in the Cavitation Research Laboratory (CRL) water tunnel at the Australian Maritime College. The tunnel test section is 0.6 m square by 2.6 m long in which the operating velocity and pressure ranges are 2 to 12 m/s and 4 to 400 kPa absolute, respectively. The tunnel volume is 365 m^3 with demineralised water (conductivity of order 1μS/cm). The test section velocity is measured from one of two (high and low range) Siemens Sitransp differential pressure transducers models 7MF4433-1DA02-2AB1-Z and 7MF4433-1FA02-2AB1-Z (measuring the calibrated contraction differential pressure) with estimated precisions of 0.007 and 0.018 m/s, respectively. A detailed description of the facility is given in Brandner et al. (2007).

A schematic representation of the test set-up is given in figure 2.1 with definition of the coordinate system used and the main geometric parameters shown in figure 2.2. The models were mounted on either a static or dynamic 6-component force balance. The hydrofoils extended vertically into the flow through a 160 mm diameter penetration in the tunnel ceiling. The 160 mm diameter penetration was made fair (to 50 μm) using a disk mounted on the measurement side of the balance. The fairing disk has a nominal 0.5 mm radial clearance to avoid interference with the force measurement. Of the total load vector measured, steady and unsteady components of normal force, axial force and pitching moment are presented. Spanwise forces and roll/yaw moments are not considered as they may be contaminated by the ceiling pressure distribution acting on the disk with this setup. Measurements were made at streamwise locations of 0.7 and 1.9 m downstream from the test section entrance to maximise the range of hydrofoil immersion in the ceiling boundary layer. Data was sampled at 1,024 Hz for durations sufficient to capture 1,000 and

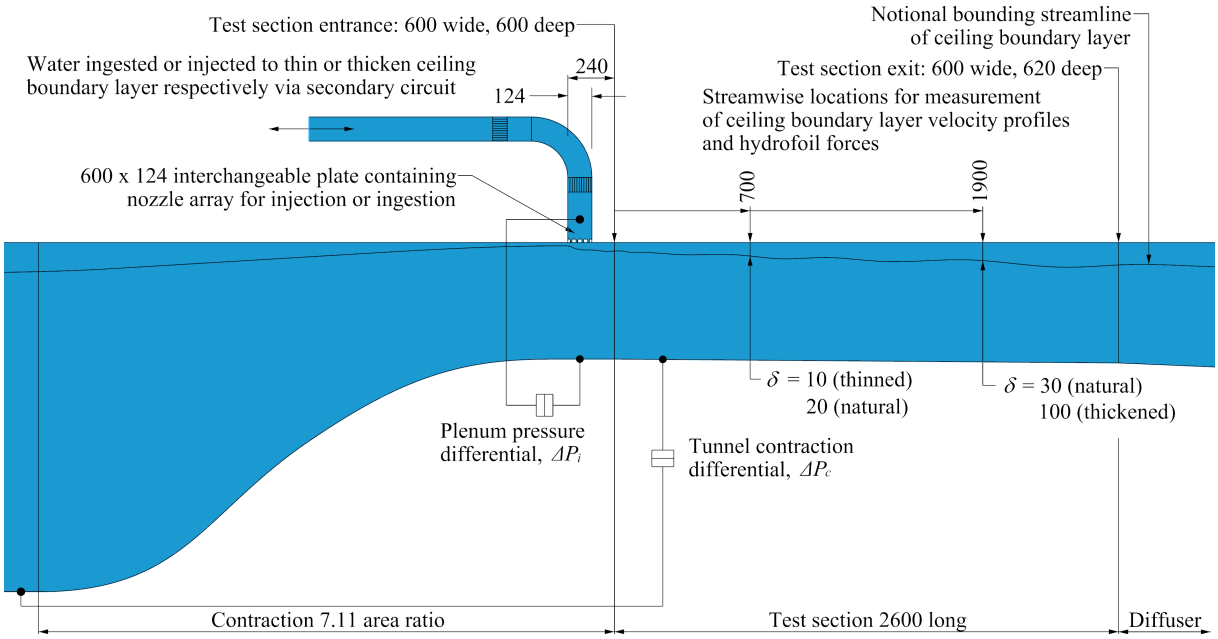

Figure 2.1: Schematic of the experimental setup whereby a ceiling mounted hydrofoil encounters a turbulent boundary layer that immerses it to varying degrees (All dimensions are in mm).

22,000 chord passages, $n = TU_\infty/c$, where T is the acquisition period, U_∞ is the freestream velocity and c is the mean chord, for steady and unsteady measurements, respectively. Test section free-stream velocity was varied to achieve chord-based Reynolds numbers, $Re = U_\infty c/\nu$, ranging from 0.4×10^6 to 1.2×10^6, where ν is the kinematic viscosity of the water.

2.3.2 Model Hydrofoil Details

Hydrofoil geometry has been selected based on the requirements discussed above for the modelling of unsteady conditions typical of those experienced by control surfaces. The chosen geometry was a NACA0012 profile with a symmetric (unswept) trapezoidal planform with a 80 mm tip and 120 mm root chord. Two models were constructed with spans (b) of 120 mm and 240 mm giving aspect ratios (b/c) of 1.2 and 2.4, respectively. This achieved a wide range of oncoming ceiling boundary layer thickness to hydrofoil span ratios, δ/b, from 0.08 up to 0.90 (with δ being the thickness where the streamwise velocity is equal to $0.99U_\infty$). The chord length was chosen to be compatible with mounting to the water tunnel test section and sufficient to obtain Re values of 1.2×10^6.

The response spectrum of both hydrofoils was determined from an impact test by Khoo et al. (2015) with results summarized in table 2.1. First-mode natural frequencies were obtained in air at 536 Hz and 170 Hz, and in-water at 273 and 86 Hz for the 120 mm and 240 mm models, respectively. The mode shapes of the hydrofoils were predicted based on unpublished results from experiments conducted by Clarke et al. (2014) as well FEA modal analyses. The results showed the first mode of both hydrofoils as well as

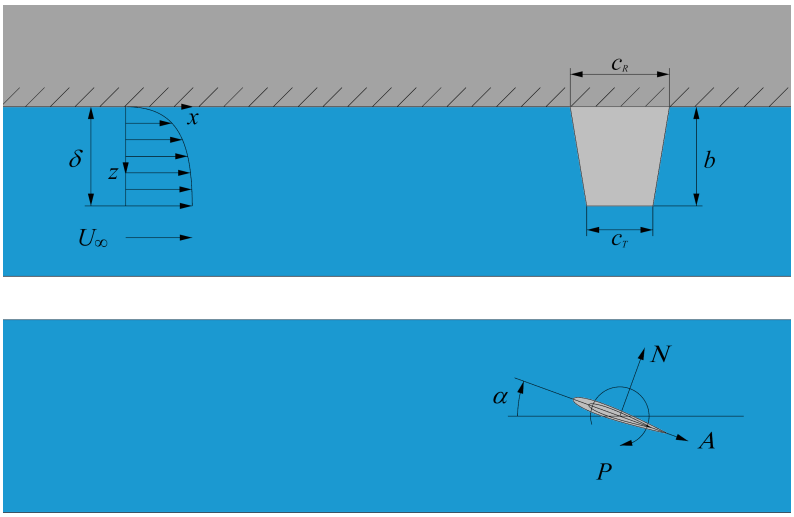

Figure 2.2: Schematic of the experimental setup whereby a ceiling mounted hydrofoil encounters a turbulent boundary layer that immerses it to varying extents.

Hydrofoil Dynamic Properties	Hydrofoil span	
	120 mm	240 mm
First bending mode in air (Hz)	536	170
First bending mode in water (Hz)	273	86
Second bending mode in air (Hz)	–	783
Second bending mode in water (Hz)	–	399
Added mass for first and second bending modes, $2m_a$(kg)	0.94	1.88
Mass of hydrofoil, m (kg)	0.33	0.60

Table 2.1: Natural frequencies, mass and added mass values of the model hydrofoils utilized in the experiment with added mass estimates calculated as per the method of Blevins (1979).

the second mode of the 240 mm hydrofoil were all of the bending type. To predict the in-water natural frequencies added mass estimations were calculated using formulas from Blevins (1979) where the hydrofoil was treated as a cantilevered rectangular flat plate. Both models were machined from solid Aluminium 6061-T6 billets to 0.8 µm surface finish and 0.1 mm surface tolerance. The models were anodised to a thickness of approximately 5 µm.

A body-fixed coordinate system was used to define the loads acting on the hydrofoil which is presented in figure 2.2. The normal force, N, axial force, A, and pitching moment, P, acting on the hydrofoils are presented as dimensionless coefficients with $C_N = 2N/\rho U_\infty^2 cb$, $C_A = 2A/\rho U_\infty^2 cb$ and $C_P = 2P/\rho U_\infty^2 c^2 b$, respectively. The unsteady component of the forces is represented with $'$ denoting the standard deviation of the time varying quantities. The centre of pressure, x_{cop}, is calculated as $x_{cop} = (c/2 - P/N)$ where $x_{cop}/c = 0.0$ and 1.0 denotes the leading and trailing edge, respectively, at midspan of the hydrofoil. To utilize the large dataset obtained using the static force balance to

gain insight on the unsteady component, the time series required filtering to remove the static force balance response from the spectra. This was achieved by applying an infinite impulse response lowpass filter to the time series with a cut-off frequency of 100 Hz and a steepness value of 0.95. The standard deviation calculated from the filtered time series compared favourably with those obtained from the dynamic force balance with the filtered standard deviation values presented in Section 2.4.2.

2.3.3 Static and dynamic force balances

To obtain both steady as well as unsteady forces with a high resolvable frequency range, two force balances were utilized. Steady forces were measured using a *'static'* force balance incorporating six MTI 4856-500 beam load cells and flexures to connect the measurement and non-measurement consoles of the balance (figure 2.3). The static force balance is relatively electronically stable with sensor drift seen to be negligible over measurements spanning many hours making it suitable for steady force measurements. The natural frequency of the static force balance is measured to be between 139 and 148 Hz (Khoo et al., 2015). For unsteady force measurements, the dynamic force balance (figure 2.4) was utilized for its increased resolvable frequency range compared to the static force balance. A *'dynamic'* force balance features four 3-component Kistler 9602 piezoeletric force sensors with integrated charge amplifier electronics that are compressed between the measurement and non-measurement consoles. The high stiffness of the piezoelectric force sensors in combination with force balance architecture results in a maximum resolvable frequency of approximately 1,000 Hz.

The calibration of both the static and dynamic force balance is performed on a purpose-built calibration frame. An accurately machined mounting plate and calibration arm is attached to the measurement side disk of the force balances to which static forces are applied in six orientations, loading the force balance in the A, N, S, R, N and P directions (figures 2.3 and 2.4). The static forces are generated using precision weights and gravity that are either directly slung off the calibration arm or via an air bearing depending on the loading orientation. Static calibration of the dynamic force balance is made possible by integrated charge amplifier electronics in the piezoelectric force sensors that result in sufficiently low drift that can be compensated for by employing a pilgrim step loading technique (Mack, 2006).

The static force balance was calibrated by a least squares fit between a basis vector loading cycle and the 6 outputs giving a 6×6 matrix. The dynamic force balance was calibrated by a least squares fit between a basis vector loading cycle and the 12 outputs to produce a 12×6 matrix. The calibration matrix was calculated by taking the right pseudo-inverse of the non-square voltage matrix using the Moore-Penrose method and multiplying it with the force matrix. The estimated precision of all components for the

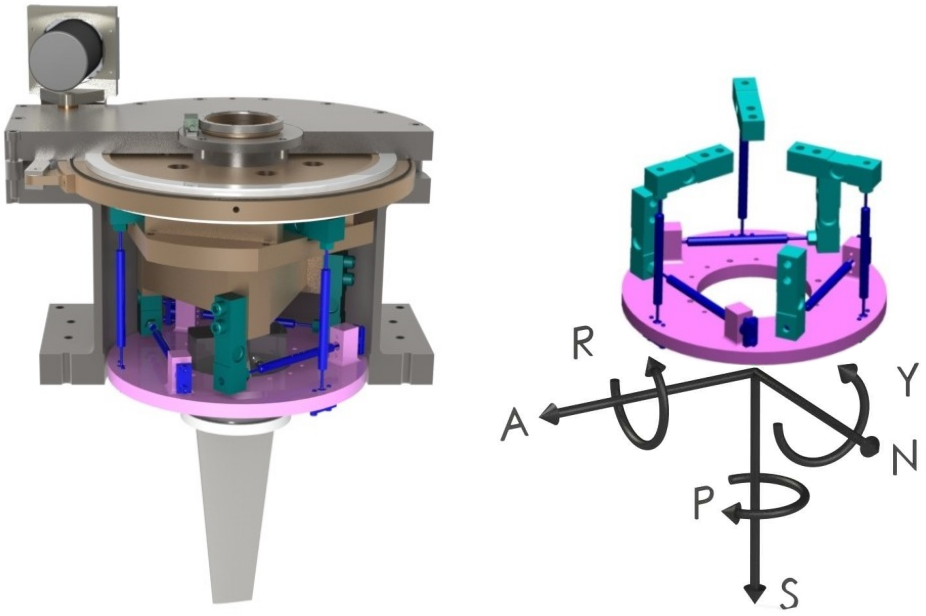

(a) (b)

Figure 2.3: Static force balance configuration showing (a) casing sectioned view, with a hydrofoil attached, to show internal assembly and (b) load cell and flexure layout on the measurement side console (in pink) with the coordinate system used as shown.

static and dynamic force balances are less than 0.1% and 0.5%, respectively.

Forces were measured at a set of mean chord-based Reynolds numbers, $Re = U_\infty c/\nu$, where ν is the kinematic viscosity and c denotes the mean chord, $c = (c_T + c_R)/2 = 0.1\text{m}$, with the subscripts T and R representing the tip and root of the hydrofoil. Measurements were conducted at Re values ranging from 0.2×10^6 to 1.2×10^6 in increments of 0.2×10^6. For each Re value, force measurements were acquired over the range of α from $-1°$ to beyond stall. The upper limit varied between 25° and 20° for the 120 mm and 240 mm span hydrofoils, respectively. The incidence was adjusted using the balance automated indexing system incremented in 0.5° steps with an incremental precision less than 0.001°. The tunnel was pressurised up to 350 kPa to suppress cavitation occurrence for all test conditions.

2.3.4 Boundary Layer Manipulator

To obtain a test section ceiling boundary layer of the desired scale, it was artificially thickened via an array of cross flow jets located upstream of the test section. At the test locations, the boundary layer thickness, δ, at which the mean velocity, $U = 0.99U_\infty$, was adjusted from its natural state of 19.1 mm at $x = 0.7\,\text{m}$, to a maximum of 107.4 mm at $x = 1.9\,\text{m}$. The boundary layer thickness, δ, was controlled by adjustment of the flow rate through the jet array. A detailed description and performance characteristics of the CRL boundary layer manipulator is given in Belle et al. (2016). Based on the performance

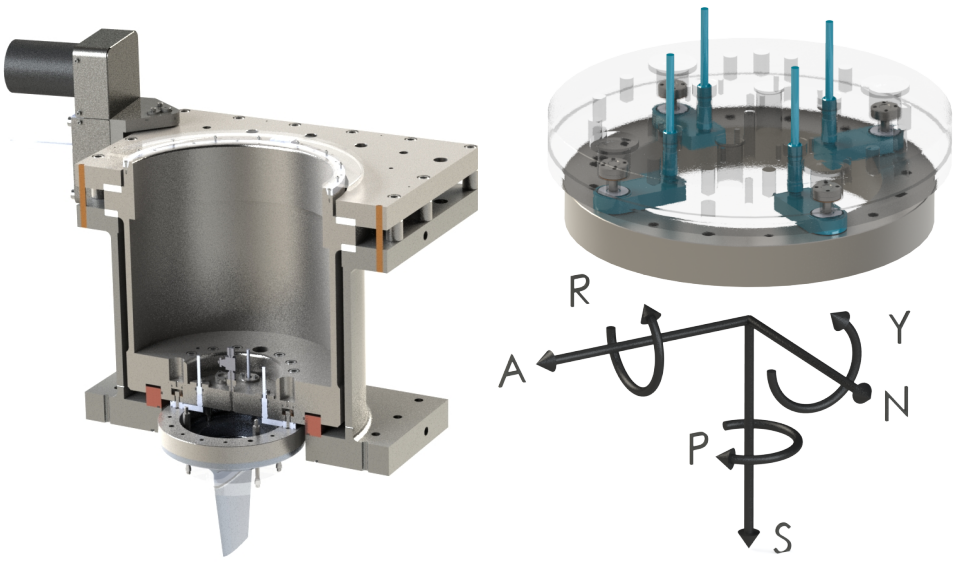

(a) (b)

Figure 2.4: (a) Dynamic force balance section view and (b) a view showing the orientation of the four Kislter 9602 piezoelectric loadcells. The loadcells (teal) are preloaded between a non-measurement (transparent) and measurement side console (grey), with the coordinate system used defined as shown.

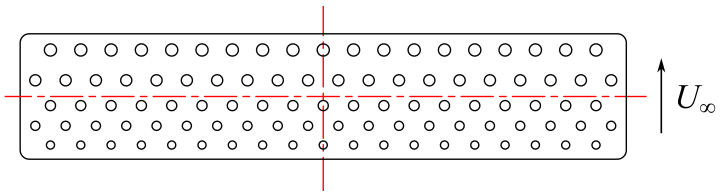

Figure 2.5: Test plate used in the artificial thickening of the oncoming ceiling boundary layer. The plate features a nozzle configuration with triangular spacing and varying nozzle diameter as detailed in table 2.2.

of the plate geometries previously tested for boundary layer thickening, a revised design (figure 2.5) was developed to optimize the velocity profile in the outer or wake region. It is this region which extends over the largest portion of the boundary layer thickness and it contains the larger turbulent structures. The plate features 5 rows of holes in a triangular configuration which increase in diameter in the downstream direction. A summary of key geometrical properties of the plate is given in table 2.2.

The artificial boundary layer thickness was varied by adjusting the mass flux, or jet, to freestream velocity ratio which is controlled and set by the injection pressure coefficient, given by:

$$C_{pi} = \frac{p_i - p_\infty}{\frac{1}{2}\rho U_\infty^2} \tag{2.1}$$

where p_i is the injection pressure and p_∞ is the free stream static pressure (see figure 2.1 for the pressure measurement locations). C_{pi} was varied between 0.04 and 0.62 to obtain

Property	Value
Number of holes	97
Hole diameter (mm)	8 – 12
Bellmouth radius (mm)	5
Open area (mm^2)	7769
Streamwise hole spacing (mm)	30 – 19
Transverse hole spacing (mm)	30
Plate thickness (mm)	15

Table 2.2: Geometric properties of the artificial thickening plate which featured rows of holes where the diameter of the first row of holes was equal to 8 mm. The hole diameter increases by 1 mm in the following row in the downstream direction, with the last row hole diameter being 12 mm.

a wide range of boundary layer thickness to span ratios, δ/b.

2.3.5 Boundary Layer Measurements

Boundary layer mean velocities were obtained using a 0.7 mm outside, by 0.4 mm inside, diameter total head tube traversed along the vertical centre plane of the test section. A wall reference static tapping of 1 mm diameter was located on the test section ceiling 75 mm off the centre plane. The total head tube was mounted within a support tube that tapered from 0.7 mm at the probe head to 6 mm. The support tube was mounted to a 30 mm by 10 mm elliptical stem section that penetrated through the test section ceiling (figure 2.6). The total head tube was traversed using an automated linear traverse with an estimated precision of 3 μm. Long-range macro-optics and back-lighting were used to establish the probe position on the ceiling. Pressures were measured using a Validyne Model DP15TL differential pressure transducer via an automated pressure multiplexer.

Boundary layer velocity profile measurements were comprised of 50 data points on a log distribution being sampled at 1,024 Hz. Measurements were taken for durations sufficient to capture a minimum of 5,000 boundary layer turnover times (TU_∞/δ), where T is the measurement duration, sufficient to obtain converged results (Belle et al., 2016). Preston tube measurements provided the wall shear stress, τ_w, using the calibration by Head and Ram, as presented in Goldstein (1996). Pitot probe corrections were applied to the measurements following the method outlined in Bailey et al. (2013) where shear layer and wall proximity effects were taken into account using equations by McKeon et al. (2003). These corrections were applied in the same manner as detailed by Belle et al. (2016). All boundary layer measurements were conducted at $Re = 1 \times 10^6$.

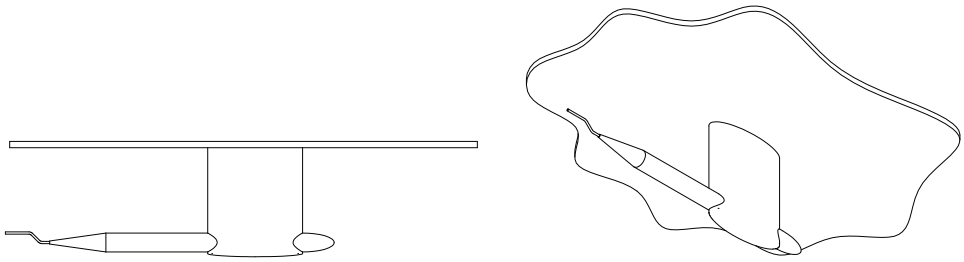

(a) Side View (b) Isometric View

Figure 2.6: Elliptical stem total head tube used for measurement of the natural and thickened boundary layer mean velocity profiles. The major and minor diameters of the elliptical stem are 30 and 10 mm. The tubes have a inner and outer diameter of 0.72 and 0.4 mm respectively. The total head tube on the elliptical stem probe is cranked in the vertical plane to enable the probe to be traversed to the ceiling for Preston tube measurements.

2.3.6 Electrical Noise Removal

The design of the dynamic force balance to possess a high natural frequency incorporated piezoelectric force sensors due to their high stiffness, which in turn have a low sensitivity. This results in a low signal to noise ratio and force measurements that are contaminated by electrical noise, particularly at the mains frequency fo 50 Hz and its harmonics. To overcome this, a modified version of the noise removal technique developed by Alamshah et al. (2013) was used. This technique which was initially developed for the removal of wind-induced noise in shielded microphones utilizes cross-spectral analysis to obtain the incoherent output power (IOP) that distinguishes the contribution of one signal from another.

The modified IOP method was applied to the datasets by first determining the magnitude-squared coherence, γ^2, between the normal force and one of the voltage channels. This was achieved using the auto-spectra of the normal force and voltage channel, $G_{NN}(f)$ and $G_{VV}(f)$ respectively, along with the cross spectrum of the two signals, $G_{VN}(f)$, as shown in equation 2.2.

$$\gamma^2 = \frac{|G_{VN}(f)|^2}{G_{VV}(f)G_{NN}(f)} \tag{2.2}$$

Some coherency exists between the two signals at frequencies other than 50 Hz and its harmonics. To avoid removing components of the signal at these other frequencies, the IOP method was modified to consider only a 6 Hz bandwidth at 50 Hz and harmonics. This was achieved when calculating the IOP of the normal force auto-spectrum in equation 2.3, by setting the coherence value to zero for frequencies that lie outside of the bandwidth. The IOP normal force spectra are presented in Section 2.4.3.

$$IOP(f) = \left[1 - \gamma^2(f)\right] G_{NN}(f) \tag{2.3}$$

2.4 Results

2.4.1 Ceiling Boundary Layer Profile

The measured natural and artificially thickened ceiling boundary layer profiles are shown in figure 2.7. Using parameters derived from the natural boundary layers, the inner profiles have been scaled using inner and outer variables and compared to the law of the wall:

$$U^+ = \frac{1}{\kappa} \ln z^+ + A \tag{2.4}$$

where $U^+ = U/U_\tau$, $z^+ = zU_\tau/\nu$, U is the measured mean velocity and $U_\tau = \sqrt{\tau_w/\rho}$ is the wall friction velocity.

The inner profile can be seen to be linear and closely follows the law of the wall for C_{pi} values ≤ 0.42. As C_{pi} is increased to 0.52, the profile is seen to deviate slightly in the wake region, shifting below the law of the wall. This trend continues as C_{pi} is increased to 0.62 and is an indication of insufficient mixing and profile development between the injection and measurement positions. This is due to the increased boundary layer thickness reducing the development length in terms of number of boundary layer thicknesses (or turnovers), that occur upstream of the measurement position (Belle et al., 2016).

The outer profile is compared against the defect form of the modified Coles law of the wake given by Guo et al. (2005):

$$U_\infty^+ - U^+ = -\frac{1}{\kappa}\left(\ln \eta + 2\Pi \cos^2 \frac{\pi\eta}{2} + \frac{1-\eta^3}{3}\right) \tag{2.5}$$

where $\eta = z/\delta_c$ and δ_c is the boundary layer thickness at which the mean velocity, $U = U_\infty$, which is determined by performing a least squares fit of the outer 0.6δ to equation 2.5. The wake strength factor, Π, was determined using the relationships given by Guo et al. (2005) shown below in equation 2.6 which is based on the measured natural boundary layer properties. This resulted in $\Pi = 0.62$ and was applied to the thickened profiles.

$$\frac{\delta^*}{\delta_c} = \frac{1}{U_\infty^+ \kappa}\left(\Pi + 0.75\right) \tag{2.6}$$

The outer profiles show that the natural boundary layers follow the modified Coles law at both streamwise positions closely. In comparison, the artificially thickened boundary

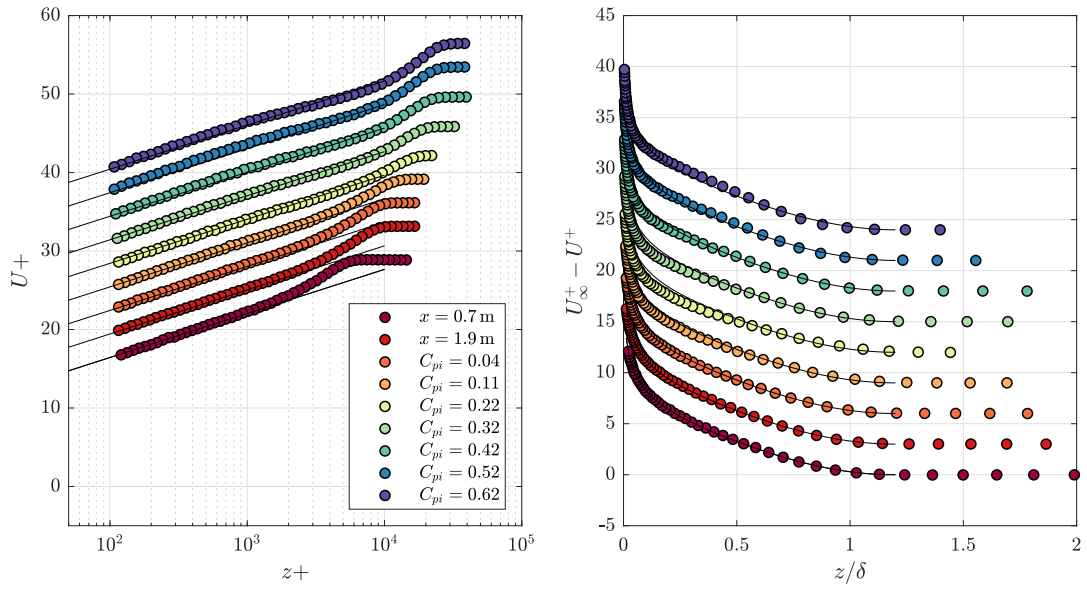

(a) (b)

Figure 2.7: Variation of the inner (a) and outer (b) boundary layer profiles at $Re = 1\times10^6$ for the natural boundary layers at $x = 0.7$ and 1.9 m as well as the artificially thickened boundary layers for $x = 1.9$ m. The inner boundary layer profiles are compared against the log law (equation 2.4) where the outer profiles are compared against modified Coles law (equation 2.5). The profiles are staggered by a $U+$ of 3 in both plots.

layers exhibit a velocity excess in the inner wake region that increases with C_{pi} up to 0.32 where it reaches a maximum. Further increase in C_{pi} sees the velocity excess decrease and remains evident at $C_{pi} = 0.62$. Additionally, the deviations observed in the inner scaled profiles at $C_{pi} = 0.62$ and 0.52 are also evident in the outer profiles manifesting as velocity deficits between $z/\delta = 0.25$ and 0.55.

Performance of the artificially thickening of the boundary layer is also assessed using the thickness and integral properties as a function of C_{pi} (figure 2.8). This is done by normalizing the boundary layer, momentum and displacement thickness by their natural values, δ_N, θ_N and δ_N^*, respectively, at the same location with the results presented in figure 2.8. All thicknesses show a consistent and steady increase with C_{pi} between 0.1 and 0.5. The shape factor shows good results for all values of C_{pi}, only ranging between 1.23 and 1.27.

To assess the conformity of certain thickened boundary layer properties to those of fully developed flat plate zero pressure gradient boundary layers, asymptotic relations are used. The logarithmic skin friction law described in Jones et al. (2001); Guo et al. (2005); Nagib et al. (2007) provides a relationship between C_f and $Re_\theta = U_\infty\theta/\nu$ and is given as

$$U_\infty^+ = \sqrt{\frac{2}{C_f}} \approx \frac{1}{\kappa}\ln(Re_\theta) + C \tag{2.7}$$

where C = 5.1 which is derived from a least squares fit of the natural boundary layer.

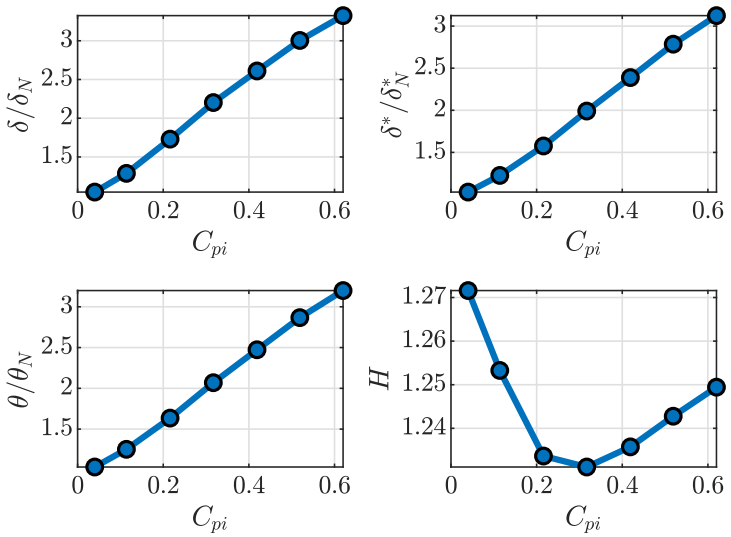

Figure 2.8: Variations of thickness and integral properties of the artificially thickened boundary layer.

Additionally, a logarithmic relation between $Re_\tau = U_\tau \delta_c/\nu$ and C_f is derived by Guo et al. (2005) and is given as

$$\sqrt{\frac{2}{C_f}} \approx \frac{1}{\kappa_1} \ln(Re_\tau) + B_1 \tag{2.8}$$

where $\kappa_1 = 0.402$ and $B_1 = 6.94$ are derived from least-squares fitting of the natural boundary layer data. The results presented in figure 2.9 show that the thickened boundary layers show favorable comparison to equation 2.7 for $Re_\theta > 4\times10^4$. These results indicate that the boundary layers of $Re_\theta \approx 3\times10^4$ and $Re_\tau = 1\times10^4$ can be thickened to just below $Re_\theta = 1 \times 10^5$ and $Re_\tau = 4 \times 10^4$, respectively, using this method of artificial thickening. Properties of the natural and artificially thickened boundary layers are summarized in table 2.3.

Comparing results with those provided by Belle et al. (2016) highlights the improved artificially thickened boundary layer properties of the redesigned thickening plate. The outer velocity profiles are shown to be as accurate, if not more accurate than the ones produced by previous designs for a much wider range of C_{pi}. With the large open area of the plate, this allowed relatively larger boundary layer thicknesses to be generated without sacrificing profile accuracy and allowing a larger range of immersion ratios to be investigated. Integral properties and asymptotic relations of the redesigned plate reinforce the conformity of the artificially thickened boundary layers to those developed on a flat plate in a zero pressure gradient.

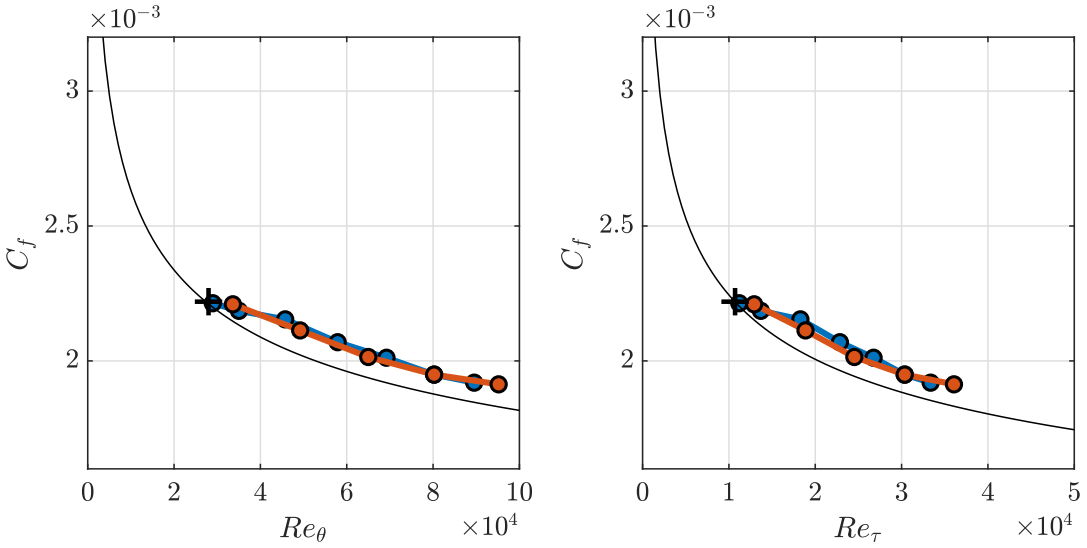

Figure 2.9: Comparison of the variation in C_f with Re_θ (left) and Re_τ (right) for the thickened and natural boundary layers. The asymptotic relations of C_f with Re_θ and Re_τ are defined in equations 2.7 and 2.8, respectively, and are represented as black lines with the measured natural boundary layer at $x = 1.9$ m represented by a black cross. Measurements taken at a constant C_{pi} are shown in orange with measurements taken a constant Re shown in blue.

C_{pi}	δ (mm)	δ^* (mm)	θ (mm)	H	Re_θ	Re_τ	C_f
			Artificial				
0.04	33.8	4.45	3.50	1.27	28,971	11,197	0.0022
0.11	41.6	5.31	4.24	1.25	35,034	13,699	0.0022
0.22	55.9	6.82	5.53	1.23	45,746	18,280	0.0022
0.32	71.1	8.62	7.00	1.23	57,896	22,855	0.0021
0.42	84.3	10.34	8.37	1.24	69,204	26,753	0.0020
0.52	97.1	12.06	9.70	1.24	80,241	30,360	0.0019
0.62	107.4	13.52	10.82	1.25	89,523	33,365	0.0019
			Natural				
$x = 0.7$ m	19.1	2.59	2.04	1.28	17,601	6,681	0.0024
$x = 1.9$ m	32.3	4.22	3.38	1.28	27,987	10,712	0.0022

Table 2.3: Summary of the measured artificial and natural boundary layer properties at $Re = 1 \times 10^6$. All artificially thickened boundary layer measurements were taken at a streamwise position of $x = 1.9$ m.

2.4.2 Steady and unsteady forces

Effect of Reynolds number

The effect of Re on the steady normal force acting on a hydrofoil in low and high boundary layer immersion situations is presented in figures 2.10 and 2.11, respectively. First analyzing the low-immersion case, the 240 mm hydrofoil is partially immersed in a relatively thin natural boundary layer resulting in an immersion ratio, δ/b, of approximately 0.08. As α is increased from 0°, all Re cases are seen to exhibit a steady increase in C_N before deviating from the linear trend with an increase in the normal force gradient highlighted in the $\partial C_N/\partial\alpha$ plot (figure 2.10). This deviation first occurs for $Re = 0.4 \times 10^6$ at $\alpha \approx 2.5°$ followed by the remaining cases in quick succession in order of ascending Re. As α is increased further, the $\partial C_N/\partial\alpha$ reaches a maximum with all Re cases $\leq 1.0 \times 10^6$ decreasing by $\alpha = 10°$. This increase in $\partial C_N/\partial\alpha$ for $Re = 0.4 \times 10^6$ corresponds with a local increase in the unsteadiness shown in C'_N.

This C_N deviation and unsteadiness behaviour is similar to that observed when a laminar separation bubble (LSB) forms on a hydrofoil. The adverse pressure gradient causes the laminar flow to separate and quickly transition to turbulent flow (Lissaman, 1983) before reattaching further downstream and forming a region of re-circulating flow known as a laminar separation bubble (Hoerner and Borst, 1985). At lower incidences where the adverse pressure gradient is low, a relatively large LSB can form between mid-chord and the trailing edge of the hydrofoil. This relatively large LSB has the ability to induce fluctuations such as those observed at $\alpha \approx 5.5°$ in figure 2.10. As the incidence increases to 7°, the resulting change in the suction side pressure distribution has been shown to cause the LSB to shrink and shift towards the leading edge (Hoerner and Borst, 1985). This has the effect of increasing the effective camber of the hydrofoil (Hansen et al., 2014) and thereby increasing the C_N and potentially causing the previously mentioned deviation. This deviation observed in current C_N results, potentially due to an LSB, exhibits a Re dependence with the deviation occurring at a higher incidence for higher Re. This has previously been attributed to the increased resistance to separation a higher Re flow provides where the flow over the hydrofoil would require an increased adverse pressure gradient to separate, which does not occur until higher incidences (Swalwell et al., 2001).

As α increases past 10°, $\partial C_N/\partial\alpha$ continues to reduce before leveling out as the hydrofoil approaches stall with the $Re = 0.4 \times 10^6$ case stalling first at $\alpha = 16°$. The other Re cases stall soon after in order of ascending Re with the $Re = 1.2 \times 10^6$ case being the last to stall at 17°. The sudden drop in C_N is an indication of leading-edge type stall similar to that observed when a short LSB bursts (Hoerner and Borst, 1985). Stall due to a short LSB bursting occurs when the increased adverse pressure gradient from the

increasing incidence strains a short LSB to the point the separated flow is unable to reattach to the hydrofoil (Hoerner and Borst, 1985). This results in separated flow covering the majority of the hydrofoils suction side and causing a sudden drop in the normal force and rise in unsteadiness as observed in figure 2.10. Stall is delayed with increasing Re as the increased kinetic energy of the higher Re flow is more resistant to separation.

It is worth noting the changes in the hysteresis characteristics between the Re cases. For the low-immersion case in figure 2.10, the width of the C_N hysteresis loop is seen to increase with Re from approximately 3.0° at $Re = 0.4 \times 10^6$ to 5.5° at $Re = 1.0 \times 10^6$, similar to that observed by Timmer (2008). The hysteresis behaviour is discussed further in section 2.4.2 where the role of boundary layer immersion is considered.

Comparing the C_N behaviour of the 240 mm hydrofoil low-immersion case to the 120 mm hydrofoil high-immersion case, i.e. the two extremes, for various Re reveals some interesting differences. In the high-immersion case, the 120 mm hydrofoil is immersed in the thickest artificially thickened boundary layer resulting in a $\delta/b = 0.81$ with the forces acting on the hydrofoil for various Re presented in figure 2.11. As α is increased from 0°, all Re cases exhibit a similar $\partial C_N/\partial\alpha$ up to 10°. Compared to the low-immersion case, the high-immersion case exhibits a lower $\partial C_N/\partial\alpha$, attributed to lower aspect ratio and increased exposure to lower momentum flow of the ceiling boundary layer. Additionally, the high-immersion case exhibits no indication of LSB formation for any of Re case unlike that observed in the low-immersion case. This may be attributed to the transfer of momentum and TKE from the encountered ceiling boundary layer to the one developing over the hydrofoil. This transfer of TKE energizes the boundary layer developing over the hydrofoil, promoting earlier transition to the turbulent regime, increasing its resistance to separation (Hoffmann and Kassir, 1988) and thereby preventing LSB formation.

Increasing the incidence past 10° sees a gradual reduction in the normal force gradient in the high-immersion cases. This behaviour is shown to have a Re dependence with the reduction in $\partial C_N/\partial\alpha$ occurring first in the $Re = 0.4 \times 10^6$ case at $\alpha \approx 10°$, followed by the other Re cases in ascending order. Further increase in incidence sees the Re cases approach stall with the $Re = 0.4 \times 10^6$ case stalling first at $\alpha = 21.5°$ with the remaining Re cases stalling in succession in ascending order with all cases stalled by $\alpha = 26°$. The gradual stall behaviour observed in the high-immersion case is typical of the trailing-edge type where the flow starts to separate close to the trailing-edge with the separation point migrating upstream as α increases. This differs to the sudden leading-edge type stall observed in the low-immersion case with the difference attributable to the increased transfer of TKE and momentum as well as the reduced aspect ratio.

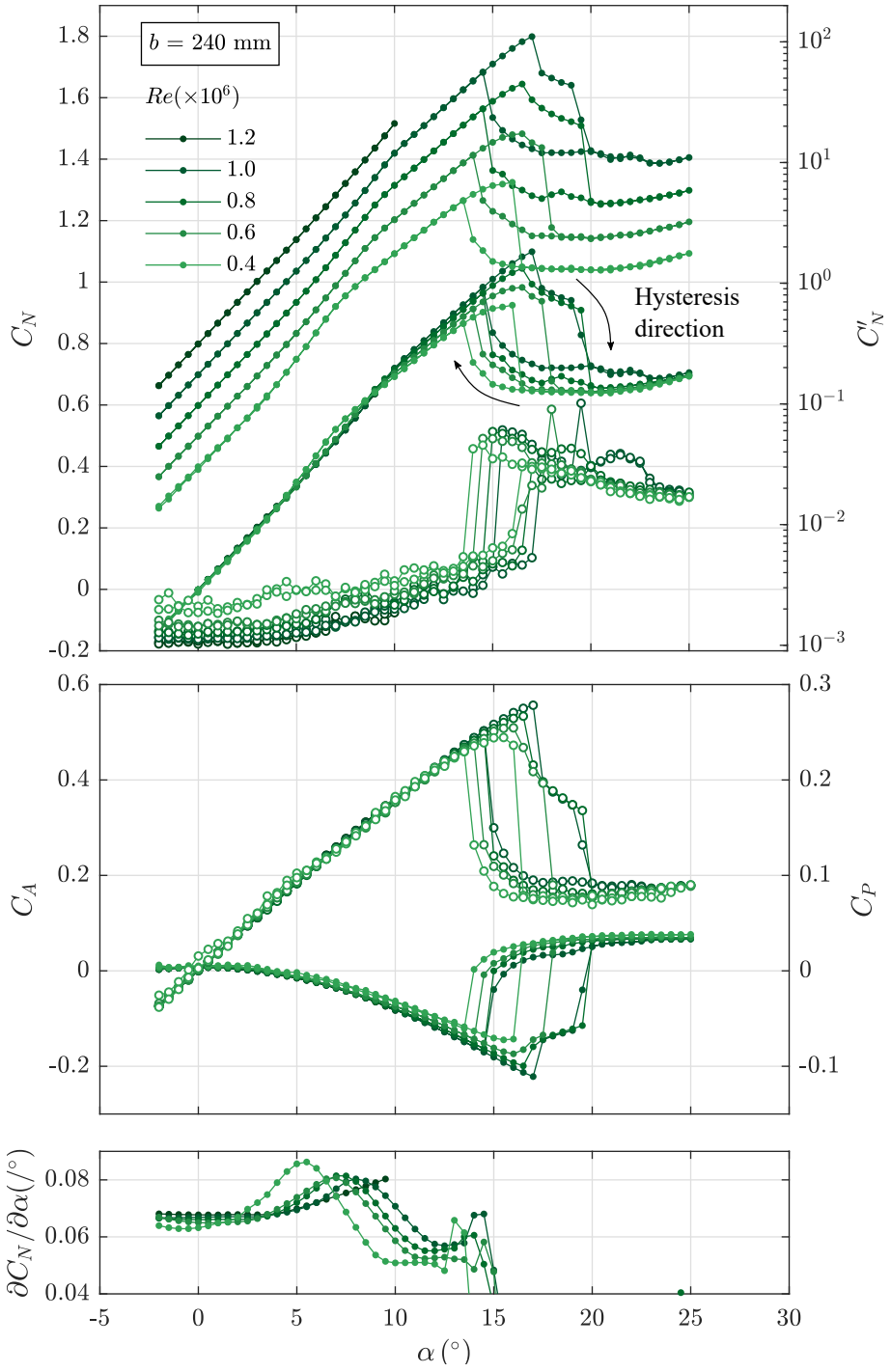

Figure 2.10: Mean (•) and standard deviation (○) of the time-varying normal force, C_N and C'_N respectively, with incidence, α, acting on the 240 mm span hydrofoil for different free-stream velocities showing the influence of Re (top). The hydrofoil is immersed in the natural boundary layer, resulting in an immersion ratio, δ/b, of 0.08. C_N is plotted twice with the second plotted with an initial C_N offset of 0.4 for $Re = 0.4 \times 10^6$ and then staggered by 0.1 with increasing Re. Mean of C_A (•) and C_P (○) for varying incidences (middle) provides insight into the mechanics of the excitations. The normal force slope, $\partial C_N/\partial\alpha$, is used to highlight trends in the normal force behaviour (bottom).

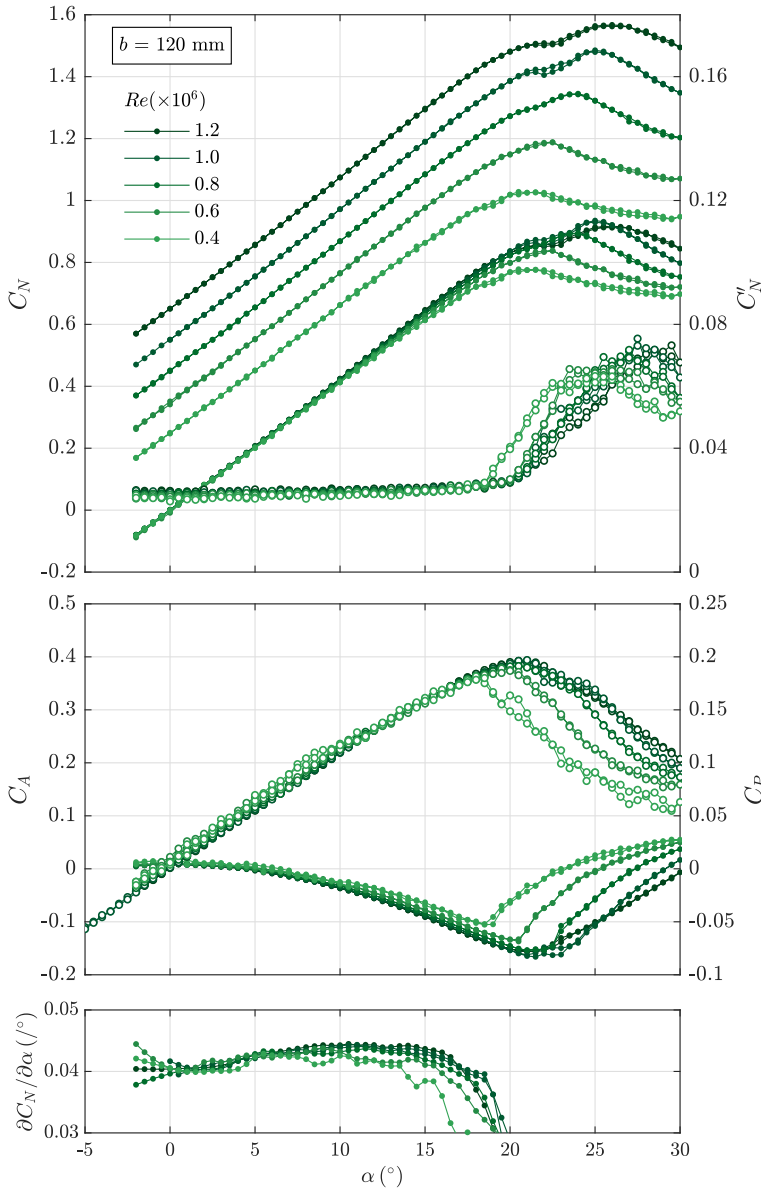

Figure 2.11: Mean (•) and standard deviation (○) of the time-varying normal force, C_N and C'_N respectively, with incidence, α, acting on the 120 mm span hydrofoil for different free-stream velocities showing the influence of Re (top). The hydrofoil is immersed in an artificially thickened boundary layer where $\delta/b = 0.81$. The C_N data is also replotted to provide clarity of the individual curves with an initial C_N offset of 0.4 for $Re = 0.4 \times 10^6$ and then staggered by 0.1 with increasing Re. Mean of C_A (•) and C_P (○) for varying incidences (middle) provides insight into the mechanics of the excitations. The normal force slope, $\partial C_N/\partial\alpha$, is used to highlight trends in the normal force behaviour (bottom).

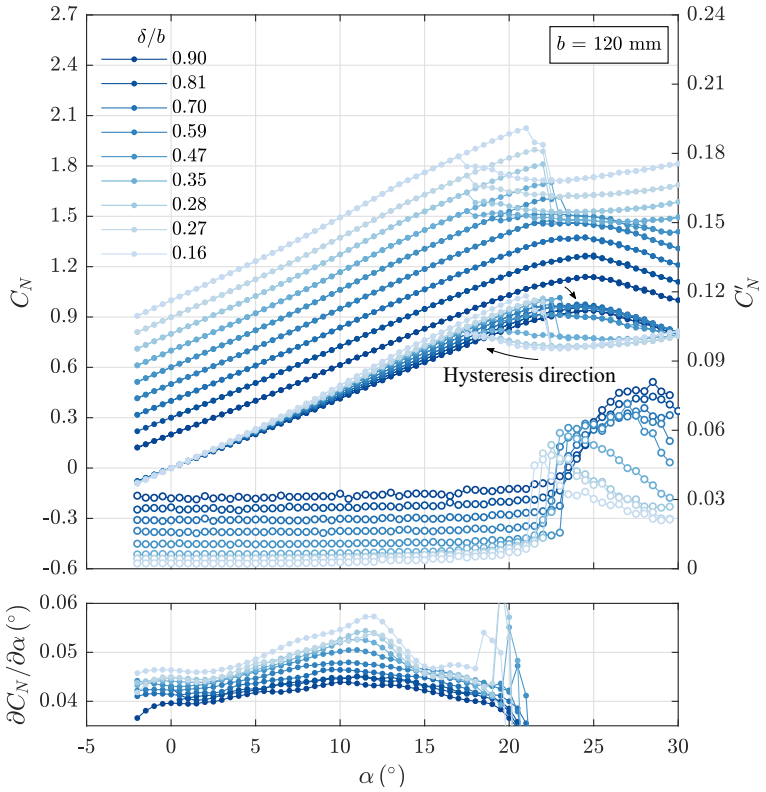

Figure 2.12: Mean (•) and standard deviation (○) of the time-varying normal force, C_N and C'_N respectively, with incidence, acting on the 120 mm span hydrofoil for δ/b ranging from 0.16 to 0.90 (top). The C_N data is also replotted to provide clarity of the individual curves with an initial C_N offset of 0.2 and then staggered in 0.1 increments for each δ/b case. Characteristics in the C_N behaviour for varying α is highlighted in the $\partial C_N/\partial\alpha$ plot (bottom) which is passed through a Savitsky-Golay filter of the 2$^{\text{nd}}$ order to smooth out the data.

Effect of boundary layer immersion

A comparison of the C_N behaviour for a range of δ/b acting on the 120 mm and 240 mm span hydrofoils (for $Re = 1.0 \times 10^6$) is presented in figures 2.12 and 2.13, respectively. In both cases, C_N decreases as δ/b increases for all pre-stall α. This is due to the increased span that is subjected to the lower momentum flow within the ceiling boundary layer resulting in a reduction in normal force. In addition, step increases to the level of unsteadiness can be observed with C'_N increasing incrementally with δ/b at all pre-stall α. This can be attributed to the increased exposure of the hydrofoils to the turbulent flow within the ceiling boundary layer and ceiling-junction horseshoe vortex as δ is increased. The flow at the ceiling-junction is characterized by a horseshoe vortex that forms at the leading edge and wraps around the wing with the turbulence in the vicinity of the vortex remaining high (Awasthi et al., 2020).

On the 120 mm hydrofoil, there are indications of an LSB forming with a deviation evident in $\partial C_N/\partial\alpha$ at $\alpha \approx 11°$ for the lower immersion ratio cases that disappears as the boundary layer thickens (figure 2.12). This trait is more evident on the 240 mm hydrofoil in figure 2.13 and can potentially be attributed to the shrinking of the LSB either in the

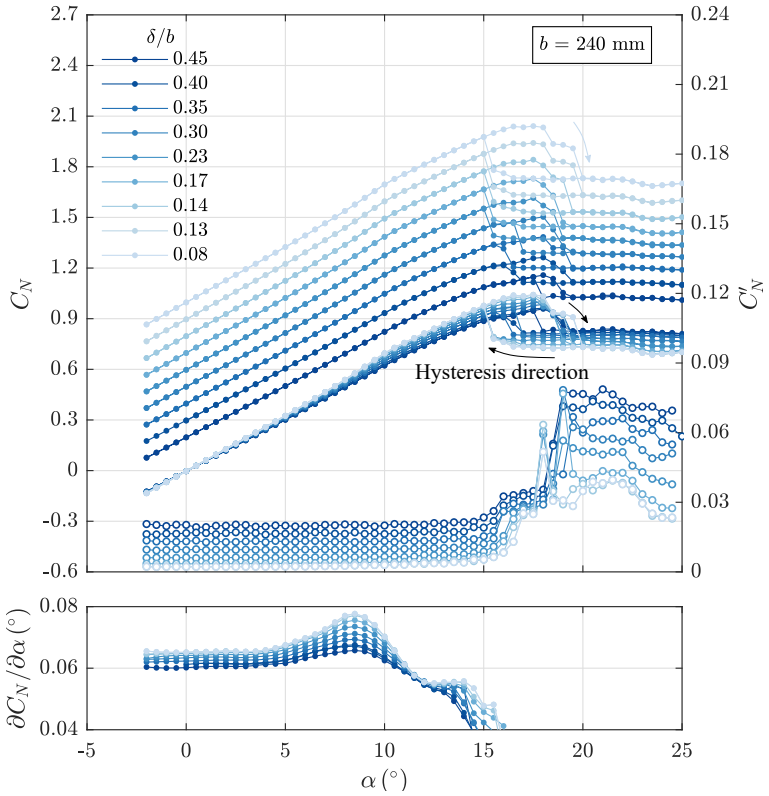

Figure 2.13: Mean (•) and standard deviation (○) of the time-varying normal force, C_N and C'_N respectively, with incidence, acting on the 240 mm span hydrofoil for δ/b ranging from 0.08 to 0.45 (top). The C_N data is also replotted to provide clarity of the individual curves with an initial C_N offset of 0.2 and then staggered in 0.1 increments for each δ/b case. Characteristics in the C_N behaviour for varying α is highlighted in the $\partial C_N/\partial\alpha$ plot (bottom) which is passed through a Savitsky-Golay filter of the 2$^{\text{nd}}$ order to smooth out the data.

chordwise direction, spanwise direction or both. As mentioned earlier in section 2.4.2, the behaviour of the LSB is influenced by the transfer of TKE and momentum (Hoffmann and Kassir, 1988) which would increase with increased immersion in the ceiling boundary layer. In regards to the chordwise length of the LSB, this transfer of TKE and momentum promotes earlier transition of the separated flow encouraging reattachment closer to the leading edge, shrinking the chordwise length of the LSB and therefore its influence on the C_N force generated. In regards to the spanwise length of the LSB, sufficient transfer of TKE and momentum to the early stages of the hydrofoil boundary layer could cause it to transition before reaching the maximum adverse pressure gradient, giving it the ability to resist separation, preventing an LSB from forming. This would result in LSB formation only being suppressed in the spanwise portion of the hydrofoil that is immersed in the ceiling boundary layer. This would result in the LSB influence decreasing with increased immersion on parameters such as the deviation in $\partial C_N/\partial\alpha$. The relative amplitude of the $\partial C_N/\partial\alpha$ peak decreasing with increasing immersion is seen to disappear by $\delta/b \geq 0.59$ with little non-linearity in the normal force gradient at pre-stall incidences, suggesting an LSB no longer forms on the hydrofoil (figure 2.12).

Similar behaviour is observed in C_A and C_P (figures 2.14 and 2.15) as seen with C_N where the absolute of each force decreases steadily with increased immersion in the boundary layer. Utilizing C_N and C_P to determine the x_{cop} provides insight into how boundary layer immersion influences the pressure distribution over the suction side of the hydrofoil. Upon initial comparison of the two hydrofoils (figures 2.14 and 2.15), it is revealed that x_{cop}/c shifts further along the 120 mm hydrofoil moving steadily towards the trailing edge with increasing incidence. x_{cop}/c is observed only to shift from $x_{cop}/c \approx 0.23$ at $\alpha = 5°$ to $x_{cop}/c \approx 0.25$ at $\alpha = 10°$ where it remains in the same position up to $\alpha = 15°$ for all δ/b. This *'shoulder'* can partially be seen on the 120 mm hydrofoil at low δ/b suggesting it is affected by the presence of an LSB.

Furthermore, the increased immersion of the 120 mm hydrofoil within the ceiling boundary layer is observed to have significant influence on the stall characteristics (figure 2.12). At low-immersion ratios, $\delta/b \leq 0.47$, stall is sudden with C_N dropping significantly at $\alpha = 21.0°$ for $\delta/b = 0.16$ to $\alpha = 23.0°$ for $\delta/b = 0.47$. As mentioned previously, this is typical of leading-edge type stall where the LSB *'bursts'* as the separated flow is unable to reattach with an increase in α. This results in separated flow covering the majority of the chord causing a sudden drop in C_N and a jump in C'_N. As δ/b is increased to 0.59, the hydrofoil is seen to exhibit a gradual drop in C_N as the hydrofoil stalls at $\alpha = 23.5°$, typical of trailing-edge stall (Hoerner and Borst, 1985). This transition from leading-edge to trailing-edge type stall as δ/b is increased from 0.47 to 0.59 also coincides with the disappearance of the deviation in the normal force curve attributed to the LSB. Further increases in δ/b sees stall become more gradual as well as being delayed, again attributable to the increased transfer of TKE. With the increased TKE, the hydro-

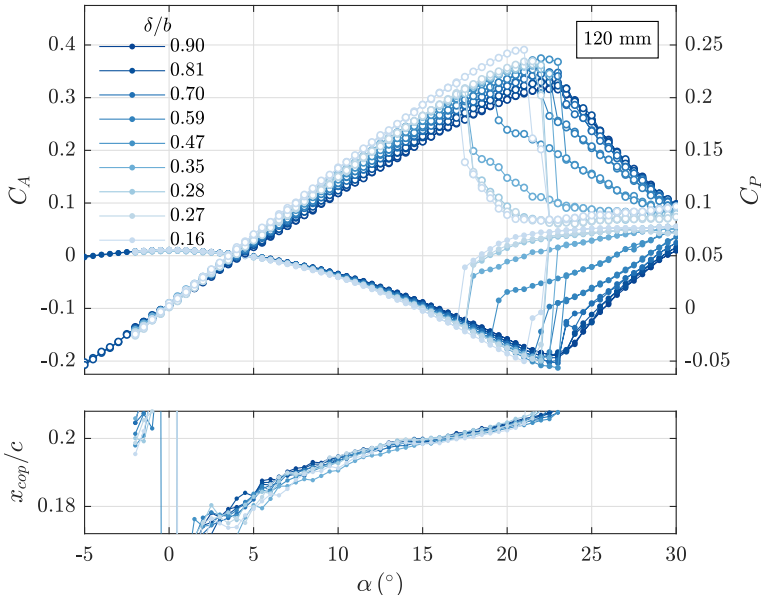

Figure 2.14: Mean of C_A (•) and C_P (○) with varying incidence (top) acting on the 120 mm hydrofoil for δ/b ranging from 0.16 to 0.90 provides insight into the mechanics of the excitations. Behaviour of x_{cop}/c with varying α (bottom) shows how increasing immersion shifts the centre of pressure along the chord.

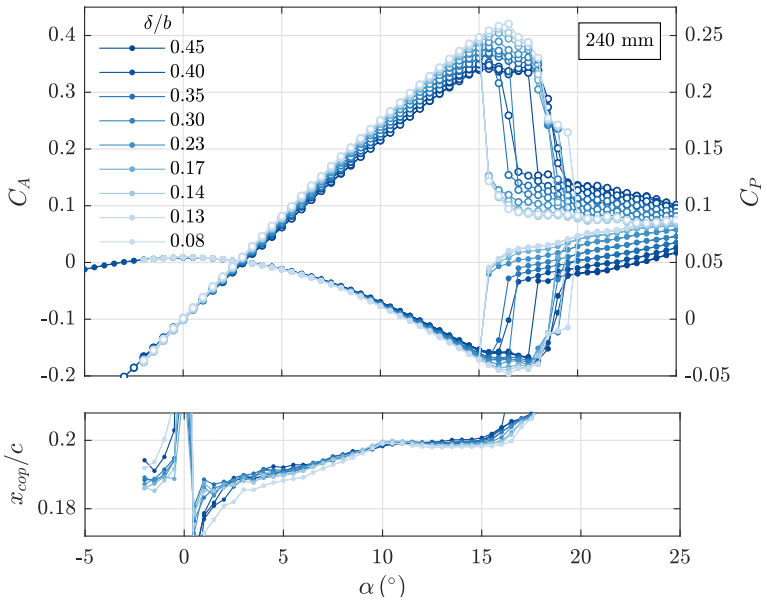

Figure 2.15: Mean of C_A (•) and C_P (○) with varying incidence (top) acting on the 240 mm hydrofoil for δ/b ranging from 0.08 to 0.45 provides insight into the mechanics of the excitations. Behaviour of x_{cop}/c with varying α (bottom) shows how increasing immersion shifts the centre of pressure along the chord.

foil boundary layer can resist separation, preventing leading-edge type stall and delaying trailing-edge type stall.

As mentioned previously in section 2.4.2, the width of the C_N hysteresis loop is shown to increase with Re for the low-immersion case ($\delta/b = 0.08$) in figure 2.10. Analysing the influence of boundary layer immersion on the hysteresis behaviour in figure 2.13, it is observed that increased immersion reduces the hysteresis loop width from 5.0° at $\delta/b = 0.08$ to 2.0° at $\delta/b = 0.45$ This hysteresis loop width variation is primarily attributed to changes in the stall incidence with little variation in the incidence that the flow reattaches.

2.4.3 Force Spectra

To allow unsteady loading characteristics to be identified, spectra have been obtained from the time series of the normal force and presented non-dimensionally as C_N in the form of power spectral density (PSD), with reduced frequency, $f' = fc/U_\infty$. Peak frequencies are present in all spectra due to the frequency response of the coupled force balance and hydrofoil system. The natural frequencies of the hydrofoils are clearly evident in the C_N spectra with peaks occurring at the reduced frequency equivalents of the modes stated in table 2.1. Variation between the estimated (table 2.1) and measured modal frequencies can be attributed to the simplification of a rectangular plate in added mass calculations and a low aspect ratio planform where 3D effects are more pronounced. Due to this inherent dynamic response from the coupled balance/hydrofoil system, the resolvable frequency range for the present measurements extends to about 250 and 60 Hz for the 120 and 240 mm span hydrofoils, respectively. This equates to an f' for the 120 and 240 mm hydrofoils of 0.9 & 2.0 for $Re = 1.0 \times 10^6$, and 4.0 & 4.5 at $Re = 0.4 \times 10^6$, respectively. Effective reduction of electrical noise contamination in the spectra was achieved using the modified IOP method as described in section 2.3.6. However, power supply odd harmonics are still partially evident in the spectra, along with by-products of the modified IOP method, appearing as tonal low amplitude peaks and troughs.

Effect of Incidence

The effect of incidence on the C_N spectra for both hydrofoils is highlighted in figure 2.16 for Re ranging from 0.2×10^6 to 1.2×10^6. In the low-immersion cases where the 240 mm span hydrofoil is partially immersed in a thin boundary layer with $\delta/b = 0.06$, the pre-stall incidences exhibit a relatively uniform power distribution at all Re in the resolvable frequency range. Increases in α from 0° to 5° and then to 10° causes broadband excitation in the C_N spectra within an order of magnitude. This broadband excitation at pre-stall incidences is potentially due to self-generated turbulence of the hydrofoil. The increase in power with incidence does reduce with increasing f' presumably due to spatial filtering where turbulence spatial scales are much smaller than the hydrofoil chord.

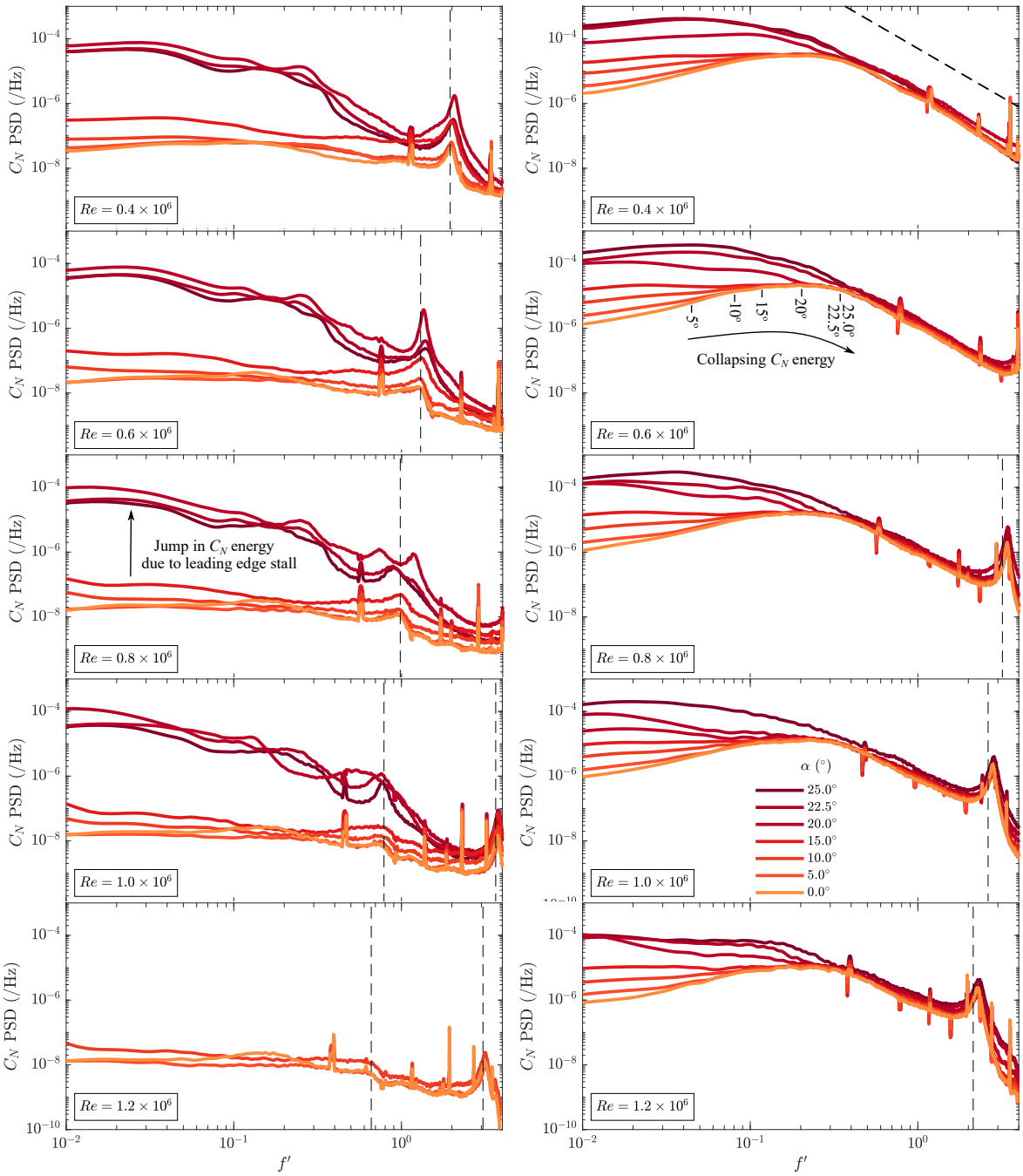

Figure 2.16: Spectra of C_N highlighting the influence of α at multiple Re for the 240 mm span hydrofoil in a thin boundary, $\delta/b = 0.06$, (left) and the 120 mm span hydrofoil in a artificially thick boundary layer, $\delta/b = 0.83$, (right). The non-dimensional natural frequency of the hydrofoils (vertical dashed line) have significant effect on the loading spectra, particularly the 240 mm hydrofoil. A $f'^{(-3)}$ reference for the slope of the roll-off is provided in the 120 mm hydrofoil spectra at $Re = 0.4 \times 10^6$ (diagonal dashed line).

Analysis of the spectra at higher incidences shows that when α is increased sufficiently, there is a large jump in power of 3 to 4 orders of magnitude, particularly at low f'. This jump in power coincides with the hydrofoil stalling for all Re as shown in the steady C_N forces in figure 2.10. With this jump in power characterized particularly by increases predominately at low f' suggests the sudden leading-edge type stall is associated with large-scale low-frequency excitations. Additionally, each of the stalled spectra are observed to exhibit a frequency band where the C_N power remains constant. The limits of the frequency band vary between incidences occurring around $0.07 \leq f' \leq 0.2$.

Changes in spectral features as α is varied are observed to be less pronounced in the high-immersion case ($\delta/b = 0.83$) with variation more gradual between incidences compared with those observed in the low-immersion case with $\delta/b = 0.06$ (figure 2.16). This indicates immersion in the ceiling boundary layer tends to homogenize the unsteady flow resulting in a broadband range of disturbances as opposed to more defined and tonal disturbances that would result in a more pronounced spectral features as evident in the low-immersion cases. C_N power at all incidences eventually collapse to the $\alpha = 0°$ case beyond a certain frequency, which increases with α in all Re cases, and all spectra converge by $f' = 0.4$. In other words, increases in incidence are shown to have significant effect at low frequencies, the frequency range of which increases with incidence up to a reduced frequency of about 0.4. Beyond $f' = 0.4$, incidence changes have negligible effect. Over this region, the unsteadiness is entirely due to the wall boundary layer with a constant roll-off slope of -3.

Furthermore, the high-immersion cases exhibit a broadband peak at $f' \approx 0.2$ in which the peak amplitude does not vary with α. This peak becomes lost at high α in the broadband C_N excitation from the self-generated turbulence of the hydrofoil. With the broadband peak not evident in the low-immersion case and not varying with α or Re, results suggest the disturbance is due to the ceiling boundary layer which is discussed further later.

There are indications of vortex-induced vibrations (VIV) in the C_N spectra for both the 240 mm hydrofoil in a thin boundary layer and 120 mm hydrofoil in a thick boundary layer (figure 2.16). Both hydrofoils are subjected to a range of disturbances depending on the conditions with potential excitations including transition instabilities and coherent shedding from the leading edge. The amplitude of the peak attributed to the resonant response of the hydrofoil is seen to exhibit significant amplification depending on the incidence and Re. This suggests excitations are inducing VIV that would result in increased C_N spectral levels. When comparing the C_N spectra for the 240 mm hydrofoil in a thin boundary layer to that of the 120 mm hydrofoil in a thick boundary layer, the resonant response is significantly different. The C_N power of the resonant response for the low-immersion case shows amplification with decreasing Re and increasing α, particularly at stall incidences (figure 2.17). In comparison, the high-immersion case at all Re

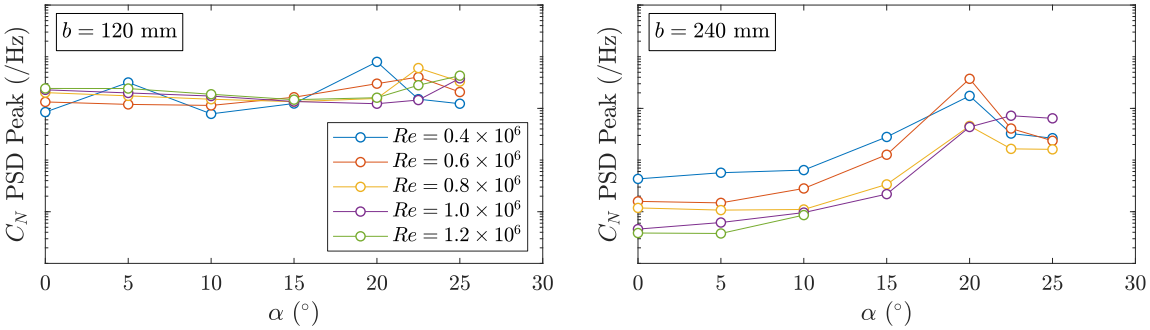

Figure 2.17: Peak C_N PSD values for resonant response of the 120 mm (left) and 240 mm (right) hydrofoils in relatively thin and thick boundary layers, respectively.

shows minimal increase with α. This suggests that for the high-immersion case there is no substantial vortex shedding at the resonant frequency that would cause significant VIV.

Effect of Reynolds number

The effect of Re on the unsteady loading experienced by the hydrofoils in both low and high-immersion cases is shown in figure 2.18. For the low-immersion case where $\delta/b = 0.06$, the lowest Re case ($Re = 0.4 \times 10^6$) exhibits the highest C_N power in the resolvable frequency range for pre-stall incidences, $\alpha \leq 15°$. For all Re cases there is a general decrease in the normal-force power across the measured frequency range with increased Re.

At $\alpha = 5°$ in the low-immersion case, the $Re = 0.4 \times 10^6$ data shows significantly higher broadband energy levels compared to the other cases. As indicated in figure 2.11, the formation of an LSB is inferred, a known source of vortex shedding and hence, unsteady loading (Baragona et al., 2003). High-speed flow visualization and velocity measurements by Kirk and Yarusevych (2017) have shown coherent structures associated with the LSB occur at reduced frequencies ranging from 0.89 to 6.37, depending on incidence. This has the potential to cause vortex induced vibration at the same frequency as the natural frequency of the hydrofoil which occurs at $f' \approx 2.0$ for $Re = 0.4 \times 10^6$. This would lead to resonance that could cause amplification in the response such as that observed in the C_N spectra of the 240 mm hydrofoil where the magnitude is shown to increase with both incidence and Re. In contrast, the 120 mm hydrofoil highly immersed showed no variation in the amplitude of the resonant peak with incidence or Re. Further investigation with coupled flow measurements are required to determine the source of these excitations.

Increasing α from 5° to 15° results in a small increase in C_N broadband energy with the hydrofoil still at a pre-stall incidence. Further increase in α to 20° sees a sudden increase in C_N energy, particularly at low f' as the hydrofoil experiences stall (figure 2.11), characterized by separation from the leading edge. As mentioned previously in section 2.4.3, vortex shedding at stall can lead to VIV, resulting in amplification of the hydrofoil

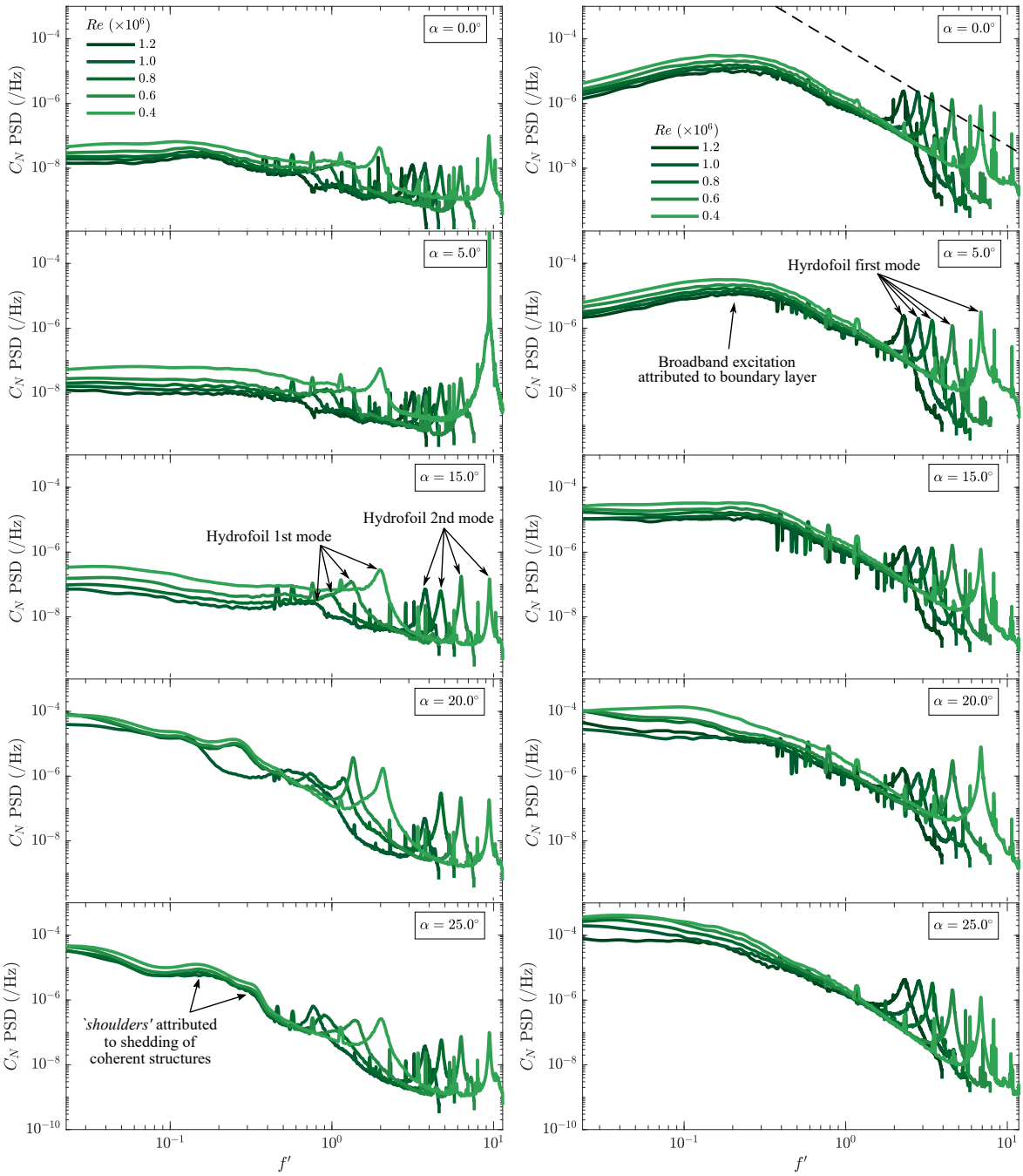

Figure 2.18: Spectra of C_N highlighting the influence of Re at multiple α for the 240 mm span hydrofoil in a thin boundary, $\delta/b = 0.06$, (left) and the 120 mm span hydrofoil in a artificially thick boundary layer, $\delta/b = 0.83$, (right). The non-dimensional natural frequency of the hydrofoils (vertical dashed line) have significant effect on the loading spectra, particularly the 240 mm hydrofoil. A $f'^{(-3)}$ reference for the slope of the roll-off is provided in the 120 mm hydrofoil spectra at $\alpha = 0°$ (diagonal dashed line).

resonant response as observed at $Re = 0.4$ and 0.6×10^6 for $\alpha = 20°$. At $\alpha = 25°$, all Re cases are experiencing stall with separation along the full chord of the hydrofoil. The C_N spectra are seen to exhibit similar trends for $f' \leq 0.8$ with all Re cases exhibiting multiple shoulders at $f' \approx 0.18$ and 0.34 with matching roll-off rates. These shoulders indicate the presence of coherent structures shedding off the hydrofoil due to the separated flow indicative of shedding leading-edge structures. These results provide insight into the range of frequencies and hence size distribution in the wall boundary layer that affect the unsteady loading of the hydrofoil. Based on the observed f', it is unlikely that these are due to the shedding of roll-up vortices which are observed to occur around $f' \geq 1.5$. These excitation occur at a much lower frequency closer to that observed of wake vortex shedding (Yarusevych et al., 2009). However, further insight into the phenomena involved through flow measurements is required to identify the physics responsible for the excitations.

The high-immersion cases where $\delta/b = 0.83$ exhibit different trends to those observed in the low-immersion case as well as similarities. At $\alpha = 0°$, the C_N energy is seen to increase steadily as Re decreases, similar to that observed in the low-immersion cases. Increased immersion and exposure to the embedded turbulence of the ceiling boundary layer results in a broadband increase in C_N energy. The increased immersion is also seen to result in a broadband peak at $f' \approx 0.2$ for all Re which is not observed in the low-immersion cases. As f' increases past 1, the energy levels are seen to converge due to varying roll-off rates between the different Re cases.

Increasing the incidence to 5° sees minimal change in the C_N spectra for all Re, unlike that observed in the low-immersion case. This is attributed to the encountered ceiling boundary layer preventing an LSB from forming on the hydrofoil and causing unsteady loading. As α is increased to 15°, a rise in low-frequency C_N energy is evident for all Re cases. This sees the $f' \approx 0.2$ peak begin to diminish in the power rise attributable to self-generated turbulence of the hydrofoil from separation at the trailing edge.

Re is shown to alter the stall behaviour of the hydrofoil with stall being delayed and max C_N being increased with rising Re, particularly in the high-immersion case (figure 2.11). At an incidence of 20°, the unsteady loading characteristics at various stages of stall is captured by the 5 Re cases. At relatively low speeds with $Re = 0.4 \times 10^6$, the hydrofoil is close to max C_N at 20° with the C_N spectra showing high energy at low f'. This increased low f' excitation sees the broadband peak at $f' \approx 0.2$ disappear with a plateau in the spectra forming for frequencies up to $f' \approx 0.1$ before rolling off. For $Re = 0.6 - 0.8 \times 10^6$, the hydrofoil is at a pre-stall incidence at 20° but would still be experiencing separation for a large portion of the chord that would cause substantial unsteady loading. The reduced excitation sees evidence of the broadband peak at $f' \approx 0.2$ as well as the shoulder at $f' \approx 0.1$ observed at $Re = 0.4 \times 10^6$. This indicates that the broadband peak at $f' \approx 0.2$ is associated with the encountered ceiling boundary layer where the peak at 0.1 is associated with self-generated turbulence from the hydrofoil

stalling.

Effect of boundary layer immersion

The effect of boundary layer immersion on the unsteady loading of the 120 mm and 240 mm hydrofoil is both complex and broad as shown in figure 2.19. At an incidence of 0° where self-generated turbulence of the hydrofoil is at a minimum, the direct influence of the encountered ceiling boundary layer is highlighted. Both hydrofoils are seen to experience an incremental increase in energy across the entire frequency range with increased δ/b. The primary feature in the spectra of both hydrofoils is the previously mentioned broadband peak at $f' \approx 0.2$ which is shown to increase in relative amplitude with δ/b. An exception to this is the lowest immersion case which instead exhibits a more defined peak at $f' \approx 0.13$ on both hydrofoils. Additionally, the roll-off slope past the $f' \approx 0.2$ broadband peak is observed to increase with δ/b.

Behaviour of the broadband peak at $f' \approx 0.2$ increasing in relative magnitude with δ/b suggests the excitation is due to coherent structures within the ceiling boundary layer. Occurring at a consistent f', the coherent structures must have a compatible length scale and advection velocity that results in an excitation at a reduced frequency of approximately 0.2 at all boundary layer thicknesses. Experiments conducted by Hutchins and Marusic (2007) revealed inner and outer energy peaks in one-dimensional streamwise pre-multiplied spectra of a turbulent boundary layer. The outer energy peak was characterized by coherent structures, referred to as *'superstructures'*, with a consistent length scale, λ_x, of 6δ and outer coordinates of $z/\delta \approx 0.06$. Unfortunately, the advection speed of the these *'superstructures'* are difficult to measure experimentally. However, results from boundary layer simulations conducted by Del Álamo and Jiménez (2009) indicated the larger *'global'* modes travel at a speed proportional to the bulk velocity as opposed to the local mean velocity in the boundary layer. Based on a length scale of 6δ and assuming the advection velocity is sufficiently close to the free-stream, i.e. $U_x = U_\infty$, this would result in $f' \approx 0.156$ for the largest boundary layer. This is relatively close considering the broadband nature of the peak suggesting it could be the potential cause of the excitation. However, without flow measurements to provide sufficient insight into the phenomena involved, the cause of the broadband excitation cannot be identified.

Closer inspection of the 120 mm high δ/b spectra at 0° reveals a *'shoulder'* in the broadband peak where the C_N power starts to roll-off, known as the cut-off frequency. The cut-off frequency can be seen to decrease as δ/b increases. Furthermore, the rate of decay in the C_N power past the cut-off frequency, known as the roll-off, can be seen to vary between δ/b cases with the roll-off increasing with δ/b. This provides insight into the size distribution of the eddies encountered in the ceiling boundary layer that affect the hydrofoil unsteady loading. This is not as clear in the 240 mm hydrofoil spectra due

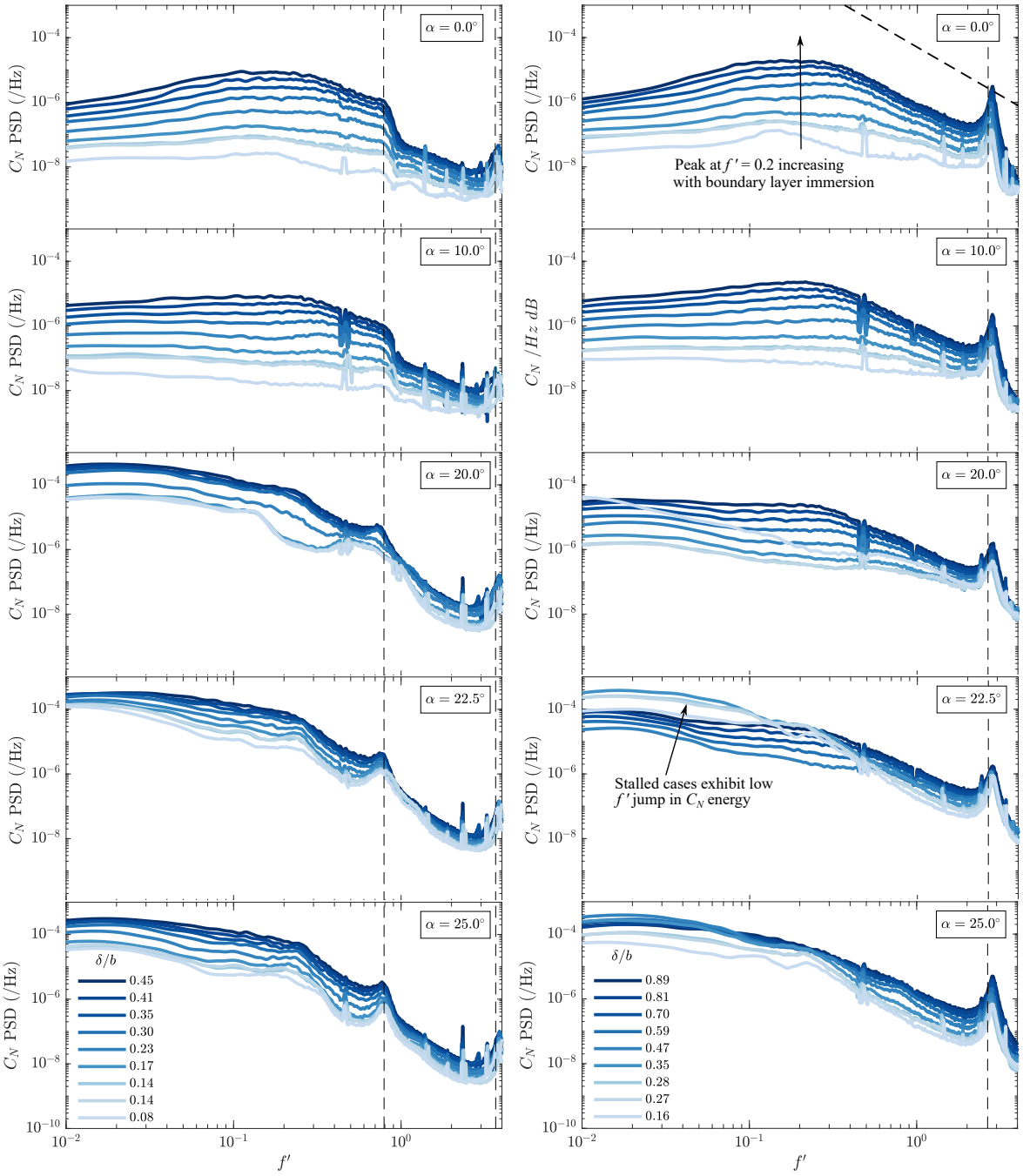

Figure 2.19: Spectra of C_N highlighting the influence of the level of boundary layer immersion at various α for the 240 mm (left) and 120 mm (right) hydrofoils at $Re = 1.0 \times 10^6$. The non-dimensional natural frequency of the hydrofoils (vertical dashed line) have significant effect on the loading spectra, particularly the 240 mm hydrofoil. A $f'^{(-3)}$ reference for the slope of the roll-off is provided in the 120 mm hydrofoil spectra at $\alpha = 0°$ (diagonal dashed line).

to contamination of the model vibrating at its (lower) natural frequency.

As α increases to 10°, the broadband peak at $f' \approx 0.2$ starts to diminish due to increased low-frequency excitations ($f' < 0.2$) attributed to self generated turbulence of the hydrofoil. Further increase in α to 20° sees the 120 mm hydrofoil stall for the smallest δ/b case and the 240 mm hydrofoil for all cases. With the 120 mm hydrofoil, the C_N spectra of the stalled case exhibits a large jump in low-frequency power that steadily decays as f' increases. This low-frequency jump at stall is attributed to the large-scale separation from the suction side of the hydrofoil with the self generated turbulence characterized by large, low-frequency disturbances. As mentioned previously, the higher δ/b cases have been able to delay stall due to the transfer of TKE.

For the 240 mm hydrofoil at 20°, all cases have completely stalled but still exhibit different spectral characteristics. The four lowest immersion cases, $\delta/b = 0.08 - 0.18$, all exhibit similar trends with a *'shoulder'* exhibiting a cut-off frequency of $f' \approx 0.15$, then leveling out between 0.2 and 0.3 before increasing again due to the hydrofoil natural frequency. On the other hand, the four highest immersion cases, $\delta/b = 0.30 - 0.45$, also possess the previously mentioned *'shoulder'* with the cut-off at $f' \approx 0.22$ before rolling off at a rate greater than that observed for the 120 mm hydrofoil.

Increasing α further to 22.5° sees the 120 mm hydrofoil stall for δ/b cases up to and including 0.28, as shown in figure 2.12. The C_N spectra of these cases (figure 2.19) show a similar low-frequency jump in power as observed at $\alpha = 20°$ for $\delta/b = 0.16$. This can also be seen in the $\delta/b = 0.35$ case where maximum C_N occurs at $\alpha = 22.5°$. Interestingly, the $\delta/b = 0.16$ case exhibits lower power than the 0.269 and 0.282 cases for $f' < 0.1$, following a similar trend to the high-immersion case of $\delta/b = 0.90$ up to $f' = 0.2$ before rolling off sharply. In the cases of $\delta/b = 0.27 - 0.35$, C_N power levels gradually roll-off as f' increases until leveling out at $f' \approx 0.15$. This is followed by the power rolling-off again past $f' = 0.2$ with power levels becoming ordered for $f' > 0.6$ with higher δ/b correlating to higher C_N power.

For the 240 mm hydrofoil at 22.5°, all δ/b cases are well beyond stall and exhibit similar C_N power levels at low frequencies ($f' < 0.01$). As f' increases, power levels gradually decrease with the roll-off being greater for lower δ/b. As f' approaches 0.2, a *'shoulder'* appears in the spectra for all cases that is more defined in the lower power cases (i.e. low δ/b). Further increase in f' sees all the C_N spectra roll-off at similar rates until reaching the peak induced by the natural frequency vibration of the hydrofoil. These characteristics, along with those observed on the 120 mm hydrofoil at 22.5°, indicate that the majority of self-generated unsteady loading from phenomena such as stall, flow separation and vortex shedding predominately occurs at relatively low frequencies, $f' < 0.2$. On the other hand, unsteady loading directly induced by the encountered ceiling boundary layer predominantly occurs at relatively high frequencies, $f' > 0.2$.

2.5 Conclusion

The steady and unsteady loading on a hydrofoil immersed in a turbulent boundary layer has been investigated. Measurements were obtained using model hydrofoils vertically mounted in a cavitation tunnel via static and dynamic force balances and immersed in boundary layers of varying thicknesses. The artificially thickened boundary layers were measured with the inner and outer profiles comparing well to the law of the wall and modified Coles law of the wake. For the low-immersion case with $\delta/b = 0.08$, a deviation in the normal-force curve is observed at medium to high pre-stall incidences attributed to the presence of a laminar separation bubble. The incidence in which the deviation occurs shows a Re dependence with the deviation being delayed with increasing Re. Stall in the low-immersion cases are of the sudden leading-edge type with the stall angle being delayed and width of the associated hysteresis loop increasing with Re. For a high-immersion case with $\delta/b = 0.81$, the normal-force slope is reduced and stall angle delayed compared to the low-immersion case attributed to increased exposure to the lower momentum flow of the ceiling boundary layer and lower aspect ratio. Additionally, it is observed with increasing immersion the reduction and eventual disappearance of the normal-force curve deviation attributed to the prevention of LSB formation from increased transfer of TKE from the ceiling to hydrofoil boundary layer. This transfer of TKE with increased immersion is also attributed to the prevention of leading-edge separation, causing a shift to trailing-edge type stall, the stall angle of which shows a strong Re dependence. Increasing immersion is also shown to cause the normal force standard deviation to increase linearly with δ/b.

The normal-force spectra show that for the low-immersion cases, at low incidence, the power is uniform across the measured frequency range. Increases in pre-stall incidences in low-immersion cases are shown to cause a broadband increase in excitation within an order of magnitude also across the measured frequency range. However, once stalled, there is significant amplification in the self-generated excitations, characterized by low-frequency disturbances and decreasing toward low-incidence values at $f' > 0.1$. This behaviour is associated with wake vortex shedding from leading-edge stall. In contrast, for the high-immersion case, increases in incidence have a significant effect at low frequencies, the reduced frequency range of which increases with incidence up to a $f' \approx 0.4$. Beyond $f' = 0.4$, incidence changes and hence the hydrofoil boundary layer have negligible effect. Over this region, the unsteadiness is entirely due to the wall boundary layer with a constant roll-off slope of approximately $f'^{(-3)}$. This indicates that as α increases, the frequency distribution of the self-generated excitations is increased, creating a greater population of low-frequency disturbances.

Normal-force spectra for varying δ/b at low incidence exhibit a broadband peak at $f' \approx 0.2$ that could be attributable to large-scale structures that have previously been observed in high Re boundary layers. The relative amplitude of this peak is seen to

increase with δ/b along with the roll-off slope, converging as δ/b approaches 1. For all cases there is a general power decrease in the normal-force spectra across the measured frequency range with an increase in Re.

On both hydrofoils, signs of vortex-induced vibration are apparent in the normal force spectra as the first natural frequency of both hydrofoils occurs within the measured frequency range. This is exhibited on the 240 mm hydrofoil at low level of immersion where the amplitude of the resonant peak in the C_N spectra increases with incidence. In addition, the amplitude of the resonant peak is seen to increase with Re reflecting the more general Re dependence. In contrast, the 120 mm hydrofoil at a high level of immersion showed no variation in the resonant peak amplitude with incidence or Re. Additional features observed in the normal force spectra included local peaks in at low frequencies beyond stall on the 240 mm hydrofoil which are indicative of the coherent shedding of leading-edge structures. These results provide insight into the range of frequencies and hence size distribution in the wall boundary layer that affect the unsteady loading of the hydrofoil.

2.6 Acknowledgements

This project was supported by the Research Training Centre of Naval Design and Manufacturing (RTCNDM), US Office of Naval Research (Dr. Ki-Han Kim, Program Officer) and ONR Global (Dr. Woei-Min Lin) through NICOP S&T Grant no. N62909-11-1-7013. The RTCNDM is a University-Industry partnership established under the Australian Research Council (ARC) Industry Transformation grant scheme (ARC IC140100003). The authors would like to acknowledge the assistance of Mr Steven Kent and Mr Robert Wrigley from the Australian Maritime College for their essential help with setting up and carrying out the experiments.

2.7 Nomenclature

Symbol	Definition	Unit
α	Flow incidence angle	$^\circ$
γ^2	Magnitude-squared coherence	-
δ	Boundary layer thickness ($U = 0.99U_\infty$)	m
δ_c	Boundary layer thickness ($U = U_\infty$)	m
δ^*	Displacement thickness ($U = U_\infty$)	m
θ	Momentum thickness	m

κ	von Karman constant	-
ν	Kinematic viscosity	m^2/s
Π	Wake strength factor	-
ρ	Water density	kg/m^3
τ_w	Wall shear stress	Pa
b	Span	m
C_f	Skin friction coefficient	-
C_N	Normal force coefficient	-
C_P	Pitching moment coefficient	-
C_{pi}	Injection pressure coefficient	-
c	Mean chord	m
c_R	Root chord	m
c_T	Tip chord	m
f	Frequency	Hz
f'	Reduced frequency	-
f_n	Natural frequency	Hz
$G_{NN}(f)$	Auto-spectra of normal force	1/Hz
$G_{VV}(f)$	Auto-spectra of voltage	1/Hz
$G_{VN}(f)$	Cross spectrum of normal force and voltage	1/Hz
H	Shape factor	-
I	Turbulence intensity	-
$IOP(f)$	Incoherent Output Power	W
m	Mass of hydrofoil	kg
N	Normal force	N
P	Pitching moment	Nm
p_∞	Absolute freestream static pressure	Pa
p_i	Injection pressure	Pa
Re	Reynolds number (chord based)	-
Re_θ	Reynolds number (Momentum thickness based)	-
Re_τ	Reynolds number (δ_c based)	-
Re_T	Reynolds number (test section based)	-
T	Acquisition period	s

U_∞	Freestream velocity	m/s
U^+	Non-dimensional velocity	-
U_τ	Wall friction velocity	m/s
w	Test section width	m
x	Test section streamwise location	m
x_{cop}	Streamwise centre of pressure	m
z^+	Non-dimensional wall coordinate	-

Chapter 3

The influence of fluid-structure interaction on cloud cavitation about a stiff hydrofoil. Part 1.

This chapter is a modified version of the article published in the *Journal of Fluid Mechanics* to aid alignment of the research with the scope of the thesis.

The citation for the paper is:

Smith, S. M., Venning, J. A., Pearce, B. W., Young, Y. L. and Brandner, P. A. (2020) The influence of fluid-structure interaction on cloud cavitation about a stiff hydrofoil. Part 1. *Journal of Fluid Mechanics,* **884** (A1). doi:10.1017/jfm.2020.321

3.1 Abstract

The physics associated with various cavitation regimes about a hydrofoil are investigated in a variable-pressure water tunnel using high-speed photography and synchronized force measurements. Experiments were conducted on a relatively stiff stainless steel hydrofoil at $Re = 0.8 \times 10^6$ for cavitation numbers, σ, ranging from 0.2 to 1.2, with the hydrofoil experiencing sheet, cloud and super-cavitation regimes. The NACA0009 model of tapered planform was vertically mounted in a cantilevered configuration to a six-component force balance at an incidence, α, of 6° to the oncoming flow. Tip deformations and cavitation behaviour were recorded with synchronized force measurements utilizing two high-speed cameras mounted underneath and to the side of the test section. Break-up and shedding of an attached cavity was found to be due to either interfacial instabilities, re-entrant jet formation, shockwave propagation or a complex coupled mechanism, depending on σ.

Three primary shedding modes are identified. The Type IIa & IIb re-entrant jet driven oscillations exhibiting a linear dependence on σ, decreasing in frequency with decreasing σ due to growth in the cavity length, occurring at higher σ values (Type IIa: 0.4-1.0; Type IIb: 0.7-0.9). Shockwave-driven Type I shedding occurs for lower σ values (0.3-0.6) with the oscillation frequency being practically independent of σ. The Type IIa oscillations locked in to the first sub-harmonic of the hydrofoil's first bending mode in water which has been modulated due to the reduced added mass of the vapour cavity.

3.2 Introduction

The increasing importance of flow-induced vibrations over time is being driven by advancements in materials technology and ever increasing optimisation, resulting in structures becoming lighter, more flexible and susceptible to vibrations (Blevins, 1977). Flow induced vibration phenomena have a profound influence on the the performance of the vast range of aerodynamic and hydrodynamic objects and are therefore significant in geometrical and structural design (Bisplinghoff et al., 2013). Cavitation about a hydrofoil involves a range of complex dynamical phenomena including mass transfer via phase change and diffusion, shockwaves, large and small-scale instabilities and turbulence, some of which are discernible in figure 3.1. These phenomena have the potential to cause significant and destructive vibrations (Franc and Michel, 2004). Understanding these fluid-structure interaction (FSI) phenomena is of interest as flow over a lifting body can significantly alter the performance of maritime propulsion and control systems.

Experimental studies investigating the influence of cavitation on flexible (i.e. compliant) hydrofoil's has previously been conducted by Kaplan and Lehman (1966); Brennen et al. (1980); Ausoni et al. (2007); Ducoin et al. (2012b) with Kaplan and Lehman (1966) first observing modest vibration amplitudes due to cavitation about a hydrofoil. Examining the coupling between the hydro-elasticity and the trailing-edge vortex cavitation, Ausoni et al. (2005, 2007) observed that not only does the cavitation influence the structural vibrations, but the structural vibrations also affect cavitation behaviour. Numerical simulations by Akcabay and Young (2014) modelling the bending and torsional compliance of a cantilevered hydrofoil revealed maximum force and deflection fluctuations occurred when the maximum cavity length approaches the trailing-edge. Additionally, hydrofoil compliance was seen to increase the cavity length, thus decreasing the cavitation shedding frequency. However, the influence of compliance was only significant when the cavity length was near the trailing-edge. The unsteady two-phase flow has effect on the spectral content of a compliant hydrofoil compared to a relatively stiff one, causing frequency modulation (Akcabay and Young, 2015), broadening of the frequency content (Akcabay et al., 2014) and leading to phenomena such as lock-in that leads to significant

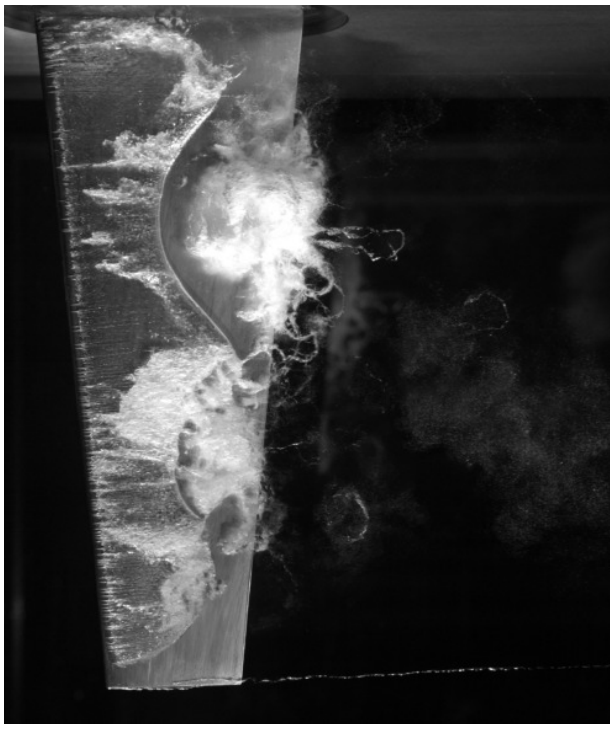

Figure 3.1: Cloud cavitation about a finite-span stainless steel hydrofoil exhibiting multiple shedding events along the span due to the re-entrant jet instability and spanwise compatibility of the cavitation. The hydrofoil is vertically mounted at an incidence of 6° to the flow with $Re = 0.8 \times 10^6$ and $\sigma = 0.7$.

amplification of vibrations (Kato et al., 2006; Akcabay and Young, 2015).

Cloud cavitation was first extensively investigated by Knapp (1955) where the detachment of a vapour cloud from an attached cavity due to a re-entrant jet was observed. Since then, several mechanisms have been identified as potential instabilities causing periodic shedding, depending on the flow conditions, in a particular streamwise pressure gradient. These included growth of interfacial instabilities such as Kelvin-Helmholtz waves (Brennen, 1969; Avellan et al., 1988; Brandner et al., 2010), re-entrant jet formation (Furness and Hutton, 1975; Le et al., 1993; Kawanami et al., 1997; Stutz and Reboud, 1997; Pham et al., 1999; Callenaere et al., 2001; Laberteaux and Ceccio, 2001a,b; Smith et al., 2017, 2018, 2019), and shock propagation (Jakobsen, 1964; Reisman et al., 1998; Ceccio, 2015; Ganesh et al., 2016; Smith et al., 2018). In certain conditions, multiple instabilities can be present simultaneously with Ganesh et al. (2016) showing both bubbly shock propagation and re-entrant jet flow from measurements of the void fraction field with X-ray densitometry. In addition, Brandner et al. (2010), and more recently de Graaf et al. (2017), using high-speed photography observed all three mechanisms either occurring in isolation or as a complex, coupled mechanism in cloud cavitation about a sphere. Furthermore, experiments on a NACA0015 hydrofoil revealed complex multi-stage shedding cycles involving both re-entrant jet and shockwave instabilities (Venning et al., 2017, 2018b).

A re-entrant jet forms by flow over the cavity interface forming an instantaneous stag-

nation on the wall associated with the cavity closure, resulting in some flow directed back upstream along the hydrofoil surface (Brennen, 1995). The re-entrant jet travels upstream towards the cavity detachment until it impinges upon and breaks up the cavity surface, resulting in a detached cavity that is advected downstream as a bubbly mixture, termed a 'cloud' structure due to its similarity in visual appearance. As mentioned previously, the re-entrant jet shedding mechanism has been extensively studied and it has been found that for re-entrant jet driven cloud cavitation to occur, the cavity needs to close in a region with a sufficiently large adverse pressure gradient as well as being thick enough to limit interaction between the re-entrant jet and the cavity interface (Franc, 2001). Cloud cavitation driven by the re-entrant jet instability, referred to as Type II oscillation in literature, has a shedding frequency that is dependant on the cavity length, and therefore σ as well as incidence, α (Callenaere et al., 2001). In the case of a hydrofoil, the cavity closes in a reducing adverse pressure gradient as it grows and approaches the trailing-edge. This leads to degradation of the re-entrant jet and a transition of the primary instability driving shedding to a shockwave instability (Kjeldsen and Arndt, 2001).

As the attached cavity grows on a hydrofoil, a change in the shedding mechanism is observed with the re-entrant jet instability transitioning to a shockwave instability. Shockwave driven cloud cavitation, referred to as Type I oscillations (Kjeldsen and Arndt, 2001), occurs when a reduction in σ or increase in α causes increased cavity size and significant reduction in local void fraction to allow shockwave formation and propagation from the collapse of bubbles. For shockwave formation and propagation, the shed clouds need to be densely populated with bubbles that interact and collapse coherently (Reisman et al., 1998). Additionally, the sound speed of the liquid-vapour mixture is required to fall below the local flow speed (Ganesh et al., 2016; Wu et al., 2019). This can occur under cavitating conditions as the presence of bubbles increases the local void fraction which has been shown to significantly reduce the speed of sound in the bubbly mixture (Shamsborhan et al., 2010). These conditions are met when the cavity has increased in size to shed large-scale vapour structures that raise the local void fraction sufficiently.

To reduce the complexity of the cavitation dynamics in three-dimensional (3D) flows, a large number of past studies have focused on two-dimensional (2D) flows. However, even in the 2D case, the resulting shedding physics still exhibit significant 3D characteristics, as observed by Kubota et al. (1989); De Lange and De Bruin (1998); Kawanami et al. (1998), resulting in spanwise variations of the cloud cavitation. Furthermore, Kawanami et al. (1998) show that cloud cavitation can have a spanwise spatial periodicity on a 2D hydrofoil where periodic shedding occurs at multiple locations along the span, depending on the streamwise length of the cavity. This is also observed by Prothin et al. (2016) and Smith et al. (2018, 2019) showing multiple stable shedding locations along a finite-span hydrofoil, highlighting the role of compatibility between the cavity length and the span first noted by Kawanami et al. (1998). In both 2D and 3D flows, incompatible

cavity lengths are seen to result in incoherent shedding along the span (Kawanami et al., 1998; Kjeldsen et al., 2000; Smith et al., 2018; Harwood et al., 2019). The formation of stable shedding sites is seen to be reinforced by the spanwise component of shedding mechanisms, such as re-entrant jets, as they prevent other instabilities from interfering in the local shedding process (De Lange and De Bruin, 1998).

Investigations into the effect of hydrofoil planform geometry by Ihara et al. (1989) have shown sweep to minimise lift and drag force fluctuations associated with the absence of large cavity break-off that is observed on an unswept hydrofoil. Furthermore, the highly swept hydrofoil is seen to confine full-chord cloud cavitation to the downstream portion of the hydrofoil, with the upstream portion forming a stable cavity. This cavitation behaviour is due to the strong spanwise flow component redirecting the re-entrant jet away from the cavity detachment, thus preventing cavity break-off and allowing a stable cavity to form (Laberteaux and Ceccio, 2001b). Time-resolved particle image velocimetry experiments on a 3D hydrofoil by Foeth et al. (2006) also shows significant cavitation stability sensitivity due to 3D flow effects. The influence on cloud cavitation of a free tip, tapered planform and spanwise cavity oscillations remain largely to be investigated, despite several investigations into the effect of a varying spanwise geometry.

This research consists of two parts and is devoted to understanding the influence of FSI on cloud cavitation about a hydrofoil. Cavitating conditions are achieved about the vertically mounted cantilevered hydrofoil through precise pressure control of the variable-pressure water tunnel. Forces acting on the hydrofoil were acquired simultaneously with tip deflections and cavitation behaviour measurements using high-speed photography at various cavitation regimes by varying the freestream water tunnel pressure. The results produce further insight and correlation between the shedding physics, hydrofoil loading and structural deformations. Part 1 is dedicated to establishing a reference through utilising a relatively stiff hydrofoil whereby the deformations are small compared to the dimensions. Hence, structural dynamics of the hydrofoil have minimal effect on the loading and cavity dynamics. Part 2 investigates the influence of FSI by utilising a compliant hydrofoil with observations informed by those made on the relatively stiff reference in Part 1.

3.3 Experimental Overview

3.3.1 Experimental Facility

Measurements were undertaken at the Australian Maritime College in the Cavitation Research Laboratory variable-pressure water tunnel. The tunnel test section measures 0.6 m square by 2.6 m long in which the operating velocity and absolute pressure can be varied from 2 to 12 m/s and 4 to 400 kPa, respectively. The medium sized tunnel contains

$365\,\mathrm{m}^3$ of demineralized water. While there is a permanent background nuclei population present in the water, these are of sufficiently high strength and sparsity to be considered inactive in this flow (Venning et al., 2018c). The circuit architecture has been developed for continuous elimination of nuclei achieved through a combination of coalescence/gravity separation in a downstream tank and dissolution via extended residence in a resorber (Brandner, 2018). This allows consistent long duration measurements as the oncoming recirculated flow is free from nuclei produced from the cavitating hydrofoil that might influence the cavitation behaviour, as observed by Arndt and Keller (2003); Russell et al. (2018). A detailed description of the facility is given in Brandner et al. (2007).

Measurements were taken at a fixed incidence, α, of 6° and a chord-based Reynolds number, $Re = U_\infty \bar{c}/\nu$, equal to 0.8×10^6, where $\bar{c}$ is the mean chord, U_∞ is the freestream velocity and ν is the kinematic viscosity of the water. The cavitation number, $\sigma = 2(p_\infty - p_\mathrm{v})/\rho U_\infty^2$, where p_∞ is the absolute static pressure at the level of the hydrofoil tip, p_v is the vapour pressure, and ρ is the water density, was incrementally varied from 1.2 to 0.2 to investigate various cavitation regimes. Dissolved oxygen levels were kept between $3 - 4\,\mathrm{ppm}$ for all measurements.

3.3.2 Model Hydrofoil

The model hydrofoil was mounted vertically on the centreline, 1.3 m downstream of the test section entrance through a 160 mm diameter penetration in the ceiling. A schematic of the experimental setup is shown in figure 3.2. The hydrofoil was attached to a six-component force balance, with an estimated precision of 0.1%, via a housing which clamped the hydrofoil into place using two profiled plates (figure 3.3). The penetration is made fair (to 50 µm) using an acrylic disk mounted to the measurement side of the force balance. The fairing disk has a 0.5 mm radial clearance to avoid interference with the force measurement. This type of mounting arrangement was implemented to accommodate the manufacturing of composite models used in part 2 and to ensure common fixed-end conditions for comparative measurements between the stainless steel and composite models (Zarruk et al., 2014).

The geometric and mechanical properties of the hydrofoil have been selected based on the requirements for modeling the static and dynamic FSI typical of control surfaces and propellers. The hydrofoil features a symmetric (unswept) trapezoidal planform of 300 mm span, b, with a 60 mm tip chord, c_{tip}, and 120 mm root chord, c_{root}, resulting in a mean chord, $\bar{c} = (c_{root} + c_{tip})/2$, of 90 mm. This gives an aspect ratio ($b/\bar{c}$) of 3.33, typical of marine propellers. The model has a modified NACA0009 section profile that features a thicker trailing-edge for improved robustness against trailing-edge damage and to allow for manufacturing of the compliant composite models (Zarruk et al., 2014). Experiments performed by Zarruk et al. (2014) show that the modified profile has minimal effect on the

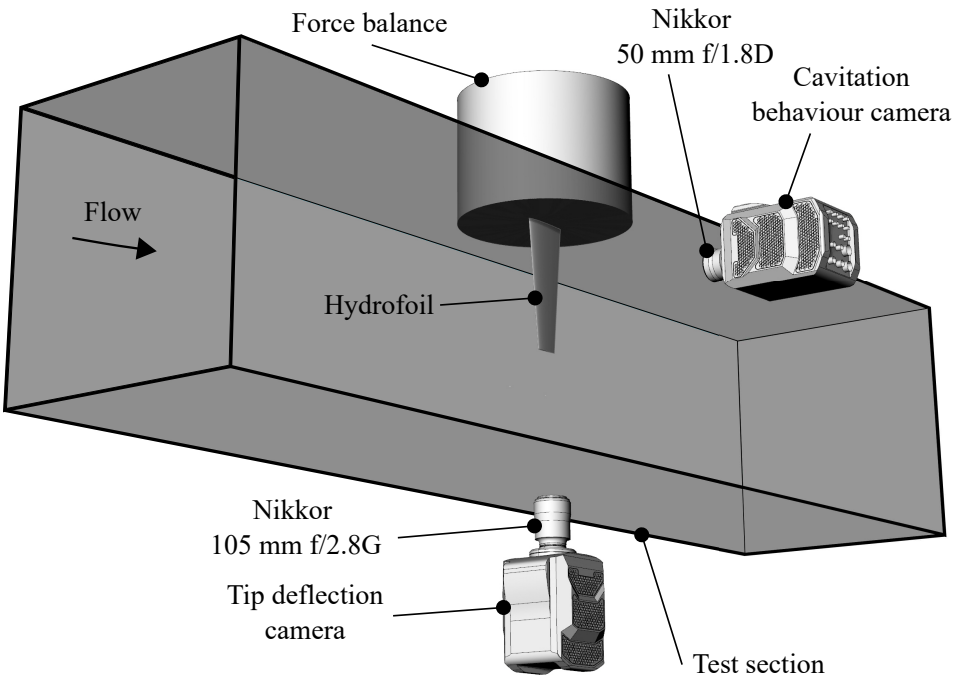

Figure 3.2: Experimental setup whereby the hydrofoil is attached to a force balance and mounted vertically on the test section ceiling. Cavitation behaviour and tip deflections were recorded using high-speed photography utilizing two Phantom v2640 high-speed cameras mounted on the side and below the test section, respectively.

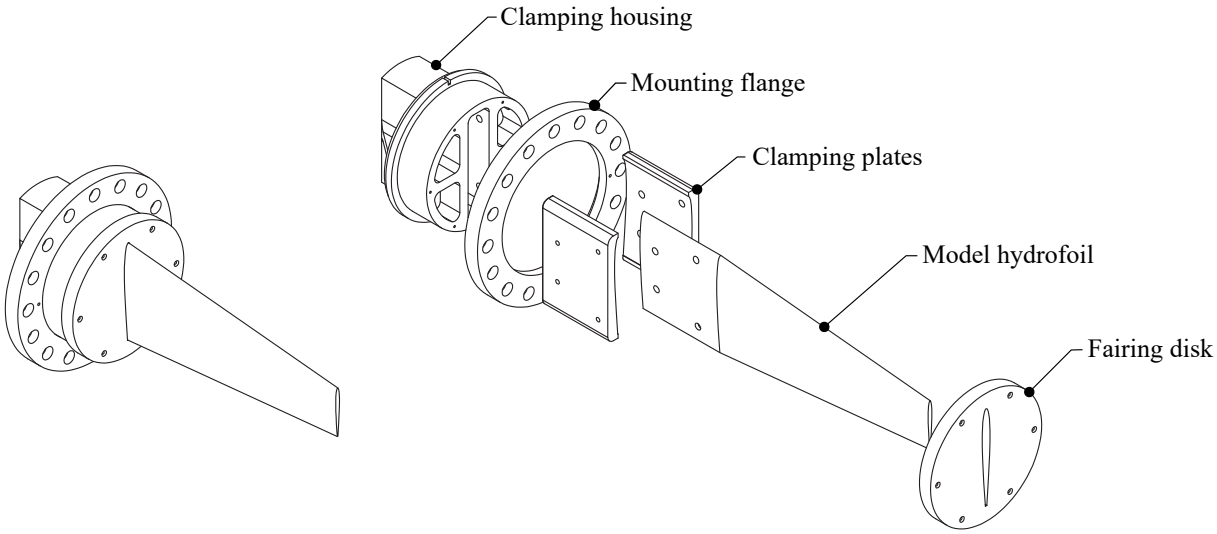

Figure 3.3: Hydrofoil model assembly showing an exploded view of the clamping housing arrangement that allows continuity of the model.

Fluid	Technique	Mount	f_n (Hz)	$St_\mathrm{n} = f_\mathrm{n}c/U_\infty$
Air	Impact / Accelerometer	Rigid	96	0.90
Water	DIC	Rigid	62	0.58
Water	DIC	Force balance	57	0.53
Water	Force measurements	Force balance	54	0.51

Table 3.1: First mode frequencies in bending of the NACA0009 stainless steel hydrofoil for various conditions as reported by Clarke et al. (2014). The in-water (fully wetted) measurements were made using Digital Image Correlation (DIC) and force measurements and the in-air using impact/accelerometer.

forces and deflections experienced by the hydrofoil compared to the original NACA0009 profile. The stainless steel model was machined from a billet of Type 316 stainless steel and manufactured to a ± 0.1 mm surface tolerance and 0.8 µm surface finish.

The normal force, N, and pitching moment, P, acting on the hydrofoil are presented as dimensionless coefficients as $C_N = 2N/\rho U_\infty^2 \bar{c} b$ and $C_P = 2P/\rho U_\infty^2 \bar{c}^2 b$, respectively, with the coordinate system presented in figure 3.4(a). The hydrofoil first mode is in bending as shown by Clarke et al. (2014) and measured frequencies for various conditions and techniques are summarised in table 3.1. These results show the difference in frequencies for in-air, fully wetted and the influence of mounting compliance. The natural frequency, f_n, reduces by about 10% when mounted from the force balance compared with rigid mounting. Excitation of the first mode should then be expected to occur between $St_\mathrm{n} = f_\mathrm{n}\bar{c}/U_\infty$ values of about 0.5 and 0.9 depending on cavity extent affecting added mass as marked on figure 3.8.

3.3.3 Experimental Techniques

To obtain detailed information of loading variations on the hydrofoil through various cavitation regimes, long-duration force measurements were made at σ increments of 0.025. Tip deflection and cavitation behaviour measurements, discussed further below, were obtained simultaneously (including force measurements) using high-speed photography at σ increments of 0.1. For these simultaneous measurements, due to limitations with respect to camera memory storage, 'medium' length, reduced temporal resolution runs were acquired suitable for statistical analysis of the imaging data sets and 'short' length, high temporal resolution data sets were acquired for a detailed analysis of the cavitation physics. Details of all three run types are summarised in table 3.2.

The force time-series were analysed using the continuous wavelet transform, following the procedure of Torrence and Compo (1998). The Morlet wavelet was applied and correlated at various scales with the time series, allowing events and intermittent components in the force and tip displacement history to be identified. Time-series data is presented

Run Type	σ	T (s)	f_{HSP} (Hz)	f_{FB} (Hz)
Long	0.2-(0.025)-1.2	360	N/A	1 000
Medium	0.2-(0.1)-1.2, 0.65, 0.75	36	500	500
Short	0.2-(0.1)-1.2, 0.65, 0.75	1	6 600	6 600

Table 3.2: Test matrix for the various run types detailing the σ range, run duration, T, high-speed photography frame rate, f_{HSP}, and force balance sampling rate, f_{FB}. The Long acquisition periods provided high-resolution loading behaviour with σ. Due to camera storage limitations, simultaneous force measurement and high-resolution imaging of the cavitation behaviour and tip deflections was obtained with the Medium and Short run types, respectively.

with time, t, being non-dimensionalized as $t' = tU_\infty/\bar{c}$.

Tip deflection

The tip deflection of the hydrofoil was measured via high-speed photography utilizing a Phantom v2640 with a Nikkor 105 mm f/2.8G lens (figure 3.2). Operating with a resolution of 512 × 1 504 pixels and a spatial resolution of 0.049 mm/px. The tip deflection was determined using edge detection of the hydrofoil tip profile and comparing each frame to the hydrofoil under zero load based on the assumption that the profile locally remains undeformed. The edge detection process involved first rotating each frame by the angle of the hydrofoil under zero load relative to the frame using bicubic interpolation and then applying a 2-D Gaussain filter to smooth the image. The edge was detected along the profile based on peaks in the pixel intensity gradient along each row. Outliers were identified as being more than three standard deviations away from the local mean within a 50 element window and replaced using linear interpolation. The difference between the loaded and unloaded case gave the tip deflection with tip bending displacement, δ, taken as the average distance of every row with the twist, θ, determined from a line of best fit through the data with the tip displacement subtracted. Positive δ is defined as translation towards the suction side with positive θ defined as nose-up, as shown in figure 3.4. For the stainless steel model, no twist was clearly resolved within the precision of the method employed, indicating it is negligible, as was also reported by Zarruk et al. (2014) using high-resolution still photography for static deflections.

Cavitation behaviour

The cavitation behaviour over the suction side of the hydrofoil was recorded using a second Phantom v2640 high-speed camera with a Nikkor 50 mm f/1.8D lens (figure 3.2). The camera was operated with a resolution of 2048 × 1952 pixels and a spatial resolution of 0.185 mm/px with the same optical arrangement used for both the medium and short run acquisition types.

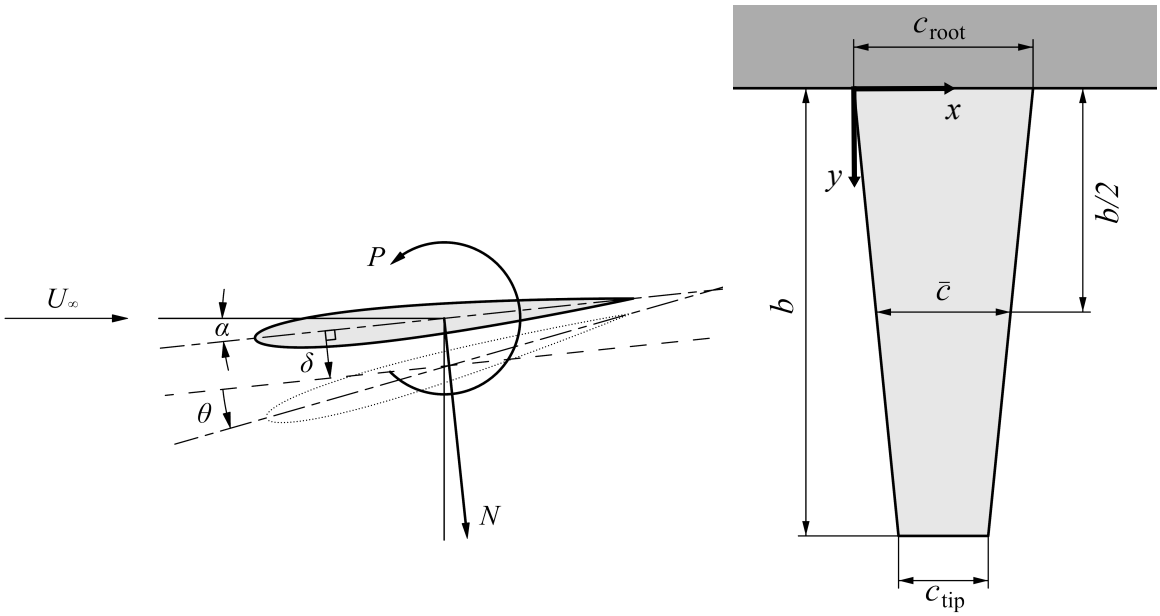

Figure 3.4: Coordinate system used for both the forces and tip deflection of the hydrofoil (left) is located at the mid-chord along the centreline. The deformed hydrofoil tip is represented by the dotted outline where the tip bending displacement, δ, is measured by taking the mean displacement of the profile edge perpendicular to the centreline at the zero-load case. The tip twist deflection, θ, is the rotation of the profile centreline from the zero-load case. A schematic of the hydrofoil's tapered planform (right) shows the coordinate system used in the analysis of the cavitation behaviour (e.g. cavity length) is located at the leading edge of the root chord.

To identify coherent structures in the dynamic cloud cavitation behaviour, spectral proper orthogonal decomposition (SPOD) is employed using the technique outlined by Towne et al. (2018). In this instance the SPOD is applied to the time varying image intensity as opposed to time varying velocity data from time resolved particle image velocimetry as typically used. SPOD optimally represents the space-time flow statistics by identifying energy ranked modes that are dynamically significant (Schmidt et al., 2018). Each high-speed photography acquisition provided time varying data (with image sequence) of the spatial variation (2 dimensional) of pixel intensity. Due to light scattering from interfacial surfaces, a high intensity was recorded where there was the presence of a cavity or bubbly mixture/shed cloud. Analyzing these image data sets with SPOD allowed for the identification of various shedding modes, both in frequency content and the spatial location.

SPOD utilizes multiple realizations of the temporal Fourier transform of the flow field, in this case the dynamic behaviour of the cavity, to obtain convergent estimates of the spectral densities by appropriately averaging the spectra, achieved using Welch's method (Welch, 1967) with a Hanning window. The decomposition was performed on the high-speed photography data, consisting of n_x rows and n_y columns, obtained from the medium run types at each σ . The pixel intensity time series of each pixel was broken up into blocks with a length, N_f, of 256 snapshots, representing 0.512 s. The overlap between

blocks, N_o, was 128 snapshots, representing 0.256 s. This results in 128 blocks, N_b, for the 18 000 snapshot long sequence, and producing a frequency resolution of 1.95 Hz for the extracted SPOD modes.

An overview of the SPOD calculation procedure applied to the data is given in the following with a detailed description of the SPOD methodology and algorithm given by Towne et al. (2018). For the n^{th} block, the matrix, $\boldsymbol{Q}^{(n)}$, is built from a portion of the high-speed movie, reshaped to have as many rows as pixels, $N = n_x \times n_y$, and N_f columns, being the number of frames in each block. Each block is structured with the k^{th} frame in the n^{th} block represented as $\boldsymbol{q}_k^{(n)}$ (equation 3.1). These are considered to be statistically independent realizations of the flow under the ergodic hypothesis.

$$\boldsymbol{Q}^{(n)} = [\boldsymbol{q}_1^{(n)}, \boldsymbol{q}_2^{(n)}, ..., \boldsymbol{q}_{N_f}^{(n)}] \in \mathbb{R}^{N \times N_f} \tag{3.1}$$

Once the data matrix is correctly structured into N_b blocks, the Fourier transform is calculated for the n^{th} block using equation 3.2. Each block is then structured again as shown in equation 3.3 with $\hat{\boldsymbol{q}}_k^{(n)}$ being the n^{th} realization of the Fourier transform at the k^{th} discrete frequency.

$$\hat{\boldsymbol{q}}_k^{(n)} = \frac{1}{2N_f} \sum_{j=1}^{N_f} w_j \boldsymbol{q}_j^{(n)} e^{i2\pi(k-1)[(j-1)/N_f]} \tag{3.2}$$

$$\hat{\boldsymbol{Q}}^{(n)} = [\hat{\boldsymbol{q}}_1^{(n)}, \hat{\boldsymbol{q}}_2^{(n)}, ..., \hat{\boldsymbol{q}}_{N_f}^{(n)}] \tag{3.3}$$

The scalar weights, w_j, are nodal values of the Hanning window function that can be used to reduce spectral leakage due to non-periodicity of the data in each block.

For each frequency, k, the Fourier coefficients of each block are collected into the new matrix $\hat{\boldsymbol{Q}}_{f_k}$, as shown in equation 3.4.

$$\hat{\boldsymbol{Q}}_{f_k} = [\hat{\boldsymbol{q}}_k^{(1)}, \hat{\boldsymbol{q}}_k^{(2)}, ..., \hat{\boldsymbol{q}}_k^{(N_b)}] \in \mathbb{R}^{N \times N_b} \tag{3.4}$$

This allows the weighted cross spectral density tensor, S_{f_k}, at frequency f_k to be written as equation 3.5 where $(\cdot)^*$ denotes the Hermitian transpose.

$$\boldsymbol{S}_{f_k} = \hat{\boldsymbol{Q}}_{f_k} \hat{\boldsymbol{Q}}_{f_k}^* \tag{3.5}$$

From $\boldsymbol{S}_{f_k}$, the SPOD modes of the k^{th} frequency, $\boldsymbol{\Phi}_{f_k}$, can be found as the eigenvectors from equation 3.6.

$$\boldsymbol{S}_{f_k} \boldsymbol{W} \boldsymbol{\Phi}_{f_k} = \boldsymbol{\Phi}_{f_k} \boldsymbol{\Lambda}_{f_k} \tag{3.6}$$

where $\boldsymbol{W}$ is a positive-definite Hermitian matrix that accounts for both the weight $\boldsymbol{W}(x)$ and the numerical quadrature of the integral of the discrete grid.

However, solving this is computationally expensive and it has been shown by Towne et al. (2018) that the modes can be recovered by solving the $N_b \times N_b$ eigenvalue problem in equation 3.7.

$$\hat{\boldsymbol{Q}}^*_{f_k} \boldsymbol{W} \hat{\boldsymbol{Q}}_{f_k} \boldsymbol{\Theta}_{f_k} = \boldsymbol{\Theta}_{f_k} \tilde{\boldsymbol{\Lambda}}_{f_k} \tag{3.7}$$

The non-zero eigenvalues of equation 3.6 are recovered and indicated by $\tilde{(\cdot)}$. By projecting the Fourier coefficients, $\hat{\boldsymbol{Q}}_{f_k}$, onto the new eigenvectors, $\tilde{\boldsymbol{\Theta}}_{f_k}$, as shown in equation 3.8, the mode shapes are obtained exactly.

$$\tilde{\boldsymbol{\Phi}}_{f_k} = \hat{\boldsymbol{Q}}_{f_k} \tilde{\boldsymbol{\Theta}}_{f_k} \tilde{\boldsymbol{\Lambda}}^{-1/2}_{f_k} \tag{3.8}$$

The modes ($\tilde{\boldsymbol{\Phi}}_{f_k}$) are ranked in order of intensity by their eigenvalues in equation 3.9. As shown in Venning et al. (2018a), the first mode of each frequency, $\phi^{(1)}_{f_k}$, is the most indicative of the 'mean' flow state and as such will be the only modes presented throughout the paper.

$$\tilde{\boldsymbol{\Phi}}_{f_k} = [\phi^{(1)}_{f_k}, \phi^{(2)}_{f_k}, ..., \phi^{(N_b)}_{f_k}] \tag{3.9}$$

This information gives insight into the excitation spectra induced by the cloud cavitation and can be compared to the response spectra to aid in identifying certain components such as cloud cavitation induced force fluctuations and structural natural frequencies. Intensity maps are generated through colour-scaled plots where the intensity level of each pixel is proportional to the intensity level of the corresponding frequency. This provides spatial information revealing the distribution across the image of the shedding modes. By plotting the phase of the Fourier coefficients across the domain, insight into shedding cycle behaviour and interaction between events across the hydrofoil may be gained.

Spatio-temporal information of the cavitation behaviour is also represented through the use of space-time plots. These plots are generated by extracting either the same row or column of pixels from each frame and placing them sequentially next to one another, producing chordwise and spanwise space-time plots, respectively. Interpretation of these plots are discussed in detail by Smith et al. (2019).

3.4 Results and discussion

As σ is progressively reduced beyond inception the hydrofoil experiences various forms of cavitation. The extent of the cavitation varies from short partial sheet cavities through to supercavitation (Franc and Michel, 2004). The characteristics of each regime vary in appearance and an overview of the various regimes is presented in figure 3.5. Traits are observed to not only vary between each of the cavitation regimes, but also within

Cavitation Mode	Mechanism	σ
Type I	Shockwave	0.3 – 0.6
Type IIa	Re-entrant jet (root/tip)	0.4 – 1.0
Type IIb	Re-entrant jet (tip)	0.7 – 0.9

Table 3.3: Summary of the cavitation modes experienced by the hydrofoil for the σ range tested. As σ is reduced from 1.2, the hydrofoil first starts experiencing the re-entrant driven Type IIa mode at $\sigma = 1.0$ with the Type IIb becoming active shortly after at $\sigma = 0.9$. Further reduction in σ sees the disappearance of the Type IIb mode below 0.7 with the shockwave driven Type I becoming active at $\sigma = 0.6$. The Type IIa mode remains active along with the Type I mode down to $\sigma = 0.4$ before disappearing, resulting solely shockwave driven shedding at $\sigma = 0.3$. Supercavitation is reached at $\sigma = 0.2$ where no cavitation modes are active.

the regimes themselves. Characterising the cavitating behaviour and the corresponding influence on the hydrofoils performance is achieved by establishing correlations between the measured forces and deflections with the cavitation behaviour observed in the high-speed photography. For the σ range tested, three primary cavitation modes experienced by the hydrofoil were identified which varied in both the mechanism driving shedding as well as the location on the hydrofoil. These cavitation modes are summarized in table 3.3 as well as indicated on the spectrograms in figure 3.8.

3.4.1 Cavity length

The length of the attached cavity was measured for each σ with the cavity length, L_c, taken as the furthest downstream extent of the cavity while remaining attached. When shedding is present, this is the cavity extent in each cycle prior to the shedding event. Cavity lengths were obtained at 4 spanwise positions from chordwise space-time diagrams extracted from the long-duration videos as an average from at least 50 cavity growth/shedding cycles.

The presence and extent of an attached cavity influences the pressure distribution over the hydrofoil and therefore the forces that result. In cloud cavitation conditions, the attached part of the cavity limits the minimum pressure on the suction side to the vapour pressure of the water (Franc, 2001). Figure 3.6 shows the maximum attached cavity length, L_c normalized by the local chord, c, as a function of σ and spanwise position. For $0.4 \leq \sigma \leq 0.6$, the cavity length exhibits a reduction in the rate of increase with reducing σ compared to higher σ ranges. This reduction in cavity-length growth rate corresponds to the attached cavity reaching the trailing-edge, i.e. $L_c/c = 1.0$. At this stage of development the cavity closure will now directly interact with the flow from the pressure side of the foil, possibly causing the rate of growth to reduce. When σ is reduced to 0.2 the cavity length increases to well beyond the local chord, indicating the cavity closure is away from the trailing-edge and hence is in the supercavitating regime.

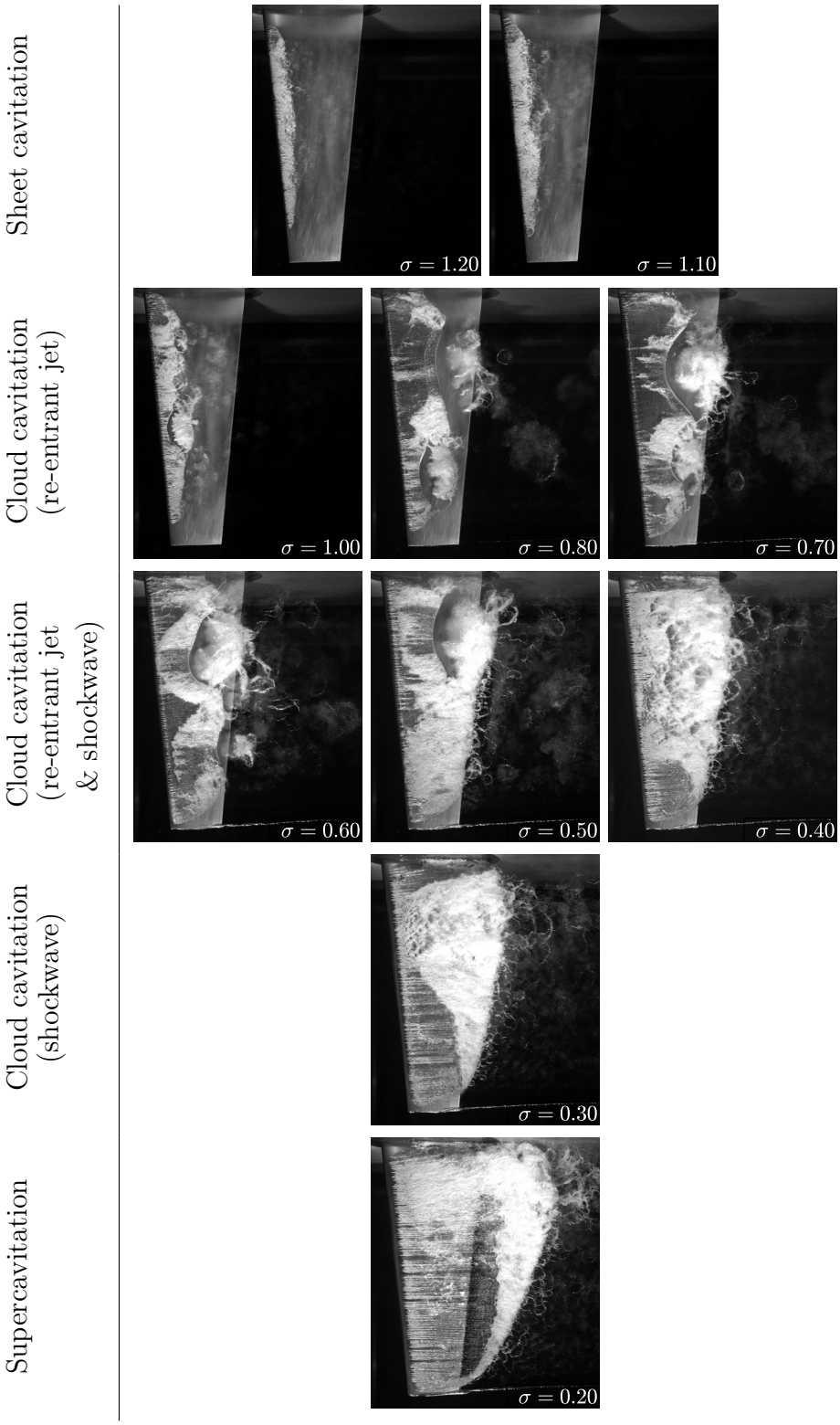

Figure 3.5: Photographs of the hydrofoil with different cavitation regimes through the range of σ below inception. The hydrofoil first experiences stable sheet cavitation ($1.1 \leq \sigma < 1.2$), with development of re-entrant jet driven cloud cavitation as σ is reduced ($0.4 \leq \sigma \leq 1.0$). A further reduction in σ, with cavity length extending to the trailing-edge, upstream propagating condensation shockwaves become the dominant mechanism for shedding ($0.3 \leq \sigma < 0.4$). For $\sigma < 0.3$, the cavity envelopes the hydrofoil (supercavitation) and the break-up region is downstream of the trailing-edge.

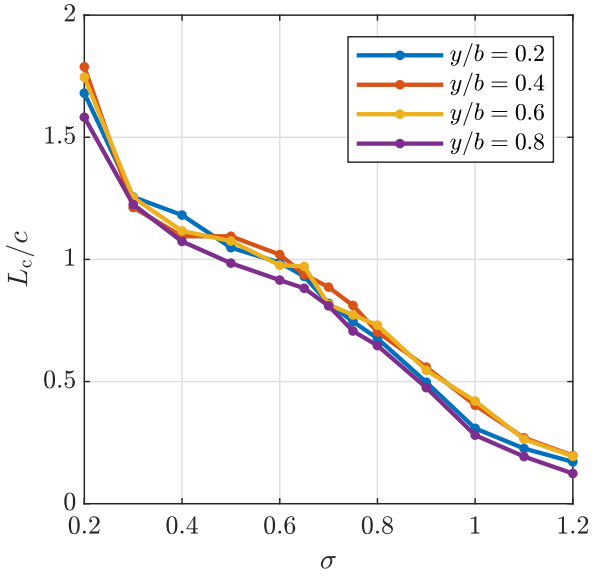

Figure 3.6: Maximum attached cavity length, L_c, as a function of σ, for four spanwise positions. The cavity length is the average length at cavity break-off, and is non-dimensionalised by the local chord, c, at each position. The cavity growth is continuous as σ is reduced.

3.4.2 Steady and unsteady components of the forces and deflections

The mean and standard deviation of the normal force (C_N) and pitching moment (C_P) loads provide insight into the impact of the cavitation on the hydrofoil in terms of both the steady and unsteady forces. Spatial information is obtained through the centre of pressure, x_{cop}, which gives the centre of action of the forces acting along the hydrofoil and is calculated as C_P/C_N and presented as a ratio of the mean chord, $x_{cop}/\bar{c}$, from the leading edge at the root. The non-dimensional tip displacement, $\delta/\bar{c}$, is presented to assess the level of structural response resulting from the hydrodynamic loading.

The mean and standard deviation of C_N, C_P, $x_{cop}/\bar{c}$ and $\delta/\bar{c}$ are shown in figure 3.7 as functions of σ, with $'$ denoting the standard deviation of the time-varying quantities. As σ is decreased from 1.2 to 1.1 (sheet cavitation regime, see figure 3.5), all standard deviations increase despite little change in the mean load and displacement. Further reduction in σ to 1.0 sees a significant change in the unsteady loading with C'_N approximately doubling and is attributed to the transition to the cloud cavitation regime with re-entrant jet driven shedding at $\sigma \approx 1.0$. This increased unsteadiness is attributed to the increased volume of the shedding clouds associated with re-entrant jet driven shedding compared to sheet cavitation having greater impact on the hydrofoils pressure distribution.

Initially as σ is reduced into the cloud cavitation regime ($0.3 \leq \sigma \leq 1.0$), C_N continues to increase, reaching a maximum at $\sigma = 0.71$, corresponding with the maxima in C'_N, $\delta/\bar{c}$ and $\delta'/\bar{c}$. This is attributed to the increase in effective camber of the cavitating hydrofoil due to the presence of the cavity and is discussed further in §3.4.4. There is a marked

increase in C'_N and $\delta'/\bar{c}$ for $\sigma = 0.8$ to 0.7 which is associated with the lock-in phenomena discussed later in §3.4.4. Further reduction in σ below 0.7 sees a steady decrease in C_N and C'_N with the mean normal force reducing monotonically into the supercavitating regime.

Despite C_N initially increasing with reducing σ, C_P decreases with the onset of unsteady shedding, dropping more sharply as σ is reduced from 1.0 to 0.7. This is due to the growing cavity shifting the x_{cop} towards mid-chord, reducing the lever arm of the applied load. The rate C_P decreases is reduced as the cavity approaches the trailing edge at $\sigma \approx 0.6$ with $x_{cop}/\bar{c}$ reaching a maximum of 0.57 at $\sigma = 0.56$. Interestingly, x_{cop} starts moving back towards the leading edge as σ drops further despite the cavity covering the entire chord as the pressure field varies around the combined hydrofoil/growing cavity system. This is unexpected given the vapour pressure limitation imposed on the suction side by the growing cavity attributed to the initial downstream migration of x_{cop}. Potential drivers for the reversal of x_{cop} downstream migration include lateral migration of the stagnation point and effective camber imposed by the cavity altering the streamlines and therefore the pressure distribution. However, a justification for this behaviour can not be provided given the available data, warranting further investigation. The displacement and normal force measurements, both mean and standard deviation, exhibit similar trends, indicating a strong correlation between the two as expected. A strong correlation is also observed between x'_{cop} and C'_P.

3.4.3 Force and deflection spectra

The amplitude and frequency content of the forces acting on the hydrofoil is dependent on multiple factors including hydrodynamic loading, cavitation dynamics and the structural response. A spectrogram of C_N for varying σ (figure 3.8) provides a global perspective of how the cavitation behaviour modulates the spectral characteristics. The spectrogram is constructed from spectra of the long-duration measurements at 0.025 increments of σ. Spectra of C_N were obtained using the Power Spectral Density (PSD) derived with the Welch estimate (Welch, 1967) utilizing a Hanning window with size and overlap of 2 048 (2.05 s) and 512 (0.51 s) samples, respectively, on the 360 000 (360 s) sample time series. Frequency is non-dimensionalized as a chord-based Strouhal number, $St = fc/U_\infty$. Individual spectra plots at σ values of particular interest are presented in figure 3.9 along with the corresponding tip deflection spectra calculated from the medium duration time series data.

There are 3 primary modes identified in the spectra which are referred to as Types I, IIa and IIb in the text. The Type I mode is associated with shockwave-driven periodic shedding occurring along a majority of the span with the shedding frequency observed to be essentially independent of σ. The Type IIa and IIb modes are both driven by a re-entrant jet instability and are dependant on σ. Type IIa 'root shedding' events occur

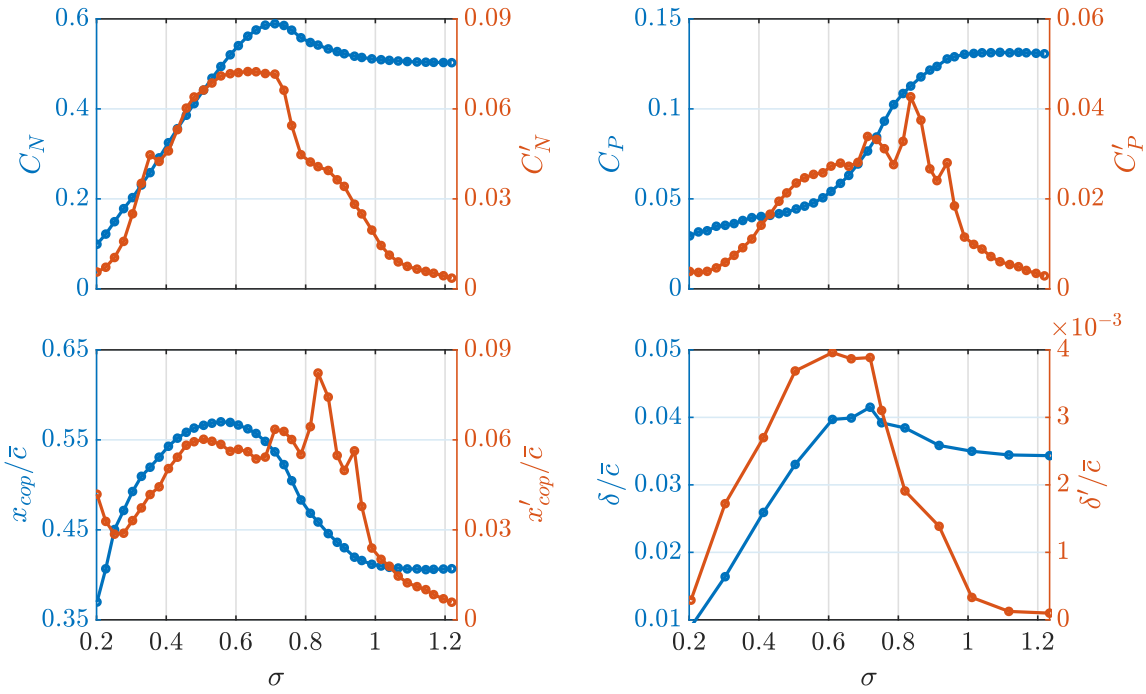

Figure 3.7: Mean (blue) and standard deviation (orange) of the normal force (C_N), pitching moment (C_P), location of the centre of pressure ($x_{cop}/\bar{c}$) and tip displacement ($\delta/\bar{c}$) at various σ where $'$ indicates the standard deviation of the time varying quantity. The results show the effect of various cavitation regimes revealing unique characteristics in the steady and unsteady components.

at various spanwise positions depending on σ, while Type IIb 'tip shedding' events are confined to the lower portion ($0.5 < y/b < 1.0$). This nomenclature follows that used by Kjeldsen and Arndt (2001) where shockwave and re-entrant jet type shedding mechanisms were termed Types I and II, respectively. The analysis undertaken to identify these various modes is described in §3.4.4.

As previously observed with both 2D (Kawanami et al., 1998; Prothin et al., 2016) and 3D geometries (Smith et al., 2018), the cavitation pattern over a hydrofoil varies with σ, such as shedding sites, cavity length and cavitation cloud size. The frequency at which these shedding events occurs is also dependant on their spanwise location, particularly in the present case of finite and spanwise varying geometry. Utilizing the intensity maps from the SPOD (figure 3.10) applied to the high-speed photography provides spatial information with respect to the cloud cavitation regime to qualitatively identify periodic shedding sites at each σ. Used in conjunction with the C_N and $\delta/\bar{c}$ response spectra, the intensity and phase maps allow modes evident in the response spectra to be attributed to associated cavity dynamics.

Within the stable sheet cavitation regime ($\sigma \geq 1.1$), there is little unsteady content in C_N with no tonal peaks observed in the spectra (not shown in figure 3.9). Once σ is reduced below 1.1, with cloud cavitation forming, fluctuations in both C_N and $\delta/\bar{c}$ are

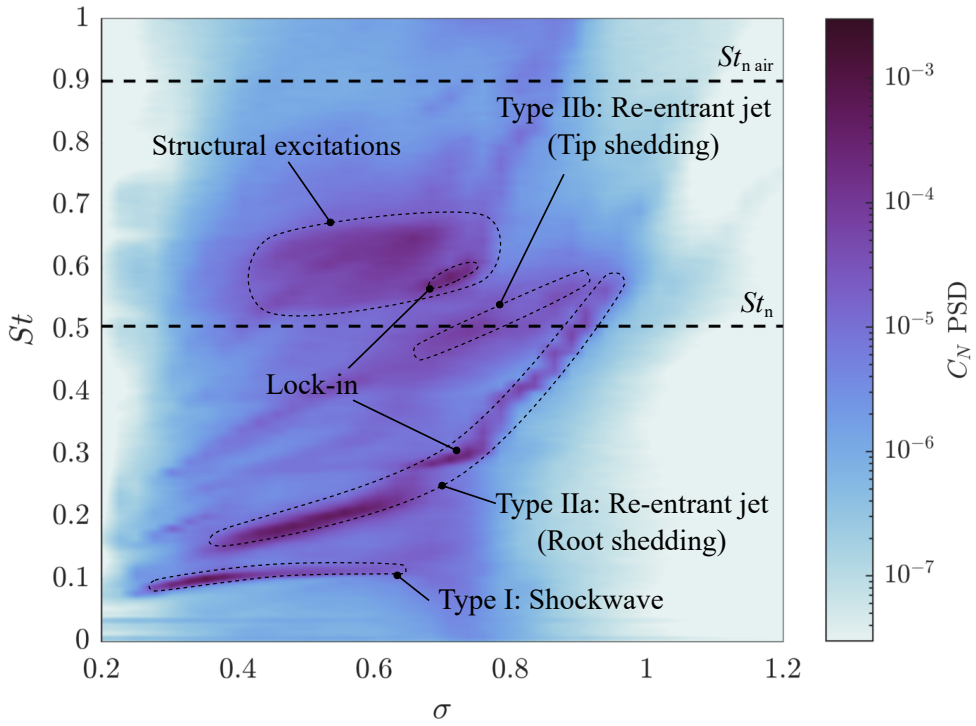

Figure 3.8: Spectrogram of the normal force for a range of σ showing the global unsteady behaviour. The results highlight the shockwave driven Type I shedding frequency is predominantly independent of σ while the re-entrant jet driven Type IIa & IIb shedding modes are highly dependant on σ. The natural frequency of the hydrofoil in-air, $St_{\text{n air}}$, and fully wetted, St_{n}, are indicated by two horizontal dashed lines.

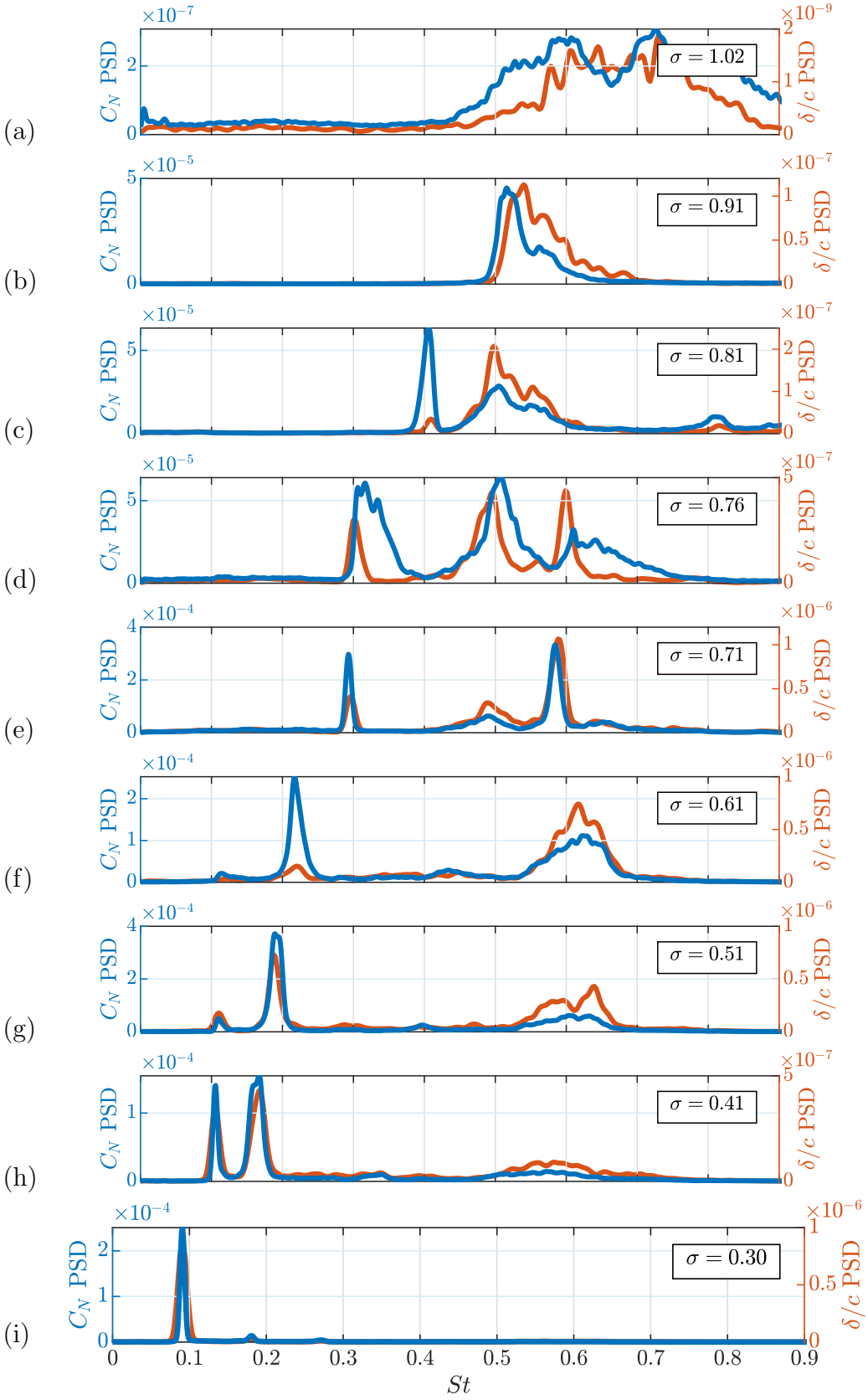

Figure 3.9: PSD of the normal force (blue) and tip displacement (orange) time series at selected σ. The various spectra show the peak frequencies shift as σ varies with both the normal force and tip displacement exhibiting similar spectral characteristics across the selected σ values. Note that the vertical scales vary (by orders of magnitude) between the plots.

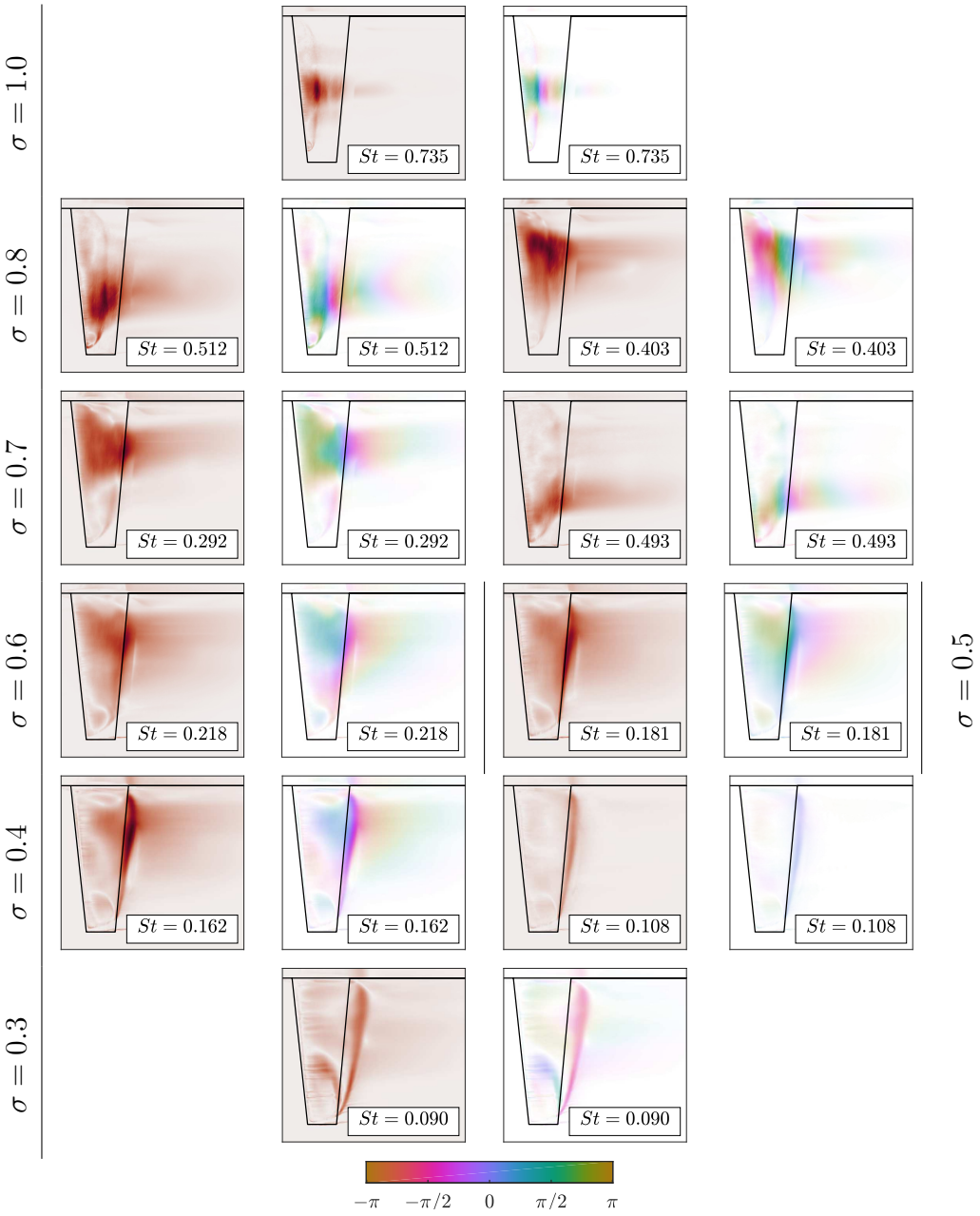

Figure 3.10: Spectral POD intensity (red) and phase maps (coloured) of key modes for various σ highlighting regions of high activity at the frequencies of interest. The color intensity distribution in each phase map is directly proportional to that of the corresponding intensity map. The spectral and spatial information aids in the identification of the mechanisms driving oscillations with phase maps providing the relative timing of each cycle.

now significant (increasing by two orders of magnitude between $\sigma = 1.02$ and 0.91) with distinct tonal peaks becoming apparent (figure 3.9b). Two distinct peaks are evident in the C_N and $\delta/\bar{c}$ spectra at $\sigma = 0.91$, both of which decrease in frequency as σ is reduced to 0.81 (figures 3.9b & 3.9c). These peaks are associated with the formation of two shedding sites along the span of the hydrofoil discussed later in §3.4.4. The shedding at these two sites are referred to as Type IIa and Type IIb oscillations for the root and the tip, respectively.

A shift in the peak frequency occurs in conjunction with the appearance of a third peak in the spectra at $\sigma = 0.76$ as σ is reduced below 0.8 (figure 3.9d). The C_N spectrogram (figure 3.8) shows the Type IIa frequency jumping down to $St = 0.31$ and increasing in magnitude with an intense peak appearing at double the frequency ($St = 0.61$) for $0.7 \leq \sigma \leq 0.76$. This feature is attributed to lock-in where the Type IIa shedding frequency has transitioned to match a sub-harmonic of the hydrofoils first bending mode (f_n). As given in table 3.1, the hydrofoil first bending mode occurs at 55 Hz ($St_n = 0.52$) in fully wetted conditions, which is lower than the third peak at $St = 0.61$. This difference in frequency is attributed to the presence of the vapour cavity reducing the added mass and causing frequency modulation. The Type IIb peak continues a steady decrease to $St = 0.51$ at $\sigma = 0.76$ (figure 3.9d).

Lock-in is also apparent in the tip displacement spectrum at $\sigma = 0.7$ (figure 3.9e) in the appearance of the third peak along with amplification of the Type IIa spectral peak (also reflected in the increase in δ'/c shown in figure 3.7). As σ is reduced below 0.65, the hydrofoil comes out of lock-in with the Type IIa oscillations dropping to $St = 0.22$, the Type IIb mode fading out and significant broadband excitation in C_N and $\delta/\bar{c}$ appearing at $St \approx 0.62$ (see figure 3.9f) attributed to structural excitations.

The Type IIa shedding frequency continues to steadily decrease as the attached cavity length grows, showing a linear dependence on σ until it disappears at $\sigma \approx 0.4$. The spectra also shows the emergence of an additional frequency at $St = 0.11$ for $\sigma \lessapprox 0.6$ that is nominally independent of σ. The appearance of this new feature coincides with the cavity reaching the trailing-edge (figure 3.6) and is attributable to the presence of the shockwave instability (Type I). In addition, the broadband excitation appearing at $St \approx 0.62$ is linked to structural excitations outside of lock-in conditions, apparent down to $\sigma = 0.4$. Type I and IIa instabilities are both present from $\sigma = 0.6$ down to 0.4 with the Type I amplitude increasing as σ is reduced.

Once σ is reduced below 0.4, only the Type I mode remains with $St \approx 0.09$ oscillations dominant, as shown in figure 3.9i. As also observed by Kjeldsen et al. (2000) and Smith et al. (2018), the Type I mode shows little to no dependence on σ, however, Kawakami et al. (2008) found this only to be valid for cases with relatively high gas content ($\sim$ 13 ppm), which was not the condition in the present study.

The shockwave-driven Type I mode is no longer apparent in the supercavitating regime

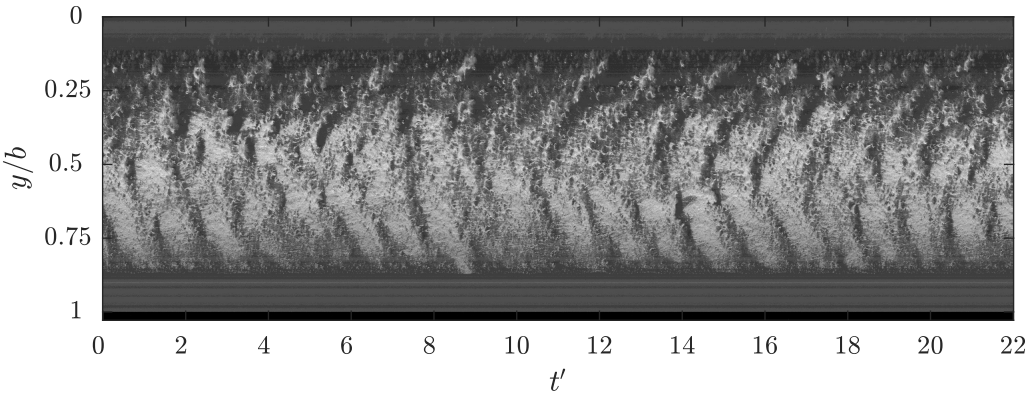

Figure 3.11: Spanwise space-time plot taken at $x/c_{root} = 0.35$ shows the shedding small-scale vapour structures along the span due interfacial instabilities for $\sigma = 1.1$. While there is evidence of periodic break-up, the influence on the forces and deflections are minimal.

($\sigma = 0.2$). The C_N spectrogram (figure 3.8) reveals minimal excitations with no tonal peaks for $\sigma = 0.2$. All associated cavity dynamics with observations made in the forces and deflections for each cavitation regime will be discussed in §3.4.4.

3.4.4 Cavity dynamics

Sheet cavitation

Sheet cavitation occurs at relatively high σ ($1.1 \leq \sigma \leq 1.2$) and is confined to a small portion of the chord towards the leading edge. The space-time plot taken at $x/c_{root} = 0.35$ (figure 3.11) shows coherent shedding of small-scale vapour structures. However, the cavity at the extreme extents (not shown in the space-time) is stabilised by the re-entrant jet at the tip and the tunnel ceiling boundary layer at the root. Cavity break-up is driven primarily by interfacial instabilities such as Kelvin-Helmholz driven spanwise vorticity lines (Avellan et al., 1988) and turbulent transition (Brennen, 1995). Some recent investigations have observed this phenomena in cavitating flows about a rectangular planform finite-span hydrofoil (Russell et al., 2018) and about a sphere (Brandner et al., 2010; de Graaf et al., 2017). The shedding of these small-scale structures only cause minimal broadband force fluctuations as they are not large enough to cause any significant changes in the flow over the hydrofoil and hence, unsteadiness in the pressure distribution and resulting developed forces.

As σ is reduced, the cavity grows into a region of an increasingly adverse pressure gradient, a re-entrant jet begins to form extending upstream along the hydrofoil surface. For the re-entrant jet to act as a mechanism for cavity break-up and cloud shedding it needs to reach the upstream extent of the cavity (Pelz et al., 2017). This will only occur in practice if the cavity is sufficiently thick (Franc, 2001). Note that for a given flow configuration the cavity thickness will increase in proportion to the length. As observed by Callenaere et al. (2001), a relatively thin cavity is highly susceptible to the interfacial

instabilities of both interfaces (i.e. re-entrant jet/cavity surface) interacting, leading to break-up of the cavity into small-scale vapour structures, rather than the re-entrant jet progressing sufficiently upstream to act as a mechanism for the cloud instability. As shown in figure 5, the conditions to satisfy these requirements for cloud shedding to form are reached by $\sigma = 1.0$.

Re-entrant jet driven shedding (pre-lock-in)

Cloud cavitation occurs when σ is reduced to 1.0 with the conditions allowing the re-entrant jet to reach the upstream extent of the attached cavity, causing periodic detachment and the formation of a cavitation cloud. As shown by the space-time plot in figure 3.12 , re-entrant jet driven shedding only occurs around mid-span with the detachment of small bubbly vortices occurring towards the spanwise extents. This behaviour is also evident in the intensity maps for $\sigma = 1.0$ at $St = 0.74$ (figure 3.10). This is due to the three-dimensionality of the geometry with localised tip flow introducing a spanwise velocity component that locally prevents the re-entrant jet reaching the leading edge.

Likewise, the ceiling boundary layer modifies the local pressure distribution and streamwise velocity component in the vicinity of the root, adversely affecting formation of the re-entrant jet in the region. This results in areas of stable cavities at the spanwise extents of the attached cavity, as seen in figure 3.5. The shedding of cavitation clouds at $\sigma = 1.0$ induces relatively low force fluctuations, as indicated by C'_N (figure 3.7), at a frequency around $St \approx 0.70$ (evident also in the C_N spectra (figure 3.9) and space-time plot (figure 3.12)). The shedding frequency is relatively broadband and can be attributed to the varying spanwise shedding location seen in the space-time plot, where the varying cavity length changes the duration for the re-entrant jet to reach the leading edge, thus broadening the shedding frequencies present in the spectra. It is also apparent that the changing shedding location doesn't move randomly, but is dependant on the previous cycle. This is due to the spanwise component of the previous cycle's re-entrant jet preventing other instabilities from interfering in the next shedding cycle at that spanwise location (De Lange and De Bruin, 1998).

As σ is decreased further to 0.9, the cavity size increases along with the re-entrant jet thickness (Callenaere et al., 2001), giving it the momentum to overcome spanwise flow components and reach the leading edge for the majority of the span. The increased cavity length and inherent cavity dynamics results in a spatial compatibility with the span, resulting in the formation of two re-entrant driven shedding modes (Type IIa & IIb). The increased cavity size results in significant excitation in C_N and $\delta/\bar{c}$ and by $\sigma = 0.8$ two tonal frequencies become evident in the spectra (figure 3.9) at $St = 0.41$ and 0.50, corresponding to multiple shedding sites along the span (figure 3.10). As noted previously, the frequency of these modes decreases with σ which is due to the re-entrant

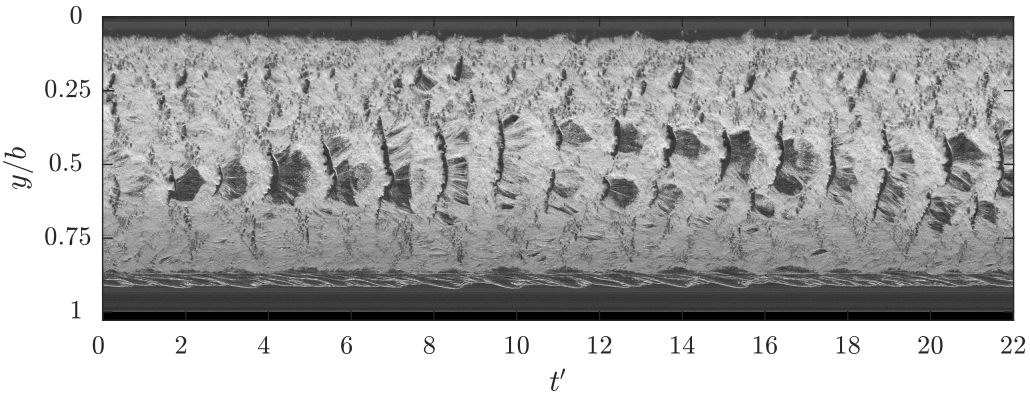

Figure 3.12: Spanwise space-time plot taken at $x/c_{root} = 0.31$ for $\sigma = 1.0$ shows the re-entrant jet instability around mid-span causing periodic shedding with its spatial distribution varying through time.

jet requiring more time to break through the attached cavity as it has more distance to travel upstream (as cavity length grows) with decreasing σ (figure 3.6).

The Type IIa & IIb shedding modes occur towards the root and tip, respectively, and are evident in the space-time plot in figure 3.13d where the shedding frequencies match those in the C_N and $\delta/\bar{c}$ spectra. SPOD intensity and phase maps of the cavitation behaviour at $\sigma = 0.8$ (figure 3.10) show the Type IIa activity ($St = 0.41$) is confined to the upper portion of the span ($0.0 < y/b < 0.4$), with the Type IIb activity ($St = 0.50$) focused to the lower portion ($0.6 < y/b < 0.8$). Additionally, the wavelet transform of C_N in figure 3.13 shows two primary frequencies occurring simultaneously and are always present over time. Comparing extracted wavelet components at $St = 0.41$ and 0.50 with the spanwise space-time plot reveals a strong correspondence with the Type IIa and Type IIb shedding events (figure 3.13).

The C_N spectrum at $\sigma = 0.8$ reveals that the $St = 0.41$ amplitude is greater than that at $St = 0.50$, where the opposite is true in the $\delta/\bar{c}$ spectra with $St = 0.50$ exhibiting the greater amplitude. This is attributed to the Type IIa shedding events being of greater magnitude from a longer cavity with the larger local chord, thus having more influence on C_N. For the Type IIb shedding events, they occur towards the tip and despite their reduced magnitude, the shedding events have more influence on the tip displacement due to the increased lever of the resulting force acting on the cantilevered hydrofoil. Hence, the spatial distribution of the cloud cavitation influences the C_N and $\delta/\bar{c}$ spectra.

As the cavity grows with the reduction in σ, it changes the flow over the suction side of the hydrofoil. The presence of the cavity increases the effective camber of the hydrofoil and therefore increasing the lift force (Young et al., 2018a), despite minimum pressure limitations imposed by the cavity. This results in a steady increase in the mean C_N as σ is reduced, reaching a maximum at $\sigma = 0.7$ (figure 3.7). The resulting pressure distribution also becomes sensitive to cavitation clouds being advected along the chord, contributing to the rise in C'_N which reaches a maximum at a point coinciding with the maximum

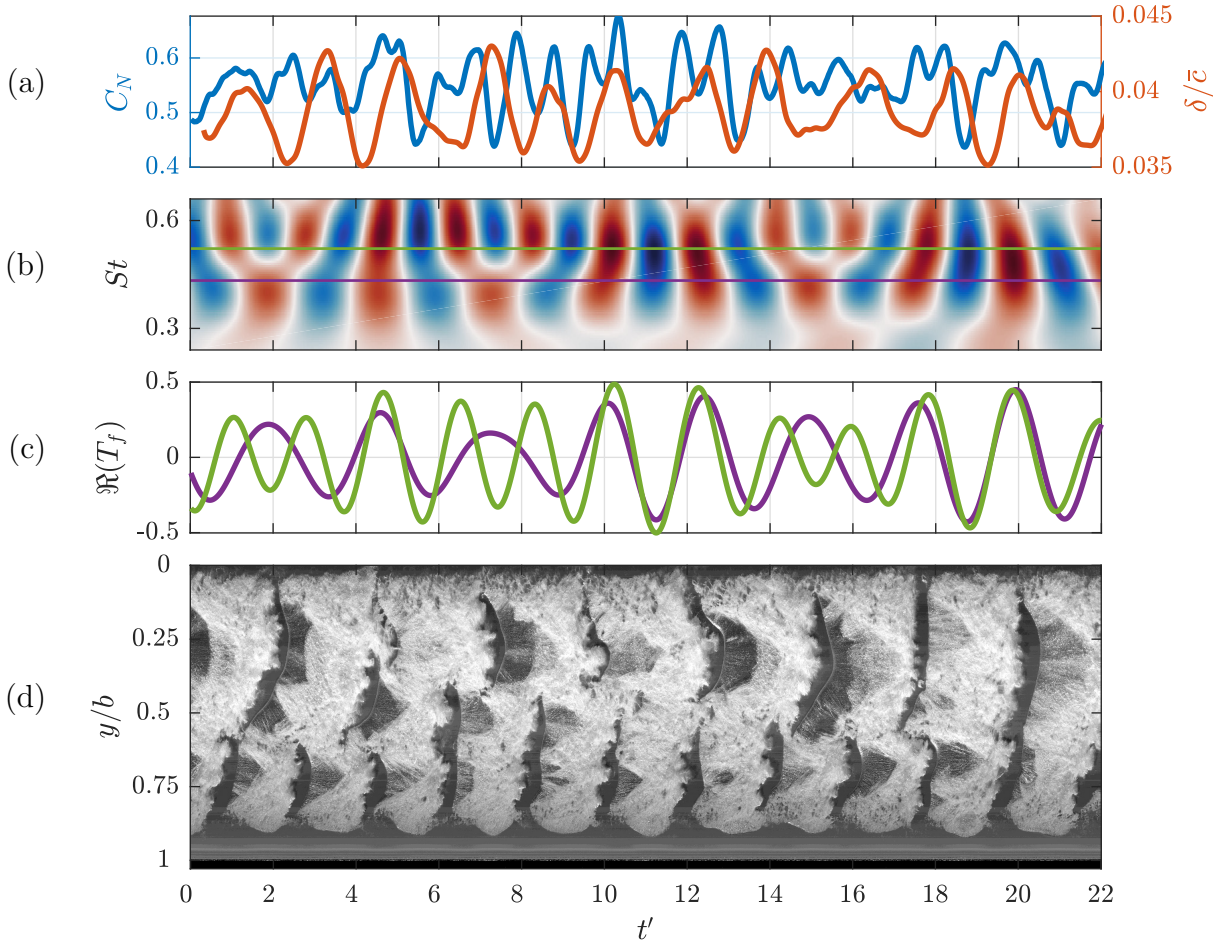

Figure 3.13: Synchronised time series of the normal force (C_N) and the tip displacement ($\delta/\bar{c}$) (a) at $\sigma = 0.8$ with the real value of the C_N Morlet wavelet transform (b). The $St = 0.41$ (purple) and 0.50 (green) components of the wavelet transform (c) show the connection between the C_N fluctuations and the Type IIa and IIb shedding events evident in the spanwise space-time plot taken at $x/c_{root} = 0.5$ (d).

C_N. With further reduction in σ from 0.7, both C_N and C'_N decrease as the minimum pressure limitation imposed by the cavity becomes more influential than the increased flow curvature.

The presence of the attached cavity significantly alters the pressure distribution over the suction side of the hydrofoil compared to the fully wetted case (Leroux et al., 2004). The cavity imposes a minimum pressure limitation equal to p_v where the vapour filled cavity is attached to the surface, reducing the mean load on the hydrofoil (Franc, 2001). Additionally, the presence of the cavity modifies the streamlines over the hydrofoil having the effect of either increasing or decreasing the effective camber (Young et al., 2018a). The increase in the mean C_N as σ is reduced to 0.7 (figure 3.7) is attributed to the increase in effective camber of the cavitating hydrofoil. As σ is reduced below 0.7, the cavity growth now alters the flow over the suction side that results in a decrease in effective camber, reducing the loading on the hydrofoil.

Lock-in

The lock-in phenomena occurs when when a structure is being excited by an instability of which its frequency will deviate to match with a relatively close structural natural frequency, resulting in significant amplification of the structural response. This has previously been observed in hydrofoil's experiencing cloud cavitation (Akcabay and Young, 2014; Akcabay et al., 2014; Pearce et al., 2017; Harwood et al., 2019, 2020) with Akcabay and Young (2015) showing that parametric excitations cause frequency modulation in the vibration response. This is due to changes in the fluid-mixture density causing fluctuations in effective fluid-added mass.

As σ is reduced below 0.8, both the Type IIa and IIb shedding frequencies decrease due to the increasing cavity length until σ reaches 0.75. The reduction in shedding frequency leads to the hydrofoil experiencing lock-in for $0.65 \leq \sigma \leq 0.75$. Lock-in occurs as the excitation frequency from the periodic shedding falls into a finite band surrounding a resonance of the hydrofoil, forcing it to lock-in to the natural frequency, leading to amplification of small motions and fluctuating fluid loads (Harwood et al., 2019). This is observed to occur on the current hydrofoil where the Type IIa excitation shedding frequency matches a sub-multiple of the hydrofoil natural frequency with an additional peak appearing in the spectra at twice the frequency. This third spectral is associated with the first bending mode of the hydrofoil which has been modulated due to the presence of the vapour cavity. With a portion of the hydrofoil oscillating in vapour instead of liquid, the added or entrained mass, along with the hydrodynamic stiffness is reduced (De La Torre et al., 2013; Harwood et al., 2019, 2020), increasing the natural frequency to $St \approx 0.61$. Hence, as the Type IIa shedding mode approaches the first sub-harmonic ($f_\mathrm{n}/2$) of the hydrofoils first bending mode, the frequency deviates to lock-in to the

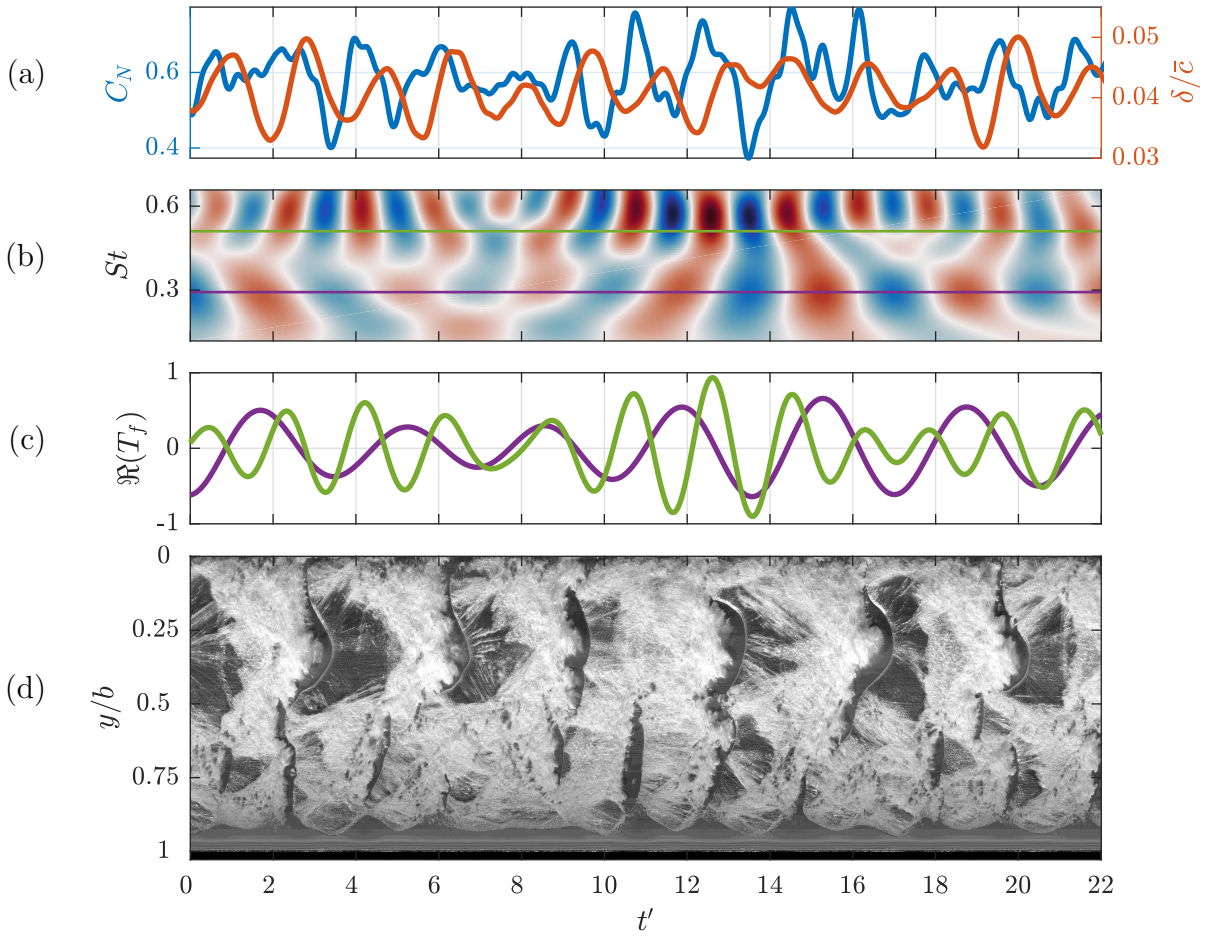

Figure 3.14: Synchronised time series of the normal force (C_N) and tip displacement ($\delta/\bar{c}$) (a) at $\sigma = 0.70$ with the real value of the Morlet wavelet transform for C_N (b) followed by the $St = 0.30$ (Type IIa, green) and 0.488 (Type IIb, purple) components (c). Peaks in the two frequency components are seen to coincide with shedding events in the upper and lower portion of the span as shown in the spanwise space-time plot taken at $x/c_{root} = 0.5$ (d).

structural excitations and causing excitations at $St = 0.61$ (structural) & $St = 0.31$ (cavity driven).

Lock-in causes the Type IIa mode to reduce to a shedding frequency of $St = 0.29$ at $\sigma = 0.7$, evident in the space-time plot in figure 3.14. The SPOD intensity map (figure 3.10) shows the Type IIa mode occupying a greater portion of the span compared to $\sigma = 0.8$, extending further towards the tip. This has resulted in a shift towards the tip for the Type IIb mode ($St = 0.49$), as well as a reduction in its area of influence.

The Type IIb mode doesn't experience any significant frequency modulation, dropping to $St = 0.49$ by $\sigma = 0.7$. However, comparison of the space-time plot (figure 3.14d) with cases just above and below ($\sigma = 0.8$ and 0.6 in figures 3.13d and 3.15c) reveals increased disruption of the cavity dynamics when lock-in is present (i.e. more bubbly appearance) towards the tip is observed as shown in the spanwise space-time diagrams. This may be attributable to the increased tip vibrations preventing stable cavity growth in the region. Besides the minimal additional surface perturbations during lock-in, the lack of frequency

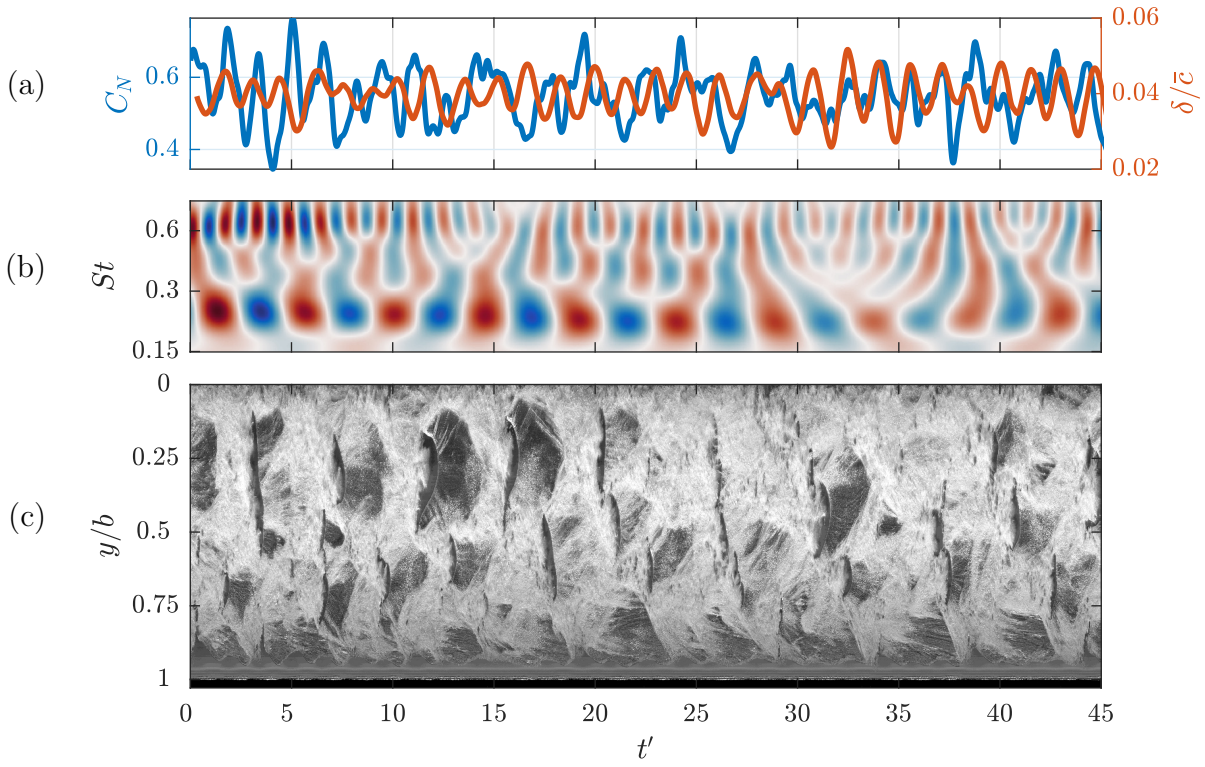

Figure 3.15: Synchronised time series of the normal force (C_N) and tip displacement ($\delta/\bar{c}$) (a) with the real value of the Morlet wavelet transform for C_N (b) at $\sigma = 0.6$. The hydrofoil experiences a relatively consistent $St = 0.22$ oscillation due to the Type IIa shedding as shown in the spanwise space-time plot taken at $x/c_{root} = 0.5$ (c). Irregular shedding of small-scale structures in the lower half of the span result in inconsistent and varying intensities at higher frequencies evident in the wavelet transform.

modulation suggests the cloud cavitation influences deformations but the deformations are not large enough to influence the primary cloud cavitation behaviour.

Re-entrant jet and shockwave driven shedding (post-lock-in)

With a sufficient reduction in σ to 0.6, the decrease in cavity shedding frequency from the increased cavity length brings the hydrofoil out of lock-in. From this point, the hydrofoil no longer experiences Type IIb shedding with the C_N and $\delta/\bar{c}$ spectra dominated solely by the Type IIa shedding mode at $\sigma = 0.6$. The increased cavity length and width of the shedding cavitation clouds is no longer compatible with the hydrofoils span to form multiple stable shedding sites. This results in a single periodic shedding site in the upper half of the span, as evident in the space-time plot in figure 3.15c. In the lower half, the cavity is shed at the same frequency, albeit with less energy (figure 3.10).

At $\sigma = 0.6$, the attached cavity has reached the trailing-edge with $L_c/c \approx 1.0$ at all spanwise positions (figure 3.6). Shortly after which the centre of pressure starts shifting back towards the leading edge with further reduction in σ. This is attributed to the suction side increasingly experiencing a uniform p_v pressure distribution along the chord due to

the attached cavity. This increases the relative contribution of the fully wetted side's pressure distribution, shifting x_{cop} back towards the leading edge, as shown in figure 3.7.

With the cavity reaching the high-pressure region near the trailing-edge and closing in a region with a low adverse pressure gradient, the shockwave instability becomes active in the flow at low σ. As the cavity grows, the re-entrant jets forms and progresses upstream, slowing down as it approaches the upstream extent of the attached cavity and stalling before it causes the cavity to detach. The re-entrant jet behaviour causes perturbations to form over the attached cavity as it grows with small-scale break-up generating a bubbly flow in the region with a high void fraction. This preconditions the flow for condensation shockwaves to propagate upstream from the collapse of the cavity as it reaches the higher pressure region downstream of the trailing-edge. Preconditioning of the flow allows shockwave propagation to cause the shedding of cloud cavitation where the re-entrant jet instability drives the frequency that the shedding occurs, therefore showing a dependence on σ with frequency dropping linearly with σ (figure 3.8) .

As σ is reduced to 0.5, the shedding frequency decreases in a linear trend to $St = 0.19$ with induced C_N fluctuations becoming more consistent as evident in the C_N wavelet transforms for $\sigma = 0.6$ and 0.5 in figures 3.15b and 3.16b, respectively. This is due to the larger cavity influencing more of the span, as evident in the SPOD intensity maps of $\sigma = 0.5$ and 0.6 (figure 3.10). This increased coherent spanwise activity is due to several shedding events (of similar length scale and hence frequency) starting near the root and then occurring successively out along the span. This is shown in the space-time plot (figure 3.16c) by groups of 3-4 gaps in the cavitation per cycle, starting at the top and moving down in a regular sequence. This is shown to occur 8 times in the space-time plot from $t' = 0$ to 45, resulting in an approximate frequency of 20 Hz, or $St \approx 0.19$, matching the C_N and $\delta/\bar{c}$ spectra.

The Type IIa shedding is apparent down to $\sigma = 0.4$ where the attached cavity extends beyond the hydrofoils trailing-edge before detaching periodically at $St = 0.17$, evident in the C_N and $\delta/\bar{c}$ spectra. Observations from the space-time plot in figure 3.17c indicates an alternating shedding behaviour where a cloud is shed from the upper portion of the span ($0.0 < y/b < 0.4$), followed by a cloud from the lower portion. This has manifested in the SPOD intensity and phase maps where two primary energetic areas that appear on the planform are out of phase for $St = 0.16$.

Shockwave driven shedding

The onset of shockwave propagation occurs as σ is reduced to 0.6 where the cavity length is now about equal to the chord, $L_c \approx c$, and closes in a relatively weak adverse pressure gradient. The increased size of the attached cavity results in larger cavitation clouds being shed which have a sufficient bubble population and void fraction to permit

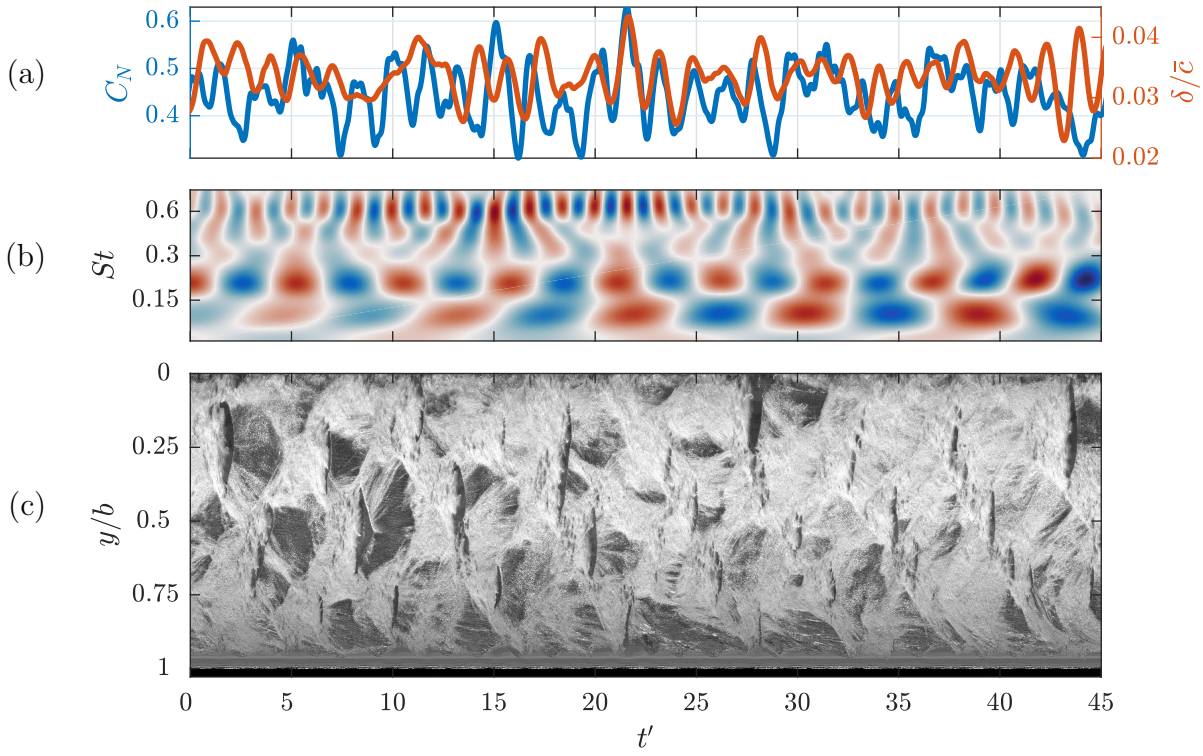

Figure 3.16: Synchronised time series of the normal force (C_N) and tip displacement ($\delta/\bar{c}$) (a) and the real value of the Morlet wavelet transform for C_N (b) at $\sigma = 0.5$. The spanwise space-time plot (c) taken at $x/c_{root} = 0.5$ reveals multiple shedding events along the span and the complex cavitation behaviour.

shockwave formation. This occurs when the cloud is advected downstream of the trailing-edge into a high-pressure region where the cluster of bubbles collapse coherently. The bubbles from the larger cavitation clouds at the reduced σ also increases the local void fraction to the point that the speed of sound in the bubbly mixture reduces significantly compared to that of the constituent water, air and vapour (Shamsborhan et al., 2010). This makes the compressible liquid-vapour mixture susceptible to condensation shocks suddenly changing the local void fraction as the shock propagates through the medium (Crespo, 1969; Noordzij and Van Wijngaarden, 1974; Brennen, 2005; Ganesh et al., 2016).

The C_N and $\delta/\bar{c}$ spectra show that both Type I and IIa modes are evident for $0.4 \leq \sigma \leq 0.6$ with the co-existence of re-entrant jet and shockwave instabilities. This complex mix of shedding mechanisms has previously also been observed by de Graaf et al. (2017) and Smith et al. (2018). High-speed photography also reveals the presence of both mechanisms, where the shedding cycle starts with the typical re-entrant jet process with flow moving upstream under the cavity. However, due to the increased void fraction promoting shockwave propagation with the collapse of the previously shed cavity, the downstream extent of the cavity starts breaking up into a bubbly mixture as the shock-wave propagates upstream. In the case of $0.5 \leq \sigma \leq 0.6$, the re-entrant jet is the primary driver of the shedding frequency with detachment of the cavity coming from shockwave

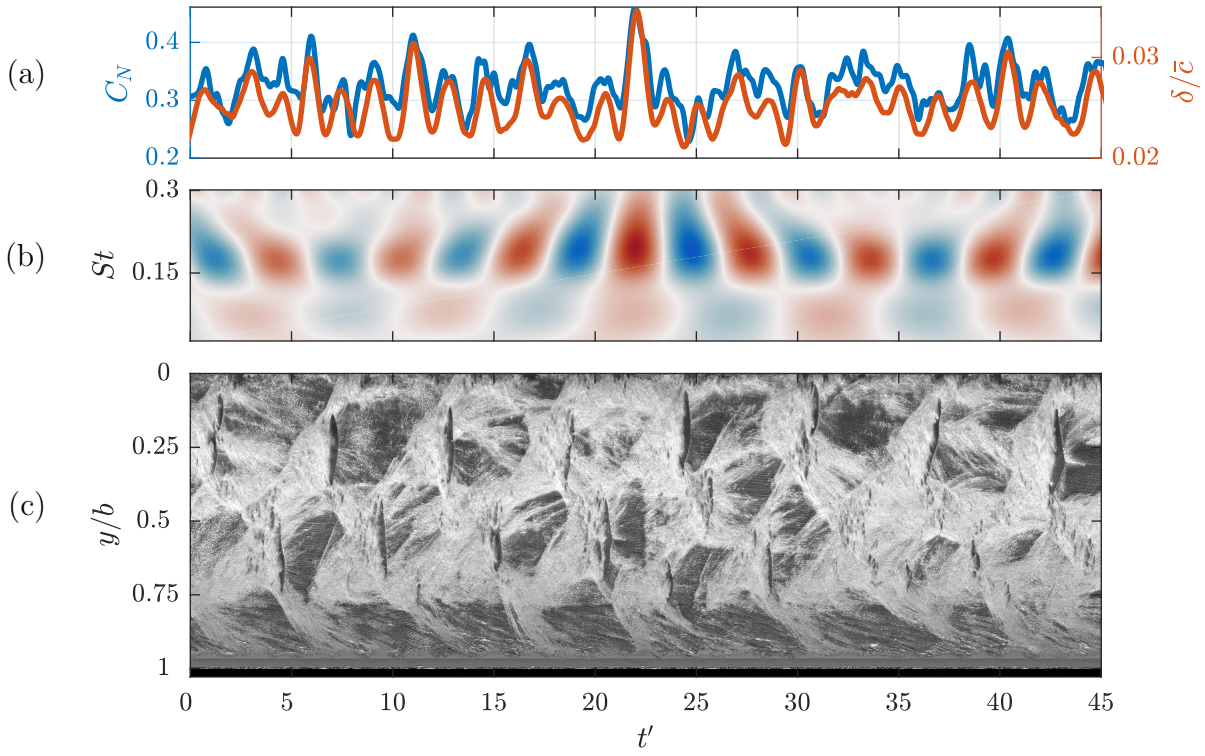

Figure 3.17: Synchronised time series of the normal force (C_N) and tip displacement ($\delta/\bar{c}$) (a) at $\sigma = 0.4$, showing strong correlation, with the real value of the Morlet wavelet transform for C_N (b) highlighting the dominant $St = 0.17$ oscillation. Spanwise space-time plot (c) taken at $x/c_{root} = 0.5$ shows the alternating shedding behaviour.

propagation through the preconditioned flow. The SPOD intensity map for $\sigma = 0.4$ at $St = 0.11$ indicates that activity in the cavitation due to the shockwave is located at the downstream extent of the cavity, a region of relatively high-pressure. However, shockwave propagation is not evident in the space-time plots at a frequency of $St = 0.11$ with minimal amplitude in the wavelet transform component shown in figure 3.17b, despite appearing in the C_N PSD in figure 3.9. This is due to the intermittent nature of the global Type I shockwave instability being inactive for periods on the scale of seconds as can be seen in the wavelet transform from the medium type run at $\sigma = 0.4$ (figure 3.18). As the short type run acquisition is only one second in duration, the data presented in figure 3.17 has seemingly not included one of the intermittent Type I shockwave events. Alternatively, a space-time diagram produced from the medium run data, due to the reduced frame rate, lacks sufficient resolution to show clearly the Type I shockwave propagation.

Further reduction in σ to 0.3 sees the cavity grow to the point that the re-entrant jet driven Type IIa mode becomes no longer evident in the spectra (figure 3.9). High-speed photography reveals a re-entrant jet still forms, however, this has insufficient time and momentum to reach the upstream extent of the cavity before the shockwave, thus preventing it from driving the shedding frequency. The shedding cycle is comprised of a complex set of events consisting of three main phases, a growth phase, a stable phase and

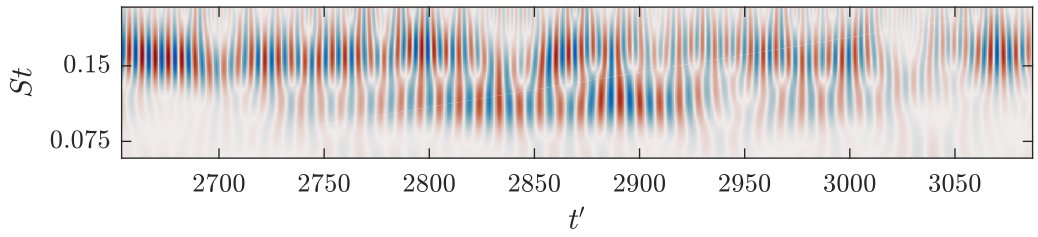

Figure 3.18: Real value of the Morlet wavelet transform for C_N from the medium duration run at $\sigma = 0.4$. The shockwave driven low mode ($St \approx 0.11$) is not continuously apparent through time, only being evident between $2800 \leq t' \leq 2950$.

a shockwave phase. These phases are noted as A, B and C, respectively, in the annotated chordwise space-time plot of figure 3.19e where the chordwise position is presented locally as x^*/c, where the streamwise position, x^*, is taken from the leading edge at the spanwise location and c is the local chord. The space-time plot shows that the growing cavity pauses once it reaches a point just downstream of the trailing-edge, remaining stable for a variable amount of time between cycles, ranging from $t' = 4.3$ to 10.7 in duration. This is followed by the attached cavity being broken up by upstream shockwave propagation. The propagation velocity is seen to change between cycles as indicated by the gradient of the red lines in figure 3.19e. The spanwise space-time plot (figure 3.19c) and shows that a cycle also consists of a large-scale cloud that is shed from the upper portion of the span, shortly followed by approximately two small-scale clouds shed in quick succession from about mid-span. This shedding sequence also manifests in the SPOD phase map at $St = 0.09$ (figure 3.10) with small-scale clouds just below mid-span showing a significant phase difference in the high intensity region.

The frequency of the Type I mode does not vary significantly with σ. This is due to the shockwave initiation location being relatively invariant of σ and consequently the distance the shockwave must travel to break off the attached cavity. This is in contrast to the re-entrant jet which must travel the length of the attached cavity which does vary with σ. When acting exclusively, shockwave driven shedding is highly periodic as shown by the C_N wavelet transform in figure 3.19b exhibiting a consistent $St = 0.09$ excitation frequency through time, despite complex spanwise cavitation behaviour.

Supercavitation

The reduction of σ from 0.3 to 0.2 sees a significant growth in the cavity length to $L_c/c > 1.5$, now forming a supercavity (figure 3.5). Closing far downstream of the trailing-edge with no strong adverse pressure gradient present, the supercavity becomes more stable than partial cavities as no substantial shedding mechanisms can form. In addition, the associated turbulence and vortex shedding occur far enough downstream to have negligible influence on the hydrofoil and the forces it experiences (Brennen, 1995).

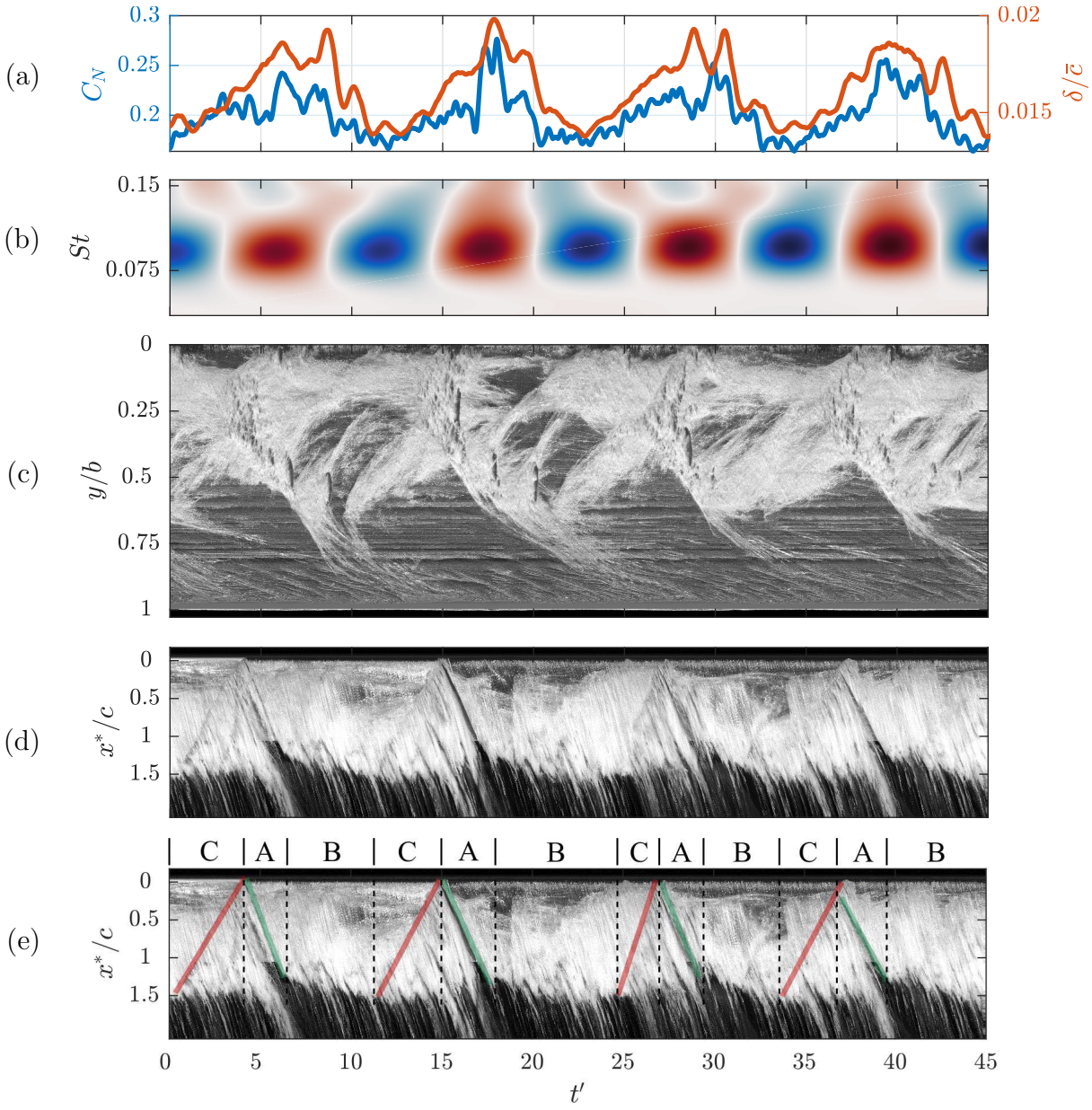

Figure 3.19: Synchronised time-series of the normal force (C_N) and tip displacement ($\delta/\bar{c}$) (a) at $\sigma = 0.3$, showing strong correlation, with the real value of the Morlet wavelet transform for C_N (b) highlighting the dominant $St = 0.09$ oscillation. Spanwise (c) and chordwise (d,e) space-time plots taken at $x/c_{root} = 0.5$ and $y/b = 0.25$, respectively, reveal that each cycle consists of a growth phase (A), indicated by green lines, a stable phase (B) and a shockwave phase (C), indicated by red lines in the annotated version of the chordwise space-time (e).

The Type I mode disappears as the hydrofoil experiences supercavitation exhibiting no significant peaks in the C_N and $\delta/\bar{c}$ spectra (figure 3.9) as no large-scale shedding events are observed in the high-speed photography, despite the vapour cavity remaining in a relatively high-pressure region. As mentioned previously, growth in the attached cavity leads to a higher void faction in the local flow, reducing the speed of sound below the local flow speed and allowing shockwave propagation. However, the speed of sound will actually increase in a liquid-vapour mixture if the void fraction is high enough (Shamsborhan et al., 2010). Reducing σ to 0.2 appears to have increased the void fraction sufficiently, inhibiting the remaining primary shedding instability from inducing periodic cloud cavitation. With no instability to break up the attached cavity, the cavity grows significantly (figure 3.6), closing far downstream to form a stable supercavity.

Spanwise cavity oscillation

Experiments conducted on the same hydrofoils by Pearce et al. (2017) observed streamwise cavity oscillations not related to re-entrant jet or shockwave mechanisms, attributing them to spanwise tip excursions. The attached cavities are observed to oscillate, not just in the streamwise direction, but the spanwise direction as well, when the hydrofoil experiences cloud cavitation. Space-time plots taken around the quarter chord show the spanwise cavity oscillations which appear to be highly periodic (figure 3.20). They also do not appear to be directly related to shedding physics evident in the upper portion of the plots.

The spanwise growth and contraction of the cavity was recorded using a column of pixels at a specific chordwise location with tracking of the cavity extent achieved using the same edge detection method utilized for tip deflection measurements. Comparison of the PSD from the resulting time series with that of $\delta/\bar{c}$ (figure 3.21) reveals highly similar spectra, indicating a strong correlation between tip displacement and spanwise cavity oscillations. Additionally, apart from the lock-in phenomena (at $0.7 \leq \sigma \leq 0.75$), this is the only clear manifestation of structural excitations in the cavitation behaviour with the spanwise cavity oscillations being the only aspect exhibiting fluctuations for $St \geq 0.55$ that isn't attributed to shedding instabilities. This is an indication that the influence of FSI on the cavitation behaviour with the stainless steel model is almost inconsequential, and therefore reinforcing its validity to serve as a relatively stiff reference.

3.5 Conclusion

The behaviour of various cavitation regimes about a relatively stiff hydrofoil was investigated using high-speed photography and force measurements. Multiple cavitation regimes occurred in the cavitation number range tested, comprising of sheet, cloud and

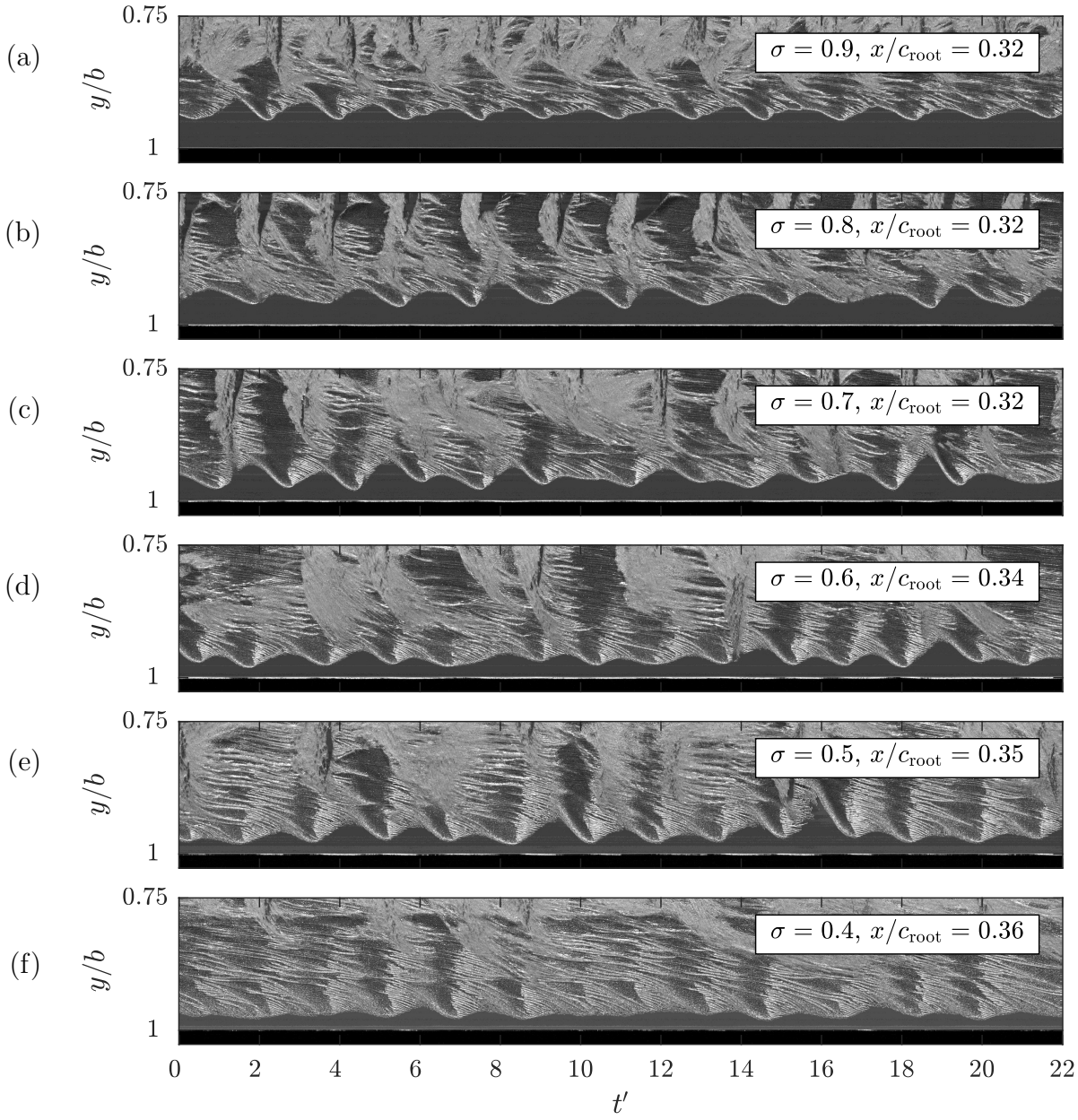

Figure 3.20: Spanwise space-time plots for various σ showing the spanwise cavity oscillation towards the tip of the hydrofoil. These oscillations are periodic and show a strong correlation with the tip displacement.

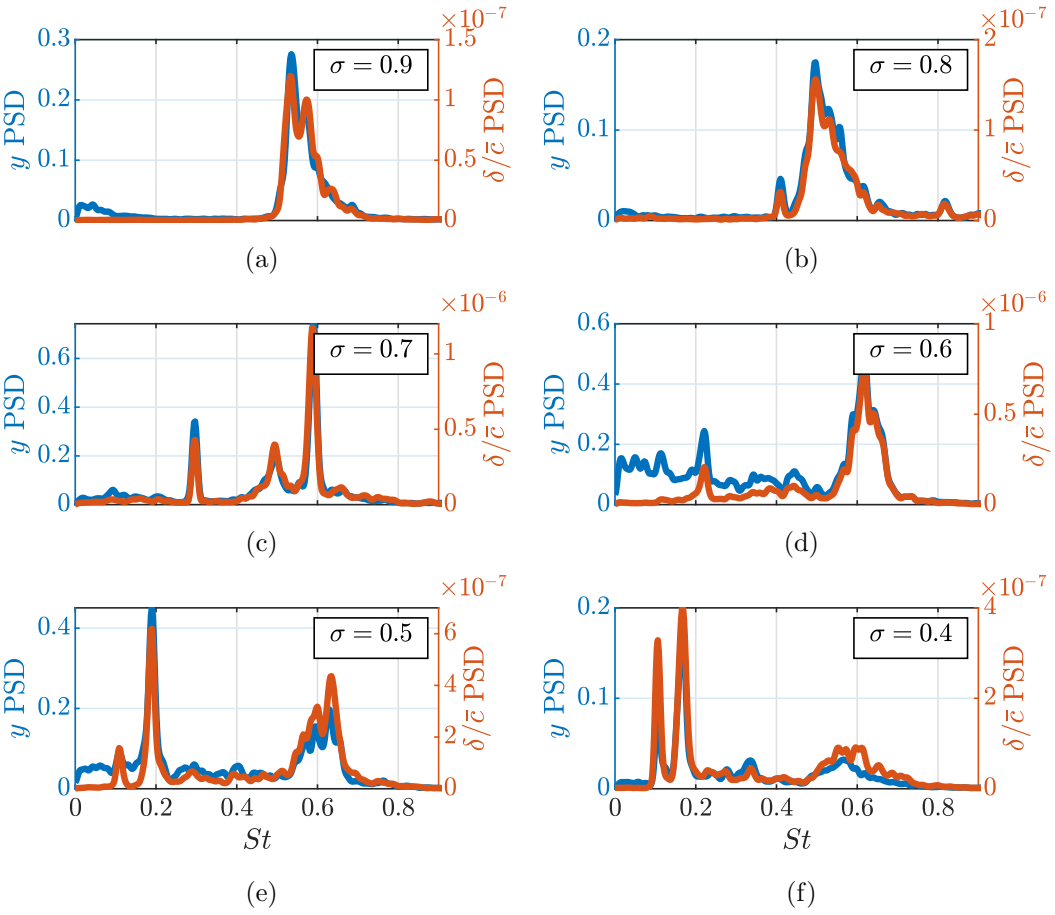

Figure 3.21: PSD of the spanwise cavity oscillations compared to that of the $\delta/\bar{c}$ showing similar spectral content at all σ, indicating a strong correlation between the two.

super-cavitation, each exhibiting unique traits. The instabilities driving the cavity shedding were identified from high-speed photography as either interfacial instabilities, re-entrant jet formation, shockwave propagation or as a complex, coupled mechanism, depending on the cavitation number. Three primary shedding modes were identified with the Type I shockwave driven shedding oscillating at a frequency nominally independent of σ. Re-entrant jet driven Type IIa & IIb oscillations exhibit a linear dependence on σ, decreasing in frequency with σ due to growth in cavity length. At higher cavitation numbers (> 1.0) where the cavity length is small, break-up is driven by small-scale interfacial instabilities that leads to small vapour pockets being shed. Reduction in σ to 1.0 moves the cavity closure into a region of sufficient adverse pressure gradient for a re-entrant jet to form and drive medium scale shedding from mid-span. For cavitation numbers between 0.9 and 0.7, the streamwise length of the cavity is geometrically compatible with the hydrofoil span to form two stable periodic shedding modes, Type IIa & IIb, driven by a re-entrant jet instability towards the root and tip, respectively. Decreasing the cavitation number below 0.6 sees the emergence of a shockwave instability with the cavity reaching the high-pressure region at the trailing-edge and reducing the local speed of sound below the local flow speed by increasing the void fraction. The re-entrant jet and shockwave instability occur concurrently, both causing complex shedding physics and behaviour for $0.3 \leq \sigma \leq 0.6$ with the Type I shockwave driven shedding being the sole shedding mechanism remaining for $0.25 \leq \sigma \leq 0.3$. Further reduction in σ to 0.2 sees the cavity grow to a point that it closes far enough downstream to form a stable supercavity as no shedding mechanisms can form. Lock-in is seen to occur at $0.70 \leq \sigma \leq 0.75$ with the Type IIa shedding frequency matching the first sub-harmonic of the hydrofoil natural frequency in cavitating conditions. Despite lock-in, the structural deformations remained relatively small compared to hydrofoil dimensions and were observed to have minimal effect on the cavitating behaviour only manifesting in spanwise cavity oscillations. Hence, the stainless steel model provides a relatively stiff reference model for comparison with, and to aid in interpretation of, a more flexible hydrofoil of the same geometry. These results will be presented as a part 2 to the present report in a follow on publication.

3.6 Acknowledgements

This project was supported by the Research Training Centre of Naval Design and Manufacturing (RTCNDM), US Office of Naval Research (Dr. Ki-Han Kim, Program Officer) and ONR Global (Dr. Woei-Min Lin) through NICOP S&T Grant no. N62909-11-1-7013. The RTCNDM is a University-Industry partnership established under the Australian Research Council (ARC) Industry Transformation grant scheme (ARC IC140100003). The authors would like to acknowledge the assistance of Mr Steven Kent and Mr Robert

Wrigley from the Australian Maritime College for their essential help with setting up and carrying out the experiments.

3.7 Nomenclature

Symbol	Definition	Unit
α	Flow incidence angle	$^\circ$
δ	Tip deflection	m
$\mathbf{\Theta}_{f_k}$	SPOD mode eigenvector matrix	-
θ	Hydrofoil tip twist	$^\circ$
$\mathbf{\Lambda}_{f_k}$	SPOD mode energy matrix	-
ν	Kinematic viscosity	m^2/s
ρ	Water density	kg/m^3
σ	Cavitation number	-
$\mathbf{\Phi}_{f_k}$	SPOD modes matrix	-
b	Span	m
C_N	Normal force coefficient	-
C_P	Pitching moment coefficient	-
c	Local chord	m
$\bar{c}$	Mean chord	m
c_{root}	Root chord	m
c_{tip}	Tip chord	m
f	Frequency	Hz
f_{FB}	Force balance sampling frequency	Hz
f_{HSP}	High-speed photography frame rate	Hz
f_n	Natural frequency	Hz
L_c	Cavity length	m
N	Normal force	N
N_b	Number of blocks	-
N_f	Block length	-
N_o	Block overlap	-
n_x	Number of rows of pixels in snapshot	-

n_x	Number of columns of pixels in snapshot	-
P	Pitching moment	Nm
p_∞	Absolute freestream static pressure	Pa
p_v	Vapour pressure	Pa
$\boldsymbol{Q}^{(n)}$	SPOD block matrix	-
$\hat{\boldsymbol{Q}}_{f_k}$	SPOD Fourier coefficients matrix	-
$\boldsymbol{q}_k^{(n)}$	SPOD block matrix vector	-
$\hat{\boldsymbol{q}}_k^{(n)}$	SPOD Fourier Transform realization of vector	-
Re	Reynolds number (chord based)	-
$\boldsymbol{S}_{f_k}$	Weighted cross spectral density tensor	-
St	Strouhal number	-
St_n	Strouhal number of natural frequency	-
T	Run duration	s
t	Time	s
t'	Non-dimensional time	-
U_∞	Freestream velocity	m/s
$\boldsymbol{W}$	Weighted Hermitian matrix	-
w_i	Scalar weight	-
x	Streamwise location	m
x^*	Streamwise location (relative to local leading edge)	m
x_{cop}	Streamwise centre of pressure	m
y	Spanwise location	m

Chapter 4

The influence of fluid-structure interaction on cloud cavitation about a flexible hydrofoil. Part 2.

This chapter is presented in article form and has been published in the *Journal of Fluid Mechanics*.

The citation for the paper is:

Smith, S. M., Venning, J. A., Pearce, B. W., Young, Y. L. and Brandner, P. A. (2020) The influence of fluid-structure interaction on cloud cavitation about a flexible hydrofoil. Part 2. *Journal of Fluid Mechanics,* **897** (A28). doi:10.1017/jfm.2020.323

4.1 Abstract

The influence of fluid-structure interaction (FSI) on cloud cavitation about a hydrofoil is investigated by comparing results from a relatively stiff reference hydrofoil, presented in Part 1, with those obtained on a geometrically identical flexible hydrofoil. Measurements were conducted with a chord-based Reynolds number, $Re = 0.8 \times 10^6$ for cavitation numbers, σ, ranging from 0.2 to 1.2 while the hydrofoil was mounted at an incidence, α, of 6° to the oncoming flow. Tip deformations and cavitation behaviour were recorded with synchronised force measurements utilising two high-speed cameras. The flexible composite hydrofoil was manufactured as a carbon/glass-epoxy hybrid structure with a lay-up sequence selected principally to consider spanwise bending deformations with no material-induced bend-twist coupling. Hydrodynamic bend-twist coupling is seen to result in nose-up twist deformations causing frequency modulation from the increase in cavity

length. The lock-in phenomena driven by re-entrant jet shedding observed on the stiff hydrofoil is also evident on the flexible hydrofoil at $0.70 \leq \sigma \leq 0.75$, but occurs between different modes. Flexibility is observed to accelerate cavitation regime transition with reducing σ. This is seen with the rapid growth and influence the shockwave instability has on the forces, deflections and cavitation behaviour on the flexible hydrofoil, suggesting structural behaviour plays a significant role in modifying cavity physics. The reduced stiffness causes secondary lock-in of the flexible hydrofoil's one-quarter sub-harmonic, $f_n/4$, at $\sigma = 0.4$. This leads to the most severe deflections observed in the conditions tested along with a shift in phase between normal force and tip deflection.

4.2 Introduction

Marine propulsors and control surfaces are typically manufactured from metallic alloys due to their high stiffness and resistance to both corrosion fatigue and cavitation erosion. There has been extensive research conducted on the performance of metal propellers focusing on the relatively simple decoupled hydrodynamic and structural analysis (Young et al., 2018b). However, due to the high cost associated with machining the complex geometry of a propeller and poor acoustic damping properties of metallic alloys (Mouritz et al., 2001), the use of alternative materials has recently been investigated (Young, 2008). Composite materials offer high-strength-to-weight and stiffness-to-weight ratios that lead to significant weight reduction, allowing the construction of flexible hydrofoils that improve hydrodynamic performance and increase cavitation inception speeds through passive load-dependent shape adaptation (Young et al., 2016, 2017). From extensive testing on a range of marine vessels, Ashkenazi et al. (1974) showed that the performance of several composite propellers was virtually equal to that of a metal counterpart in terms of speed, fuel consumption and engine workload, but significantly reduced engine and shaft vibrations.

However, these propellers did not exploit hydroelastic tailoring where the anisotropic characteristics of laminated fibre composites can be utilised to tailor blade deformations for improved performance. This flexibility introduces complex fluid-structure interaction (FSI) phenomena, particularly in cavitating conditions as shown in figure 4.1 and discussed by Smith et al. (2020) (hereafter referred to as Part 1), that are not fully understood and need to be investigated. Developments made in the construction of composite structures has led to the hydroelastic tailoring of hydrofoils where geometric aspects are tailored to achieve a desired passive structural response based on the loading distribution to improve performance (Young, 2007, 2008; Young et al., 2016, 2017). The material-induced bend-twist coupling deflections affect flow separation, cavitation behaviour (Pearce et al., 2017; Smith et al., 2018; Young et al., 2018a; Smith et al., 2019; Liao et al., 2019), inception

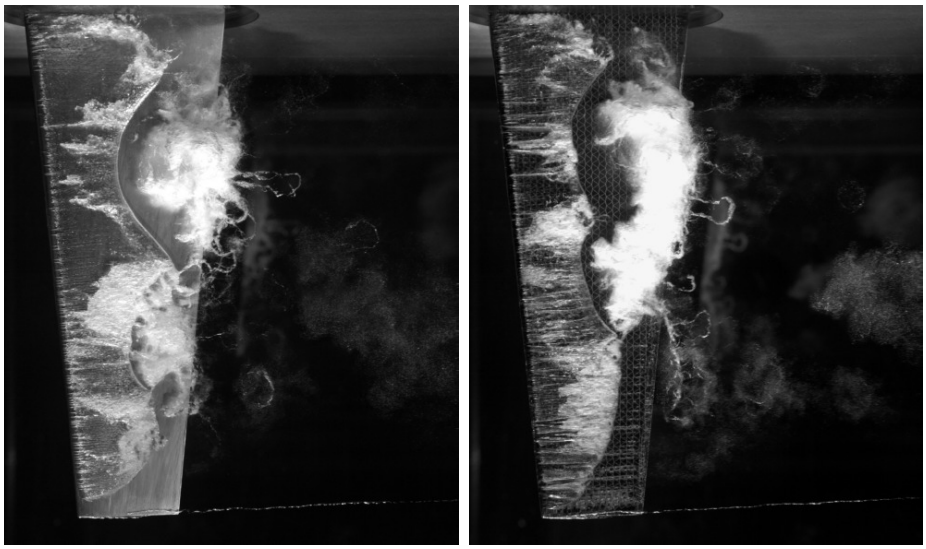

(a) Stiff hydrofoil (b) Flexible hydrofoil

Figure 4.1: Cloud cavitation about a finite span hydrofoil exhibiting multiple shedding events along the span due to the re-entrant jet instability and spanwise compatibility of the cavitation. The hydrofoil is vertically mounted at an incidence of 6° to the flow with a chord-based Reynolds number, $Ry = 0.8 \times 10^6$ and $\sigma = 0.7$.

boundaries, modal vibration characteristics (Akcabay and Young, 2014; Akcabay et al., 2014; Akcabay and Young, 2015) and hydroelastic instability boundaries (Young et al., 2018b; Harwood et al., 2019, 2020). This self-adaptive behaviour has been utilised in the development of composite propellers (Young, 2008; Motley et al., 2009; Young et al., 2016) and active control surfaces (Turnock and Wright, 2000; Young et al., 2018b) to improve energy efficiency as well as delaying and mitigating the adverse effects of cavitation. One of these effects is the unsteady loading and vibration induced by the shedding of cloud cavitation.

As discussed in Part 1, the presence of unsteady cloud cavitation about a hydrofoil has a significant effect on the structural response, even when the hydrofoil is relatively stiff. The unsteady two-phase flow is shown to cause frequency modulation (Akcabay and Young, 2015), broaden the frequency content (Akcabay et al., 2014) and lock-in (Kato et al., 2006; Akcabay and Young, 2015). Due to FSI, the structural response is seen to modify the cavity dynamics as well (Ausoni et al., 2007; Ducoin et al., 2012b; Wu et al., 2015) with Akcabay et al. (2014) showing greater hydrofoil compliance caused increased cavity length, resulting in a reduction of the shedding frequency.

Experiments using composite hydrofoils with varying anisotropic characteristics were conducted by Pearce et al. (2017) and Young et al. (2018a) to investigate the influence of hydroelastic tailoring on hydrofoil performance in cavitating conditions. The hydrofoil featured fibre orientation that resulted in bending-up and nose-up material-induced bend-twist coupling was observed to accelerate cavitation inception, increase cavity length and reduce shedding frequency compared to the relatively stiff reference due to the in-

creased effective angle of attack. The opposite was observed for the hydrofoil with fibre orientations resulting in negative material-induced bend-twist coupling. However, global shedding dynamics was deemed dominant over any FSI effect in determining the resultant structural behaviour at low cavitation numbers (Pearce et al., 2017).

Smith et al. (2018) and Smith et al. (2019) conducted experiments using a composite hydrofoil principally exhibiting tip bending deformations by utilising certain fibre orientations in the lay-up of the hydrofoil. It was shown that the hydrofoil's compliance increased the magnitude of the force fluctuations for the low-frequency shockwave-driven shedding, compared to the relatively stiff hydrofoil. However, hydrofoil compliance was seen to dampen the fluctuating magnitude of the higher-frequency re-entrant jet-driven modes. Furthermore, the cavitation pattern over the flexible hydrofoil was also altered compared to the stiff hydrofoil with both streamwise and spanwise characteristics being affected. These alterations included cavity length, cavitation cloud width and spanwise shedding location with similar observations made by Pearce et al. (2017) and Young et al. (2018a). In spite of the advantages that the use of composite material may bring in regard to performance, composite materials tend to be more susceptible to cavitation erosion damage (Young et al., 2016), and hence the choice of surface coating must be carefully considered.

The influence of FSI on cloud cavitation about a hydrofoil is examined through experiments conducted on a composite hydrofoil with fibres orientated to consider principally bending deformations, i.e. without material bend-twist coupling. The results and discussions are complemented by those made in Part 1 on the relatively stiff reference hydrofoil. Experiments were conducted in the same manner outlined in Part 1 where forces acting on the hydrofoil were acquired simultaneously with tip deflections and cavitation behaviour measurements using high-speed photography. Differences observed in the results between hydrofoils are attributed to FSI effects.

4.3 Experimental Overview

The experimental set-up and techniques utilised in the investigation were as previously described in part 1 and are therefore only briefly summarised. Detailed descriptions are reserved for unique aspects of Part 2 of the experiment not previously described in Part 1.

4.3.1 Experimental Facility

Testing was undertaken at the Australian Maritime College in the Cavitation Research Laboratory water tunnel with a detailed description of the facility given in Brandner et al. (2007). Measurements were repeated for the flexible hydrofoil in the same conditions as for the stiff hydrofoil where it was mounted at a fixed incidence, α, of 6° and tested

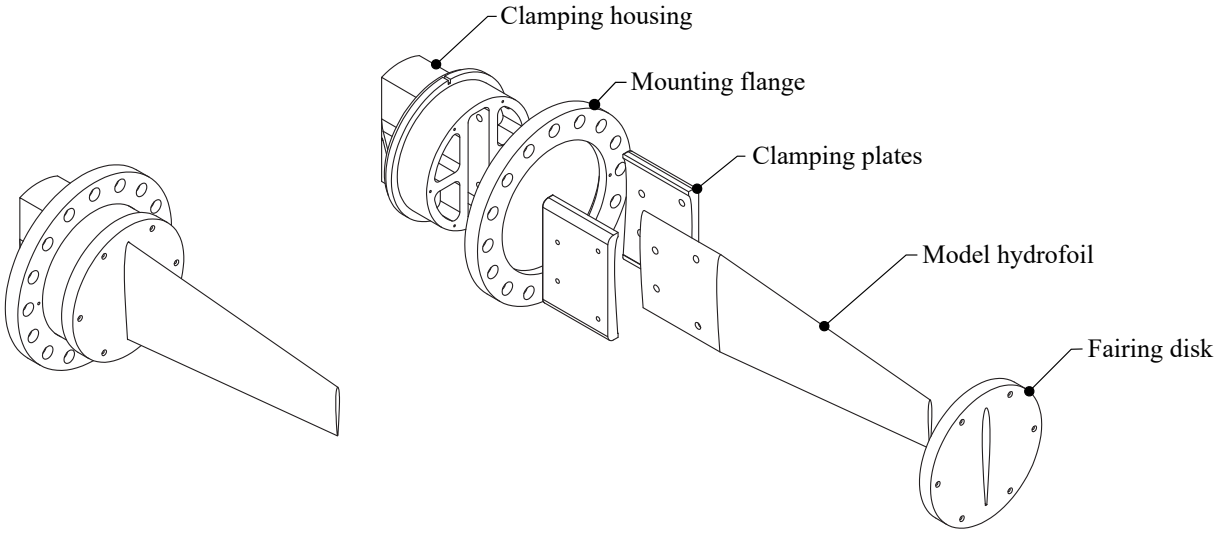

Figure 4.2: Hydrofoil model assembly showing an exploded view of the clamping housing arrangement allowing continuity of the hydrofoil.

at a chord-based Reynolds number, $Re = U_\infty \bar{c}/\nu$, equal to 0.8×10^6, where $\bar{c}$ is the mean chord, U_∞ is the free-stream velocity and ν is the kinematic viscosity of the water. The cavitation number, $\sigma = 2(p_\infty - p_\mathrm{v})/\rho U_\infty^2$, where p_∞ is the absolute static pressure at the level of the hydrofoil tip, p_v is the vapour pressure, and ρ is the water density, was incrementally varied from 1.2 to 0.2 to investigate various cavitation regimes. Dissolved oxygen levels were kept between 3 and 4 ppm for all measurements.

The flexible hydrofoil, described in §4.3.2, was attached to a six-component force balance, with an estimated precision of 0.1%, via a housing that clamped the hydrofoil in place using two profiled plates (figure 4.2), as for the stiff hydrofoil.

4.3.2 Model Hydrofoil

The flexible hydrofoil features an identical undeformed geometry to the stiff hydrofoil described in Part 1 with a symmetric (unswept) trapezoidal planform of 300 mm span, b, a 60 mm tip chord and 120 mm root chord resulting in a mean chord, $\bar{c}$, of 90 mm. The hydrofoils feature an extended base section for the reinforcing fibres in the flexible hydrofoil to run continuously, resulting in cantilevered structural boundary conditions by providing sufficient clamping length (Young et al., 2018b). The modified NACA0009 section profile features a thicker trailing edge for improved manufacturing of the flexible composite hydrofoil. Both hydrofoils are manufactured to a ± 0.1 mm surface tolerance and 0.8 µm surface finish. Despite the efforts made, small imperfections were still evident on the surface of the composite hydrofoil. Their influence on cavitation behaviour is discussed later in §4.4.4.

The composite hydrofoil model was manufactured as a carbon/glass-epoxy hybrid structure using a closed mould resin transfer moulding process. A two-part epoxy system

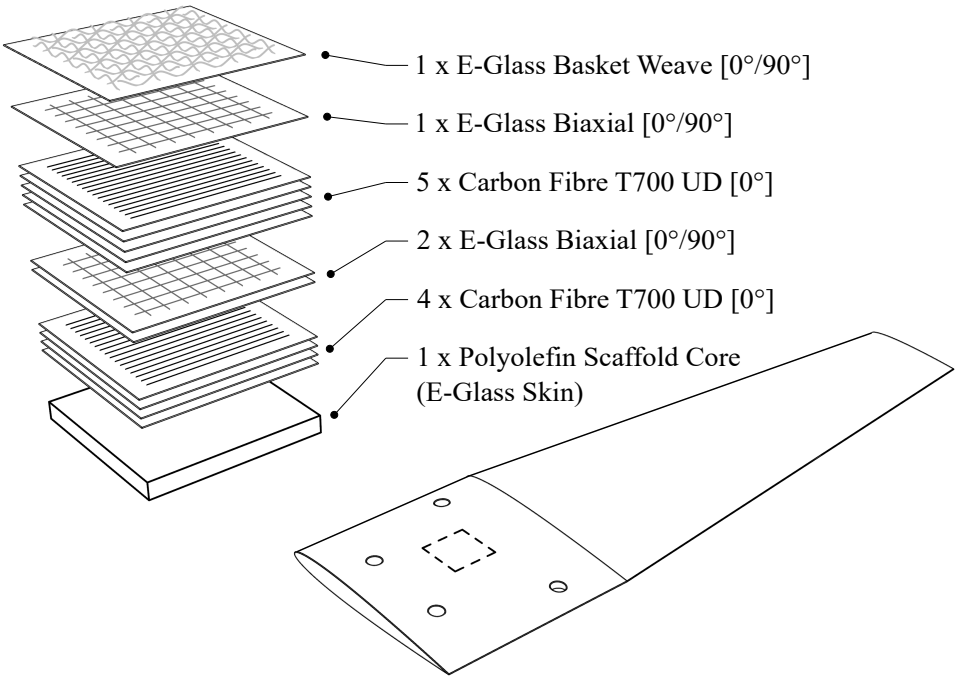

Figure 4.3: Lay-up sequence of the flexible composite hydrofoil.

(Kinetix R118/H103 manufactured by ATL Composites) was used for the matrix resin due to its low viscosity and long pot life properties. The structural component of the hydrofoil comprised of layers of T700 unidirectional carbon fibre (Carbon-UD) and non-crimp biaxial E-glass fabrics (Glass-[0°/90°]). To aid surface finish, protect structural layers from damage during handling and to prevent any unwanted galvanic effects during testing, a light basket weave E-glass fabric (Glass-Basket) was placed on the outermost layer (Phillips et al., 2017). A sandwich glass mat was placed at the centre of the hydrofoil which comprised of two continuous filament random E-glass layers with a polyolefin scaffold core. Further details of the composite hydrofoil construction can be found in Zarruk et al. (2014).

The lay-up sequence of the structural layers consisted of alternating blocks of Glass [0°/90°] and unidirectional carbon layers. The flexible hydrofoil had the carbon unidirectional layers aligned with the spanwise axis of the hydrofoil. The stacking sequence of the structural layers starts with a single Glass-[0°/90°] layer, followed by 5 Carbon-UD layers, then 2 Glass-[0°/90°] layers and finished with 4 Carbon-UD layers making the inner-most structural layer, as depicted in figure 4.3. The stacking sequence is symmetrical about the hydrofoil mid-plane with the profile and spanwise taper accommodated by dropping plies internally to guarantee that the longest layers were on the outside of the hydrofoil (further details provided by Zarruk et al. (2014)). The lay-up of the flexible hydrofoil, along with its geometry, was intentionally chosen to principally consider spanwise bending deformation of the flexible hydrofoil. Structural properties of both the stiff and flexible hydrofoils are summarised and compared in table 4.1.

Hydrofoil	Stiff	Flexible
K (N/mm)	60.2	20.0
E (GPa)	193	65
I (mm^4)	6148	6148
J (mm$^4 \times 10^3$)	854.5	854.5
ρ_H (kg/m^3)	7900	1600
ρ_H/ρ_W	7.9	1.6

Table 4.1: Summary of the material and structural properties of the hydrofoils (Zarruk et al., 2014).

Fluid	Technique	Mount	Stiff		Flexible	
			f_n (Hz)	St_n	f_n (Hz)	St_n
Air	Impact/accelerometer	Stiff	96	0.90	112	1.05
Water	DIC	Stiff	62	0.58	44	0.41
Water	DIC	Force balance	57	0.53	41	0.38
Water	Force measurements	Force balance	54	0.51	41	0.38

Table 4.2: First mode frequencies in bending of the NACA0009 stiff and flexible hydrofoils for various conditions as reported by Clarke et al. (2014) and Zarruk et al. (2014). The in-water (fully wetted) measurements were made using DIC and force measurements and the in-air using impact/accelerometer.

Response spectra of the hydrofoils mounted to the force balance were determined by Zarruk et al. (2014) using impact hammer experiments for in-air results and hydrodynamic loading spectra for in-water results. Spectra of C_N in fully wetted conditions (4.4) from Zarruk et al. (2014) was calculated based on power spectral density (PSD) estimates and indicates f_n of 54 and 41 Hz for the stiff and flexible hydrofoils, respectively. Natural frequency of the hydrofoils was also measured using digital image correlation (DIC) where the hydrofoils were mounted to both a hard mount and a force balance (Clarke et al., 2014; Clarke and Butler, 2019). These results are compared and summarised for both hydrofoils in table 4.2 with natural frequency, f_n, presented dimensionlessly using a Strouhal number where $St_\mathrm{n} = f_\mathrm{n}\bar{c}/U_\infty$. The normal force, N, and pitch moment, P, acting on the hydrofoil are presented as dimensionless coefficients with $C_N = 2N/\rho U_\infty^2 \bar{c} b$ and $C_P = 2P/\rho U_\infty^2 \bar{c}^2 b$ with the coordinate system presented in figure 4.5. The coordinate system origin is located along the hydrofoil's root centreline, aligning vertically with the leading edge of the root chord. Horizontal position, x, is measured positive in the downstream direction with the vertical position, y, measured positive downwards.

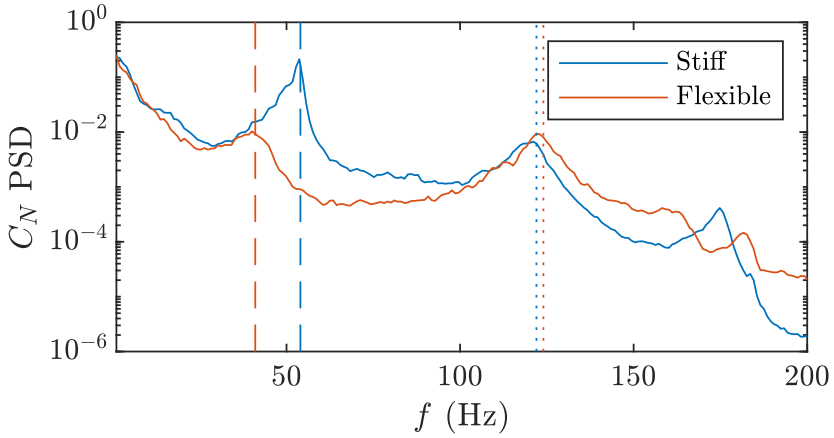

Figure 4.4: Mean C_N PSD of the stiff (blue) and flexible (orange) hydrofoils for incidences ranging from 0° to 14° in increments of 2° in non-cavitating conditions at $Re = 0.6 \times 10^6$ (Zarruk et al., 2014). The results show the fully wetted natural frequency for the stiff and flexible hydrofoils (dashed lines) to be 54 and 41 Hz, respectively, with the force balance natural frequency (dotted lines) appearing at 122 and 124 Hz.

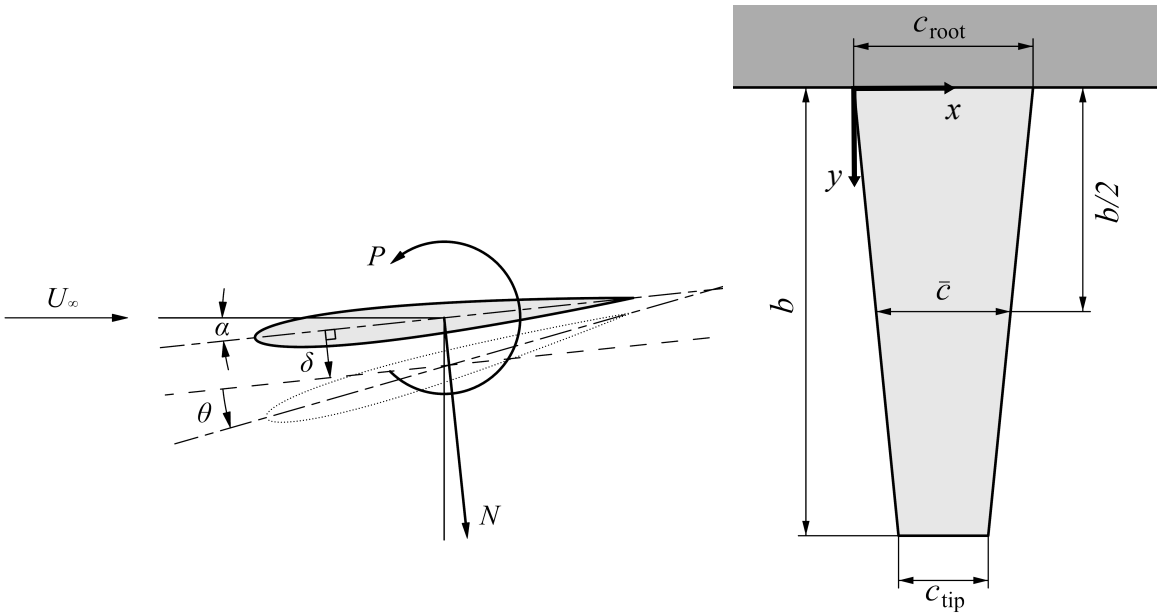

Figure 4.5: The coordinate system used for both the forces and tip deflection of the hydrofoil (left) is located at the mid-chord along the centreline. The deformed hydrofoil tip is represented by the dotted outline where the tip bending displacement, δ, is measured by taking the mean displacement of the profile edge perpendicular to the centreline at the zero-load case. The tip twist deflection, θ, is the rotation of the profile centreline from the zero-load case. A schematic of the hydrofoil's tapered planform (right) shows the coordinate system used in the analysis of the cavitation behaviour (e.g. cavity length) is located at the leading edge of the hydrofoil root.

Run Type	σ	T (s)	f_{HSP} (Hz)	f_{FB} (Hz)
Long	0.2-(0.025)-1.2	360	N/A	1000
Medium	0.2-(0.1)-1.2, 0.55, 0.65, 0.75	36	500	500
Short	0.2-(0.1)-1.2, 0.55, 0.65, 0.75	1	6600	6600

Table 4.3: Test matrix of the flexible hydrofoil for the various run types detailing the σ range, run duration, T, high-speed photography frame rate, f_{HSP} and force balance sampling rate, f_{FB}. Long run types provided accurate high frequency resolution loading behaviour with σ, where both statistical and high temporal resolution data of the cavitation behaviour and tip deflection was obtained efficiently with the medium and short run types, respectively.

4.3.3 Experimental Techniques

Measurements were conducted in the same manner as for those with the stiff hydrofoil discussed in Part 1 consisting of three different run types, Long, Medium and Short. Forces were measured in all run types but cavitation behaviour and tip deflection high-speed videos were taken only for the Medium and Short run types. Further information is provided in Part 1 with details of all three run types summarised in table 4.3. Additional medium and short runs for the flexible hydrofoil at $\sigma = 0.55$ were required to provide additional data in an area of interest.

Tip deflection

Tip deflection measurements were conducted in a similar manner as for the stiff hydrofoil detailed in Part 1 with some adaptations to suit the flexible hydrofoil. The operating resolution of the tip deflection camera was increased from 512×1504 to 896×1504, maintaining a spatial resolution of 0.049 mm/px, to accommodate the increased tip deflection of the flexible hydrofoil. Additionally, due to a lack of contrast of the black hydrofoil tip on the dark background, edge detection was only executed on the upstream and downstream 20% of the tip chord where a clear and consistent edge could be detected. As with the stiff hydrofoil, positive δ is defined as translation towards the suction side with positive θ defined as nose-up, as shown in figure 4.5. The induced twist deformation modifies the effective incidence along the span, $\alpha_e(y/b)$, where $\alpha_e(y/b) = \alpha + \bar{\theta}\sin(\pi y/2b)$ based on the twist mode shape function given by Ducoin and Young (2013). To account for the varying $\alpha_e(y/b)$ along the span the twist mode shape function is integrated from root to tip of the hydrofoil yielding a factor of $2/\pi$. Therefore, the mean effective incidence of the twisted hydrofoil is calculated as $\bar{\alpha}_e = \alpha + 2\theta/\pi$.

Cavitation behaviour

As discussed in Part 1, cavitation behaviour was recorded using a side-mounted high-speed camera operated with a resolution of 2048×1952 pixels and a spatial resolution of 0.185 mm/px. The cavity length, L_c, was measured using the same method as discussed in Part 1. Identification of coherent structures in the dynamic cloud cavitation behaviour was achieved by employing spectral proper orthogonal decomposition (SPOD) using the technique outlined by Towne et al. (2018). A total of 18 000 snapshots were used in the SPOD with further details on the SPOD methodology outlined in Part 1 with identical parameters applied to the high-speed photography of the cavitating flexible hydrofoil.

4.4 Results and discussion

Once cavitation develops past the stage of inception, as σ is progressively reduced, the hydrofoil experiences various forms of cavitation. The extent only varies from cloud cavitation to supercavitation on the flexible hydrofoil with short partial sheet cavities observed only on the stiff hydrofoil in the σ range tested. As mentioned in Part 1, the characteristics of each regime, such as the shedding instabilities, vary substantially in appearance, not just varying between each of the cavitation regimes, but within the regimes themselves. Hydrofoil compliance is observed to influence cavitation behaviour and in-turn hydrofoil performance where correlations made with FSI can be obtained. This is achieved through comparison of the measured forces and deflections with the cavitation behaviour observed on each hydrofoil. Attributes of the two primary shedding mechanisms, re-entrant jet formation and shockwave propagation, are identified in annotated images in figure 4.6 with an overview of the various cavitation regimes about the flexible hydrofoil presented in figure 4.7. The cavitation behaviour on the carbon fibre hydrofoil is seen to differ from that of the stainless steel hydrofoil in many ways, not just due to the increased flexibility, but due to surface imperfections as well. This is evident in the supercavitation where streaks are apparent in the case of the carbon fibre hydrofoil due to surface imperfections. This is discussed further in §4.4.4.

4.4.1 Cavity length

As discussed in Part 1, the attached cavity has a significant influence on the pressure distribution over the hydrofoil and therefore the forces that result. Comparison of the cavity behaviour between hydrofoils is presented in figure 4.8 using the ratio of cavity length, L_c, over the local chord, c, at various spanwise positions, y, for a range of σ. The results show the overall trend is similar, however, there are some key differences. L_c/c of the flexible hydrofoil is approximately 20% larger than that of the stiff at $\sigma = 1.2$ at all

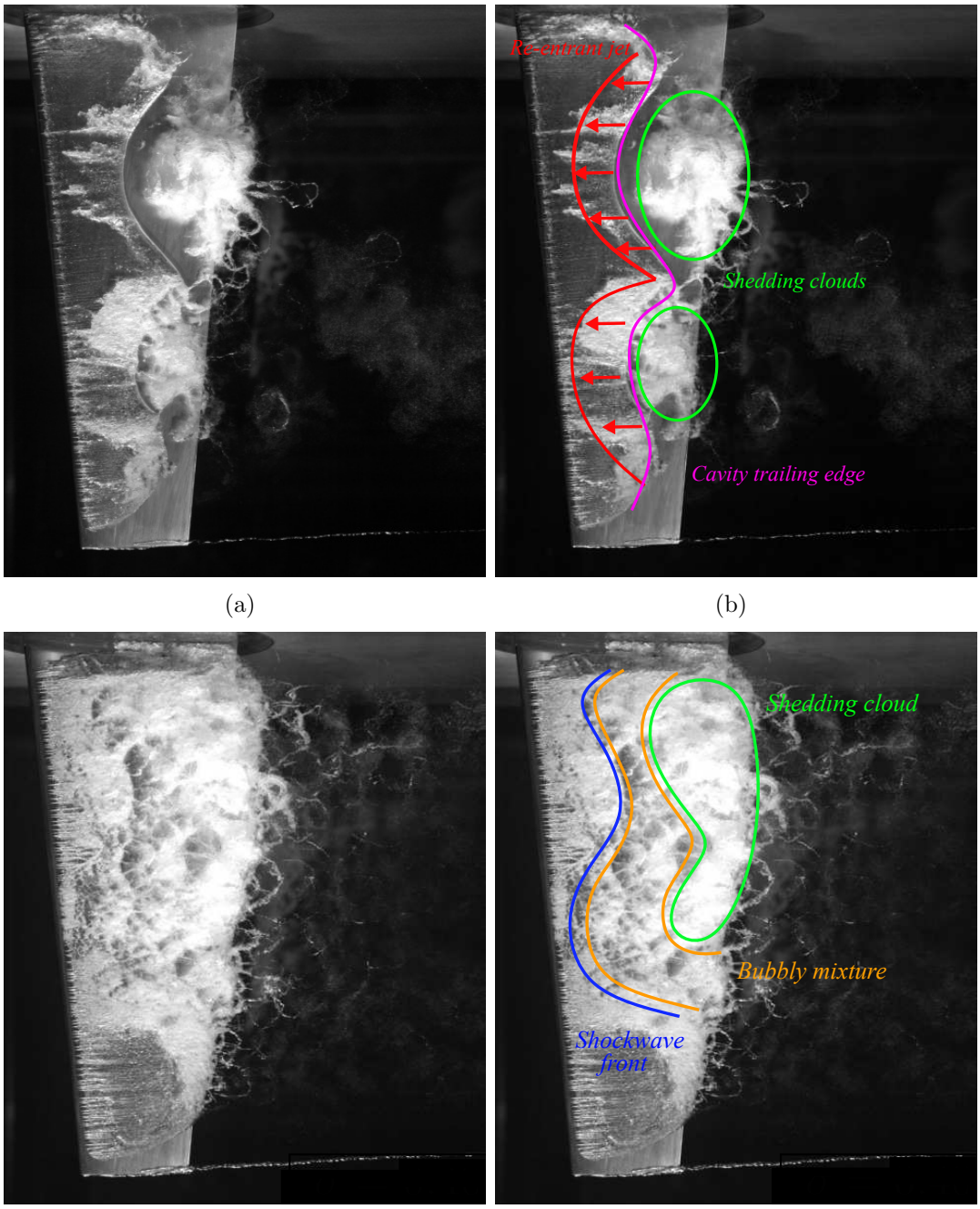

Figure 4.6: Typical example images of cloud cavitation due to re-entrant jet formation at $\sigma = 0.7$ (a) and shockwave formation at $\sigma = 0.4$ (c). In the annotated version of re-entrant jet-driven shedding (b), flow over the attached cavity reaches the cavity trailing edge (purple), where it impacts the hydrofoil surface, forming a re-entrant jet (red) underneath the cavity, eventually causing it to break-off and form shed clouds (green). In the annotated version of shockwave-driven shedding (d), collapse of the large attached cavity occurs first in the high pressure region downstream, causing a condensation shockwave (blue) to propagate upstream, breaking up the attached cavity into a bubbly mixture (orange) which forms a shedding cloud (green).

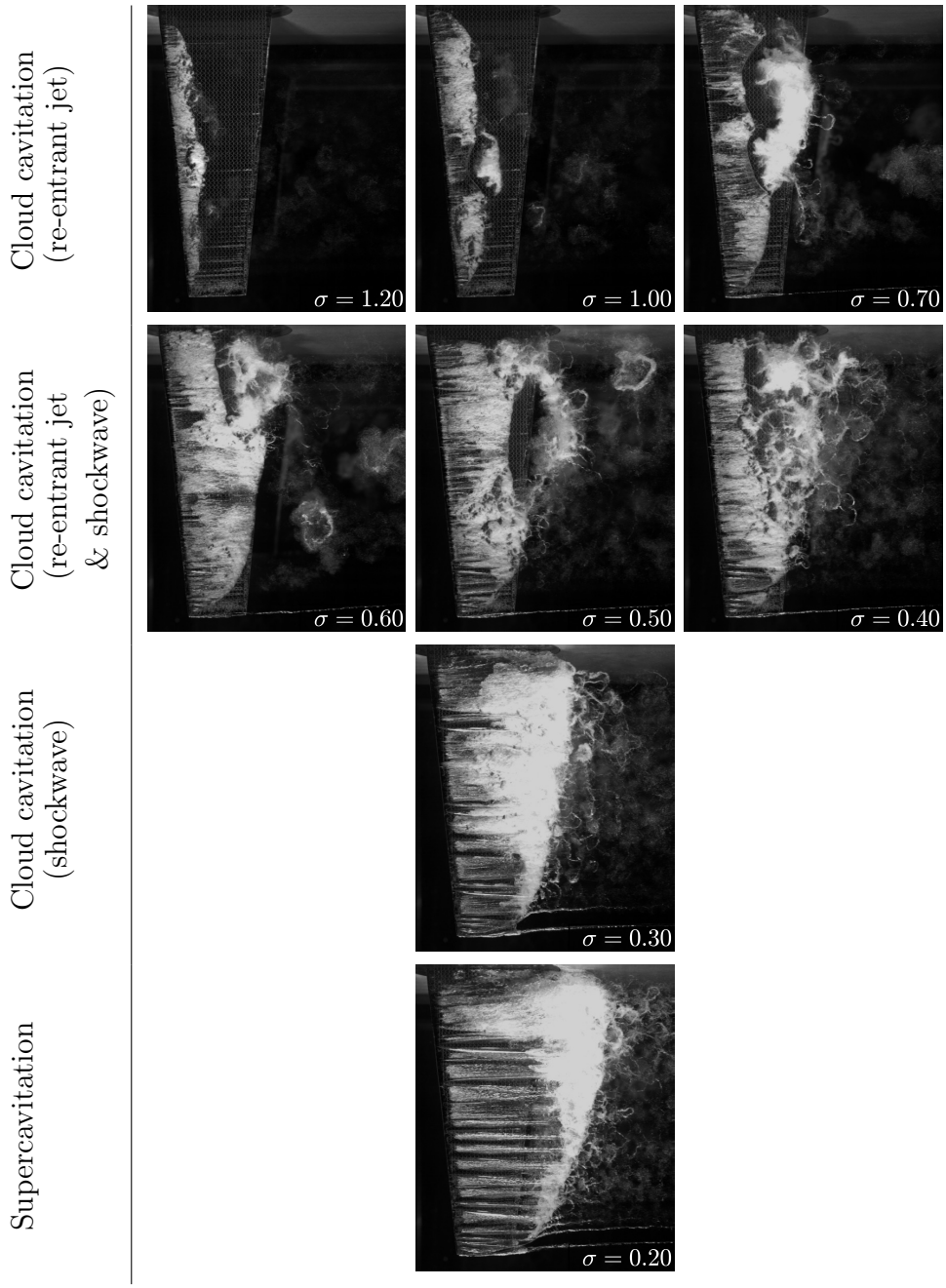

Figure 4.7: Images of the flexible hydrofoil experiencing the differing cavitation regimes through the range of σ below inception. The flexible hydrofoil first experiences re-entrant jet-driven cloud cavitation for the conditions tested, not experiencing stable sheet cavitation as observed on the stiff hydrofoil for $\sigma \geq 1.1$. The attached cavity and re-entrant jet-driven cloud cavitation develops further as σ is reduced ($0.65 \leq \sigma \leq 1.2$). A further reduction in σ, with cavity length extending to the trailing edge, upstream propagating condensation shockwaves develop, resulting in a complex coupled mechanism involving both the re-entrant jet and shockwave instabilities for $0.4 \leq \sigma \leq 0.6$. Once σ reaches 0.3, shedding is solely driven by shockwave propagation. Supercavitation is present for ($\sigma < 0.3$) with a stable sheet cavity present over all the hydrofoil surface and the cavity break-up restricted to the cavity closure region downstream of the trailing edge.

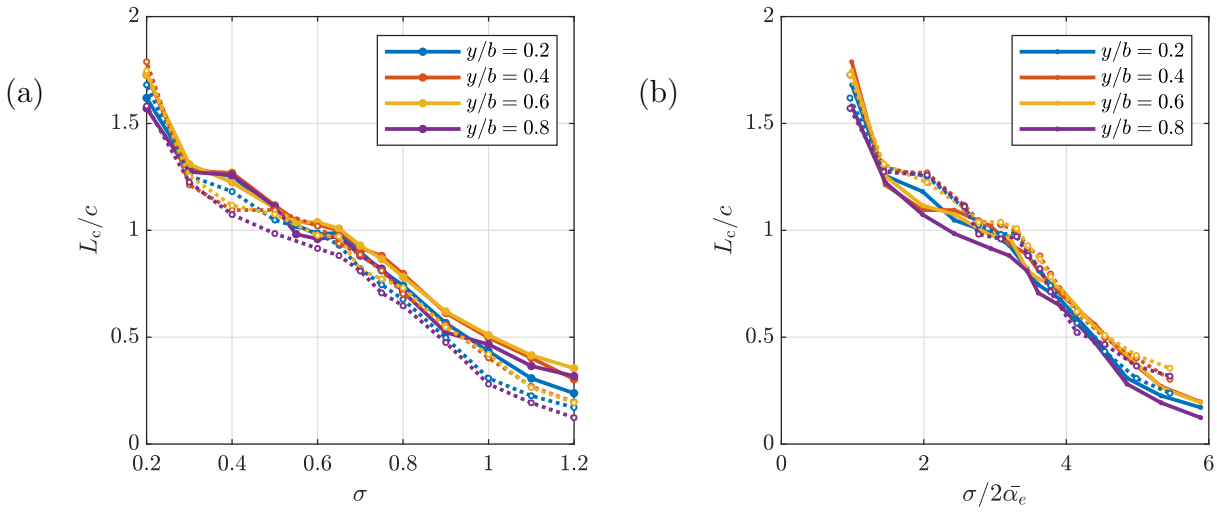

Figure 4.8: Attached cavity length, L_c, against σ (a) and $\sigma/2\bar{\alpha}_e$ (b) with cavity length taken at the point of cavity break-off for various positions along the span for the stiff (·····) and flexible (——) hydrofoils. The cavity length is non-dimensionalized by the local chord, c, at each of the spanwise positions, showing continuous cavity growth as σ is reduced.

spanwise positions. This is due to the centre of pressure being upstream of the hydrofoil elastic axis resulting in nose-up twist deformations ($\theta > 0$ in figure 4.9) that increase $\bar{\alpha}_e$, thus reducing the pressure on the suction side and increasing the cavity length. As σ is reduced, L_c of both hydrofoils start to converge with the stiff hydrofoil only exhibiting slightly longer cavity length from $\sigma = 0.9$ down to 0.55. This is attributable to the centre of pressure shifting downstream and towards to the elastic axis, reducing the nose-up twist of the hydrofoil. For $\sigma < 0.6$, L_c on the stiff hydrofoil exhibits fluctuating cavity growth as σ is reduced, where L_c on the flexible hydrofoil is seen to grow more consistently. The cavity lengths are seen to converge on both hydrofoils as σ reaches 0.3 before a significant rise in L_c occurs as σ reaches 0.2 with the onset of supercavitation.

The difference in L_c/c between hydrofoils decreases with σ to approximately 10% for $0.7 < \sigma < 1.0$. The attached cavity on the flexible hydrofoil reaches the trailing edge earlier than the stiff counterpart with $L_c/c = 1$ at $\sigma = 0.65$ compared to 0.6, respectively. The cavity length of both hydrofoils exhibits a reduction in the rate of increase with reducing σ at the point of $L_c/c = 1$. This only occurs for $0.55 \leq \sigma \leq 0.65$ on the flexible hydrofoil compared to $0.4 \leq \sigma \leq 0.6$ on the stiff before the cavity growth rates accelerate with reducing σ, resulting in a significantly larger cavity on the flexible hydrofoil at $\sigma = 0.4$. Interestingly, cavity growth stalls on the flexible hydrofoil between $\sigma = 0.4$ and 0.3 with comparable L_c/c values between the two hydrofoils at all spanwise positions. With both hydrofoils entering the supercavitating regime at $\sigma = 0.2$, i.e. where the unsteady closure has moved downstream away from the hydrofoil trailing edge, the rate of cavity growth with σ increases substantially.

Comparison of the cavity lengths at the various spanwise positions reveals the greatest

difference in L_c/c between the hydrofoils occurs at the point furthest from the root, i.e. $y/b = 0.8$. This coincides with the spanwise position of the highest deflections compared to the other positions, indicating significant FSI due to hydrofoil compliance. The influence of the twist deformations is also evident when comparing the images of the cavitating hydrofoils in figure 4.7 with figure 5 in Part 1. The cavity is seen to always extend the entire span on the flexible hydrofoil due to the nose-up twist deformations for $\sigma \geq 0.8$ and large cavity size for $\sigma < 0.8$ linked to increased dynamic deformations discussed in §4.4.4. The negligible twist deformations on the stiff hydrofoil result in the attached cavity only extending the full span once σ is reduced to approximately 0.7 and below.

The effect of $\bar{\alpha}_e$ on the cavitation behaviour can be captured using the cavitation parameter $\sigma/2\bar{\alpha}_e$, as increasing the incidence has a similar effect to decreasing σ, as shown by Le et al. (1993). This is shown in figure 4.10, where the nose-up deformations on the flexible hydrofoil for $\sigma \geq 0.8$ result in a decreased $\sigma/2\bar{\alpha}_e$ value. Hence, the increased $\bar{\alpha}_e$ has the same influence as reducing σ, thereby accelerating the transition between cavitation regimes for decreasing σ. The opposite occurs for $0.4 \leq \sigma \leq 0.75$ with negative θ increasing $\sigma/2\bar{\alpha}_e$, suggesting delayed regime transition compared to the stiff hydrofoil. When the data are plotted as a function of $\sigma/2\bar{\alpha}_e$ (figure 4.8b), the collapse is better between the two hydrofoils.

4.4.2 Mean and standard deviations of forces and deflections

The mean and standard deviation of C_N, C_P, x_{cop} (defined from the leading edge, as shown in figure 4.5) and $\delta/\bar{c}$ (normalised tip deflection) for both hydrofoils are shown in figure 4.9 as a function of σ, with $'$ denoting the standard deviation of the time varying quantities. The tip twist deformation, θ, and it's standard deviation, θ', of the flexible hydrofoil is also shown in figure 4.9. Note that the twist deformation of the stiff hydrofoil was too small to measure, and hence not reported in figure 4.9. The structural deformations are seen to be significantly greater for the flexible hydrofoil for the majority of the σ range in both the mean and standard deviation. At $\sigma = 1.2$, the flexible hydrofoil experiences increased loading in C_N and C_P due to increased effective incidence, α_e, as discussed in §4.4.1. Despite negligible difference in $\delta'/\bar{c}$ at $\sigma = 1.2$, C'_N and C'_P are considerably higher for the flexible hydrofoil, matching those values of the stiff hydrofoil for $\sigma < 1.0$. $\sigma = 1.0$ on the stiff hydrofoil correlates to the upper σ limit of the cloud cavitation regime, indicating accelerated transition of the flexible hydrofoil into the cloud cavitation regime; C'_N on the flexible hydrofoil exhibits four local peaks for the range of σ tested, showing increased fluctuations at $\sigma = 1.0$, 0.875, 0.7 and 0.425. Comparing the cavitation behaviour between the flexible hydrofoil at $\sigma = 1.2$ and the stiff at 1.0, both experience periodic cloud cavitation of similar scale which is linked to unsteady loading as discussed in Part 1.

The flexible and stiff hydrofoils show a similar steady increase in C_N as σ is reduced but for the flexible case at a slightly reduced rate, resulting in both reaching a maximum of 0.59 at $\sigma \approx 0.7$, corresponding also to the maxima in $\delta/\bar{c}$ and θ'. The reduction in σ sees the C'_N of the flexible hydrofoil increase in a step-like manner with each of the local peaks noted above where it reaches a global maximum with $\delta'/\bar{c}$ exhibiting a very similar trend. Reduction in σ below 0.7 sees a steady decrease in C_N for both hydrofoils with the mean normal force reducing monotonically through into the supercavitating regime.

Observed on both hydrofoils, C_P decreases with σ with the onset of unsteady shedding, dropping more sharply as σ is reduced from 1.0 to 0.7 despite C_N increasing over this range. This is due to the shift in x_{cop} which has pronounced effects on the flexible hydrofoil as the θ deformations are strongly correlated to the x_{cop} indicated by opposing trends as σ is varied; C_P is seen to reduce with σ, which is due to x_{cop} shifting closer to the hydrofoil elastic axis, reducing θ, and therefore $\bar{\alpha}_e$. As $x_{cop}/\bar{c}$ increases from 0.40 at $\sigma = 1.2$ to 0.57 (passing the mid-chord) at $\sigma = 0.6$, θ decreases from 0.75° to −0.5° at 0.6, before increasing to 0° at $\sigma = 0.2$. It is also noted that the two instances where $\theta = 0°$ at $\sigma = 0.75$ and 0.3, $x_{cop}/\bar{c} = 0.5$ in both occurrences, indicating the elastic axis on the flexible hydrofoil is approximately located 35% along the root chord. It is also observed that for $0.2 \leq \sigma \leq 0.7$, C_N and C_P are practically the same between the stiff and flexible hydrofoils, as the twist deformation of the flexible hydrofoil is less than 0.5° in that region. The spike in the $\delta'/\bar{c}$ at $\sigma = 0.4$ for the flexible hydrofoil is due to lock in, which will be explained later in §4.4.3.

Interestingly, despite the induced θ reaching negative values for $0.3 \leq \sigma \leq 0.75$, the mean value for C_P is positive for the range of σ tested. This occurs due to the centre of pressure shifting downstream of the elastic axis causing nose-down deformations but still upstream of the mid-chord about which C_P is measured.

4.4.3 FSI Response

Both the stiff and flexible hydrofoils experience a variety of FSI occurring between the structure and cavitation for the σ range tested. The variations in FSI are summarised in table 4.4, which identifies the cavitation and structural modes interacting for certain σ ranges. In addition, the FSI coupling is classified as either being one-way, where either the cavitation or structural mode drives the other, or lock-in, where both modes are coupled, leading to large amplification of the response. Although there are apparent similarities in the PSD and lock-in phenomenon for each hydrofoil these are via different mechanisms.

As discussed in Part 1, the amplitude and frequency content of the forces acting on the hydrofoil are dependent on multiple factors including hydrodynamic loading, cavitation dynamics and the structural response. Spectrograms of C_N and $\delta/\bar{c}$ with varying σ for both the stiff and flexible hydrofoils are shown in figures 4.11 and 4.12, respec-

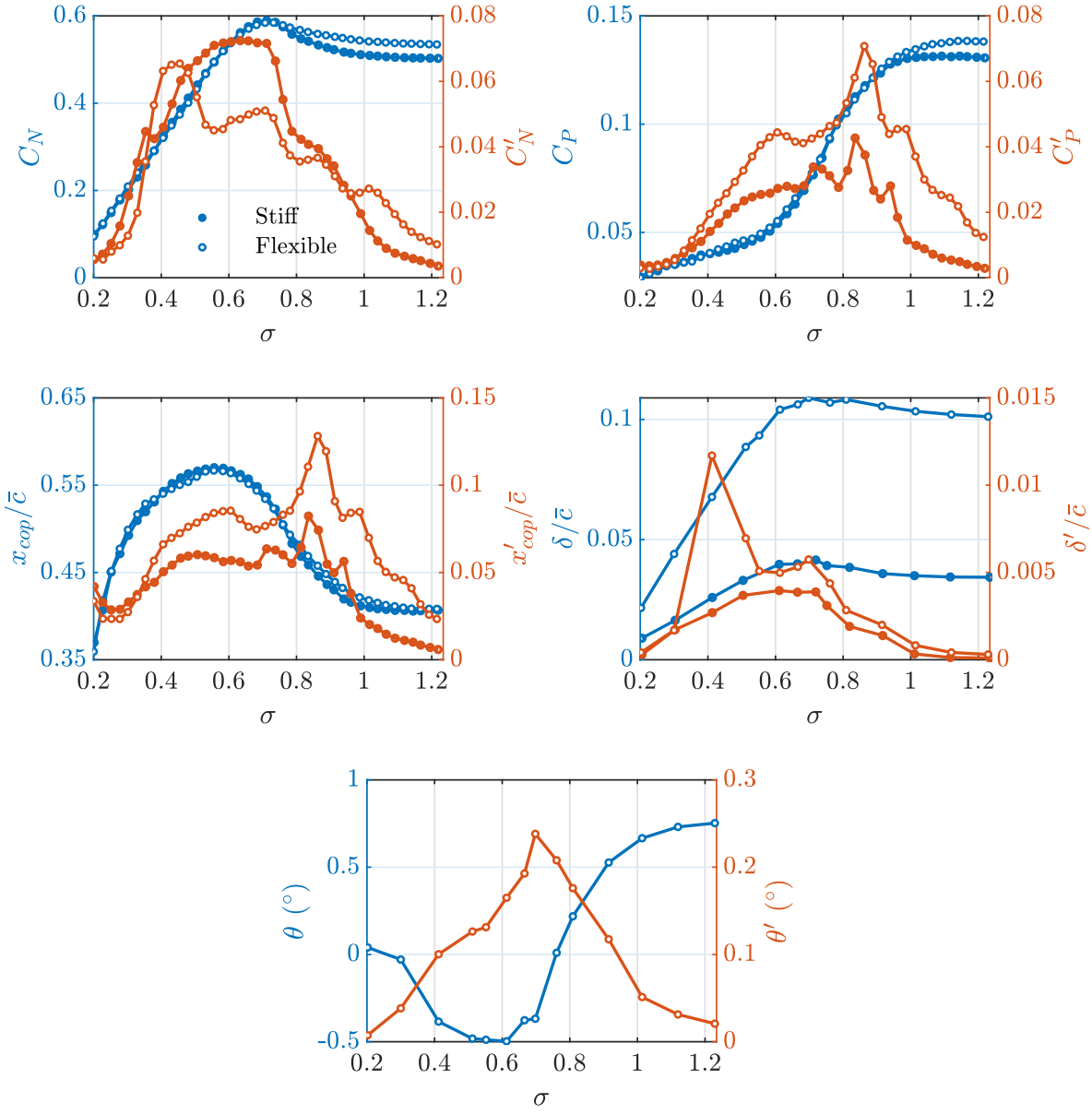

Figure 4.9: Mean and standard deviation values of the non-dimensional forces and deflections experienced by the stiff and flexible hydrofoils at various σ where $'$ indicates the standard deviation of the time varying quantity. The results show similar behaviour between the hydrofoils in the mean values of the normal force (C_N), pitching moment (C_P) and location of the centre of pressure ($x_{cop}/\bar{c}$) for varying σ. However, the degree of unsteadiness in the forces varies significantly between hydrofoils as indicated by the standard deviation. Tip displacement ($\delta/\bar{c}$) is much larger on the flexible hydrofoil for all σ with the twist angle (θ) shifting from positive to negative based on $x_{cop}/\bar{c}$ relative to the hydrofoils elastic axis.

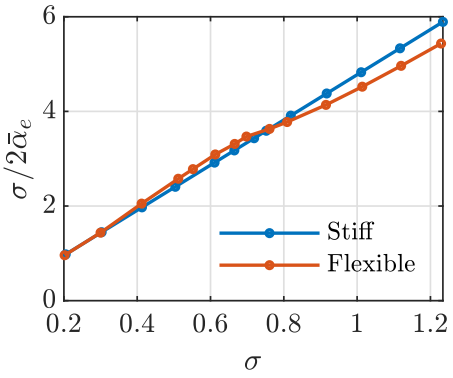

Figure 4.10: Comparing the cavitation parameter $\sigma/2\bar{\alpha}_e$ of each hydrofoil for the σ range tested reveals the influence of θ deformations on the cavitation behaviour. The flexible hydrofoil's nose-up deformations for $\sigma \geq 0.8$ result in a decreased $\sigma/2\bar{\alpha}_e$ value, suggesting accelerated cavitation regime transition for decreasing σ. The opposite occurs for $0.4 \leq \sigma \leq 0.75$ with negative θ increasing $\sigma/2\bar{\alpha}_e$, suggesting delayed regime transition.

Label	σ	Cavitation Mode	Structural Mode	FSI
		Stiff Hydrofoil		
s_1	0.90–0.75, 0.65–0.30	Types I, IIa, IIb	Quasi-steady	One-way C $\rightarrow$ S
s_2	0.75–0.65	Type IIa	Bending ($f_n/2$)	Lock-in C $\leftrightarrow$ S
s_3	0.90–0.30	Spanwise modulation	Quasi-steady	One-way S $\rightarrow$ C
		Flexible Hydrofoil		
c_1	0.90–0.75, 0.60–0.30	Types I, IIa, IIb	Quasi-steady	One-way C $\rightarrow$ S
c_2	0.75–0.65	Type IIa	Bending ($2f_n/3$)	Lock-in C $\leftrightarrow$ S
c_3	0.75–0.60	Type IIb	Bending (f_n)	Lock-in C $\leftrightarrow$ S
c_4	0.4	Type I	Bending ($f_n/4$)	Lock-in C $\leftrightarrow$ S

Table 4.4: Summary of hydrofoil/cloud cavitation FSI variation with σ. The one-way FSI can occur in the form of the cavitation mode driving the structure (C $\rightarrow$ S), or the structural mode driving the cavitation (S $\rightarrow$ C). The FSI lock-in phenomena observed on the hydrofoils occurs when both the cavitation and structural modes are coupled (C $\leftrightarrow$ S).

tively. They provide a global perspective of how cloud cavitation behaviour modulates spectral characteristics on each hydrofoil. A comparison of the significant C_N spectral features is shown in figure 4.14 whereby only high amplitude features are shown based on a predetermined threshold. The C_N and C_P spectrograms are constructed from spectra of the long-duration runs taken at 0.025 increments of σ with the PSD parameters used detailed in Part 1. Frequency is non-dimensionalised as a chord-based Strouhal number, $St = f\bar{c}/U_\infty$. Individual C_N spectrum plots at σ values of particular interest comparing the hydrofoils are presented in figure 4.15 along with the corresponding $\delta/\bar{c}$ spectra in figure 4.16 calculated from the medium duration time series data. A summary of all the modes is provided in table 4.4 with the modes discussed in detail below.

The C_N spectrogram of the flexible hydrofoil (figure 4.11b) reveals the same 3 primary cavity shedding modes observed on the stiff hydrofoil (figure 4.11a). These include the shockwave-driven Type I mode and the re-entrant jet-driven Type IIa and IIb modes along with structural excitations. The Type IIa mode is the primary re-entrant jet-driven shedding mode whereas the Type IIb mode refers to the formation of a second cell in the lower portion of the hydrofoil while Type IIa is confined to the upper portion, which are evident via the SPOD and phase plots shown in figure 4.17. Comparing the key spectral characteristics (figure 4.14), there exist several similarities, however, there are significant variations between the two hydrofoils due to the increased FSI of the flexible hydrofoil.

Both hydrofoils are seen to exhibit no significant spectral excitation in either C_N or $\delta/\bar{c}$ for $\sigma \geq 1.1$. This is despite the flexible hydrofoil experiencing cavity lengths greater than those encountered on the stiff hydrofoil where significant spectral excitation is observed at $\sigma = 1.0$. SPOD intensity maps for the flexible hydrofoil in figure 4.17 show high activity for $St = 0.607$ occurring at mid-span for $\sigma = 1.0$ linked to re-entrant jet-driven shedding that is of too small of a scale to significantly excite the hydrofoil. For σ below 1.0, the re-entrant jet instability causes the shedding of clouds on a sufficient scale (Type IIa mode) to excite both hydrofoils with the flexible hydrofoil shedding at a slightly lower frequency of $St = 0.48$ compared to 0.51 on the stiff at $\sigma = 0.9$ (figure 4.15b). The difference in frequency is attributed to the longer cavity on the flexible hydrofoil (figure 4.8) increasing the duration of each cycle brought about by induced twist deformations. The decrease in σ from 1.0 to 0.9 also sees a significant increase in both the C_N and $\delta/\bar{c}$ PSD, with the C_N PSD increasing two orders of magnitude with the stiff hydrofoil exhibiting the same trend. This shedding mode has the potential to be two-way FSI should cavity volume oscillations become large. However, in this case, the shed vapour cavities are small, limiting the response of the hydrofoil to one-way FSI i.e. small vibrations/deformations, forced by the global flow field, drive small-scale cavity length modulation.

As σ is reduced to 0.8, both the C_N and $\delta/\bar{c}$ spectra exhibit a dominant peak that matches the fully wetted natural frequency of the flexible hydrofoil, at $St = 0.40$, while the $\delta/\bar{c}$ spectrum features a secondary peak at $St = 0.47$. The lower frequency is associated

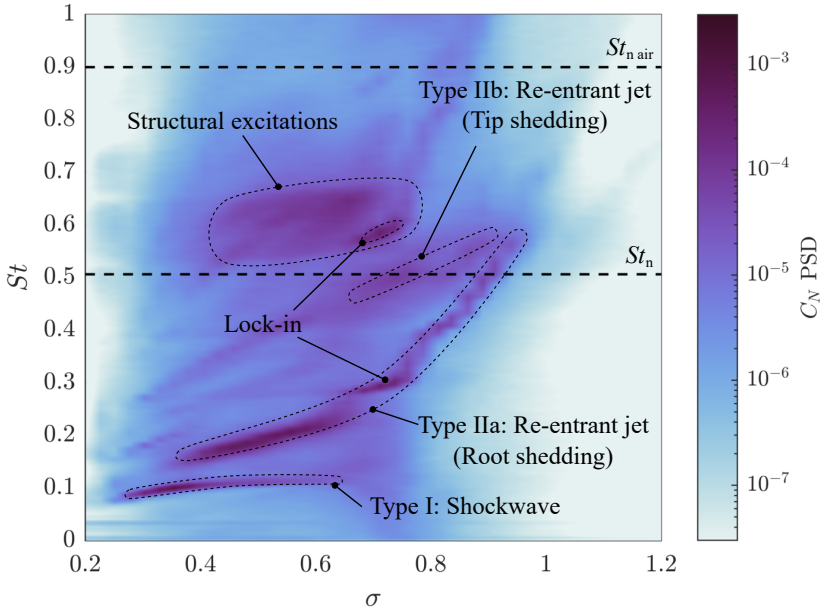

(a) Stiff hydrofoil

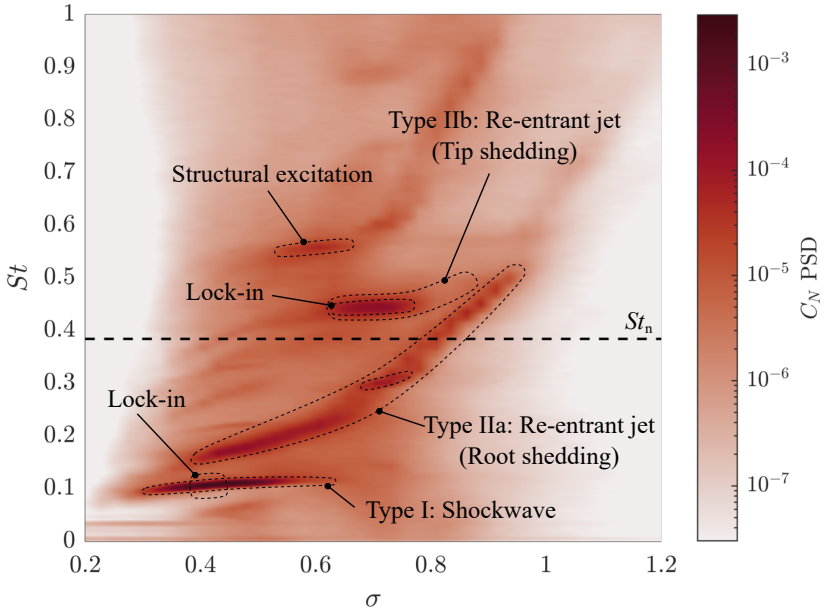

(b) Flexible hydrofoil

Figure 4.11: Spectrograms of C_N for a range of σ showing the global unsteady behaviour of the normal force. The results highlight the shockwave-driven Type I shedding frequency is predominately independent of σ while the re-entrant jet-driven Type IIa & IIb shedding modes are highly dependant on σ. Lock-in is observed to occur on the stiff hydrofoil (a) between the Type IIa mode and the first structural sub-harmonic ($f_n/2$) at $\sigma = 0.70 - 0.75$, where on the flexible (b), two instances of lock-in are observed. Firstly between Type IIb mode and the first structural mode (f_n) for $\sigma = 0.70 - 0.75$, and secondly at $\sigma = 0.4$ between the Type I mode and the second structural sub-harmonic ($f_n/4$). The fully wetted natural frequency of the hydrofoils, shown non-dimensionally, St_n, as a horizontal dashed line, is modulated due to the presence of the vapour cavity reducing the added mass, thereby increasing the natural frequency.

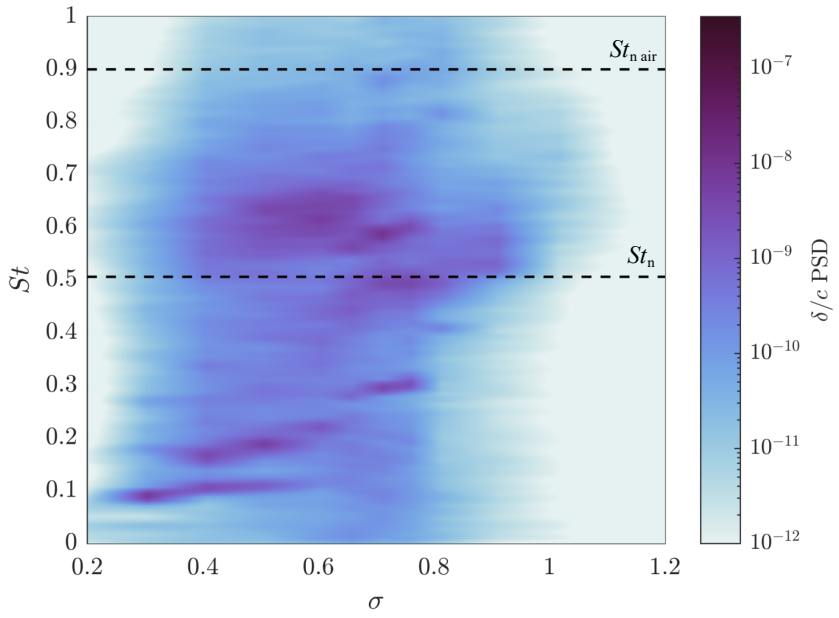

(a) Stiff hydrofoil

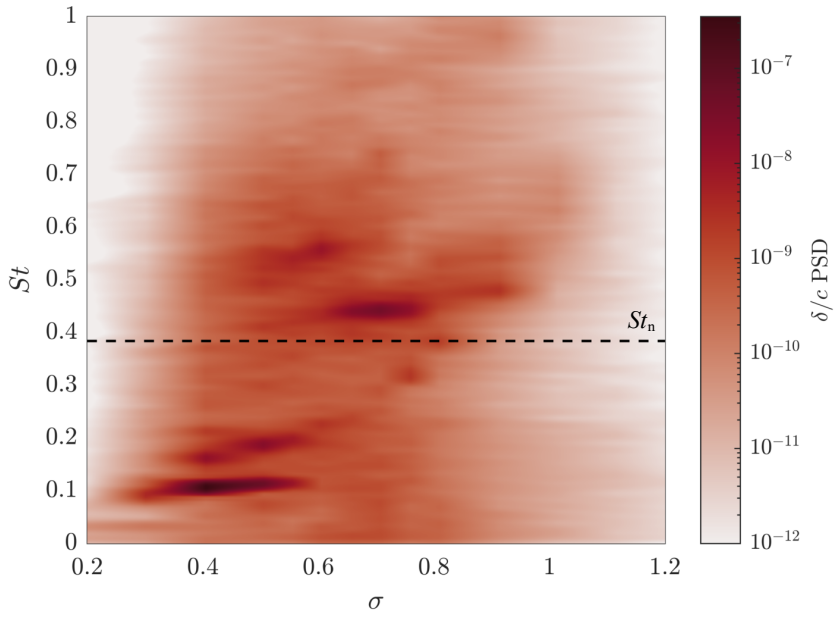

(b) Flexible hydrofoil

Figure 4.12: Spectrograms of $\delta/\bar{c}$ for a range of σ showing the global unsteady behaviour of the bending deformations. Comparison of the stiff (a) and flexible (b) hydrofoils highlights the increased power of structural deformations on the flexible hydrofoil. This causes increased FSI, particularly at points of lock-in. Both hydrofoils exhibit similar trends observed in the C_N spectrograms with strong interactions with structural modes where the fully wetted natural frequency of the hydrofoils, shown non-dimensionally, St_n, as a horizontal dashed line.

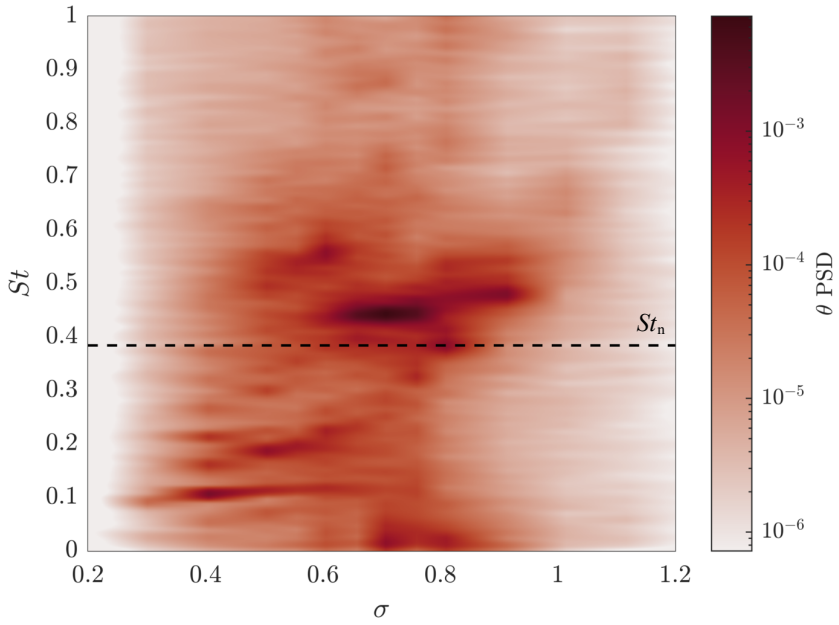

Figure 4.13: Spectrogram of θ for a range of σ on the flexible hydrofoils shows similar trends observed in both the C_N and $\delta/\bar{c}$ spectrograms with evidence of the Type I, IIa and IIb shedding modes. The highest power occurs at the lock-in frequency of $St = 0.45$ for $\sigma = 0.7$ with the fully wetted natural frequency of the hydrofoils, shown non-dimensionally, St_n, as a horizontal dashed line. Significant power is also observed during lock-in at $St = 0.11$ for $\sigma = 0.4$.

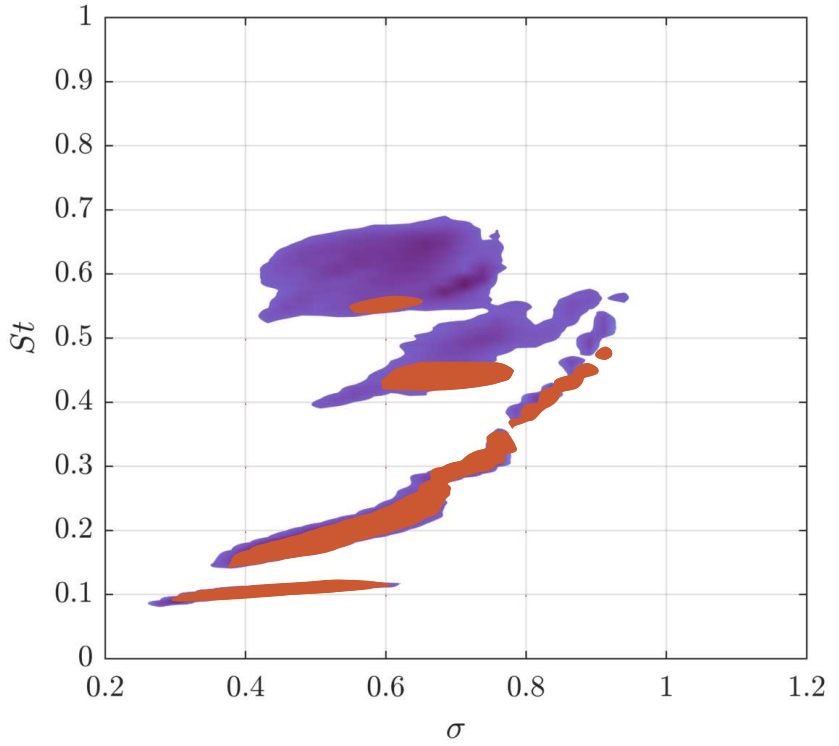

Figure 4.14: Comparison of the C_N spectrograms between the stiff (blue) and flexible (red) hydrofoils for C_N PSD values greater than a threshold of 0.2×10^{-5}. The St - σ relationship is seen to be similar between either hydrofoil for the Type I and IIa shedding modes. Differences are observed for the Type IIb shedding mode due to its susceptibility to structural deformations which are largest towards the tip.

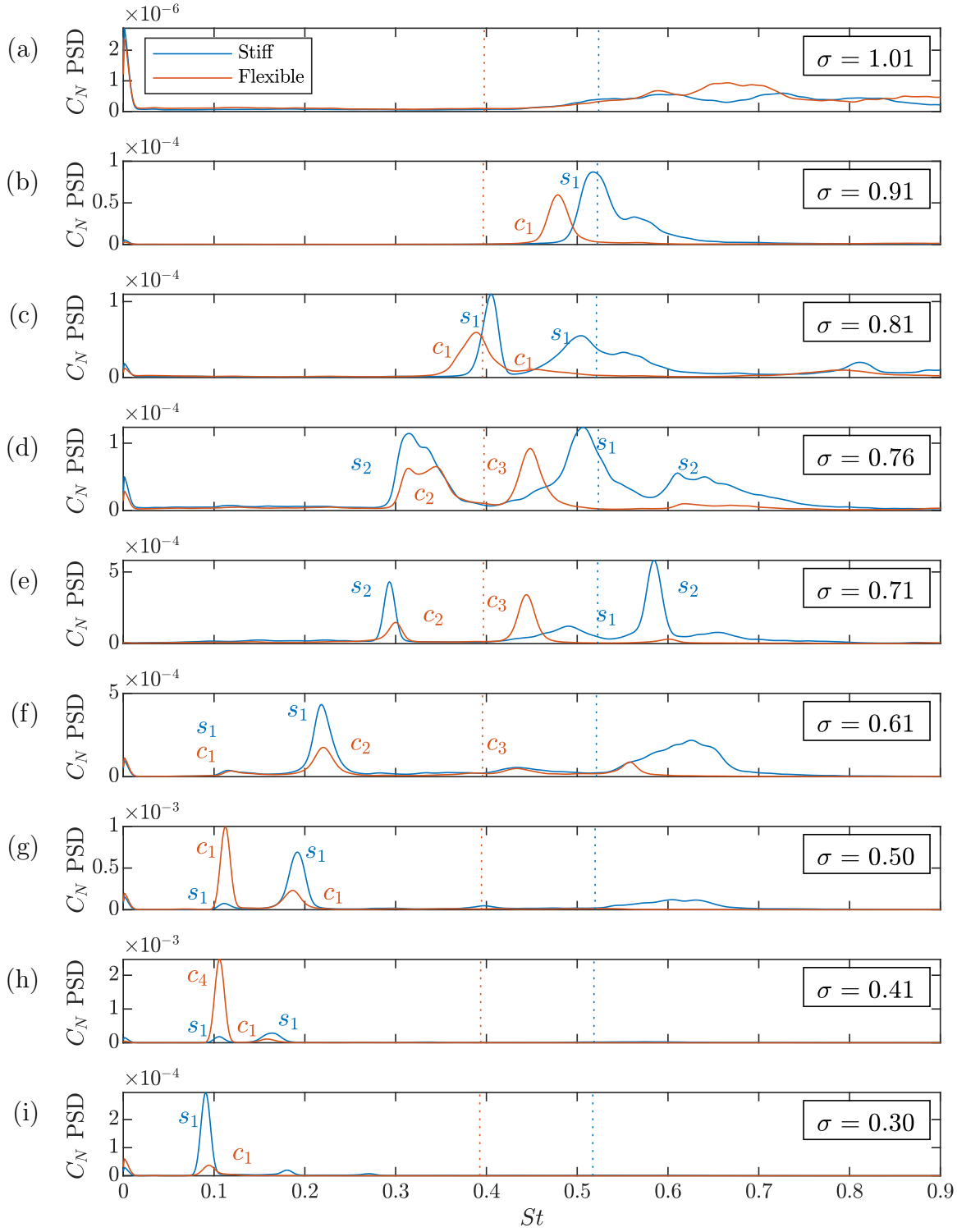

Figure 4.15: C_N PSD for both the stiff and flexible hydrofoils at key values of σ with the modes annotated using the labels from table 4.4. The spectra show the shedding modes shift in frequency as σ varies. The lock-in phenomena is evident in both hydrofoils with large amplification of C_N at $\sigma = 0.7$ and 0.4. Lock-in occurs when the excitation frequency from the shedding matches either the natural frequency (dashed lines) itself, or one of its harmonics. Note the change in the order of magnitude between each plot.

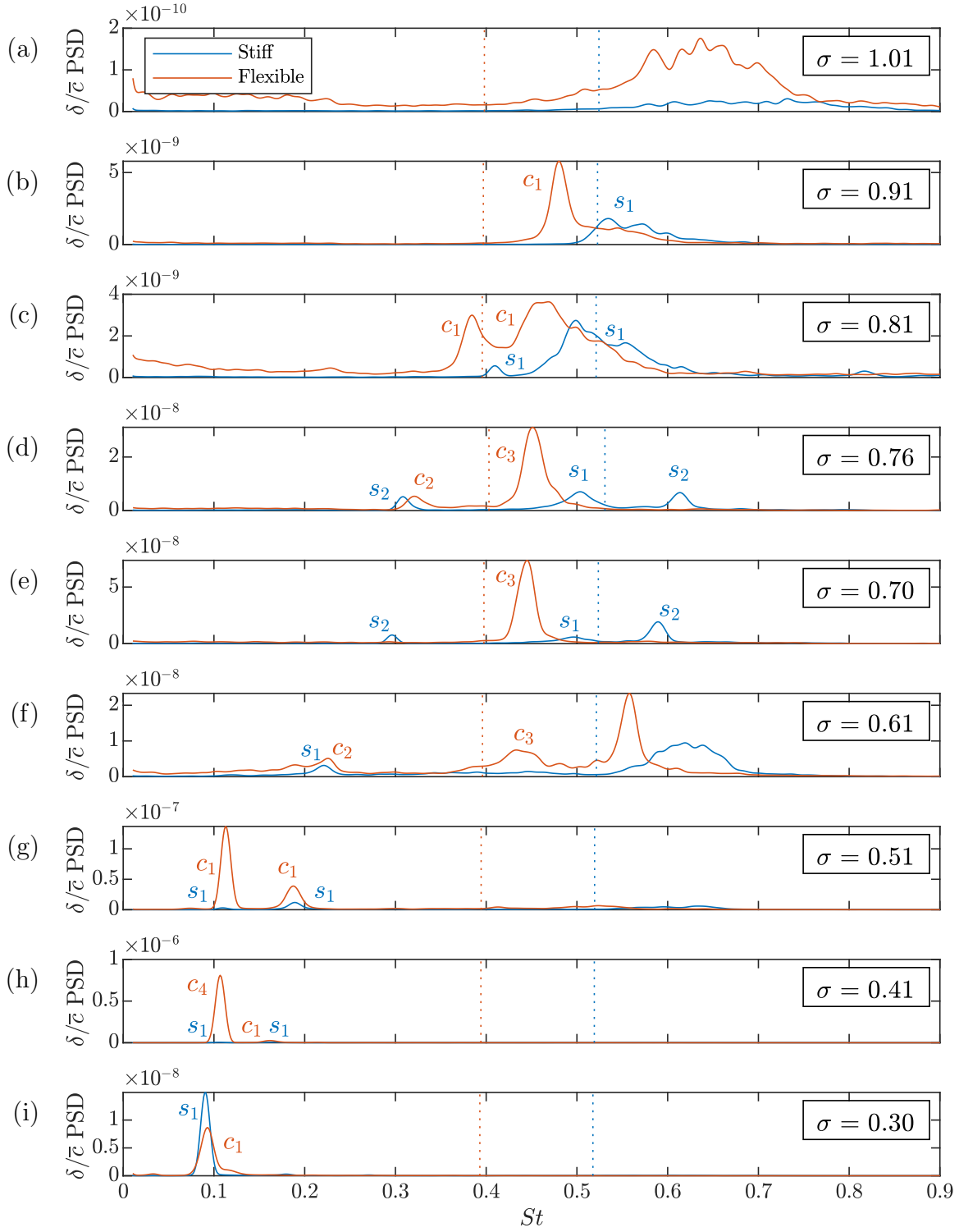

Figure 4.16: $\delta/\bar{c}$ PSD for both the stiff and flexible hydrofoils at key values of σ with the modes annotated using the labels from table 4.4. The spectra show the shedding modes modulates as σ varies. Lock-in of the shedding events with either the natural frequency (dashed lines) or the harmonics of the hydrofoils is evident, particularly on the flexible hydrofoil at $St = 0.44$ and 0.11 for $\sigma = 0.7$ and 0.4, respectively, due to its lower stiffness. Note the change in the order of magnitude between each plot.

with the Type IIa shedding of cavitation clouds in the upper portion of the span ($0.1 \leq y/b \leq 0.4$), with the $St = 0.45$ oscillation in the $\delta/\bar{c}$ linked to Type IIb shedding in the lower portion of the span ($0.55 \leq y/b \leq 0.85$), as evident in the SPOD energy maps in figure 4.17. The formation of two shedding sites matches that observed with the stiff hydrofoil, however, the Type IIb mode occurred at a higher frequency on the stiff hydrofoil at the sane σ because of shorter cavities. Interestingly, comparison of the hydrofoil's C_N spectra at $\sigma = 0.8$ reveals the absence of any clear Type IIb excitation on the flexible hydrofoil despite being evident on the stiff. This shows signs of significant FSI towards the tip of the flexible hydrofoil. The relatively large tip deformations appear to be interfering with the manifestation of induced hydrofoil loading from shedding cloud cavitation where compliance of the flexible hydrofoil appears to be having the influence of dampening higher-frequency oscillations.

When reducing σ further to 0.76, there is a shift in the Type IIa shedding frequency down to $St = 0.31$ with a similar frequency step change observed on the stiff hydrofoil, as seen in figure 4.11. As mentioned in Part 1, this step change is due to the hydrofoil reaching lock-in where an excitation frequency close enough to the structure's natural frequency shifts to match this natural frequency, leading to significant amplification of forces and deflections. The Type IIb mode becomes clearly evident on the flexible hydrofoil, exhibiting high amplitude not just in the $\delta/\bar{c}$ spectra, but in the C_N and θ spectra as well, shown in figures 4.11 and 4.13, respectively. With the Type IIa and IIb frequencies remaining constant as σ is decreased further to 0.7, significant amplification occurs in both the C_N and $\delta/\bar{c}$ spectral peaks with an order of magnitude increase (figure 4.15e). This is due to the lock-in phenomenon occurring with one of the shedding frequencies locking-in to one of the natural frequencies of the cavitating hydrofoil, causing resonance.

As shown in Part 1, the stiff hydrofoil experiences lock-in for $0.7 \leq \sigma \leq 0.75$ where the Type IIa root-shedding frequency closely matched the first sub-harmonic of the natural frequency, $f_n/2$, with added mass considerations, causing maxima in C'_N and $\delta'/\bar{c}$. However, the Type IIa frequency does not match the first sub-harmonic in the case of the flexible hydrofoil. With a lower natural frequency compared to the stiff hydrofoil, the flexible hydrofoil instead experiences lock-in with between the Type IIb oscillations at $St = 0.45$, with the first natural frequency, f_n, with added mass considerations. This lock-in phenomenon is clearly evident in figures 4.11b, 4.12b and 4.13 with defined high amplitude regions at the lock-in frequency for C_N, C_P, $\delta/\bar{c}$ and θ along local peaks in C'_N, C'_P, $\delta'/\bar{c}$ and θ' (figure 4.9). Comparison of the C_N spectrograms in figure 4.14 shows how the Type IIb mode locks-in on the flexible hydrofoils structural response with the excitation frequency remaining constant as σ varies, where in comparison the Type IIb frequency reduces with σ on the stiff hydrofoil. Lock-in with the Type IIb shedding is also shown in the SPOD maps where energy is concentrated in the lower half of the span for $St = 0.46$. The lower spectral content observed at higher frequencies in the flexible hy-

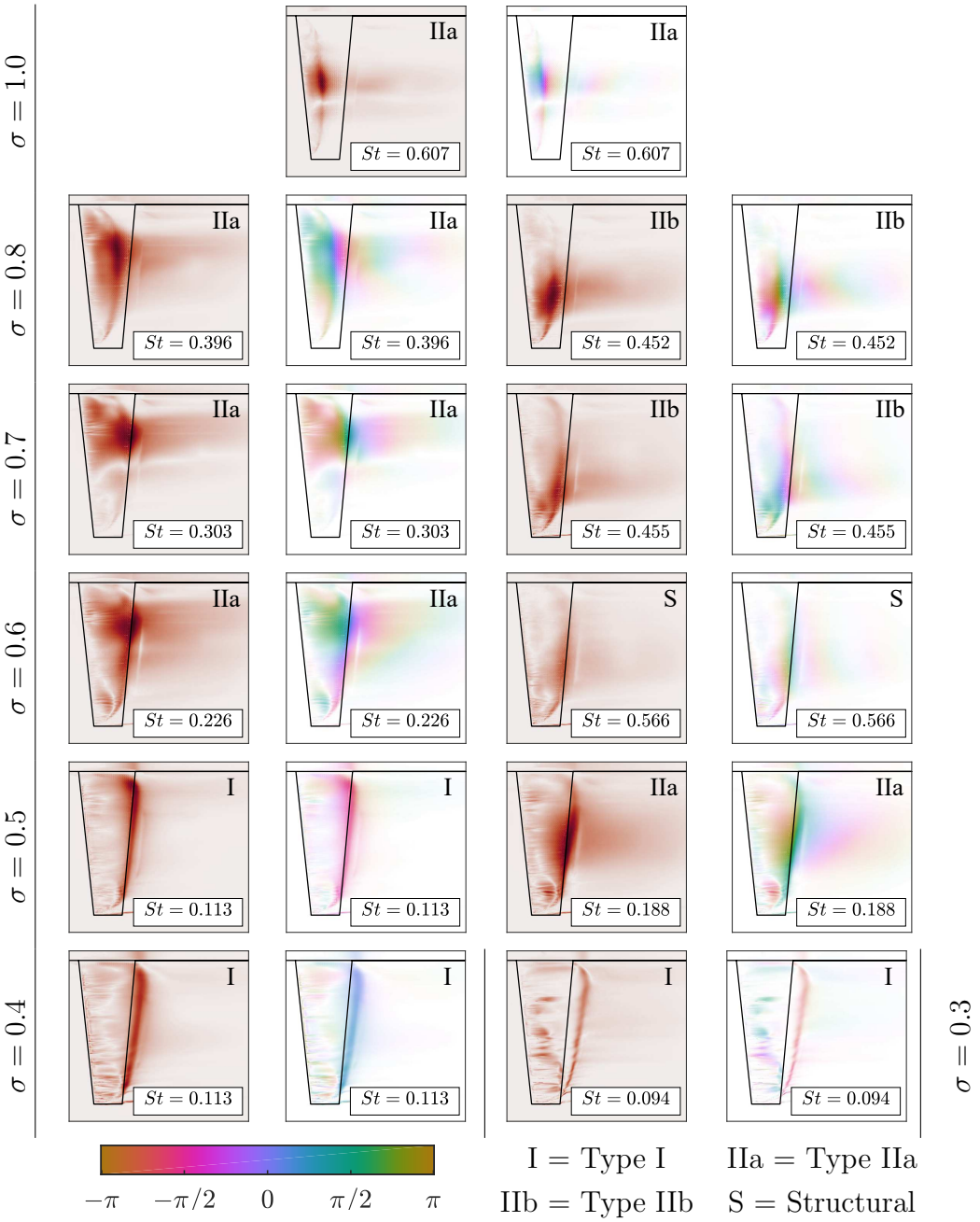

Figure 4.17: Spectral POD intensity (red) and phase maps (coloured) of key modes for various σ highlighting regions of high activity at the frequencies of interest. The colour intensity distribution in each phase map is directly proportional to that of the corresponding intensity map. The spectral and spatial information aids in the identification of the mechanisms driving oscillations with phase maps providing the relative timing of each cycle.

drofoil C_N spectra compared to that of the stiff is linked to the higher structural damping associated with the composite hydrofoil.

The flexible hydrofoil shifts out of lock-in conditions as σ is decreased down to 0.6 with the Type IIa shedding frequency stepping down to $St = 0.21$ from 0.45 at $\sigma = 0.71$. The reduction in σ sees the Type IIb mode decay significantly in the C_N spectra while a tonal peak emerges at $St = 0.46$ particularly evident in the $\delta/\bar{c}$ spectra, as shown in figure 4.15f; $\sigma = 0.61$ corresponds to the point that the attached cavity now extends slightly downstream of the trailing edge, the x_{cop} has reached its maximum and the deformed hydrofoil possesses its most negative $\bar{\alpha}_e$ with $\theta = -0.5°$.

The shedding behaviour on the flexible hydrofoil at $\sigma = 0.6$ resembles that of the stiff hydrofoil on the comparison of the SPOD energy maps at each respective Type IIa shedding frequency (figure 4.17). The high intensity region at the trailing edge extends the majority of the span for approximately $St = 0.226$ where the phase maps show the upper and lower halves to be out of phase. This indicates that the Type IIa and IIb modes are oscillating at the same frequency where the shed clouds alternate between the upper and lower portions of the span.

The Type IIa shedding frequency continues to reduce steadily at the same rate as the stiff hydrofoil with the attached cavity continuing to grow, showing a linear dependence on σ before disappearing for $\sigma < 0.4$, as shown in figure 4.11. The reduction of σ below 0.6 also shows the emergence of the Type I mode at $St = 0.11$ as observed on the stiff while remaining nominally independent of σ. As mentioned in Part 1, the emergence of the Type I mode coincides with the attached cavity reaching the trailing edge (figure 4.8) and is attributed to the presence of the shockwave instability. The SPOD energy maps at $\sigma = 0.5$ show that at the Type I frequency of $St = 0.113$, the shedding activity is concentrated along the trailing edge for the majority of the span with the phase map indicating uniform detachment (figure 4.17). In comparison, the Type IIa mode oscillations at $St = 0.188$ appear to be concentrated towards the mid-span of the hydrofoil with an isolated region towards the tip forming due to interaction between the cavity and the spanwise tip flow.

The amplitude of the Type I peak in both the C_N and $\delta/\bar{c}$ spectra starts growing rapidly and earlier compared to the stiff as σ is reduced as shown in the C_N, $\delta/\bar{c}$ and θ spectrograms (figures 4.11, 4.12 and 4.13). This leads to the Type I spectral peaks far exceeding the Type IIa peaks at $\sigma = 0.50$, unlike on the stiff (figures 4.15g and 4.16). This is followed by a twofold increase in the Type I peak as σ is reduced further to 0.41 (figure 4.15g) with the amplitude on the flexible hydrofoil far exceeding that of the stiff while maintaining a shedding frequency of $St = 0.11$. The high amplitude of the spectral peak is because the Type I cavity shedding frequency matched with a subharmonic of the first natural frequency, $f_n/4$, of the flexible hydrofoil; $\sigma = 0.4$ also coincides with the point of maximum C_N' and $\delta'/\bar{c}$ (figure 4.9), as well as the normal force and tip deflection being significantly out of phase linked to dampening.

Further reduction in σ to 0.3 sees the Type I mode decays quickly for the flexible hydrofoil with the peak amplitude continuing to grow on the stiff hydrofoil and exceeding the power of the flexible (figure 4.15). This is an indication of the flexible hydrofoil entering the supercavitation regime where the cavity is starting to extend far enough downstream to prevent the shockwave instability from forming and causing break-off. This is supported by the $\sigma = 0.30$ SPOD intensity maps in figure 4.17, where decreased intensity and definition in comparison to the Type I mode at $\sigma = 0.41$ is observed as the hydrofoil transitions to supercavitation. The earlier transition from the cloud cavitation to supercavitation regime can be linked to the longer cavity on the flexible hydrofoil clearly evident at $\sigma = 0.4$ and still evident at $\sigma = 0.3$.

As observed on the stiff hydrofoil, the shockwave-driven Type I mode is no longer apparent on the flexible hydrofoil as σ is reduced to 0.2 with the flow conditions fully shifting the hydrofoil into the supercavitating regime (figure 4.7). The C_N spectrogram (figure 4.11b) shows minimal excitation with no tonal peaks as the hydrofoil no longer experiences large-scale shedding with the cavity closing far downstream, preventing shockwave instabilities from forming. All cavity dynamics with observations made from the forces and deflections for each cavitation regime is discussed in §4.4.4.

4.4.4 Cavity dynamics

Sheet cavitation

Sheet cavitation is experienced by the flexible hydrofoil at high σ as observed on the stiff albeit only intermittently and limited to $\sigma = 1.2$. From the cavity dynamics analysis of the stiff hydrofoil, there is little to no evidence of re-entrant jet formation with cavity break-up primarily driven by interfacial instabilities for $1.1 \leq \sigma \leq 1.2$, as illustrated in figure 4.18. In comparison, the driver of cavity break-up is observed to interchange between interfacial instabilities and re-entrant jet formation over time on the flexible hydrofoil. This is shown in the spanwise space-time plot for $\sigma = 1.1$ taken at $x/c_{root} = 0.31$ (figure 4.18b) where manifestations of the re-entrant jet are temporarily evident for $0 \leq t' \leq 3$ and $9 \leq t' \leq 18$. This indicates that the flexible hydrofoil is in the transition region between sheet cavitation and cloud cavitation.

The acceleration of the transition from sheet to cloud cavitation on the flexible hydrofoil as σ is reduced is associated with the induced θ deformations increasing $\bar{\alpha}_e$. The resulting lower pressure on the suction side of the hydrofoil causes the larger attached cavity to grow into a region of an increased adverse pressure gradient that allows a re-entrant jet to form and cause shedding. Influence of the θ deformation is taken into account with the cavitation parameter $\sigma/2\bar{\alpha}_e$, where at $\sigma = 1.2$, the stiff and flexible hydrofoils have values of 5.89 and 5.43, respectively. These drop to 5.33 and 4.96 as σ is reduced to 1.1 for the stiff and flexible hydrofoils, respectively. This suggests more similar cavity dynamics

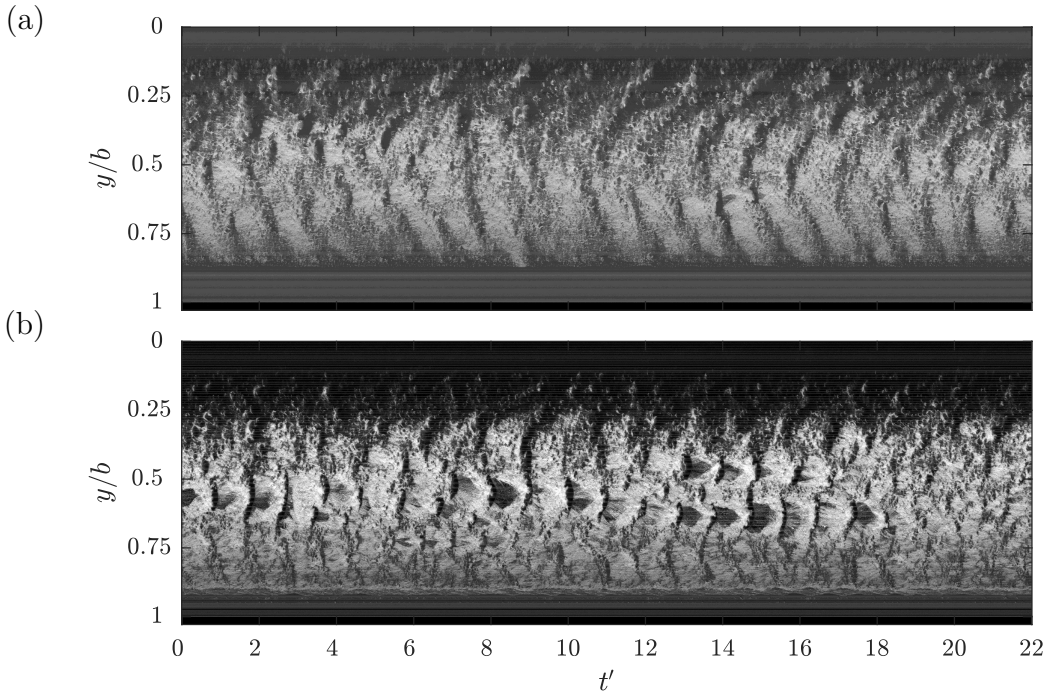

Figure 4.18: Spanwise space-time plots representing sheet cavitation just prior to a regime transition with reducing σ of the stiff hydrofoil (a) taken at $x/c_{root} = 0.35$ and $\sigma = 1.1$ as well as the flexible hydrofoil (b) taken at $x/c_{root} = 0.31$ and $\sigma = 1.2$. Where the stiff hydrofoil is seen to experience cavity break-up solely driven by interfacial instabilities, the flexible hydrofoil shows intermittent manifestations of re-entrant jet formation as it is closer to cloud cavitation transition.

should be observed between the hydrofoils when comparing $\sigma = 1.1$ on the stiff hydrofoil with $\sigma = 1.2$ on the flexible, which is observed to be reasonable.

Re-entrant jet-driven shedding (pre-lock-in)

As described in Part 1, cloud cavitation occurs when reduction in σ results in the formation of a re-entrant jet that has the ability to reach the upstream extent of the attached cavity, causing periodic cavity detachment. This occurs earlier on the flexible hydrofoil with reducing σ due to the flow-induced deformations with the onset of cloud cavitation evident at approximately $\sigma = 1.1$ compared to 1.0 on the stiff hydrofoil.

The early stages of Type IIa re-entrant jet-driven cloud cavitation appears similar for both hydrofoils with each exhibiting a rise in force fluctuations, C'_N and C'_P (figure 4.9) with the shift into the cloud cavitation regime. Analysis of the cavitation behaviour on each hydrofoil at $\sigma = 1.0$ (figure 4.19) shows the re-entrant jet mechanism confined to around mid-span due to three-dimensional flows effects mentioned in Part 1. Comparison of the space-time plots shows different frequencies with the stiff experiencing a slightly higher shedding frequency at $St = 0.74$ compared to $St = 0.61$ on the flexible which can be linked to the difference in $\sigma/2\bar{\alpha}_e$ and cavity length.

As σ is decreased further down to 0.8, x_{cop} shifts downstream where it lies close to

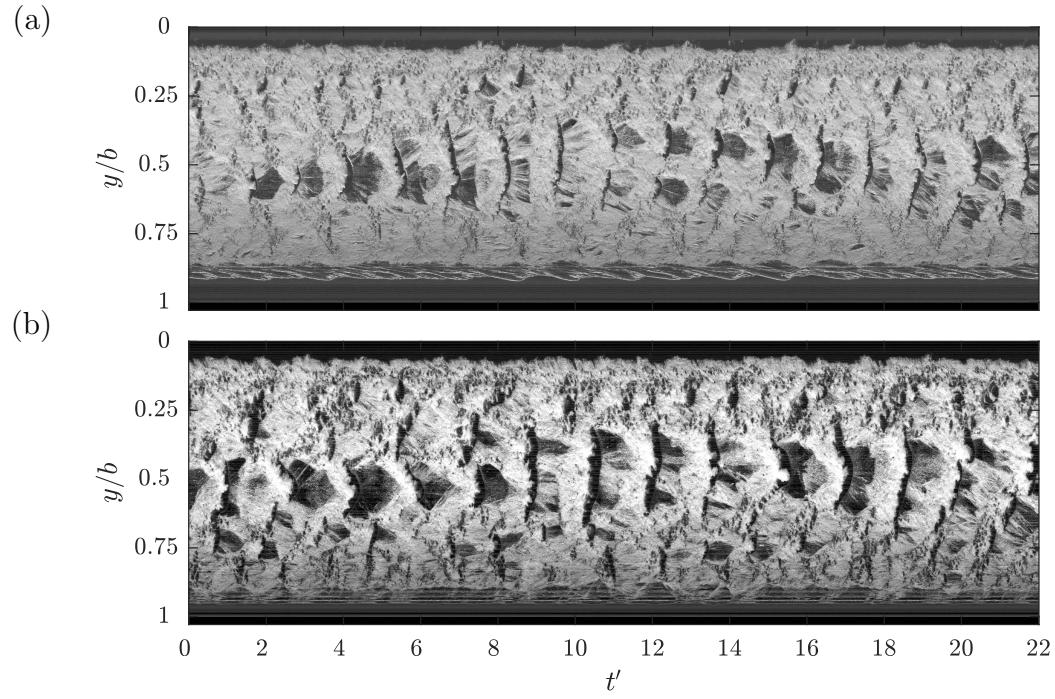

Figure 4.19: Spanwise space-time plots showing cloud cavitation of the stiff (a) and flexible (b) hydrofoil taken at $x/c_{root} = 0.31$ and $x/c_{root} = 0.35$, respectively, for and $\sigma = 1.0$. The re-entrant jet remains confined to around mid-span due to three-dimensional effects on each hydrofoil. The stiff hydrofoil exhibits a slightly higher shedding frequency of $St = 0.74$ compared to $St = 0.61$ on the flexible which is linked to induced θ angle increasing $\sigma/2\bar{\alpha}_e$ and cavity length.

the elastic axis, resulting in minimal twist deformations and therefore similar conditions for the stiff and flexible hydrofoils. As observed on the stiff hydrofoil, the reduction in σ sees the cavity along with the re-entrant jet thickness grow, giving the re-entrant jet enough momentum to overcome spanwise flow components and reach the leading edge for majority of the span (figure 4.20). This growth in the attached cavity and inherent cavity dynamics results in spatial compatibility with the hydrofoil where a secondary shedding mode appears on each hydrofoil, the Type IIb shedding mode. The formation of two defined shedding cells is clearly evident on the stiff hydrofoil as discussed in Part 1 and shown in figure 4.20b, but not as defined on the flexible hydrofoil (figure 4.20d).

Analysis of the space-time plot in figure 4.20d shows strong periodic shedding of the Type IIa mode at $St = 0.41$ in the upper portion, although large re-entrant jet shedding events are evident around mid-span not observed on the stiff hydrofoil. Comparison of the cavitation pattern in the lower portion of the span highlights the higher degree of cavity break-up on the flexible hydrofoil compared to the stiff hydrofoil, making shedding events unclear, particularly at $8 \leq t' \leq 13$. This period is seen to correspond to an interval of low structural deformations in both $\delta/\bar{c}$ and θ (figure 4.9), indicating a strong FSI influence. The induced deformations and vibrations from the fluctuating loads appear to be disrupting the cavity dynamics and inhibiting cavity formation particularly towards the tip were deformations are large.

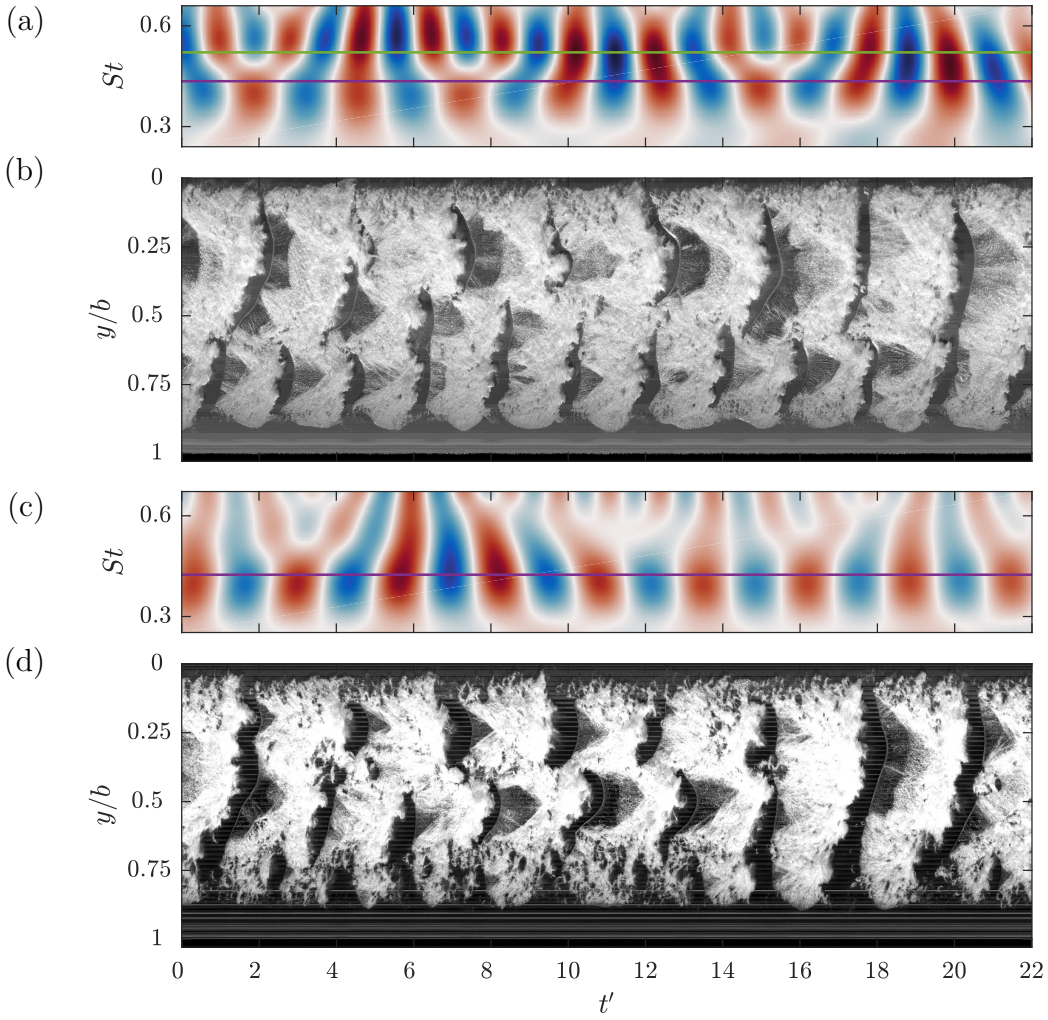

Figure 4.20: Both hydrofoils experience the formation of two shedding sites along the span at $\sigma = 0.8$ due to the spatial compatibility between the attached cavity and the planform geometry. This is shown by the spanwise space-time plots taken at $x/c_{root} = 0.5$ and 0.58 for the stiff (b) and flexible (d) hydrofoils, respectively. However, the real value C_N Morlet wavelet transform from the stiff hydrofoil (a) shows the multi-modal behaviour at $St = 0.41$ (purple horizontal line) and 0.50 (green horizontal line), while for the flexible hydrofoil (c), only the $St = 0.40$ (purple horizontal line) Type IIa mode is evident in the wavelet transform. Closer inspection of the cavitation behaviour towards the tip shows a higher degree of break-up on the flexible hydrofoil compared to the stiff, linked to the larger deformations.

Lock-in

As observed on the stiff hydrofoil in Part 1, the flexible hydrofoil experiences the lock-in phenomenon where the shedding frequency locks-in to a structural mode of the hydrofoil that leads to amplification of small motions and fluctuating fluid loads (Harwood et al., 2019). The flexible hydrofoil starts to experience lock-in with the reduction in σ down to 0.75 where we see the Type IIb tip shedding frequency lock-in to the first mode of the hydrofoil at $St = 0.44$ in figures 4.11-4.14. This is a slightly higher frequency than that in fully wetted conditions ($St = 0.38$) due to reduced added mass caused by phase change from water to vapour on the cavitation portions of the hydrofoil. Experimental measurements quantifying the change in added mass and modal frequencies with cavitation and ventilation can be found in Harwood et al. (2020). Lock-in differs between hydrofoils with the stiff experiencing lock-in between the first sub-harmonic of the structure and the Type IIa shedding due to the increased stiffness and lower added mass sensitivity. With lock-in occurring between the tip shedding mode and the first structural mode, increased FSI is observed for the flexible hydrofoil with the inherently higher deflections in the lower span.

The severity of lock-in is increased as σ is reduced further to 0.7 where the hydrofoil is observed to experience the largest θ fluctuations, along with local peaks in C'_N, $\delta'/\bar{c}$ (figure 4.9). Lock-in at $\sigma = 0.7$ on the flexible hydrofoil has more influence on the deformations compared to the stiff hydrofoil which has more influence on forces. This is due to the location of the lock-in shedding modes with the root shedding Type IIa mode occurring in a region of longer chord where the proximity of the Type IIb mode to the free tip increases the influence on deformations. This is highlighted in figures 4.15 and 4.16 with the difference between the Type IIa and IIb amplitudes in the C_N and $\delta/\bar{c}$ spectra for each hydrofoil.

Comparison of the time series at $\sigma = 0.7$ for the stiff hydrofoil in figure 4.21(*a-c*) and the flexible hydrofoil in figure 4.21(*d-g*) highlights the difference due to FSI effects. The lock-in of the first natural frequency of the flexible hydrofoil with the Type IIb shedding is exhibited in the C_N wavelet (figure 4.21*e,f*) where a more consistent and strong component is shown at $St = 0.44$ compared to $St = 0.49$ on the stiff (figure 4.21*a,b*). The strong interaction of the tip shedding with twist deformations is also exhibited in the θ time series exhibiting a strong $St = 0.44$ fluctuation in figure 4.21. Interestingly, comparison of the tip displacement time series shows a similar range of oscillation despite the significant difference in stiffness, indicating twist deformations to be the primary influence on the cavity dynamics. These structural deformations translate into defined and consistent tip shedding events, as shown in figure 4.21*g*, particularly when compared to the stiff in figure 4.21*c*. Despite tip shedding events being more defined in the flexible space-time plot, the cavity appears more broken and dispersed compared to the stiff, particularly towards the tip and downstream end of the cavity. This is attributed to the increased FSI from the

structural deformation disrupting the growth and stability of the attached cavity.

Re-entrant jet and shockwave-driven shedding (post-lock-in)

The flexible hydrofoil comes out of lock-in with enough reduction in σ down to 0.65 with fluctuations in both forces and deflections decreasing, as shown in figure 4.9. The transition out of lock-in is also made evident in the C_N and $\delta/\bar{c}$ spectra (figures 4.15 and 4.16) where amplification of the forces and deflection is no longer evident, leading to decreased interaction between the cloud cavitation and structural deformations. The decrease in σ leads to a larger cavity that now reaches the trailing edge of the hydrofoil (i.e. $L_c/c = 1.0$). This increased length results in a cavity that no longer has spanwise spatial compatibility for two cells to form, leading to the disappearance of the Type IIb mode, as observed on the stiff hydrofoil.

With the cavity reaching the trailing edge, shockwave instabilities become active as the attached cavity extends into the high pressure region downstream of the trailing edge. As described in Part 1, small-scale break-up of the cavity from surface perturbations forming as the re-entrant jet moves upstream preconditions the flow for condensation shockwaves to form. Similar to the stiff hydrofoil, the shockwave causes the shedding of cloud cavitation where the re-entrant jet instability drives the frequency. However, due to increased FSI, the emergence of the shockwave instability is accelerated on the flexible hydrofoil with similar behaviour seen between the stiff hydrofoil at $\sigma = 0.6$ and the flexible at $\sigma = 0.65$, as shown in figure 4.22.

Further reduction in σ down to 0.55 sees the Type IIa shedding frequency decrease linearly to $St = 0.20$ with the growth in cavity length resulting in partially coherent shedding along the span. As observed on the stiff hydrofoil at $\sigma = 0.5$, shedding along the span consists of several shedding events starting near the root and then occurring successively out along the span. This is evident in both space-time plots (figure 4.23*c-e*) by the 3-4 breaks in the cavitation pattern per cycle. The similarity between the cavitation behaviour and frequencies suggests that the hydrofoils should possess similar $\sigma/2\bar{\alpha}_e$ at $\sigma = 0.5$ and 0.55 for the stiff and flexible, respectively, with θ increasing $\bar{\alpha}_e$. However, the flexible hydrofoil deformations result in $\theta = -0.5°$, resulting in a significantly higher $\sigma/2\bar{\alpha}_e$ value of 2.78, compared to 2.41.

Comparison of the synchronised force and deflection time series, along with the space-time plots in figure 4.23 highlights a more complex cavitation behaviour on the flexible hydrofoil compared to the stiff. With both the re-entrant jet and shockwave instability being active while neither dominates the physics, the shedding behaviour varies through time. This was highlighted in Part 1 with the stiff hydrofoil at $\sigma = 0.4$ where the Type I mode was shown not to be continuously apparent through time in a long duration time series. This non-stationary multi-modal behaviour is shown in the flexible hydrofoils C_N

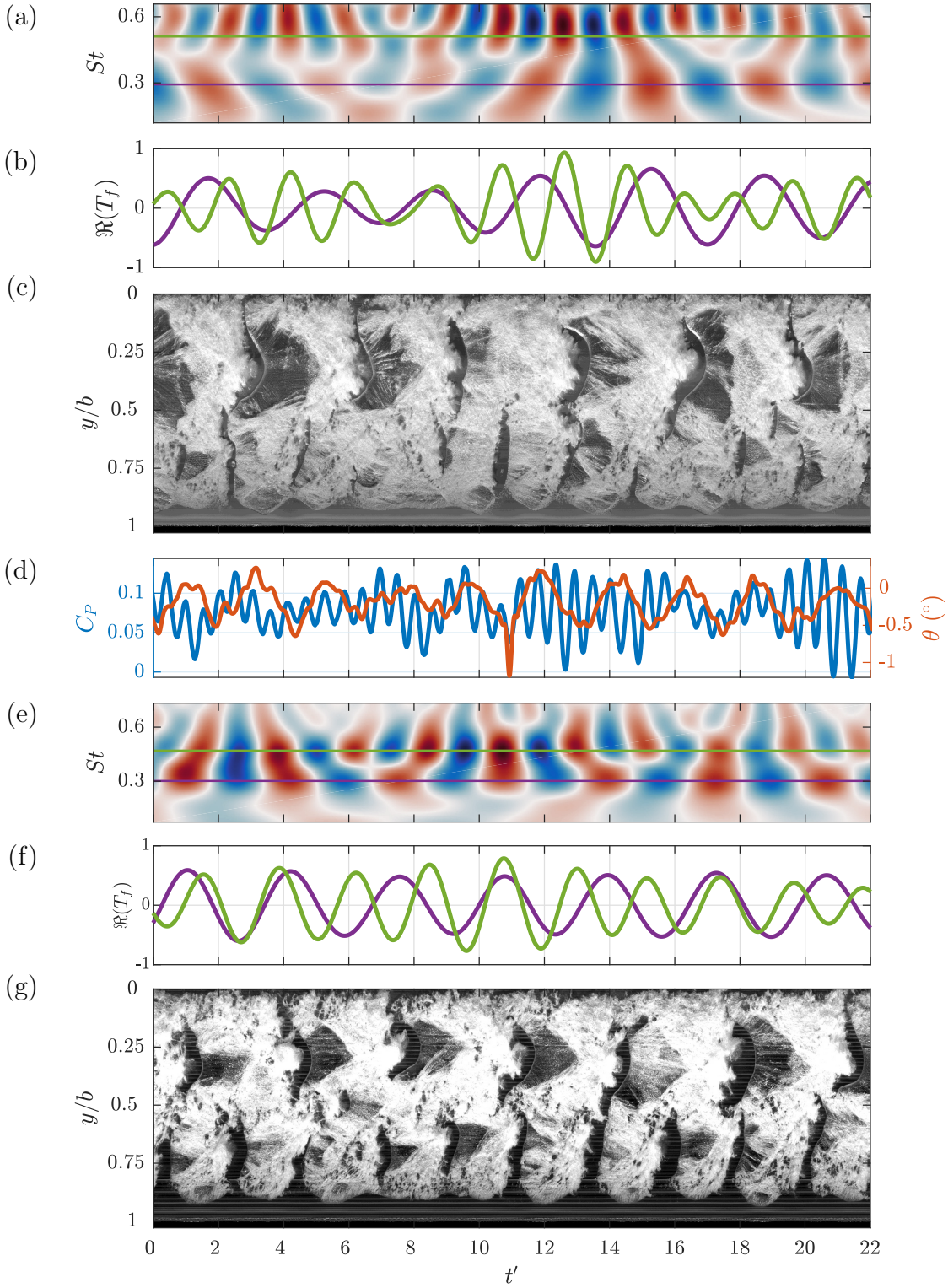

Figure 4.21: The multi-modal behaviour on either hydrofoil is shown in plots of the real values of Morlet wavelet transforms for C_N (a(stiff), e(flexible)) at $\sigma = 0.7$. Extracting the Type IIa and IIb wavelet components at $St = 0.29$ and 0.49 for the stiff hydrofoil (b) and $St = 0.30$ and 0.44 for the flexible hydrofoil (f), respectively, shows the correlation with shedding events. This shedding events along the span are evident in the spanwise space-time plots taken at $x/c_{root} = 0.5$ and 0.58 for the stiff (c) and flexible (g) hydrofoils, respectively.

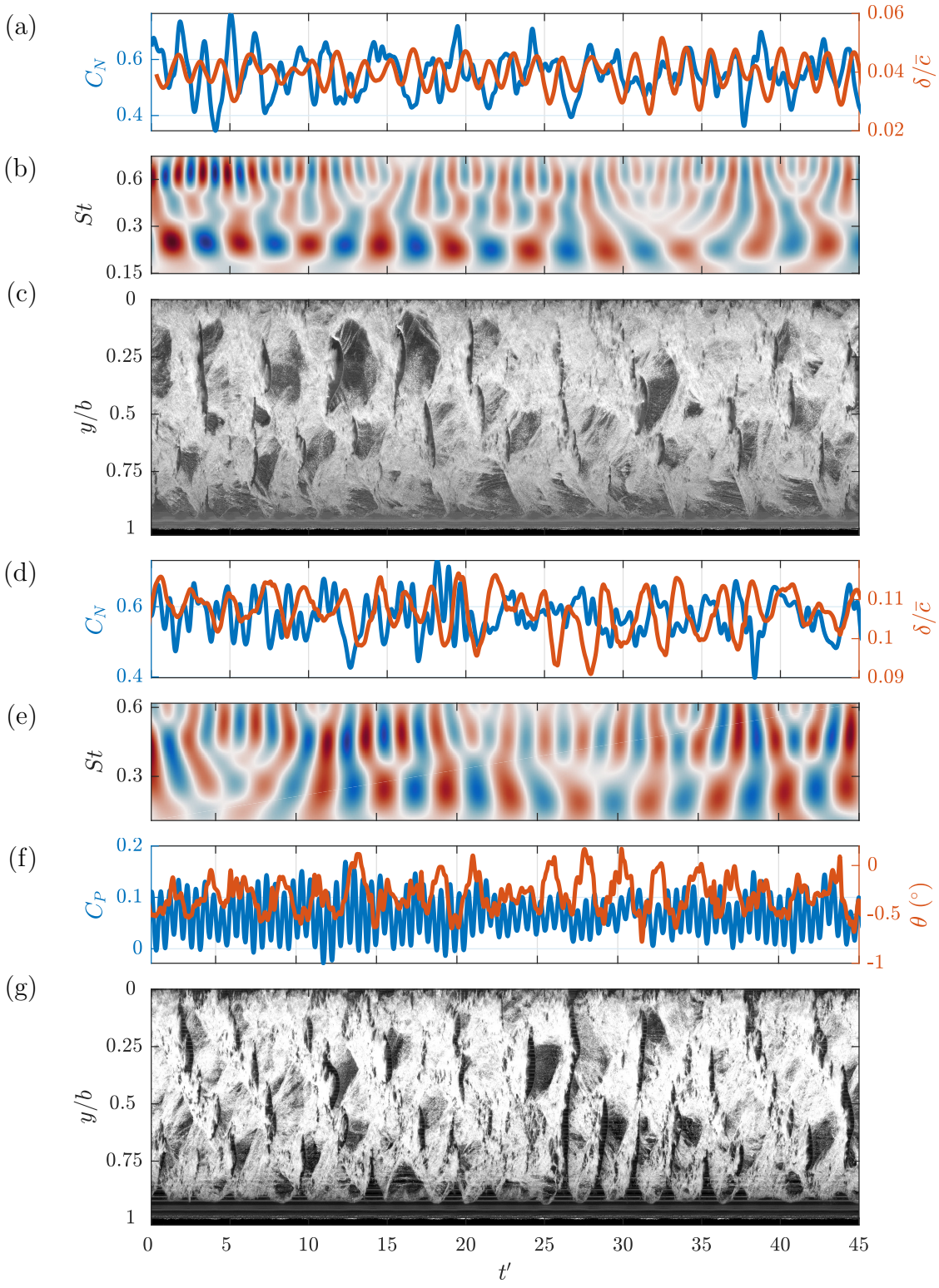

Figure 4.22: Synchronised time series of the normal force (C_N) and tip displacement ($\delta/\bar{c}$) (a (stiff), d(flexible)) along with the flexible hydrofoils pitching moment and twist (θ) (f) at $\sigma = 0.60$ and 0.65 for the stiff and flexible hydrofoil, respectively. The real value of the Morlet wavelet transforms for C_N (b(stiff), e(flexible)) shows the intermittent behaviour of shedding modes, also being evident in the space-time plots for the stiff (c) and flexible (g) hydrofoils taken at $x/c_{root} = 0.5$ and 0.58, respectively.

wavelet at $\sigma = 0.55$ (figure 4.23c) where a transition from the Type IIa mode to the Type I mode is apparent in the range $15 \leq t' \leq 25$, highlighting the need for time-frequency analysis. This transition is also evident in the θ time series where a $St \approx 0.53$ oscillation fades out at $t' \approx 15$ before a $St \approx 0.25$ oscillation appears at $t' \approx 25$, coinciding with the transition between modes shown in the C_N wavelet.

Shockwave driven shedding

As mentioned previously, the shockwave instability first becomes apparent at $\sigma = 0.6$ on the flexible hydrofoil, just as the attached cavity reaches the trailing edge, i.e. $L_c/c = 1.0$. Unlike on the stiff hydrofoil, the impact of the shockwave increases quickly as σ is reduced with the Type I mode dominating the C_N and $\delta/\bar{c}$ spectra (figures 4.15 and 4.16) by the point σ reaches 0.5. In comparison, the stiff hydrofoil spectrum is still dominated by the Type IIa mode down to $\sigma = 0.4$; $\sigma = 0.4$ and $\sigma = 0.5$ for the stiff and flexible, respectively, have been chosen for comparison in figure 4.24 due to the similarity of shedding modes and amplitudes. The dominance by the Type IIa mode is highlighted in the synchronised time series where the stiff hydrofoil C_N wavelet (figure 4.24b) is dominated by the Type IIa mode at $St = 0.16$. On the other hand, for the flexible hydrofoil, with the Type IIa mode still being present, the Type I mode dominates the time series at $St = 0.11$ for $\sigma = 0.5$ (figure 4.24e). In addition, a phase lag becomes apparent between C_N and $\delta/\bar{c}$ in the synchronised time series (figure 4.24d) with a phase difference of approximately $\pi/4$.

Comparing the spanwise space-time plots of the stiff and flexible hydrofoils at $\sigma = 0.4$ and 0.5, respectively, provides insight into the cavity physics driving the forces and deformations. As mentioned in Part 1, the stiff hydrofoil experiences alternate shedding between the upper and lower spans, as shown in figure 4.24c, driven by the re-entrant jet instability. On the other hand, shedding is more uniform along the flexible hydrofoil span, resulting in increased forces and deflections from larger shed cavities breaking off at $St = 0.11$ (figure 4.24g). This is highlighted in the SPOD energy maps, where the phase is uniform along the span for $\sigma = 0.5$ at $St = 0.11$ (figure 4.17).

Once the cavity grows to the full chord the void fraction increases, and the sound speed reduces (Shamsborhan et al., 2010), to a point where the flow is susceptible to the shockwave instability. The onset of the shockwave instability at higher cavitation numbers for the flexible case is presumably attributable to the increased compliance and the deformation. These are manifest in both the magnitude and shedding modes as apparent in the space-time diagrams and corresponding force and deflection time series in figure 4.24. As shown, the shedding modes are not as coherent for the flexible as they are for the stiff, as the stiff space-time diagram shows a regular, alternate, root-tip shedding system, but the flexible case shows coupled root-tip shedding with intermittent two-dimensional shedding events, showing the effect of compliance on the shedding topology. The increased

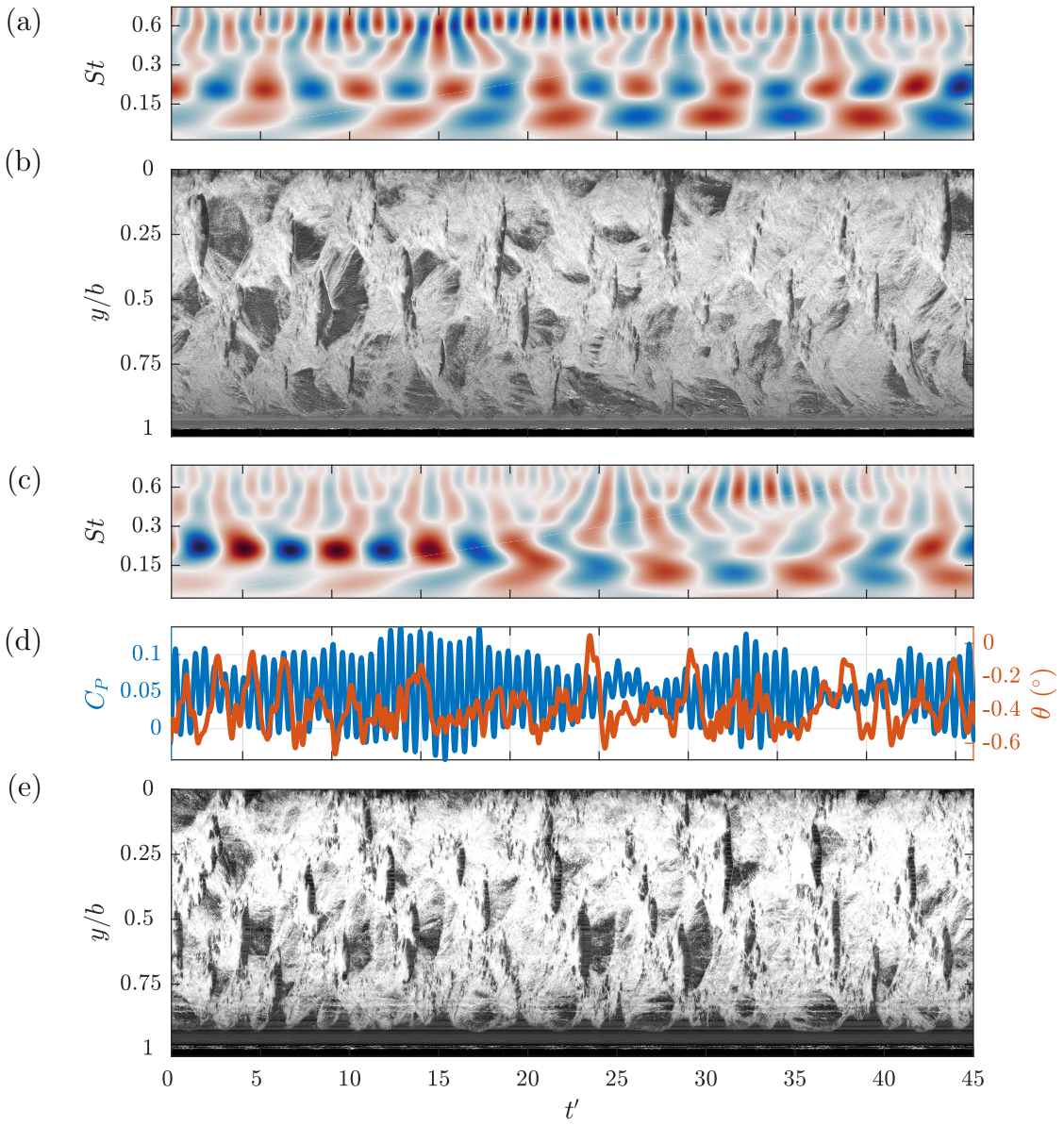

Figure 4.23: With several shedding mechanisms and modes active on each hydrofoil at a certain σ, the interactions and role of FSI becomes complex. At $\sigma = 0.5$ on the stiff hydrofoil, the C_N wavelet (a) shows the Type I ($St = 0.11$) and IIa ($St = 0.19$) modes being simultaneously active. Power of the Type I mode can be seen growing with t' in the C_N wavelet (a), corresponding with a change in the cavity physics evident in the spanwise space-time (b) taken at $x/c_{root} = 0.58$. This multi modal behaviour is also observed on the flexible hydrofoil at $\sigma = 0.55$ where a clear transition in the C_N wavelet (c) is evident from the Type II mode ($St = 0.20$) to the Type I mode ($St = 0.11$) at $t' = 20$. This transition is also evident in the θ deformations (d) with oscillations shifting from high to low, as well as in the cavity dynamics where the spanwise space-time plot (e) at $x/c_{root} = 0.65$ shows larger cavitation clouds being shed along the span when the Type I mode is active.

amplitude of C_N is due to the lock-in phenomenon described earlier, as evidenced from the associated increased deformations as shown in figures 4.15g,h and 4.16g,h. The fluid mechanics associated with shockwave phenomena in cavitating flows are highly complex and influenced by a range of factors that are not all fully understood, with observations varying between similar experiments (Leroux et al., 2004, 2005). The initiation and modes of propagation of shockwaves have been shown to vary greatly depending on the nature of the flow involved including factors such as the global cavity topology, three-dimensional effects, pressure gradients, and the level of nucleation. Observations of the high-speed imaging show shockwaves to mostly be initiated when portions of the growing cavitation reach the local chord. After which, propagation may be in the chordwise direction but also in the spanwise direction. The interaction of these shockwaves due to the tapered planform creates the shedding modes seen in the space-time diagrams, which were discussed in more detail in Part 1. Beyond the differences in compliance, some chordwise streaks are evident in the cavitation for the flexible hydrofoil that are not present for the stiff hydrofoil. These have been found to be due to leading edge imperfections resulting from the composite manufacturing process. It is possible that these streaks could affect cavity dynamics, although with the results available it is difficult to make definitive observations.

Further reduction in σ down to 0.4 on the flexible hydrofoil sees large amplification of both C_N and $\delta/\bar{c}$ PSDs at the Type I frequency of $St = 0.11$, corresponding to the points of maximum C'_N and $\delta'/\bar{c}$ for the flexible hydrofoil for the σ range tested. Additionally, a phase shift appears between C_N and $\delta/\bar{c}$ with the force and deflection becoming out of phase by approximately π for the flexible hydrofoil in figure 4.25c, not observed on the stiff hydrofoil (figure 4.25a). These phenomena are due to the flexible hydrofoil entering secondary lock-in between the Type I shedding mode and the $f_n/4$ sub-harmonic. The strong FSI effects involved in lock-in cause both uniform and periodic spanwise shedding of large-scale cavitation clouds that cause enlarged fluctuations in both the forces and deformations. The shift in phase between C_N and $\delta/\bar{c}$ fluctuations are linked to a reduction in damping brought about from the sub-harmonic lock-in and the increased cavity size allowing a greater portion of the hydrofoil to oscillate in a vapour cavity as opposed to the fluid.

Comparing cavitation behaviour on either hydrofoil at σ values corresponding to solely Type I shockwave-driven shedding reveals several key differences. The shedding cycle on the stiff hydrofoil at $\sigma = 0.3$ consists of a sequence of shedding events where a large-scale cloud is shed from the upper portion of the span, followed by two medium-scale clouds around mid-span in quick succession (figure 4.25b). This results in two small peaks in each of the $St = 0.09$ cycles in both the C_N and $\delta/\bar{c}$ time series (figure 4.25a). As for the flexible hydrofoil, it follows the behaviour observed at $\sigma = 0.5$ with uniform coherent shedding along the span with the spanwise space-time plot showing clear shockwave-driven cavity break-up (figure 4.25d). The chordwise space-time plots in figure 4.26 at the same σ

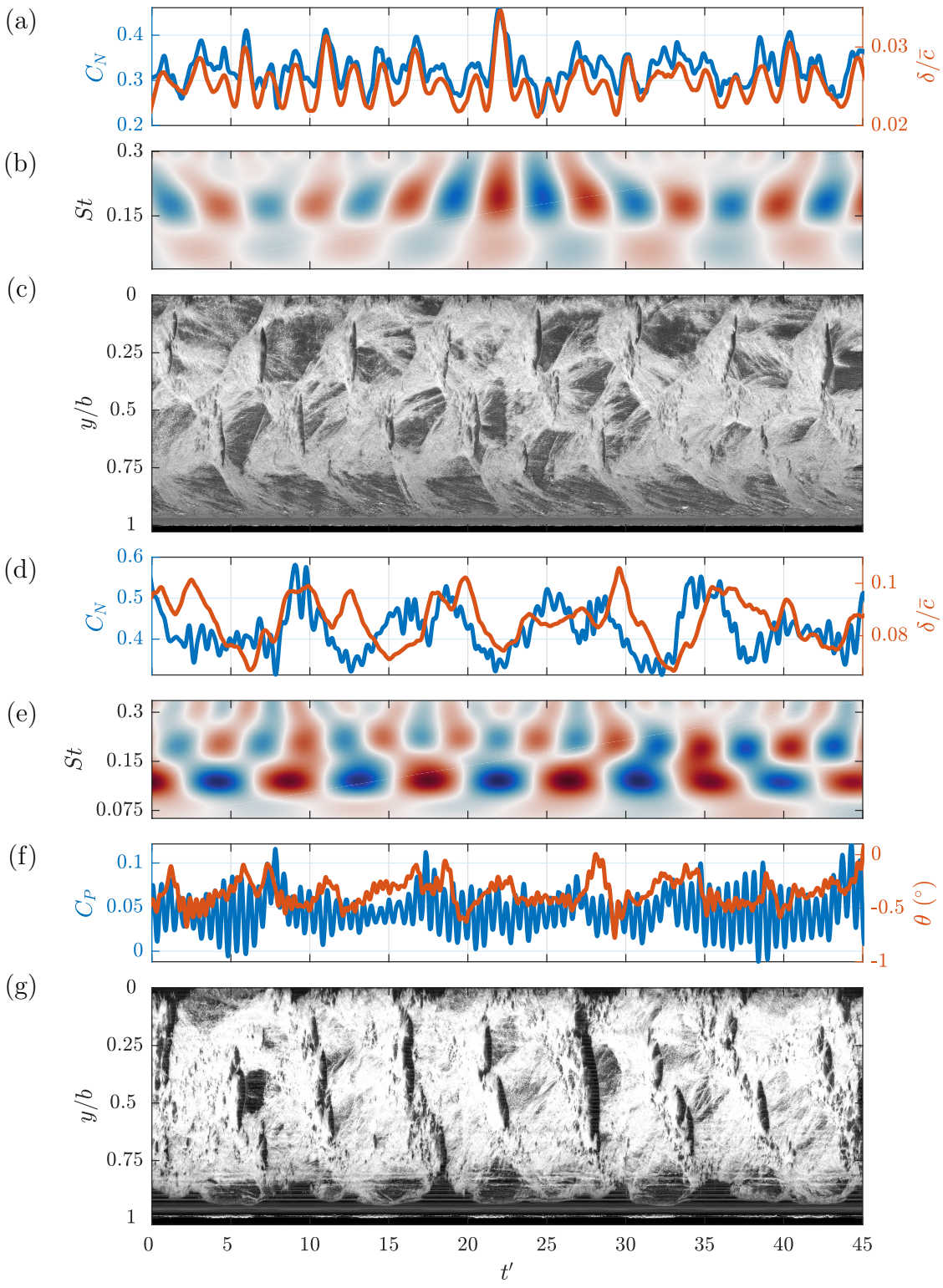

Figure 4.24: Synchronised time series of the normal force (C_N) and tip displacement ($\delta/\bar{c}$) (a (stiff), d(flexible)) along with the flexible hydrofoils pitching moment and twist (θ) (f) at $\sigma = 0.4$ and 0.5 for the stiff and flexible hydrofoil, respectively. The real value of the Morlet wavelet transforms for C_N (b(stiff), e(flexible)) shows the different dominant modes of either hydrofoil, also evident in the space-time plots for the stiff (c) and flexible (g) hydrofoils both taken at $x/c_{root} = 0.5$.

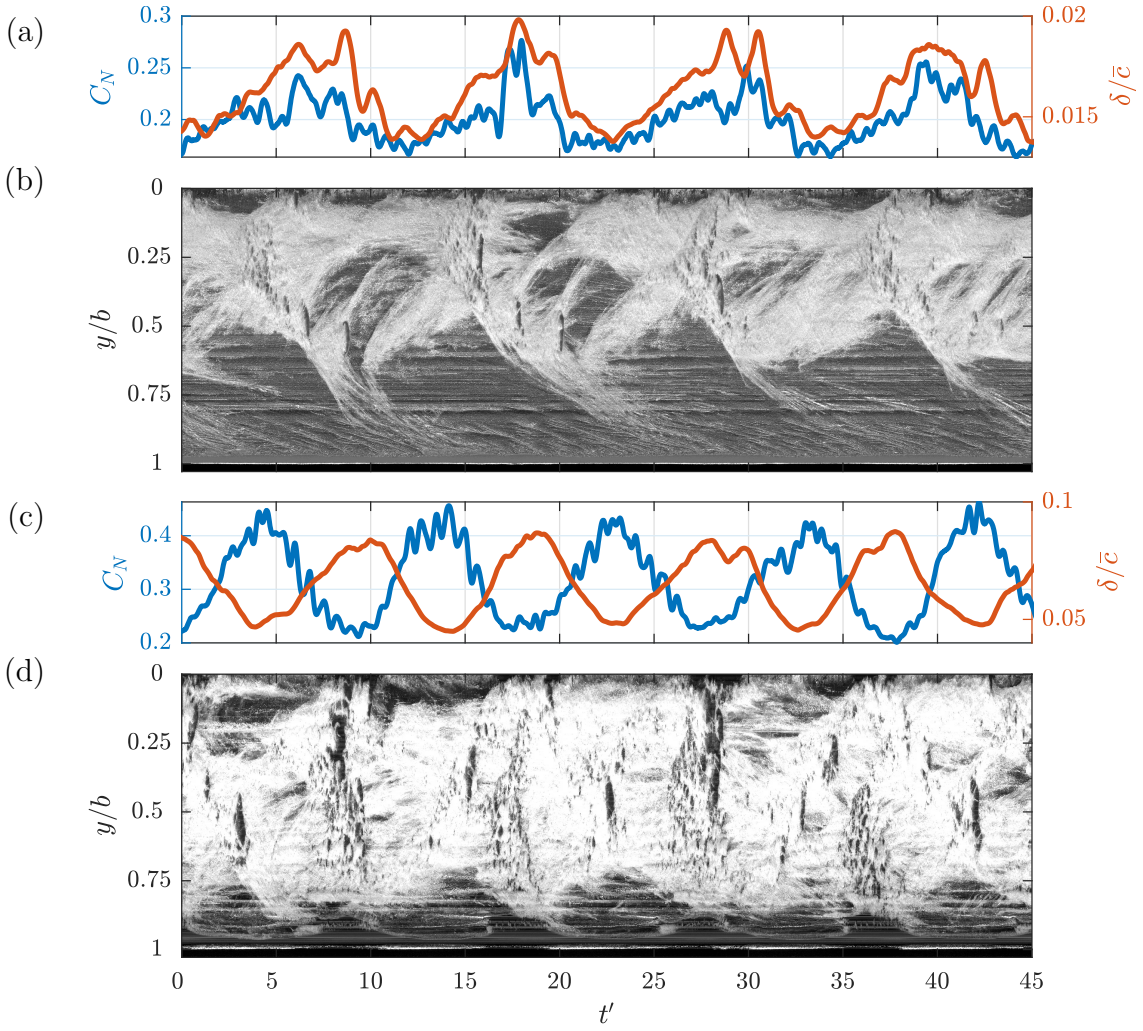

Figure 4.25: Synchronised time series of the normal force (C_N) and tip displacement ($\delta/\bar{c}$) at $\sigma = 0.3$ and 0.4 for the stiff (a) and flexible (c) hydrofoil, respectively. The spanwise space-time plots of the stiff (b) and flexible (d) taken at $x/c_{root} = 0.5$ show the dominant Type I shedding frequency that correlates well with C_N and $\delta/\bar{c}$ time series.

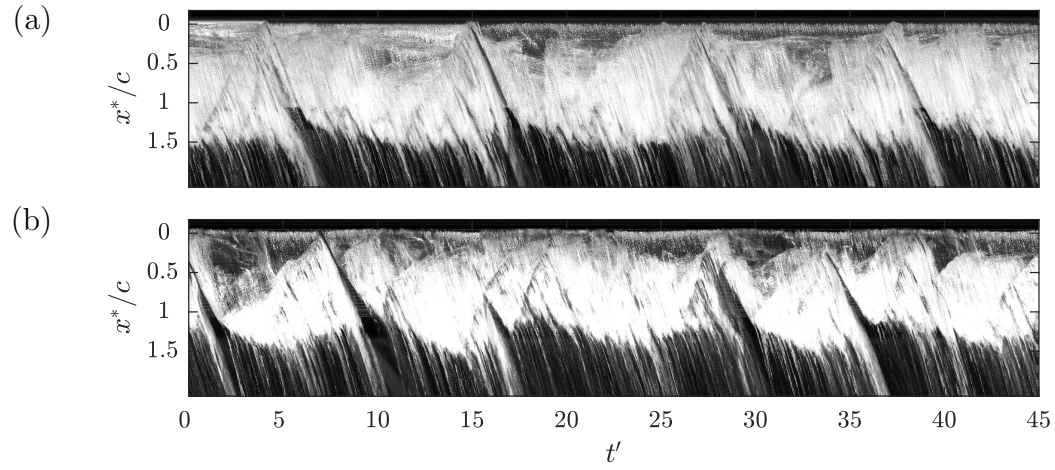

Figure 4.26: Chordwise space-time plots of the stiff (a) and flexible (b) hydrofoil both taken at $y/b = 0.25$ for $\sigma = 0.3$ and 0.4, respectively, showing the cavity dynamics for solely Type I shockwave-driven shedding. Both hydrofoils exhibit the growth, stable and shockwave phases for each cycle, however the flexible hydrofoil exhibits more inconsistent cycles in terms of cavity dynamics and cycle duration.

values show both hydrofoils experiencing the growth, stable and shockwave phases in each shedding cycle, as discussed in Part 1. However, comparing the hydrofoils, the shedding behaviour on the flexible appears more inconsistent in terms of cavity dynamics and cycle duration.

As σ is reduced down to 0.3, fluctuations in both C_N and $\delta/\bar{c}$ reduce as the shockwave instability weakens on the flexible hydrofoil with the phase lag between C_N and δ reducing to approximately $\pi/2$. The growth of the cavity has it extending far enough downstream of the hydrofoil into the region that limits the formation of certain instabilities. This results in only a relatively weak shockwave forming, reducing the impact on the forces and deflections but sufficient enough to cause shedding, as shown in figure 4.27. This stage of shockwave-driven shedding is not observed on the stiff hydrofoil as it occurs at a σ of approximately 0.25, a point not captured in the short type runs. Further reduction in σ sees the hydrofoil enter supercavitation, discussed in §4.4.4.

Supercavitation

The flexible hydrofoil transitions into the supercavitation regime as σ is reduced from 0.3 down to 0.2. As observed on the stiff hydrofoil, the significant growth in the cavity length to $L_c/c > 1.5$ has the cavity closing far downstream where it becomes more stable than a partial cavity as no substantial shedding mechanism can form (figure 4.7). There is little to no difference between the hydrofoils in terms of forces, deflections and cavitation behaviours as the forces have decreased to a point of little influence compared to the stiffness of the hydrofoil (figure 4.28). One difference observed between the hydrofoils is the presence of streaks that extend from the upstream extent of the cavity down to

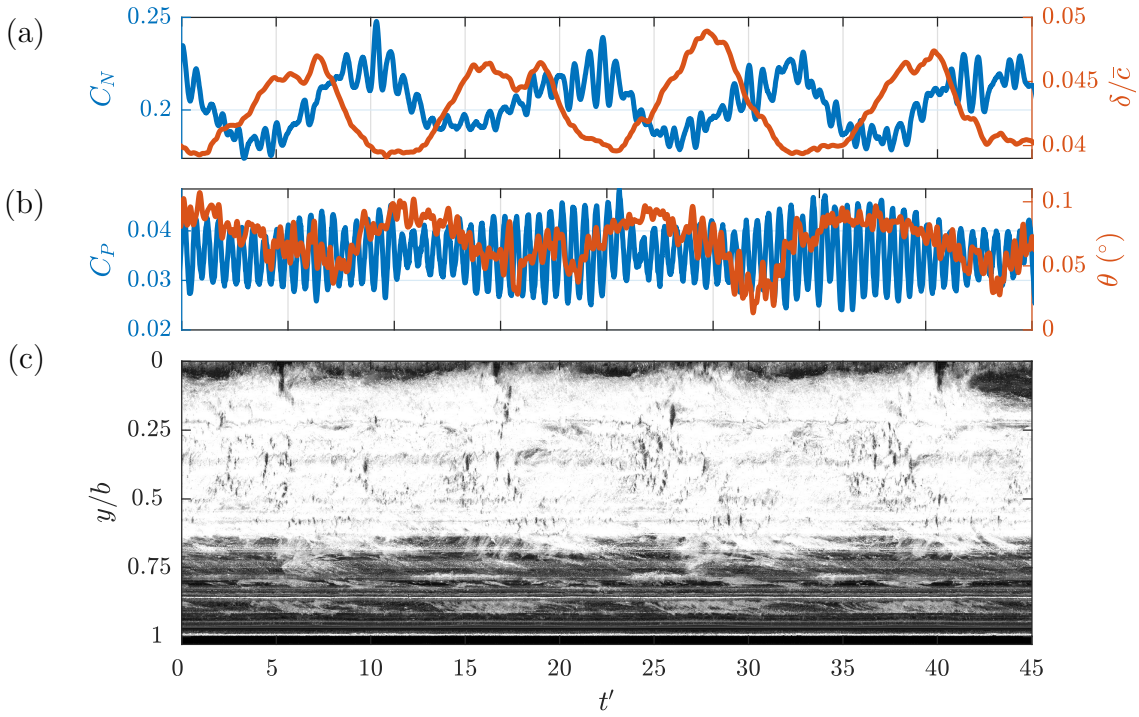

Figure 4.27: At $\sigma = 0.3$, the phase lag between C_N and $\delta/\bar{c}$ observed for the flexible hydrofoil at $\sigma = 0.4$ is still evident (a) with the θ deformations (b) showing to be in phase with C_P at the Type I $St = 0.10$ frequency. The weakening of the shockwave-driven shedding as the flexible hydrofoil approaches the transition to supercavitation is evident in the spanwise space-time plot (c) taken at $x/c_{root} = 0.73$ showing minimal cavity break-up.

the break-up region of the supercavity (figure 4.7). As discussed previously, these are due to small surface imperfections on the flexible hydrofoil stemming from the composite manufacturing process and are seen to have negligible influence on the supercavitation regime.

4.5 Conclusion

The influence of FSI on cloud cavitation about a hydrofoil was investigated through comparison of simultaneously acquired high-speed photography and force measurements on stiff and flexible hydrofoils. FSI was observed to influence all cavitation regimes with the flexible hydrofoil seen to experience accelerated cavitation regime transition with reducing σ. Hydrodynamic bend-twist coupling is seen to result in nose-up twist deformations on the flexible hydrofoil for $\sigma > 0.7$, causing an early transition from the sheet cavitation regime into the re-entrant jet-driven cloud cavitation regime at $\sigma = 1.1$. The nose-up bend-twist coupling has the added effect of increasing the cavity length, resulting in a reduced shedding frequency, particularly evident in the Type IIa mode at higher σ values. Lock-in occurs on the flexible hydrofoil for $0.70 \leq \sigma \leq 0.75$, as observed on the stiff hydrofoil. However, the flexible hydrofoil experiences lock-in between the Type IIb mode

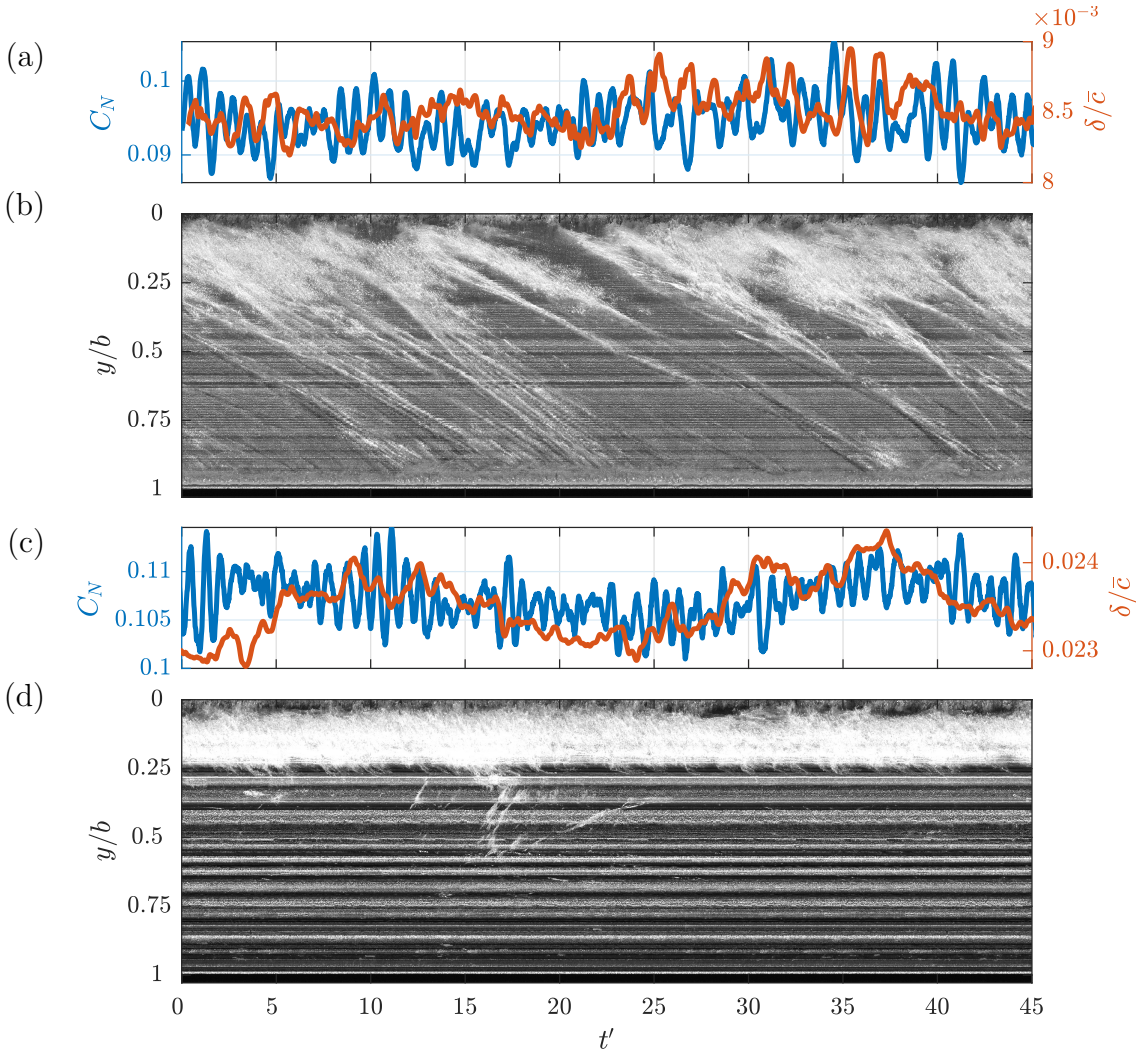

Figure 4.28: Synchronised time series of the normal force (C_N) and tip displacement ($\delta/\bar{c}$) at $\sigma = 0.2$ for the stiff (a) and flexible (c) hydrofoil. The spanwise space-time plots of the stiff (b) and flexible (d) taken at $x/c_{root} = 0.75$ show minimal activity in the supercavity as it closes far enough downstream to prevent shedding mechanisms from forming.

and the 1st structural mode (f_n). Additionally, the flexible hydrofoil appears to attenuate relatively high frequency oscillations with C_N PSD peaks on the stiff hydrofoil surpassing all those of the flexible for $0.6 \leq \sigma \leq 0.9$, despite higher deformations. Despite hydrodynamic bend-twist coupling causing nose-down twist deformations as the centre of pressure shifts downstream of the elastic axis for $\sigma \leq 0.7$, the flexible hydrofoil still experiences accelerated cavitation regime transition with reducing σ. This is seen with the rapid growth of influence the shockwave instability has on the forces, deflections and cavitation behaviour on the flexible hydrofoil, suggesting the larger dynamic structural behaviour plays a significant role in the cavity physics. As σ is reduced to 0.4, the different structural properties of the flexible hydrofoil lead to secondary lock-in, this time between the Type I mode and the $f_n/4$ harmonic. This leads to amplification of structural deformations and forces while also coinciding with a π shift in phase between C_N and $\delta/\bar{c}$ linked to a reduced damping brought about from the increased cavity size allowing a greater portion of the hydrofoil to oscillate in a vapour cavity as opposed to the liquid. Interestingly, this secondary lock-in involving the Type I mode was not observed on the stiff hydrofoil because of the higher first structural frequency. Further reduction in σ sees the flexible hydrofoil shift out of lock-in at $\sigma = 0.3$ with signs of supercavitation forming, where in comparison, the stiff hydrofoil still experiences strong shockwave-driven shedding, before both reach supercavitation at $\sigma = 0.2$. The structurally driven spanwise cavity oscillations observed on the flexible hydrofoil were not observed on the stiff hydrofoil, indicating significant differences in the conditions at the tip. Comparison of the forces, deflections and cavitation behaviour acting on the stiff and flexible hydrofoils shows significant FSI with flexibility leading to high-frequency attenuation of the forces, frequency modulation, accelerated cavitation regime transition as well as multiple lock-in modes.

4.6 Acknowledgements

This project was supported by the Research Training Centre of Naval Design and Manufacturing (RTCNDM) and the US Office of Naval Research (Dr. K.-H. Kim, Program Officer) and ONR Global (Dr W.-M. Lin) through NICOP S&T grant no. N62909-11-1-7013. The RTCNDM is a University-Industry partnership established under the Australian Research Council (ARC) Industry Transformation grant scheme (ARC IC140100003). The authors would like to acknowledge the assistance of Mr S. Kent and Mr R. Wrigley from the Australian Maritime College for their essential help with setting up and carrying out the experiments.

4.7 Nomenclature

Symbol	Definition	Unit
α	Flow incidence angle	$^\circ$
α_e	Effective flow incidence angle	$^\circ$
$\bar{\alpha_e}$	Mean effective flow incidence angle	$^\circ$
δ	Tip deflection	m
θ	Hydrofoil tip twist	$^\circ$
ν	Kinematic viscosity	m^2/s
ρ_H	Hydrofoil density	kg/m^3
ρ	Water density	kg/m^3
σ	Cavitation number	-
b	Span	m
C_N	Normal force coefficient	-
C_P	Pitching moment coefficient	-
c	Local chord	m
$\bar{c}$	Mean chord	m
c_{root}	Root chord	m
c_{tip}	Tip chord	m
E	Modulus of elasticity	N/mm
f	Frequency	Hz
f_{FB}	Force balance sampling frequency	Hz
f_{HSP}	High-speed photography frame rate	Hz
f_n	Natural frequency	Hz
I	Moment of inertia	mm^4
J	Polar moment of inertia	mm^4
K	Bending Stiffness	N/mm
L_c	Cavity length	m
N	Normal force	N
P	Pitching moment	Nm
p_∞	Absolute freestream static pressure	Pa
p_v	Vapour pressure	Pa
Re	Reynolds number (chord based)	-
St	Strouhal number	-

St_n	Strouhal number of natural frequency	-
T	Run duration	s
t	Time	s
t'	Non-dimensional time	-
U_∞	Freestream velocity	m/s
x	Streamwise location	m
x^*	Streamwise location (relative to local leading edge)	m
x_{cop}	Streamwise centre of pressure	m
y	Spanwise location	m

Chapter 5

General Conclusions and Future Recommendations

5.1 Conclusions

Within this thesis, experimental investigations into the unsteady loading experienced by a hydrofoil due to turbulence and cavitation is presented. Key insights have been gained into the steady and unsteady loading experienced by hydrofoil for varying degrees of immersion in an encountered boundary layer. In addition, a deeper understanding of the influence of FSI on cloud cavitation about a flexible hydrofoil is obtained, with experiments providing key insights into the flow physics involved.

5.1.1 Unsteady loading due to boundary layer immersion

The influence of boundary layer immersion on the normal forces acting on a hydrofoil was achieved by artificially thickening the oncoming boundary layer via an array of cross flow jets. Inner and outer profiles compared well to the law of the wall and modified Coles law of the wake, respectively, indicating a good representation of a natural boundary was utilized in the experiments. With the increased immersion of the hydrofoil in the wall boundary layer, it was observed to decrease C_N which is attributed to the increased exposure to the lower velocity flow within the boundary layer. Furthermore, the increased immersion was shown to delay stall as well as cause transition from leading-edge to trailing-edge type stall. This is attributable to the increased transfer of TKE and momentum from the wall boundary layer to the boundary layer developing on the hydrofoil, increasing the resistance to separation, and therefore stall. The increased transfer of TKE at higher δ/b is also associated with the reduction in the variation of the steady and unsteady normal force characteristics with changes in Re. This is attributed

to the transfer of TKE inhibiting LSB formation by accelerating transition of the hydrofoil boundary layer to the turbulent regime. This provides valuable insight into the flow structures involved with a hydrofoil immersed in a turbulent boundary layer, achieving a key objective of the research.

Significant insight into the unsteady loads acting on a hydrofoil immersed in a turbulent boundary layer is obtained from the spectral content of C_N where it is shown to increase in power with α across the entire resolvable frequency range for the low δ/b cases. The increase in unsteady loading is associated with the higher levels of self-generated turbulence of the hydrofoil. In contrast, high δ/b cases only showed increases in power at low reduced frequencies, with the pre-stall cases only seeing power growth at $f' < 0.1$ and $f' < 0.3$ for post-stall cases. This showed that unsteady loading due to self generated turbulence is characterized by large, low-frequency excitations where those from the wall boundary layer are more widespread, resulting in more of a broadband frequency excitation. Further analysis reveals the emergence of a wide peak amongst the broadband excitation at $f' \approx 0.2$ which increases in relative amplitude with δ/b. This peak becomes lost in the broadband excitation induced by the self-generated turbulence at high α. This indicates a disturbance associated with the wall boundary layer that is moving at $1/5^{th}$ of the free-stream advection speed. Furthermore, the cut-off frequency of the broadband peak is found to decrease with increasing δ/b while the roll-off increases. These results provide insight into the size distribution of structures in the encountered wall boundary layer that effect the unsteady loading of the hydrofoil, aiding in achieving the objective of gaining insight into the flow structures involved.

5.1.2 Influence of FSI cloud cavitation about a stiff and flexible hydrofoil

A variety of cavitation regimes occur about a hydrofoil depending on the operating conditions, consisting of sheet, cloud and super-cavitation, each exhibiting unique traits. The break-up and shedding of these cavitation regimes observed are driven by various instabilities. These include interfacial instabilities, re-entrant jet formation, shockwave propagation and complex, coupled mechanisms, depending on the cavitation number. Of these instabilities, two are identified as the primary drivers of the observed shedding modes consisting of Type I shockwave driven and Type IIa & IIb re-entrant jet driven shedding modes. The Type I shockwave driven mode is observed to oscillate at a frequency nominally independent of σ where as the Type II re-entrant jet driven mode exhibits a linear dependence on σ, decreasing in frequency with σ due to growth in cavity length. The experiments were successful in obtaining qualitative measurements of the forces, deformations and cavitation behaviour of both a stiff and flexible hydrofoil experiencing cloud cavitation.

For higher cavitation numbers (> 1.0), the cavity length is relatively small on the stiff hydrofoil with cavity break-up driven by small-scale interfacial instabilities that leads to small vapour pockets being shed. Reduction in σ to 1.0 moves the cavity closure into a region of sufficient adverse pressure gradient for a re-entrant jet to form and drive medium scale shedding from mid-span. Further reduction in the cavitation number down to 0.9 - 0.7 sees a geometrical compatibility between the cavity length and the hydrofoil span, allowing the formation of to stable periodic shedding modes. These are the Type IIa & Type IIb modes driven by a re-entrant jet instability towards the root and tip, respectively. Decreasing the cavitation number below 0.6 sees the emergence of a shockwave instability with the cavity reaching the high-pressure region at the trailing-edge and reducing the local speed of sound below the local flow speed by increasing the void fraction. The re-entrant jet and shockwave instability occur concurrently, resulting in complex shedding physics. Further reduction in σ to 0.2 sees the cavity grow to a point that it closes far enough downstream to form a stable supercavity as no shedding mechanisms can form. This provides significant insight into the physics involved with the hydrofoil with minimal fluid-structure interaction, thus aiding the identification of changes in flow physics due to fluid-structure interaction.

The phenomena known as lock-in is observed to occur on the stiff hydrofoil between the Type IIa mode and the first sub-harmonic of the hydrofoil natural frequency for $0.70 \leq \sigma \leq 0.75$. Where lock-in resulted in the large amplification of the normal force, the structural deformations remained relatively small compared to hydrofoil dimensions. These were observed to have minimal effect on the cavitating behaviour only manifesting in spanwise cavity oscillations. Hence, the stainless steel model provides a relatively stiff reference model for comparison with, and to aid in interpretation of, a more flexible hydrofoil of the same geometry.

With the introduction of flexibility, significant changes are observed in the forces, deformations and cavitation behaviour due to FSI effects. This is seen with all cavitation regimes on the flexible hydrofoil observed to experience accelerated cavitation regime transition with reducing σ. This is attributed to the nose-up twist deformations from hydrodynamic bend-twist coupling for $\sigma > 0.7$, resulting in the transition from the sheet cavitation regime into the re-entrant jet driven cloud cavitation regime at $\sigma = 1.1$. In addition to accelerating regime transition, the nose-up bend-twist coupling has the added effect of increasing the cavity length that causes a reduction in the shedding frequency. With further reduction in σ the relatively high frequency C_N oscillations appear to be attenuated on the flexible hydrofoil with the corresponding peak amplitudes on the stiff hydrofoil surpassing all those of the flexible for $0.6 \leq \sigma \leq 0.9$, despite higher deformations.

Indications that large dynamic structural deformations play a significant role in the cavity physics is observed as σ is reduced below 0.7. This reduction in σ to 0.6 sees a rapid growth in the influence and magnitude of the shockwave instability on the forces,

deflections and cavitation behaviour. Further reduction in σ sees the C_N and $\delta/\bar{c}$ PSD amplitude of the Type I mode continue to increase, until reaching $\sigma = 0.3$ where signs of supercavitation forming start to emerge. This is in contrast to the stiff hydrofoil which still experiences strong shockwave-driven shedding at $\sigma = 0.3$ with the difference attributable to the increased $\delta/\bar{c}$ fluctuations on the flexible hydrofoil as twist deformation are negligible. As σ is reduced to 0.2, a supercavity forms with the lack of shedding coinciding with disappearance of significant force and deformation fluctuations, as observed on the stiff hydrofoil.

The lock-in phenomena observed on the stiff hydrofoil is also observed on the flexible with the increased hydrofoil compliance altering the characteristics. While observed to occur at the same σ range as on the stiff hydrofoil ($0.70 \leq \sigma \leq 0.75$), lock-in occurs on the flexible between the Type IIb mode and the 1st structural mode (f_n), as oppose to the Type IIa mode and the first sub-harmonic of the hydrofoil natural frequency ($f_n/2$). Furthermore, a secondary lock-in occurs on the flexible hydrofoil at $\sigma = 0.4$ between the Type I mode and the $f_n/4$ harmonic. These differences of the interlocked modes between hydrofoils are attributed to the differing structural properties altering the natural structural response to cyclic excitations. The amplification due to the lock-in event at $\sigma = 0.4$ resulted in the largest C_N and $\delta/\bar{c}$ fluctuation observed in the experiments. These unique conditions also resulted in a π shift in phase between C_N and $\delta/\bar{c}$ linked to a reduced damping brought about from the increased cavity size allowing a greater portion of the hydrofoil to oscillate whilst exposed to a vapour cavity as opposed to liquid. Comparison of the forces, deflections and cavitation behaviour acting on the stiff and flexible hydrofoil shows significant FSI with flexibility leading to high frequency attenuation of the forces, frequency modulation, accelerated cavitation regime transition as well as multiple lock-in modes. These observations has allowed a deeper understanding to be developed of how induced deformations alter the cavitation behaviour about a flexible hydrofoil that can contribute significantly to this field of research.

5.2 Future Work

To gain further insight into the unsteady loading experienced by a hydrofoil immersed in a turbulent boundary layer it is recommend that both further experimental investigations and numerical simulations be conducted. Surface pressure measurements along the chord and span of the hydrofoil would provide valuable insight into how the pressure fluctuations vary across the hydrofoil and how these translate into the overall force fluctuations. This surface pressure data would be well complimented by turbulence spectra measurements of the encountered artificially thickened boundary layer, which would aid the understanding of how the boundary turbulence translate into the spectral content

of the loading. Numerical simulations utilizing sophisticated CFD modeling techniques, such as LES, would provide valuable insight into the flow physics involved, particularly the interaction of the encountered and hydrofoil boundary layers. Surface pressure and boundary layer turbulence measurements from the experiments would also serve as valuable validation data for the numerical simulations.

A current limitation in the experimental capabilities at the Cavitation Research Laboratory in measuring the unsteady loads on a hydrofoil is the resolvable frequency range of the coupled hydrofoil - force balance system. The dynamic force balance utilized in the *'Steady and unsteady loading on a hydrofoil immersed in a turbulent boundary layer'* experiments was developed to overcome the resolvable frequency limitations of the static force balance. Due to design constraints to ensure the dynamic force balance was compatible with the facilities model hydrofoil inventory, improvements to the dynamic response of the coupled system were limited with contamination still evident in the spectra. Development of a force balance and hydrofoil configuration without previous limitations while exploiting advanced materials technology and manufacturing techniques would allow a significant increase in the resolvable frequency range. This would provide further insight into the previously contaminated roll-off region of the spectra, an interest due to the scarcity of data in this region.

Similarly, further understanding of the experimental observations on the cloud cavitation about a hydrofoil could be gained by complementary numerical simulations. While there have been significant recent advancements in the capabilities of CFD to simulate cavitation, this topic is still a challenging one, particularly in the prediction of cloud cavitation and the associated shedding mechanisms. With the stiff hydrofoil experimental results presented here providing a valuable source of validation data, models (both analytical and numerical) can be developed further.

Bibliography

D. T. Akcabay and Y. L. Young. Influence of cavitation on the hydroelastic stability of hydrofoils. Journal of Fluids and Structures, 49:170–185, 2014. ISSN 0889-9746.

D. T. Akcabay and Y. L. Young. Parametric excitations and lock-in of flexible hydrofoils in two-phase flows. Journal of Fluids and Structures, 57:344–356, 2015. ISSN 0889-9746.

D. T. Akcabay, E. J. Chae, Y. L. Young, A. Ducoin, and J. A. Astolfi. Cavity induced vibration of flexible hydrofoils. Journal of Fluids and Structures, 49(Supplement C): 463–484, 2014. ISSN 0889-9746.

S. Alamshah, A. Zander, and V. Lenchine. Development of a technique to minimise the wind-induced noise in shielded microphones. In Proceedings of Acoustics 2013, Victor Harbour, Australia, November 2013. Australian Acoustical Society.

N. Alin, R. E. Bensow, C. Fureby, T. Huuva, and U. Svennberg. Current capabilities of DES and LES for submarines at straight course. Journal of Ship Research, 54(3): 184–196, 2010.

R. E. Arndt and A. Keller. A case study of international cooperation: 30 years of collaboration in cavitation research. In ASME/JSME 2003 4th Joint Fluids Summer Engineering Conference, pages 153–166. American Society of Mechanical Engineers, 2003.

Y. Ashkenazi, I. Gol'fman, L. Rezhkov, and N. Sidorov. Glass-Fiber-Reinforced plastic parts in ship machinery. Leningard: Sudostroyenniye Publishing House, 1974.

H. M. Atassi. The Sears problem for a lifting airfoil revisited - new results. Journal of Fluid Mechanics, 141:109–122, 1984.

P. Ausoni, M. Farhat, F. Avellan, X. Escaler, and E. Egusquiza. Cavitation effects on fluid structure interaction in the case of a 2d hydrofoil. In ASME 2005 Fluids Engineering Division Summer Meeting, pages 617–622. American Society of Mechanical Engineers, 2005.

P. Ausoni, M. Farhat, X. Escaler, E. Egusquiza, and F. Avellan. Cavitation influence on von Karman vortex shedding and induced hydrofoil vibrations. ASME J. Fluids Eng., 129(8):966–973, 2007. ISSN 0098-2202.

F. Avellan, P. Dupont, and I. L. Ryhming. Generation mechanism and dynamics of cavitation vortices downstream of a fixed leading edge cavity. In 17th Symposium on Naval Hydrodynamics, pages 1–13. National Academy Press, 1988.

M. Awasthi, J. Rowlands, D. Moreau, and C. Doolan. The effect of aspect ratio on wall pressure fluctuations at a wing-plate junction. Journal of Fluids Engineering, 2020. ISSN 0098-2202.

S. Bailey, M. Hultmark, J. P. Monty, P. H. Alfredsson, M. S. Chong, R. Duncan, J. H. Fransson, N. Hutchins, I. Marusic, B. J. McKeon, et al. Obtaining accurate mean velocity measurements in high Reynolds number turbulent boundary layers using pitot tubes. Journal of Fluid Mechanics, 715:642–670, 2013.

M. Baragona, H. Bijl, and M. Van Tooren. Bubble bursting and laminar separation unsteadiness on a multi-element high lift configuration. Flow, Turbulence and Combustion, 71(1-4):279–296, 2003.

A. Belle, P. A. Brandner, B. W. Pearce, K. L. de Graaf, and D. B. Clarke. Artificial thickening and thinning of cavitation tunnel boundary layers. Experimental Thermal and Fluid Science, 78:75–89, 2016.

R. L. Bisplinghoff, H. Ashley, and R. L. Halfman. Aeroelasticity. Courier Corporation, 2013.

R. D. Blevins. Flow-induced vibration. Van Nostrand Reinhold Co., New York, 1977.

R. D. Blevins. Formulas for natural frequency and mode shape. Van Nostrand Reinhold Co., New York, 1979.

P. A. Brandner. Microbubbles and cavitation: Microscales to macroscales. In Keynote Lecture: Tenth International Symposium on Cavitation, pages 710–715. ASME Press, 2018.

P. A. Brandner, Y. Lecoffre, and G. J. Walker. Design considerations in the development of a modern cavitation tunnel. In 16th Australasian Fluid Mechanics Conference, pages 630–637. School of Engineering, University of Queensland, 2007.

P. A. Brandner, G. J. Walker, P. N. Niekamp, and B. Anderson. An experimental investigation of cloud cavitation about a sphere. Journal of Fluid Mechanics, 656:147–176, 2010.

C. E. Brennen. The dynamic balances of dissolved air and heat in natural cavity flows. Journal of Fluid Mechanics, 37(1):115–127, 1969. ISSN 1469-7645.

C. E. Brennen. Cavitation and Bubble Dynamics. Oxford University Press, 1995.

C. E. Brennen. Fundamentals of Multiphase Flow. Cambridge University Press, 2005.

C. E. Brennen, K. T. Oey, and B. C. D. Leading-edge flutter of supercavitating hydrofoils. Journal of Ship Research, 24(3):135–146, 1980.

M. Callenaere, J. Franc, J. Michel, and M. Riondet. The cavitation instability induced by the development of a re-entrant jet. Journal of Fluid Mechanics, 444:223–256, 2001. ISSN 1469-7645.

S. L. Ceccio. Mechanisms of sheet to cloud transition for partial cavities. In Keynote Lecture in CAV 2015: 9th International Symposium on Cavitation, 2015.

D. B. Clarke and D. Butler. Private Communication, 2019.

D. B. Clarke, D. Butler, B. Crowley, and P. A. Brandner. High-speed full-field deflection measurements on a hydrofoil using digital image correlation. In 30th Symposium on Naval Hydrodynamics. Office of Naval Research, 2014.

A. Crespo. Sound and shock waves in liquids containing bubbles. The Physics of Fluids, 12(11):2274–2282, 1969.

K. L. de Graaf, P. A. Brandner, and B. W. Pearce. Spectral content of cloud cavitation about a sphere. Journal of Fluid Mechanics, 812(R1), 2017. ISSN 0022-1120.

O. De La Torre, X. Escaler, E. Egusquiza, and M. Farhat. Experimental investigation of added mass effects on a hydrofoil under cavitation conditions. Journal of Fluids and Structures, 39:173–187, 2013.

D. F. De Lange and G. J. De Bruin. Sheet cavitation and cloud cavitation, re-entrant jet and three-dimensionality. Applied Scientific Research, 58(1-4):91–114, 1998. ISSN 0003-6994.

J. C. Del Álamo and J. Jiménez. Estimation of turbulent convection velocities and corrections to taylor's approximation. Journal of Fluid Mechanics, 640:5–26, 2009.

P. Devinant, T. Laverne, and J. Hureau. Experimental study of wind-turbine airfoil aerodynamics in high turbulence. Journal of Wind Engineering and Industrial Aerodynamics, 90(6):689–707, 2002.

A. Ducoin and Y. L. Young. Hydroelastic response and stability of a hydrofoil in viscous flow. Journal of Fluids and Structures, 38:40–57, 2013.

A. Ducoin, J. A. Astolfi, and M. Gobert. An experimental study of boundary-layer transition induced vibrations on a hydrofoil. Journal of Fluids and Structures, 32: 37–51, 2012a.

A. Ducoin, J. A. Astolfi, and J. Sigrist. An experimental analysis of fluid structure interaction on a flexible hydrofoil in various flow regimes including cavitating flow. European Journal of Mechanics-B/Fluids, 36:63–74, 2012b. ISSN 0997-7546.

E. J. Foeth, C. W. H. Van Doorne, T. Van Terwisga, and B. Wieneke. Time resolved PIV and flow visualization of 3d sheet cavitation. Experiments in Fluids, 40(4):503–513, 2006. ISSN 0723-4864.

J. Franc. Partial cavity instabilities and re-entrant jet. In Keynote Lecture: Fourth International Symposium on Cavitation. California Institute of Technology, 2001.

J. Franc and J. Michel. Fundamentals of Cavitation. Kluwer Academic Publishers, Dordrecht, 2004.

R. A. Furness and S. P. Hutton. Experimental and theoretical studies of two-dimensional fixed-type cavities. Trans. ASME J. Fluids Engng, 97:515–521, 1975.

H. Ganesh, S. A. Mäkiharju, and S. L. Ceccio. Bubbly shock propagation as a mechanism for sheet-to-cloud transition of partial cavities. Journal of Fluid Mechanics, 802:37–78, 2016. ISSN 0022-1120.

S. A. Glegg and W. Devenport. Unsteady loading on an airfoil of arbitrary thickness. Journal of Sound and Vibration, 319(3-5):1252–1270, 2009.

M. E. Goldstein and H. Atassi. A complete second-order theory for the unsteady flow about an airfoil due to a periodic gust. Journal of Fluid Mechanics, 74(4):741–765, 1976.

R. J. Goldstein. Fluid Mechanics Measurements. Taylor & Francis, Philadelphia, PA, 2nd edition, 1996.

J. Guo, P. Y. Julien, and R. N. Meroney. Modified log-wake law for zero-pressure-gradient turbulent boundary layers. Journal of Hydraulic Research, 43(4):421–430, 2005.

R. J. Hakkinen and A. Richardson Jr. Theoretical and experimental investigation of random gust loads part I: Aerodynamic transfer function of a simple wing configuration in incompressible flow. Technical report, National Advisory Commitee for Aeronautics, 1957.

P. E. Hancock and P. Bradshaw. The effect of free-stream turbulence on turbulent boundary layers. Journal of Fluids Engineering, 105(3):284–289, 1983. ISSN 0098-2202.

K. Hansen, R. Kelso, A. Choudhry, and M. Arjomandi. Laminar separation bubble effect on the lift curve slope of an airfoil. In H. Chowdhury and F. Alam, editors, 19th Australasian Fluid Mechanics Conference. RMIT University, 2014.

C. Harwood, M. Felli, M. Falchi, N. Garg, S. L. Ceccio, and Y. L. Young. The hydroelastic response of a surface-piercing hydrofoil in multi-phase flow. Part 1. Passive hydroelasticity. Journal of Fluids Mechanics, 881:313–364, 2019.

C. Harwood, M. Felli, M. Falchi, N. Garg, S. L. Ceccio, and Y. L. Young. The hydroelastic response of a surface-piercing hydrofoil in multiphase flows. Part 2. Modal parameters and generalized fluid forces. Journal of Fluid Mechanics, 884(A3), 2020.

S. F. Hoerner and H. V. Borst. Fluid-dynamic lift: practical information on aerodynamic and hydrodynamic lift. Hoerner Fluid Mechanics, Brick Town, NJ, 1985.

J. Hoffmann and S. Kassir. Effects of free-stream turbulence on turbulent boundary layers with mild adverse pressure gradients. AIAA Journal, pages 88–3757, 1988.

J. A. Hoffmann. Effects of freestream turbulence on the performance characteristics of an airfoil. AIAA Journal, 29(9):1353–1354, 1991.

M. Howe. Unsteady lift and sound produced by an airfoil in a turbulent boundary layer. Journal of fluids and structures, 15(2):207–225, 2001.

M. S. Howe. Unsteady lift produced by a streamwise vortex impinging on an airfoil. Journal of Fluids and Structures, 16(6):761–772, 2002.

R. F. Huang and H. W. Lee. Effects of freestream turbulence on wing-surface flow and aerodynamic performance. Journal of Aircraft, 36(6):965–972, 1999. ISSN 0021-8669.

N. Hutchins and I. Marusic. Evidence of very long meandering features in the logarithmic region of turbulent boundary layers. Journal of Fluid Mechanics, 2007.

A. Ihara, H. Watanabe, and S. Shizukuishi. Experimental research of the effects of sweep on unsteady hydrofoil loadings in cavitation. ASME J. Fluids Eng., 111(3):263–270, 1989. ISSN 0098-2202.

R. Jackson, J. M. R. Graham, and D. J. Maull. The lift on a wing in a turbulent flow. The Aeronautical Quarterly, 24(3):155–166, 1973.

J. K. Jakobsen. On the mechanism of head breakdown in cavitating inducers. Journal of Basic Engineering, 86(2):291–305, 1964. ISSN 0021-9223.

M. Jones, N. Nishizawa, and M. Chong. Experimental study of high Reynolds number turbulent boundary layers-mean flow scaling. In 14th Australasian Fluid Mechanics Conference, Adelaide, Australia, pages 211–214, 2001.

P. Kaplan and A. F. Lehman. Experimental studies of hydroelastic instabilities of cavitating hydrofoils. Journal of Aircraft, 3(3):262–269, 1966.

K. Kato, H. Dan, and Y. Matsudaira. Lock-in phenomenon of pitching hydrofoil with cavitation breakdown. JSME International Journal Series B Fluids and Thermal Engineering, 49(3):797–805, 2006.

D. T. Kawakami, A. Fuji, Y. Tsujimoto, and R. E. Arndt. An assessment of the influence of environmental factors on cavitation instabilities. ASME J. Fluids Eng., 130(3):031303, 2008. ISSN 0098-2202.

Y. Kawanami, H. Kato, H. Yamaguchi, M. Tanimura, and Y. Tagaya. Mechanism and control of cloud cavitation. ASME J. Fluids Eng., 119(4):788–794, 1997. ISSN 0098-2202.

Y. Kawanami, H. Kato, and H. Yamaguchi. Three-dimensional characteristics of the cavities formed on a two-dimensional hydrofoil. In Third International Symposium on Cavitation, volume 1, pages 191–196. Laboratoire des Ecoulements Géophysiques et Industriels, Grenoble, France, 1998.

M. Khoo, P. Brandner, B. Pearce, D. Clarke, D. Butler, and A. Belle. An Australian capability for submarine control surface performance evaluation. In Mast Asia Conference 2015, pages 1–19, 2015.

T. M. Kirk and S. Yarusevych. Vortex shedding within laminar separation bubbles forming over an airfoil. Experiments in Fluids, 58(5):43, 2017.

M. Kjeldsen and R. E. Arndt. Joint time frequency analysis techniques: A study of transitional dynamics in sheet/cloud cavitation. In 4th International Symposium on Cavitation (CAV2001). California Institute of Technology, 2001.

M. Kjeldsen, R. E. A. Arndt, and M. Effertz. Spectral characteristics of sheet/cloud cavitation. Trans. ASME J. Fluids Engng, 122(3):481–487, 2000.

R. T. Knapp. Recent investigations of the mechanics of cavitation and cavitation damage. Transactions of the ASME, 77:1045–1054, 1955.

A. Kubota, H. Kato, H. Yamaguchi, and M. Maeda. Unsteady structure measurement of cloud cavitation on a foil section using conditional sampling technique. ASME J. Fluids Eng., 111(2):204–210, 1989. ISSN 0098-2202.

K. R. Laberteaux and S. L. Ceccio. Partial cavity flows. Part 1: Cavities forming on models without spanwise variation. Journal of Fluid Mechanics, 431:1–41, 2001a. ISSN 1469-7645.

K. R. Laberteaux and S. L. Ceccio. Partial cavity flows. Part 2. Cavities forming on test objects with spanwise variation. Journal of Fluid Mechanics, 431:43–63, 2001b. ISSN 1469-7645.

P. Lamson. Measurements of lift fluctuations due to turbulence. Thesis, California Institute of Technology, 1956.

Q. Le, J. Franc, and J. Michel. Partial cavities: Global behaviour and mean pressure distribution. ASME J. Fluids Eng., 115:243–243, 1993. ISSN 0098-2202.

J. Leroux, J. A. Astolfi, and J. Y. Billard. An experimental study of unsteady partial cavitation. ASME J. Fluids Eng., 126(1):94–101, 2004.

J. Leroux, O. Coutier-Delgosha, and J. Astolfi. A joint experimental and numerical study of mechanisms associated to instability of partial cavitation on two-dimensional hydrofoil. Physics of Fluids, 17(5):052101, 2005.

M. Li, Y. Yang, M. Li, and H. Liao. Direct measurement of the sears function in turbulent flow. Journal of Fluid Mechanics, 847:768–785, 2018.

S. Li, S. Wang, J. Wang, and J. Mi. Effect of turbulence intensity on airfoil flow: Numerical simulations and experimental measurements. Applied Mathematics and Mechanics, 32: 1029–1038, 2011. ISSN 0253-4827.

Y. Liao, J. R. Martins, and Y. L. Young. Sweep and anisotropy effects on the viscous hydroelastic response of composite hydrofoils. Composite Structures, 230:111471, 2019.

P. B. S. Lissaman. Low-Reynolds-number airfoils. Annual Review of Fluid Mechanics, 15 (1):223–239, 1983.

P. D. Lysak. Unsteady lift of thick airfoils in incompressible turbulent flow. Thesis, Penn State University, 2011.

P. D. Lysak, D. E. Capone, and M. L. Jonson. Prediction of high frequency gust response with airfoil thickness effects. Journal of Fluids and Structures, 39:258–274, 2013.

P. D. Lysak, D. E. Capone, and M. L. Jonson. Measurement of the unsteady lift of thick airfoils in incompressible turbulent flow. Journal of Fluids and Structures, 66:315–330, 2016.

O. Mack. A new calibration method with static loads for piezoelectric force transducers. In XVIII IMEKO WORLD CONGRESS, Metrology for a Sustainable Development, Rio de Janeiro, Brazil, 2006.

E. Mayda, C. Van Dam, and E. P. Duque. Bubble induced unsteadiness on wind turbine airfoils. In ASME 2002 Wind Energy Symposium, pages 115–125. American Society of Mechanical Engineers, 2002.

B. McKeon, J. Li, W. Jiang, J. Morrison, and A. Smits. Pitot probe corrections in fully developed turbulent pipe flow. Measurement Science and Technology, 14(8):1449, 2003.

P. J. McKeough and J. M. R. Graham. Effect of mean loading on the fluctuating loads induced on aerofoils by a turbulent stream. Aeronautical Quarterly, 31(Feb):56–69, 1980.

P. F. Mish and W. J. Devenport. An experimental investigation of unsteady surface pressure on an airfoil in turbulence - Part 1: Effects of mean loading. Journal of Sound and Vibration, 296(3):417–446, 2006a.

P. F. Mish and W. J. Devenport. An experimental investigation of unsteady surface pressure on an airfoil in turbulence — Part 2: Sources and prediction of mean loading effects. Journal of Sound and Vibration, 296(3):447–460, 2006b.

M. R. Motley, Z. Liu, and Y. L. Young. Utilizing fluid–structure interactions to improve energy efficiency of composite marine propellers in spatially varying wake. Composite Structures, 90(3):304–313, 2009. ISSN 0263-8223.

A. P. Mouritz, E. Gellert, P. Burchill, and K. Challis. Review of advanced composite structures for naval ships and submarines. Composite Structures, 53(1):21–42, 2001.

H. M. Nagib, K. A. Chauhan, and P. A. Monkewitz. Approach to an asymptotic state for zero pressure gradient turbulent boundary layers. Philosophical Transactions of the Royal Society A: Mathematical, Physical and Engineering Sciences, 365(1852):755–770, 2007.

L. Noordzij and L. Van Wijngaarden. Relaxation effects, caused by relative motion, on shock waves in gas-bubble/liquid mixtures. Journal of Fluid Mechanics, 66(1):115–143, 1974.

B. W. Pearce, P. A. Brandner, N. Garg, Y. L. Young, A. W. Phillips, and D. B. Clarke. The influence of bend-twist coupling on the dynamic response of cavitating composite hydrofoils. In 5th International Symposium on Marine Propulsors (SMP'17), pages 803–813. VTT Technical Research Centre of Finland, 2017.

P. F. Pelz, T. Keil, and T. F. Groß. The transition from sheet to cloud cavitation. Journal of Fluid Mechanics, 817:439–454, 2017. ISSN 0022-1120.

T. M. Pham, F. Larrarte, and D. H. Fruman. Investigation of unsteady sheet cavitation and cloud cavitation mechanisms. ASME J. Fluids Eng., 121(2):289–296, 1999. ISSN 0098-2202.

A. W. Phillips, R. Cairns, C. Davis, P. Norman, P. A. Brandner, B. W. Pearce, and Y. Young. Effect of material design parameters on the forced vibration response of composite hydrofoils in air and in water. In Fifth International Symposium on Marine Propulsors, pages 813–822, 2017.

S. Prothin, J. Billard, and H. Djeridi. Image processing using proper orthogonal and dynamic mode decompositions for the study of cavitation developing on a NACA0015 foil. Experiments in Fluids, 57(10):157, 2016. ISSN 0723-4864.

R. Reba and E. Kerschen. Influence of airfoil angle of attack on unsteady pressure distributions due to high-frequency gust interactions. Technical report, NASA Langley Research Center, 1996.

G. E. Reisman, Y. C. Wang, and C. E. Brennen. Observations of shock waves in cloud cavitation. Journal of Fluid Mechanics, 355:255–283, 1998.

P. S. Russell, J. A. Venning, P. A. Brandner, B. W. Pearce, D. R. Giosio, and S. L. Ceccio. Microbubble disperse flow about a lifting surface. In 32nd Symposium on Naval Hydrodynamics, 2018.

A. Samson and S. Sarkar. Effects of free-stream turbulence on transition of a separated boundary layer over the leading-edge of a constant thickness airfoil. Journal of Fluids Engineering, 138(2):021202, 2016. ISSN 0098-2202.

O. T. Schmidt, A. Towne, G. Rigas, T. Colonius, and G. A. Bres. Spectral analysis of jet turbulence. Journal of Fluid Mechanics, 855:953–982, 2018.

W. R. Sears. Some aspects of non-stationary airfoil theory and its practical application. Journal of the Aeronautical Sciences, 8(3):104–108, 1941.

H. Shamsborhan, O. Coutier-Delgosha, G. Caignaert, and F. A. Nour. Experimental determination of the speed of sound in cavitating flows. Experiments in Fluids, 49(6): 1359–1373, 2010. ISSN 0723-4864.

S. M. Smith, J. A. Venning, D. R. Giosio, P. A. Brandner, B. W. Pearce, and Y. L. Young. Cloud cavitation behaviour on a hydrofoil due to fluid-structure interaction. In 17th International Symposium on Transport Phenomena and Dynamics of Rotating Machinery, ISROMAC 2017, 2017.

S. M. Smith, J. A. Venning, P. A. Brandner, B. W. Pearce, D. R. Giosio, and Y. L. Young. The influence of fluid-structure interaction on cloud cavitation about a hydrofoil. In Proceedings of the 10th International Symposium on Cavitation (CAV2018). ASME Press, 2018. ISBN 0791861856.

S. M. Smith, J. A. Venning, D. R. Giosio, P. A. Brandner, B. W. Pearce, and Y. L. Young. Cloud cavitation behaviour on a hydrofoil due to fluid-structure interaction. Trans. ASME J. Fluids Engng, 141(4):041105, 2019.

S. M. Smith, J. A. Venning, B. W. Pearce, Y. L. Young, and P. A. Brandner. The influence of fluid-structure interaction on cloud cavitation about a stiff hydrofoil. Part 1. Journal of Fluid Mechanics, 896(A1), 2020.

A. J. Smits, B. J. McKeon, and I. Marusic. High-Reynolds number wall turbulence. Annual Review of Fluid Mechanics, 43:353–375, 2011.

B. Stutz and J. L. Reboud. Experiments on unsteady cavitation. Experiments in Fluids, 22(3):191–198, 1997. ISSN 0723-4864.

K. E. Swalwell, J. Sheridan, W. Melbourne, et al. The effect of turbulence intensity on stall of the NACA0021 aerofoil. In 14th Australasian Fluid Mechanics Conference, 2001.

T. Theodorsen. General theory of aerodynamic instability and the mechanism of flutter. Report, NACA Technical Report No. 496, 1935.

W. A. Timmer. Two-dimensional low-reynolds number wind tunnel results for airfoil naca 0018. Wind Engineering, 32(6):525–537, 2008.

C. Torrence and G. P. Compo. A practical guide to wavelet analysis. Bulletin of the American Meteorological Society, 79(1):61–78, 1998. ISSN 1520-0477.

A. Towne, O. T. Schmidt, and T. Colonius. Spectral Proper Orthogonal Decomposition and its relationship to dynamic mode decomposition and resolvent analysis. Journal of Fluid Mechanics, 847:821–867, 2018. ISSN 0022-1120.

S. R. Turnock and A. M. Wright. Directly coupled fluid structural model of a ship rudder behind a propeller. Marine Structures, 13(1):53–72, 2000. ISSN 0951-8339.

J. A. Venning, S. M. Smith, P. A. Brandner, D. R. Giosio, and B. W. Pearce. The influence of nuclei content on cloud cavitation about a hydrofoil. In 17th International Symposium on Transport Phenomena and Dynamics of Rotating Machinery, ISROMAC 2017, 2017.

J. A. Venning, D. R. Giosio, B. W. Pearce, and P. A. Brandner. Global mode visualization in cavitating flows. In Proceedings of the 10th International Symposium on Cavitation (CAV2018). ASME Press, 2018a.

J. A. Venning, D. R. Giosio, B. W. Smith, Samuel M Pearce, and P. A. Brandner. The influence of nucleation on the spectral content of cloud cavitation about a hydrofoil. In Proceedings of the 10th International Symposium on Cavitation (CAV2018). ASME Press, 2018b.

J. A. Venning, M. T. Khoo, B. W. Pearce, and P. A. Brandner. Background nuclei measurements and implications for cavitation inception in hydrodynamic test facilities. Experiments in Fluids, 59(4):71, 2018c.

T. von Kármán and W. Sears. Airfoil theory for non-uniform motion. Journal of the Aeronautical Sciences, 5(10):379–390, 1938.

S. Wang, Y. Zhou, M. M. Alam, and H. Yang. Turbulent intensity and Reynolds number effects on an airfoil at low Reynolds numbers. Physics of Fluids, 26(11):25, 2014.

P. Welch. The use of fast fourier transform for the estimation of power spectra: A method based on time averaging over short, modified periodograms. IEEE Transactions on Audio and Electroacoustics, 15(2):70–73, 1967. ISSN 0018-9278.

J. Wu, H. Ganesh, and S. Ceccio. Multimodal partial cavity shedding on a two-dimensional hydrofoil and its relation to the presence of bubbly shocks. Experiments in Fluids, 60 (4):66, 2019.

Q. Wu, B. Huang, G. Wang, and Y. Gao. Experimental and numerical investigation of hydroelastic response of a flexible hydrofoil in cavitating flow. International Journal of Multiphase Flow, 74:19–33, 2015. ISSN 0301-9322.

S. Yarusevych, P. E. Sullivan, and J. G. Kawall. On vortex shedding from an airfoil in low-Reynolds-number flows. Journal of Fluid Mechanics, 632:245, 2009.

Y. L. Young. Time-dependent hydroelastic analysis of cavitating propulsors. Journal of Fluids and Structures, 23(2):269–295, 2007. ISSN 0889-9746.

Y. L. Young. Fluid–structure interaction analysis of flexible composite marine propellers. Journal of Fluids and Structures, 24(6):799–818, 2008. ISSN 0889-9746.

Y. L. Young, M. Motley, R. Barber, E. J. Chae, and N. G. Garg. Adaptive composite marine propulsors and turbines: Progress and challenges. Applied Mechanics Review, 68(6), 2016.

Y. L. Young, C. M. Harwood, F. M. Montero, J. C. Ward, and S. L. Ceccio. Ventilation of lifting bodies: Review of the physics and discussion of scaling effects. Applied Mechanics Reviews, 69(1):010801, 2017.

Y. L. Young, N. Garg, P. A. Brandner, B. W. Pearce, D. Butler, D. Clarke, and A. W. Phillips. Material bend-twist coupling effects on cavitating response of composite hydrofoils. In 10th International Cavitation Symposium (CAV2018). ASME Press, 2018a.

Y. L. Young, N. Garg, P. A. Brandner, B. W. Pearce, D. Butler, D. Clarke, and A. W. Phillips. Load-dependent bend-twist coupling effects on the steady-state hydroelastic response of composite hydrofoils. Composite Structures, 189:398–418, 2018b.

G. A. Zarruk, P. A. Brandner, B. W. Pearce, and A. W. Phillips. Experimental study of the steady fluid-structure interaction of flexible hydrofoils. Journal of Fluids and Structures, 51:326–343, 2014.

Appendices

Appendix A

Steady and Unsteady loads acting on a hydrofoil immersed in a turbulent boundary layer

This paper was presented at the (peer-reviewed) 20^{th} *Australasian Fluid Mechanics Conference*, Perth, Australia, 5-8 December, 2016.

The citation for the conference paper is:

Smith, S. M., Brandner, Pearce, B. W., P. A., Venning, J. A., Moreau, D. J. and Clarke, D. B. (2016). Steady and Unsteady loads acting on a hydrofoil immersed in a turbulent boundary layer. In *20th Australasian Fluid Mechanics Conference* (paper no. 588).

20th Australasian Fluid Mechanics Conference
Perth, Australia
5-8 December 2016

Steady and unsteady loads acting on a hydrofoil immersed in a turbulent boundary layer

S. M. Smith[1], B. W. Pearce[1], P. A. Brandner[1], D. B. Clarke[2], D. J. Moreau[3] and Y. Xue[1]

[1]Australian Maritime College
University of Tasmania, Launceston, Tasmania 7250, Australia
[2] Maritime Division
Defence Science and Technology Group, Fishermans Bend, Victoria 3207, Australia
[3]School of Mechanical and Manufacturing Engineering
University of New South Wales, Sydney, New South Wales 2052, Australia

Abstract

This study investigated steady and unsteady loads acting on a hydrofoil immersed in a turbulent boundary layer. Measurements were performed in a cavitation tunnel in which the hydrofoil was mounted spanwise normal from the test section ceiling, via a 6-component force balance. The turbulent boundary layer was artificially thickened via an array of transverse jets located upstream of the test section. The effect of boundary layer thickness was investigated, in which various thicknesses were generated to allow partial or full immersion of two hydrofoils, each with different aspect ratios. The effect of varying incidence and Reynolds number on the hydrodynamic loading was also investigated. Steady forces were found to be significantly affected by the scale of the boundary layer, particularly in the stall region. Identification of a broad peak in the unsteady force spectra, was made at a constant reduced frequency of 0.2. The peak was dependent on boundary layer thickness and Reynolds number. Furthermore, a low frequency stall component, superimposed over the existing broadband excitation of the boundary layer turbulence, was apparent in the spectra past stall.

Introduction

Control surfaces for marine vessels are typically located at the stern, where the boundary layer has had the full vessel length to develop and thicken. As control surfaces are generally compact compared to overall length scales, they are at least partially immersed within the turbulent flow about the vessel stern. In addition, the boundary layer is further thickened or separated due to the adverse pressure gradient generated at the aft end of the vessel [1]. Hence, these control surfaces are subject to unsteady loading and become a source of vibration and noise. To minimise these effects, insight into the flow physics and excitation spectra are required. This would enable more rigorous analysis and design for optimisation of control surface structural response.

Despite extensive development of theoretical models [8] for the prediction of unsteady loads on a lifting surface, there is little experimental data available in literature. Previous investigations have involved aerofoils immersed in grid-generated turbulence with lift spectra measured directly or derived from surface pressure measurements [6, 7]. Although valuable for providing insight into associated phenomena, these results cannot be directly transferred to the structured wall bounded turbulent flow of a boundary layer.

This preliminary work aims to provide insights into the physics determining the loading of a hydrofoil encountering the structured turbulence of an oncoming boundary layer. Forces, both steady and unsteady, were obtained for a range of Reynolds numbers (*Re*), incidence (α) and boundary layer thicknesses (δ). Immersion of the hydrofoil span in the boundary layer was adjusted from about $^1/_8$ to the full span. Partial results were gained from a previous investigation [5] with the current work expanding from it where a greater range of parameters were examined, in particular, a range of δ. These results also provide additional guidance into the frequency response necessary from an improved force balance and model design for future unsteady measurements.

Experimental Overview

Model Hydrofoil Details

Hydrofoil geometry has been selected based on the requirements discussed above for the modelling of unsteady conditions typical of those experienced by control surfaces. The chosen geometry was a NACA 0012 profile with a symmetric (unswept) trapezoidal planform with a 80 mm tip and 120 mm root chord. Two models were constructed with spans of 120 mm and 240 mm. This achieved a wide range of oncoming boundary layer thickness to hydrofoil span ratios, from $^1/_8$, up to 1. The chord length was chosen to be compatible with mounting to the water tunnel test section and sufficient to obtain chord-based *Re* values of 1×10^6.

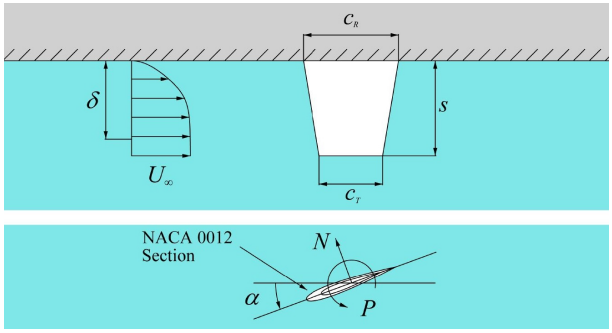

Figure 1: Schematic of the experimental setup whereby a ceiling mounted hydrofoil encounters a turbulent boundary layer that immerses it to varying degrees (top). A bottom view depicting the force balance coordinate system whose origin is located on the root mid-chord is also shown (bottom).

The response spectrum of both hydrofoils was determined from an impact test [5] with results summarized in Table 1. First mode natural frequencies were obtained in air at 536 Hz and 170 Hz, and in water at 273 and 86 Hz for the 120 mm and 240 mm models respectively. The in water values were calculated using an added mass estimate [3]. Both models were machined from solid Aluminium 6061-T6 billets to 0.8 μm surface finish and 0.1 mm surface tolerance. The models were anodised to a thickness of approximately 5μm.

Experimental Setup

Hydrofoil Dynamic Properties	Hydrofoil span	
	120 mm	240 mm
First bending mode in air (Hz)	536	170
First bending mode in water (Hz)	273	86
Second bending mode in air (Hz)	-	783
Second bending mode in water (Hz)	-	399
Added mass for first and second bending modes, $2m_a$(kg)	0.94	1.88
Mass of hydrofoil, m (kg)	0.33	0.60

Table 1: Natural frequencies, mass and added mass values of the model hydrofoils utilized in the experiment [3].

Measurements were carried out in the Cavitation Research Laboratory (CRL) water tunnel at the Australian Maritime College. The tunnel test section is 0.6 m square by 2.6 m long in which the operating velocity and pressure ranges are 2 to 12 m/s and 4 to 400 kPa absolute respectively. The tunnel volume is 365m^3 with demineralised water (conductivity of order 1μS/cm). The test section velocity is measured from one of two (high and low range) Siemens Sitransp differential pressure transducers models 7MF4433-1DA02-2AB1-Z and 7MF4433-1FA02-2AB1-Z (measuring the calibrated contraction differential pressure) with estimated precisions of 0.007 and 0.018 m/s respectively. A detailed description of the facility is given in [4].

A schematic representation of the test set-up is given in Figure 1 along with the definition of the coordinate system used and the main geometric parameters. The models were mounted on a 6-component force balance extending vertically into the flow through a 160 mm diameter penetration in the tunnel ceiling. The 160 mm diameter penetration was made fair (to 50μm) using a disk mounted, in this case, on the measurement side of the balance. The fairing disk has a typical 0.5 mm radial clearance to avoid interference with the force measurement. Of the total load vector measured, steady and unsteady components of normal force and pitching moment are presented. Spanwise forces and roll/yaw moments are not considered as they may be contaminated by the wall pressure distribution acting on the disk with this setup. Data was sampled at 1 kHz for durations sufficient to capture 1 000 and 22 000 chord passages ($= TU_\infty/c$ where T is the acquisition period, U_∞ is the freestream velocity and c is the mean chord) for steady and unsteady measurements respectively.

Measurements were made at a streamwise location 1.9 m downstream from the test section entrance to maximise hydrofoil immersion in the boundary layer. To obtain a test section ceiling boundary layer of the desired scale, it was artificially thickened via an array of cross flow jets located upstream of the test section. At the test location, δ was adjusted from its natural state of 33 mm, through to a maximum of 99 mm. δ was controlled by adjustment of the flow rate through the jet array. A detailed description and performance characteristics of the CRL boundary layer manipulator is given in [2]. Based on the performance of the plate geometries previously tested for boundary layer thickening, "Plate E" (68 $\times$ 10 mm holes triangularly spaced over 4 rows) was chosen for the present investigation. This was based on the resulting mean velocity profile of the artificial thickened boundary layer comparing most favourably with the natural profile, particularly in the outer (or wake) region [2]. This is important as the outer region is the largest portion of the boundary layer and is therefore seen as the most significant contributor to the production of unsteady forces.

The force balance was calibrated by a least squares fit between a basis vector loading cycle and the 6 outputs giving a 6×6 matrix. An estimated precision on all components is less than 0.1%. Forces were measured at mean chord-based Re values (mean chord, $c = (c_T + c_R)/2 = 0.1$m), of 0.2, 0.4, 0.6, 0.8 and 1.0×10^6. Each Re was run for a range of α, from $-1°$ to beyond stall at 25° and 20° for the 120 mm and 240 mm span hydrofoils respectively. α is adjusted using the balance automated indexing system incremented in 0.5° steps with an incremental precision less than 0.001°. The tunnel was pressurised up to 350 kPa to minimize cavitation occurrence.

Results

The measured normal force, N, and pitching moment, P, are presented as dimensionless coefficients, $C_N = 2N/(\rho U_\infty^2 A)$ and $C_P = 2P/(\rho U_\infty^2 Ac)$, respectively. U_∞ denotes the freestream velocity, ρ is the liquid density and A is the planform area. δ is where the boundary layer velocity, U, becomes equal to $0.99U_\infty$. Unsteady loads are presented using power spectral density (PSD) in a narrowband format with a frequency resolution of 1 Hz. Spectra have been calculated using Welchs averaged modified periodogram method of spectral estimation with a Hammimg window function and 50% overlap. The 95% confidence interval on the narrow band auto spectral density is $-0.3690/+0.3857$ N^{2}dB/Hz.

Steady Forces

Steady normal force and pitching moment coefficients for the thickest boundary layer (δ = 99 mm) at incremental Re are presented in Figure 2. The 240 mm span model exhibits an increased C_N slope ($\partial C_N/\partial\alpha$) and maximum C_N, as well as an earlier stall incidence. For both geometries, the α at which stall occurs increases with Re by about 6°.

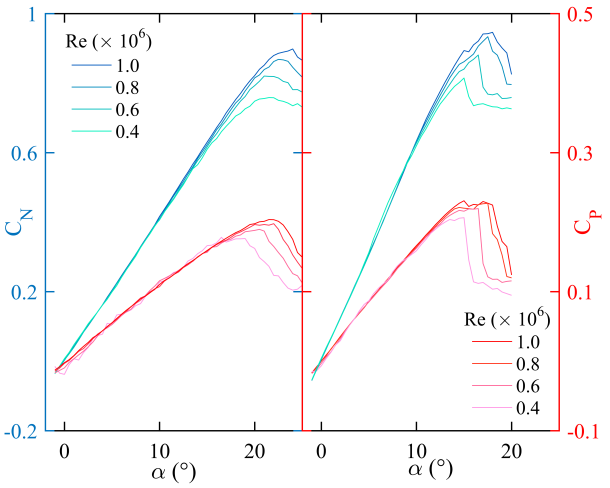

Figure 2: Normal force and pitching moment coefficients with incidence for 120 mm span (left) and 240 mm span (right) hydrofoil models. They were immersed in a turbulent boundary layer with $\delta = 99$ mm, for Re between 0.4×10^6 and 1.0×10^6.

A comparison of the normal force measured for the 120 mm span hydrofoil for 3 boundary layer thicknesses is presented in Figure 3. $\partial C_N/\partial\alpha$ is seen to decrease with an increase in δ as the hydrofoil becomes increasingly immersed in the lower velocity flow of the boundary layer. Initially, the effect is quite gradual with stall delayed by 1.5° as the foil submergence is increased, from about $1/3$, to $1/2$ of the span. This corresponds with an increase in maximum C_N of less than 1%. Increasing δ further to 99 mm (nominally fully immersing the hydrofoil within the boundary layer) sees a significant drop in max C_N to 0.868, along with a small decrease in stall angle. Notably in this condition, there is a significant change from a sudden, leading-

edge type, to a gradual, trailing-edge type, stall behaviour. This suggests that the boundary layer is having significant impact on the state of flow over the hydrofoil. The level of unsteadiness is presented using RMS of the steady measurements (C'_N), shown in Figure 3. The C'_N reveals a trend of increased fluctuation with boundary layer thickness for all pre-stall α. The significant increase in the C'_N with α in each condition, coincides with the onset of stall.

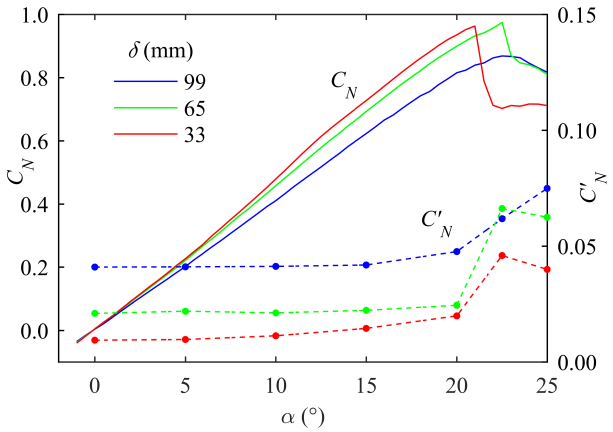

Figure 3: C_N and C'_N values with α for 120 mm hydrofoil model with $Re = 0.8 \times 10^6$ for several δ (All RMS results are derived from unsteady measurements except $\alpha = 5°, 10°, 20°$ and 25° for δ = 65 mm). Pre-stall normal forces are dependent on δ with higher RMS values for larger δ. Stall is delayed as δ increases with stall characteristics shifting from a sudden drop-off to a smooth transition.

Unsteady Forces

To allow characteristic properties to be identified, spectra have been obtained from time series of the normal force and presented non-dimensionally in the form of the power spectral density (PSD), with the excitation frequency (f) represented as reduced frequency ($f' = fc/U_\infty$). Due to space limitations, only results of the 120 mm span hydrofoil are presented. Peak frequencies are present in all spectra due to the frequency response of both the force balance and hydrofoil. Identified in a previous study [5], the first and second natural frequencies of the force balance is observed in Figure 4 to be around 150 and 180 Hz. The peak at around 310 Hz is attributable to the hydrofoil first mode natural frequency, close to the estimate of 273 Hz given in Table 1. Error in the estimation is potentially due to the simplification to a rectangular plate and a low aspect ratio planform being more susceptible to 3D effects. The additional peaks at 350 and 450 Hz is attributed to power line odd harmonics. Due to this inherent dynamic response from the coupled balance/hydrofoil system, the resolvable frequency range for the present measurements only extends out to about 100 Hz. This equates to a f' from 0.9 to 4.5 for Re of 1.0×10^6 and 0.2×10^6 respectively. An improved force balance and hydrofoil design, both resulting with increased natural frequencies, are being considered for a follow-on experimental campaign to extend the resolvable frequency range out to about 1 kHz.

Figure 5 shows the effect of Re on the PSD of C_N at $\alpha = 0°, 15°$ and 22.5° for the 120 mm span hydrofoil in a δ = 99 mm. In the lower frequency range ($f' < 0.3$), there is an increase in power with α for all Re. At $\alpha = 0°$ and 15°, the order of Re is sequential, with higher Re exhibiting greater power at $f' < 1$. This tendency does not continue at $\alpha = 22.5°$ with $Re \leq 0.8 \times 10^6$ exhibiting a different trend and jumping above higher Re spectra at approximately $0.02 < f' < 0.5$. This suggests a changeover with Re dependency after stall as at $Re \leq 0.8 \times 10^6$, the hydrofoil has stalled. This illustrates the addition of the stall phenomena, exhibiting a low frequency component (i.e. relatively large wake structures), to the existing effect of the boundary layer turbulence on the unsteady forces.

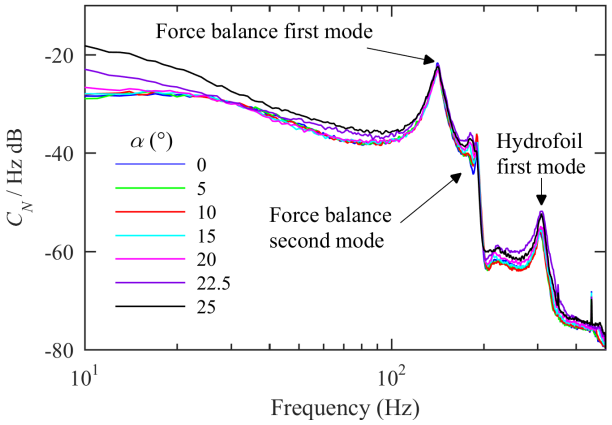

Figure 4: PSD function of C_N for 120 mm span hydrofoil with δ = 99 mm and $Re = 0.8 \times 10^6$ for various α. Contamination caused by the excitation of the force balance and model natural frequencies can easily be seen. The systems inherent dynamic response permits a resolvable frequency range up to approximately 100 Hz.

In Figure 5, a broad peak is clearly observed in all spectra for $\alpha = 0°$ at about $f' = 0.2$. The peak starts to become lost $\alpha = 15°$ with the relative broadband increase in power at $f' < 0.2$ and the peaks magnitude seemingly unaffected by the increased α .This trend continues as the peak becomes even harder to distinguish at $\alpha = 22.5°$. With the peak consistently occurring at approximately $f' = 0.2$, implies that the advection of the flow disturbance causing the unsteady force is about 1/5 of the free-stream advection speed. Furthermore, the peak appears unaffected by α, suggesting it is due to another factor.

The effect of increasing boundary layer thickness on the 120 mm span hydrofoil power spectra at various α is shown in Figure 6. As also seen in Figure 6, for $f' < 1$, there is a broadband power rise with an increase in δ for all α below stall. The broadband peak at $f' \approx 0.2$ discussed previously, is also evident in Figure 6. Furthermore, there is a noticeable increase in the relative amplitude of this peak with increasing δ for pre-stall incidences ($\alpha = 0°$ and 15°). This is attributed to the increased hydrofoil immersion in the boundary layer, resulting in greater exposure to the structured turbulence and therefor, a rise in the unsteady forces. This is in contrast to the steady normal force component decreasing with increasing δ shown in Figure 3.

At $\alpha = 15°$ in Figure 6, a significant rise in power is observed at $f' = 0.02$ for $\delta = 33$ mm and 65 mm, but not for $\delta = 99$ mm. This trait is also evident at $\alpha = 22.5°$ for $\delta = 65$ mm, but not at $\delta = 99$ mm and 33 mm, both of which have stalled. This change in trend at the lowest frequency cannot be attributed to an artefact of the processing method used. At this point, there is also no explanation in terms of the flow physics. This aspect will be further looked at in future more detailed investigations.

Conclusions

Effects of boundary layer thickness on steady and unsteady loads acting on a hydrofoil were investigated in a water tunnel. Steady forces of a hydrofoil experiencing a thicker bound-

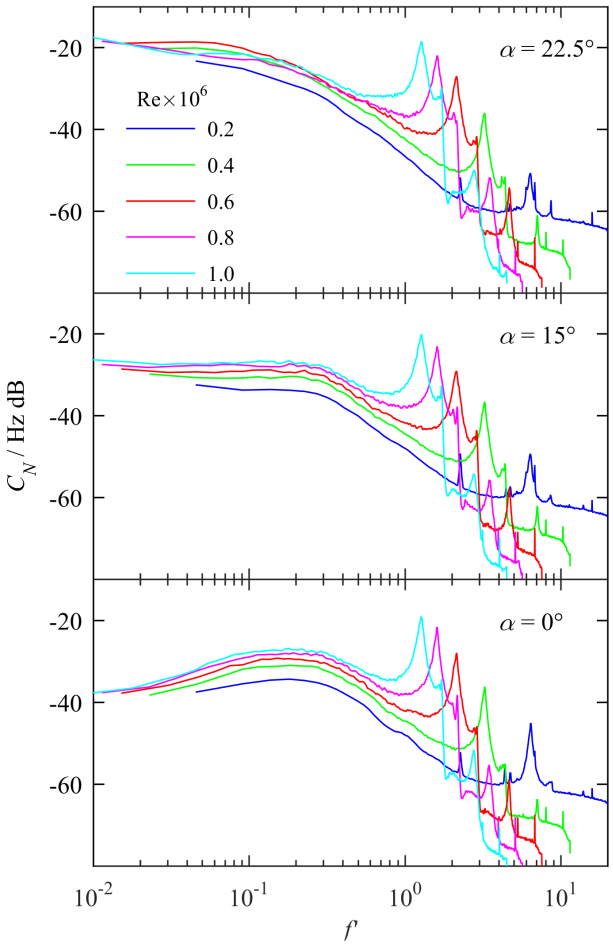

Figure 5: C_N power spectra of the 120 mm span hydrofoil at δ = 99 mm and various *Re* for α = 0° (bottom), 15° (middle) and 22.5° (top).

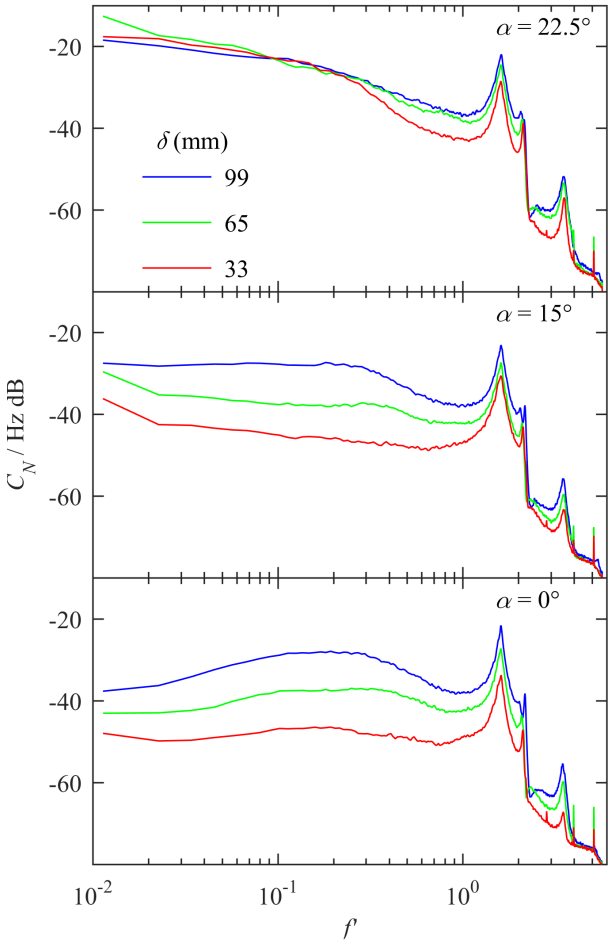

Figure 6: The effect of δ on the relationship between α and C_N spectra of the 120 mm span hydrofoil at $Re = 0.8 \times 10^6$ for α = 0° (bottom), 15° (middle) and 22.5° (top).

ary layer saw reductions in $\partial C_N/\partial\alpha$, changes in stall characteristics and experienced greater unsteadiness. The power spectra revealed the addition of a low frequency stall component (i.e. relatively large wake structures), to the existing effect of the boundary layer turbulence on the hydrofoil unsteady forces. Observations made of the broad peak at a constant reduced frequency of 0.2 imply that the advection of the flow disturbance causing the unsteady force on the hydrofoil is about $^1/_5$ of the free-stream advection speed. The results indicate that an extended frequency range out to about 1 kHz is desired for a future more detailed investigation.

Acknowledgements

The authors acknowledge the support of the Research Training Centre of Naval Design and Manufacturing (RTCNDM) in this investigation. The RTCNDM is a University-Industry partnership established under the Australian Research Council (ARC) Industry Transformation grant scheme (ARC IC140100003).

References

[1] Alin, N., Bensow, R. E., Fureby, C., Huuva, T. and Svennberg, U., Current capabilities of des and les for submarines at straight course, *Journal of Ship Research*, **54**, 2010, 184–196.

[2] Belle, A., Brandner, P. A., Pearce, B. W., de Graaf, K. L. and Clarke, D. B., Artificial thickening and thinning of cavitation tunnel boundary layers, *Experimental Thermal and Fluid Science*, **78**, 2016, 75–89.

[3] Blevins, R. D., *Formulas for natural frequency and mode shape*, Van Nostrand Reinhold Co., New York, 1979.

[4] Brandner, P. A., Lecoffre, Y. and Walker, G. J., Design considerations in the development of a modern cavitation tunnel, in *16th Australasian Fluid Mechanics Conference*, 2007, 630–637.

[5] Khoo, M., Brandner, P., Pearce, B., Clarke, D., Butler, D. and Belle, A., An australian capability for submarine control surface performance evaluation, in *Mast Asia Conference 2015*, 1–19.

[6] Lysak, P. D., Capone, D. E. and Jonson, M. L., Unsteady lift of thick airfoils in turbulent flow, in *ASME 2009 International Mechanical Engineering Congress and Exposition*, American Society of Mechanical Engineers, 57–63.

[7] Mish, P. F. and Devenport, W. J., An experimental investigation of unsteady surface pressure on an airfoil in turbulence - Part 1: Effects of mean loading, *Journal of Sound and Vibration*, **296**, 2006, 417–446.

[8] Theodorsen, T., General theory of aerodynamic instability and the mechanism of flutter, Report, NACA Technical Report No. 496, 1935.

Appendix B

Cloud cavitation behaviour on a hydrofoil due to fluid-structure interaction

This paper was presented at the (peer-reviewed) *17th International Symposium on Transport Phenomena and Dynamics on Rotating Machinery (ISROMAC 2017)*, Maui, Hawaii, 16-21 December, 2017.

The citation for the conference paper is:

Smith, S. M., Venning, J. A., Giosio, D. R., Brandner, P. A, Pearce, B. W. and Young, Y. L. (2017). Cloud cavitation behaviour on a hydrofoil due to fluid-structure interaction. In *17th International Symposium on Transport Phenomena and Dynamics on Rotating Machinery (ISROMAC 2017)*.

Cloud cavitation behaviour on a hydrofoil due to fluid-structure interaction

Samuel Smith[1]*, James Venning[1], Dean Giosio[1], Paul Brandner[1], Bryce Pearce[1], Yin Lu Young[2]

ISROMAC 2017

International Symposium on Transport Phenomena and Dynamics of Rotating Machinery

Maui, Hawaii

December 16-21, 2017

Abstract

Despite recent extensive research into fluid-structure interaction (FSI) of cavitating hydrofoils there remains insufficient experimental data to explain many of these observed phenomena. The cloud cavitation behaviour around a hydrofoil due to the effect of FSI is investigated utilizing rigid and compliant 3D hydrofoils held in a cantilevered configuration in a cavitation tunnel. The hydrofoils have identical undeformed geometry of tapered planform with constant NACA0009 section. The rigid model is made of stainless steel and the compliant model of carbon and glass fibre reinforced epoxy resin with the structural fibres aligned along the span-wise direction to avoid material bend-twist coupling. Tests were conducted at an incidence of 6°, a mean chord based Reynolds number of 0.7×10^6, and cavitation number of 0.8. Force measurements were simultaneously acquired with high-speed imaging to enable correlation of forces with tip bending deformations and cavity physics. Hydrofoil compliance was seen to dampen the higher frequency force fluctuations while showing strong correlation between normal force and tip deflection. The 3D nature of the flow field was seen to cause complex cavitation behaviour with two shedding modes observed on both models.

Keywords

Cavitation — Fluid-Structure Interaction — Hydrofoil

[1] *Cavitation Research Laboratory, Australian Maritime College, Launceston, Australia*

[2] *Department of Naval Architecture and Marine Engineering, University of Michigan, Ann Arbour, MI, USA*

*__Corresponding author__: ssmith18@utas.edu.au

1. INTRODUCTION

The FSI characteristics of flow over a lifting body can significantly effect the performance of maritime propulsion and control systems. Recent research into the development of composite propellers[1, 2] and active control surfaces [3] has taken place to exploit the ability to passively tailor geometric aspects of the hydrofoil such as skew and pitch based on the loading distribution [4]. Not only does this self-adaptive behaviour give the ability to design a more energy efficient propeller, but also delay and mitigate the adverse effects of cavitation. One of these effects is the unsteady loading and induced vibration due to the shedding of cloud cavitation.

The effect of unsteady cloud cavitation on the hydroelastic response of hydrofoils has previously been investigated [5, 6, 7, 8, 9, 10], with recently Pearce et al. [11] showing that the cavity dynamics can influence the FSI response. In addition to the classical shed vortex induced structural response in single phase flow, there is interaction between the development of cavitation on the structural dynamics [9, 8]. These effects are highlighted in experiments by Akcabay et al. [6] where increased hydrofoil flexibility was seen to increase the cavity length as well as cause a reduction in the cloud cavitation shedding frequency. Further research also shows that flexibility broadens the induced vibration frequency content potentially leading to severe vibration amplification caused by lock-in [6]. Increased vibrations also occur when the unsteady cavity closure approaches the hydrofoil trailing edge due to high amplitude load fluctuations caused by periodic shedding of sheet-cloud cavitation. In

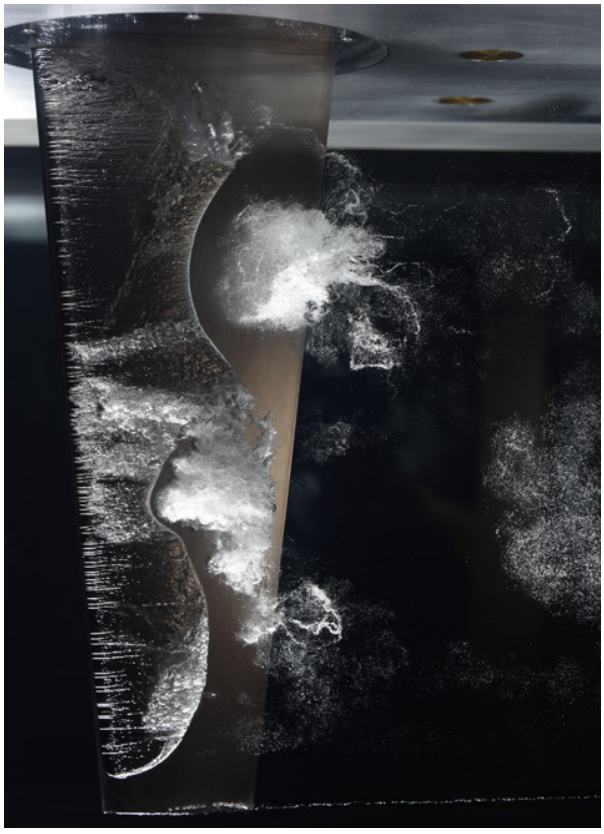

Figure 1. Cavitation about a NACA 0009 stainless steel hydrofoil at $\sigma = 0.8$, $Re_c = 0.7 \times 10^6$ and $\alpha = 6°$.

these investigations into the effect of cloud cavitation on hydroelastic response, there is limited discussion on changes in the cavitation pattern and shedding mechanisms due to the hydroelastic response.

Sheet and cloud cavitation was first extensively studied by Knapp [12] observing the detachment/shedding of cloud cavitation from a sheet cavity. Since then, several mechanisms have been identified as the primary instability causing periodic shedding depending on the condition. These included growth of interfacial instabilities such as Kelvin-Helmholtz waves [13, 14], re-entrant jet formation [15, 16, 17, 18, 19, 20] and shock propagation [21, 22, 23]. In a recent study on cloud cavitation about a sphere, all three mechanisms have been observed occuring either under varying flow conditions or as a complex coupled mechanism [24].

To reduce the complexity of the cavitation dynamics, much research into hydrofoil cloud cavitation has focused on 2D flows to limit 3D effects and span-wise variations as shown in figure 1. This is highlighted in time resolved PIV experiments on a 3D hydrofoil by Foeth et al. [25] showing significant cavitation stability sensitivity to 3D flow effects. Span-wise variations are still observed on 2D hydrofoils where the span-wise cavity length is seen to be proportional to the stream-wise length [26]. This relationship can result in span-wise cavity lengths that are compatible with the hydrofoil geometry. In these instances, the shedding cloud cavitation exhibits much stronger periodicity than in other conditions [17].

Force and tip displacement measurements are presented for a nominally rigid stainless steel and flexible composite hydrofoil experiencing cloud cavitation. Synchronised high speed photography is used to analyse the cavitation behaviour and assess the correlation between the cavity dynamics and forces experienced. The aim of this research is to further the understanding of cloud cavitation about a 3D hydrofoil and how FSI can influence its behaviour.

2. EXPERIMENTAL OVERVIEW

2.1 Model Hydrofoil Details

Geometry and mechanical properties of the hydrofoil models has been selected based on modelling the static and dynamic fluid-structure interaction typical of propellers and control surfaces. The chosen geometry was a symmetric (unswept) trapezoidal planform of 300 mm span with a 60 mm tip and 120 mm root chord, providing an aspect ratio = 3.33. The chord length was chosen to be compatible with the mounting to the water tunnel test section and to achieve a chord based Reynolds number $Re_c = 0.7 \times 10^6$. The unswept geometry, in conjunction with a span-wise alignment of the fibre orientation, was intentionally chosen to principally consider bending deformation only of the flexible hydrofoil. A modified NACA0009 section profile with a thicker trailing edge was selected for improved manufacture of the flexible composite model (see Zarruk et al [27] for further details).

The flexible (composite) model was manufactured as a carbon/glass-epoxy hybrid structure consisting of a polyolefin scaffold core, T700 unidirectional carbon fibre and biaxial E-glass fabric used as the key structural components with an outermost fine E-glass basket weave layer to aid surface finish. A full lay-up sequence and construction procedure is detailed in [27] where the composite hydrofoil model used in the present study is termed the CFRP00 hydrofoil. The rigid (stainless steel) model was machined from a Type 316 stainless steel billet with both models manufactured to ±0.1 mm surface tolerance and 0.8 μm surface finish.

The response spectrum of both hydrofoils was determined from both impact tests and hydrofoil loading spectra [27] with results summarized in table 1. First mode natural frequencies were obtained in air at 96 Hz and 112 Hz, and in water at 54 and 40 Hz for the stainless steel (rigid) and composite (flexible) models respectively.

Hydrofoil Dynamic Properties	Hydrofoil	
	Rigid	Flexible
First bending mode in air (Hz)	96	112
First bending mode in water (Hz)	54	40

Table 1. Hydrofoil natural frequencies obtained from impact tests and loading spectra for in-air and in-water frequencies, respectively[27].

2.2 Experimental Setup

Measurements were carried out in the Cavitation Research Laboratory (CRL) water tunnel at the Australian Maritime College. The tunnel test section is 0.6 m square by 2.6 m long in which the operating velocity and pressure ranges are 2 to 12 m/s and 4 to 400 kPa absolute respectively. The tunnel volume is 365 m^3 with demineralised water (conductivity of order 1 μS/cm). The test section velocity is measured from one of two (high and low range) Siemens Sitransp differential pressure transducers models 7MF4433-1DA02-2AB1-Z and 7MF4433-1FA02-2AB1-Z (measuring the calibrated contraction differential pressure) with estimated precisions of 0.007 and 0.018 m/s respectively. A detailed description of the facility is given in [28]. As shown in figure 2, two profiled plates are used to clamp the model within a housing that is attached to a 6-component force balance. The hydrofoil, located at the mid length of the test section, extends vertically into the flow through a 160 mm diameter penetration in the ceiling. The penetration is made fair (to 50 μm) using a disk mounted, in this case, on the measurement side of the balance. The fairing disk has a 0.5 mm radial clearance to avoid interference with the force measurement.

2.3 Experimental Techniques

Data was obtained for a cavitation number of 0.8 and at a velocity of 8.5 m/s which corresponds to a Reynolds number (based on mean chord length) of 0.7×10^6 with the models at an incidence of 6°. The cavitation number is defined as $\sigma = 2(p - p_v)/\rho U_\infty^2$ and Reynolds number as $Re = U_\infty c/\nu$, where p is the static pressure at the test section centreline, p_v is the vapour pressure, ρ is the water density, U_∞ is the test

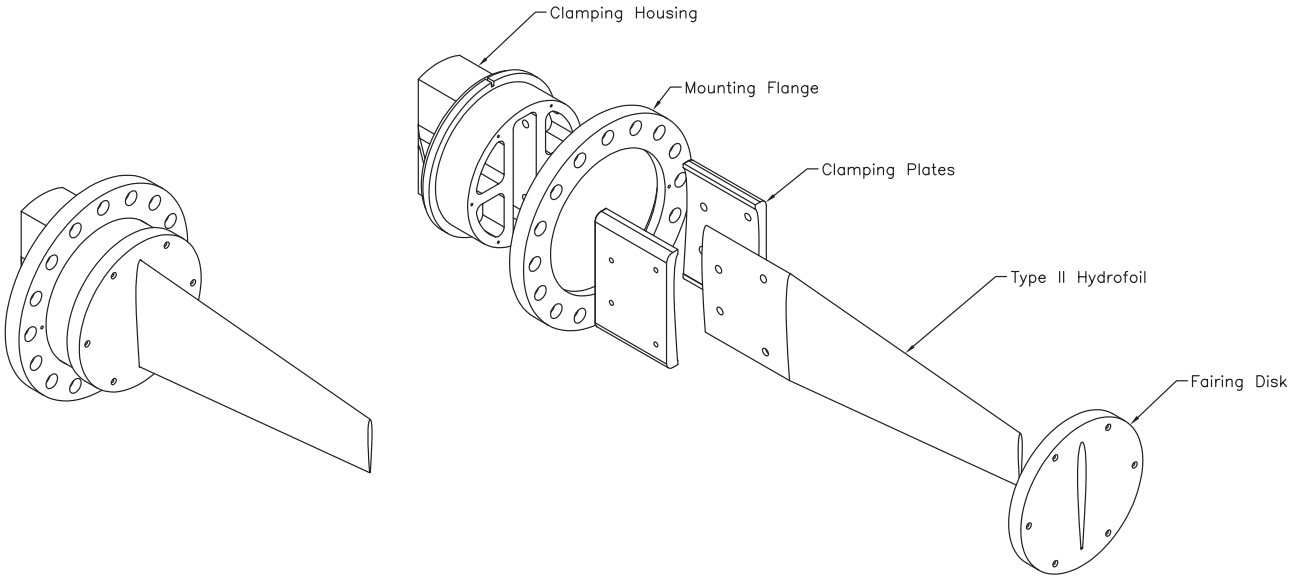

Figure 2. Hydrofoil model assembly showing an exploded view of the clamping housing arrangement allowing continuity of the reinforcing fibres for the CFRP models.

section velocity, c is the mean chord and ν is the kinematic viscosity of the water. Of the total load vector measured, only the time-varying component of the normal force is presented. The force balance was calibrated by a least squares fit between a basis vector loading cycle and the 6 outputs giving a 6×6 matrix. An estimated precision on all components is less than 0.1%.

The cavitation behaviour was recorded using high speed photography with a HighSpeedStar8 (LaVision, Germany) mounted on the side of the test section. The camera was outfitted with a Nikkor f/1.4 50 mm lens and setup with a magnification factor of 3.28 px/mm. High speed images were recorded with a spatial resolution of 1024×1024 at 7,000 Hz for the rigid hydrofoil where the flexible foil was recorded at 1,000 Hz due to data acquisition limits.

A previous study [27] has shown the stainless steel model to be nominally rigid with a maximum tip deflection of less than 5% of the mean chord compared with 15% for the composite model. The force data for the stainless steel model was found to be nominally invariant with Reynolds number for $\alpha \leq 6°$. On this basis, tip bending displacement, δ_{tip}, was only recorded for the flexible model with measurements achieved by tracking 2.3 mm diameter white dots on the tip of the hydrofoil. Further information on the technique used in similar experiments can be found in [29]. This was achieved using a HighSpeedStar5 high speed camera mounted on the bottom of the test section. The camera was outfitted with a Nikkor f/1.4 105 mm lens where images had a magnification factor of 13.38 px/mm. Images were recorded at 1,000 Hz with a spatial resolution of 512×1024.

The high speed photography was synchronized with the force measurement acquisition by simultaneous triggering from a BNC Model 575 Pulse Generator. Force and tunnel flow data were sampled at 7,000 Hz and 1,000 Hz, respectively.

3. RESULTS AND DISCUSSION

3.1 Force and Tip Displacement Time Series

The measured normal force, X, is presented as a dimensionless coefficient, $C_X = 2X/(\rho A U_\infty^2)$, where A denotes the planform area. The frequency content of the X force experienced by either hydrofoil is shown in the power spectral density in figure 3.

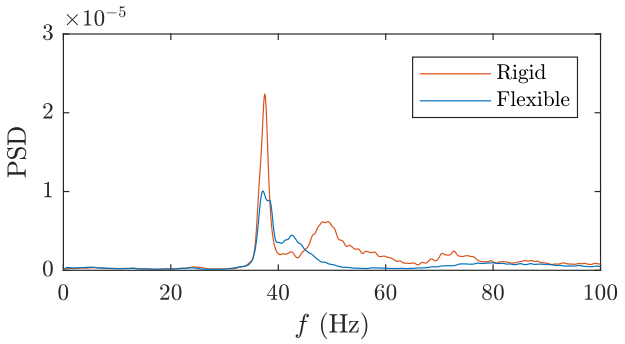

Figure 3. Narrowband X force power spectral density (PSD) for the rigid and flexible hydrofoils at $\sigma = 0.8$, $Re_c = 0.7 \times 10^6$ and $\alpha = 6°$.

Both hydrofoils exhibit a common primary frequency at approximately 37 Hz with secondary frequencies at 49 and 42 Hz for the rigid and flexible hydrofoils, respectively . The common fluctuation at 37 Hz is linked to periodic shedding of cloud cavitation from mid-span as made evident in space-time plots discussed later. These plots also reveal another shedding mechanism towards the tip of the rigid hydrofoil

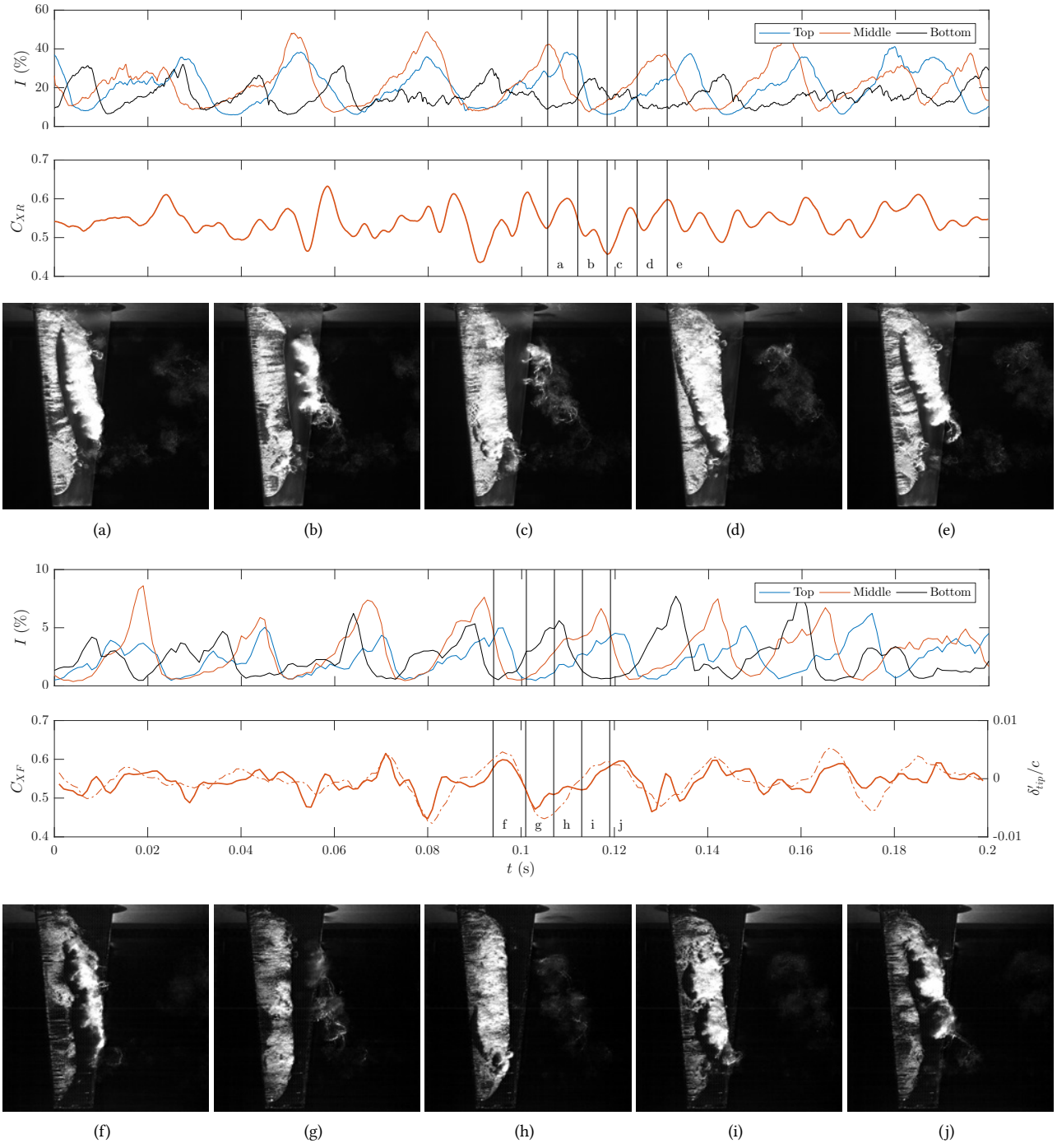

Figure 4. Sample time series of normal force coefficient with selected images from high-speed imaging for the rigid (top) and flexible hydrofoil (bottom). Simultaneous normalized unsteady tip bending displacement (dot-dashed line) is also presented for the flexible hydrofoil. The 3 curves of pixel intensity are taken at 75% of the chord for span-wise locations of $0.24s$, $0.47s$ and $0.77s$ from the root. Data was taken at $\sigma = 0.8$, $Re_c = 0.7 \times 10^6$ and $\alpha = 6°$.

fluctuating at 49 Hz explaining the secondary peak. Coupling between the dynamic response of the flexible hydrofoil and the unsteady cloud cavitation is linked to the 42 Hz peak. The slight rise in natural frequency compared to that in table 1 is attributed to reduction in added mass with the presence of vapour cavities.

Figure 4 shows a short time series of C_X, the unsteady tip bending displacement to chord ratio, δ'_{tip}/c, and pixel

intensity, I, for both the rigid and flexible hydrofoils. Pixel intensity was taken along the span, s, at $0.24s$, $0.47s$ and $0.77s$ from the root and at 75% of the local chord for both hydrofoils. Frames taken from the synchronised high speed video show one full shedding cycle at the dominant frequency with the first and last frames coinciding with the maximum force of the primary frequency component. For both hydrofoils, the primary frequency corresponds to a full length cavity being shed. The maximum force occurs just after the attached cavity breaks off and a new cavity has just formed. The minimum force coincides with maximum cavity length. Analysing pixel intensity of the rigid hydrofoil we see a rise, plateau and fall at the middle pixel ($0.47s$) during the shedding cycle shown. The top pixel ($0.24s$) shows similar behaviour and duration but slightly trails the middle pixel intensity in time. The bottom pixel ($0.77s$) exhibits peaks for a much shorter duration compared to the other pixels and primarily occurs when the top and middle pixels are low. These pixel intensity traits suggests there are two shedding modes at the top-middle and the bottom that alternate over time. The flexible hydrofoil shows similar trends but due to low temporal resolution, definitive conclusions cannot be made at this stage.

Comparing the force signals, the rigid hydrofoil exhibits a slightly lower mean C_X to that of the flexible hydrofoil, 0.5406 and 0.5497, respectively. However, the rigid hydrofoil exhibits more unsteadiness with the flexible hydrofoil appearing to almost dampen some of the lower amplitude fluctuations. This is reflected in the C_X RMS values of 0.0354 and 0.0311 for the rigid and flexible hydrofoil, respectively. The unsteady displacement of the flexible hydrofoil is seen to vary significantly over time having a strong correlation with C_X as expected.

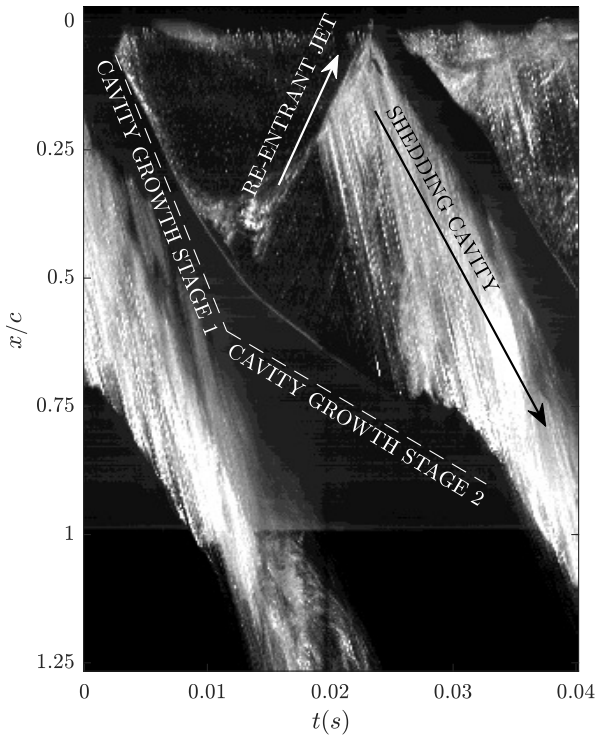

Figure 5. Space-time plot of a single shedding cycle of the rigid hydrofoil . showing the key components of the shedding cycle at $\sigma = 0.8$, $Re_c = 0.7 \times 10^6$ and $\alpha = 6°$. The flow direction from top to bottom.

3.2 Shedding Mechanisms and Cavity Dynamics

Through analysis of the high speed videos, it is evident that the primary shedding mechanism is the classical re-entrant jet. A typical shedding process can be seen in the space-time plot of the rigid hydrofoil (figure 5) generated from a line of pixels extracted at a position 100 mm along the span (i.e. at $0.33s$). Once the cavity forms, it initially grows at a constant velocity during stage 1. At a certain point ($t \approx 0.01$), the re-entrant jet starts to propagate forward as indicated by a second curve forming in the cavity. At the same instant, the cavity shifts into its second growth phase with a reduced cavity growth speed. As the re-entrant jet approaches the cavity detachment, it starts interacting with the upper surface of the cavity ($t \approx 0.2$). This is indicated by the white streaks from the secondary curve of the re-entrant jet in figure 5. Shortly after, the jet reaches the cavity detachment, breaking off the attached cavity, forming a cavitation cloud that is then advected downstream. Following cavity break-off, a new cavity forms soon after and the cycle starts again.

At the flow conditions examined here ($Re_c = 0.7 \times 10^6$, $\sigma = 0.8$ and $\alpha = 6°$), the NACA0009 hydrofoil forms a relatively thin cavity, resulting in a thin jet that initially (see stage 1 growth in figure 5) has insufficient momentum to break through to the cavity detachment point due to friction of the adjacent layers [16, 30]. A sufficiently thin cavity may also have significant interactions between the upper and lower interfaces of the cavity as surface perturbations become predominant leading to small-scale vapour structures being shed instead of a large-scale cloud [19]. This can be seen in chord-wise space-time plots (figure 6) of several shedding cycles where there is significant variation between each cycle. The interaction of surface perturbations manifest as a rough opaque surface, seen at the top of figure 6, compared the transparent region shown in figure 5. Comparison of the rigid and flexible hydrofoils sees that shedding variations over time exist for both hydrofoils but aren't as severe for the flexible hydrofoil.

The span-wise space-time plots taken 10 mm upstream of mid-chord for both hydrofoils (figure 7) illustrates how the cloud cavitation varies along the span over time. It is observed that there is significant span-wise variation for both hydrofoils with no uniform (i.e. across the whole span) shedding observed. This complex cavitation behaviour is due to the interaction of multiple effects. This includes span-wise flow disparity over the hydrofoil due to the tapered and swept geometry causing changes in re-entrant jet direction. Additionally, the nature of the vertical mounted hydrofoil

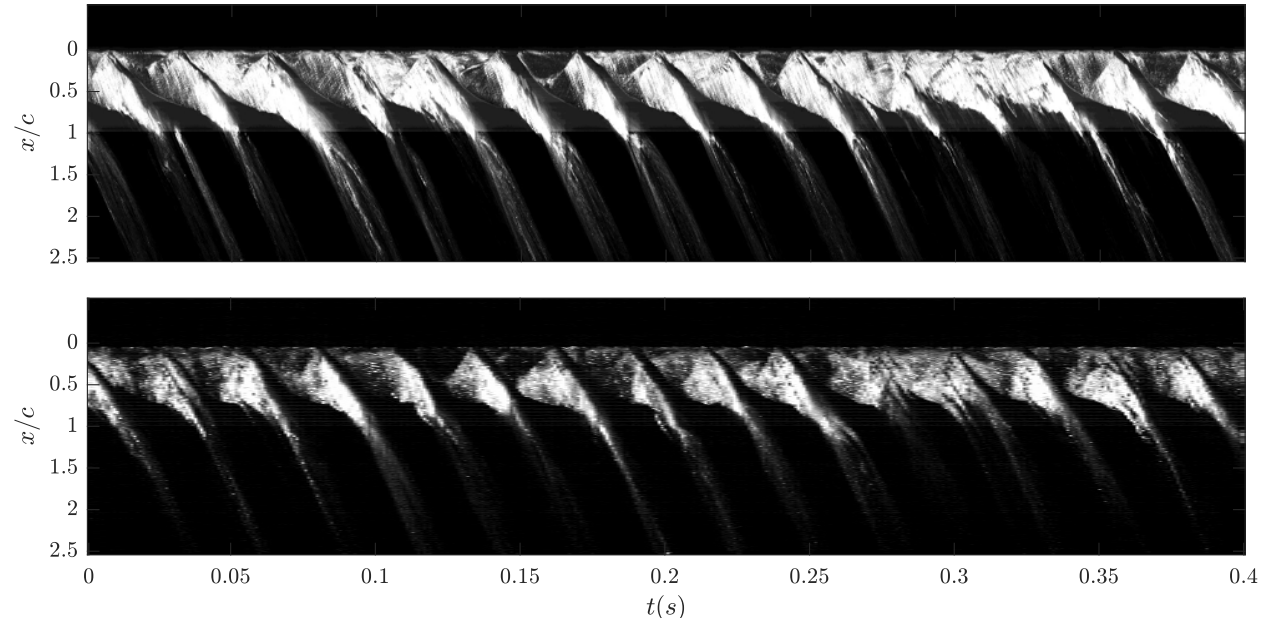

Figure 6. Chord-wise space-time plots from high speed images taken 100 mm along the span for the rigid (top) and flexible hydrofoil (bottom) at $\sigma = 0.8$, $Re_c = 0.7 \times 10^6$ and $\alpha = 6°$. The flow direction is top to bottom.

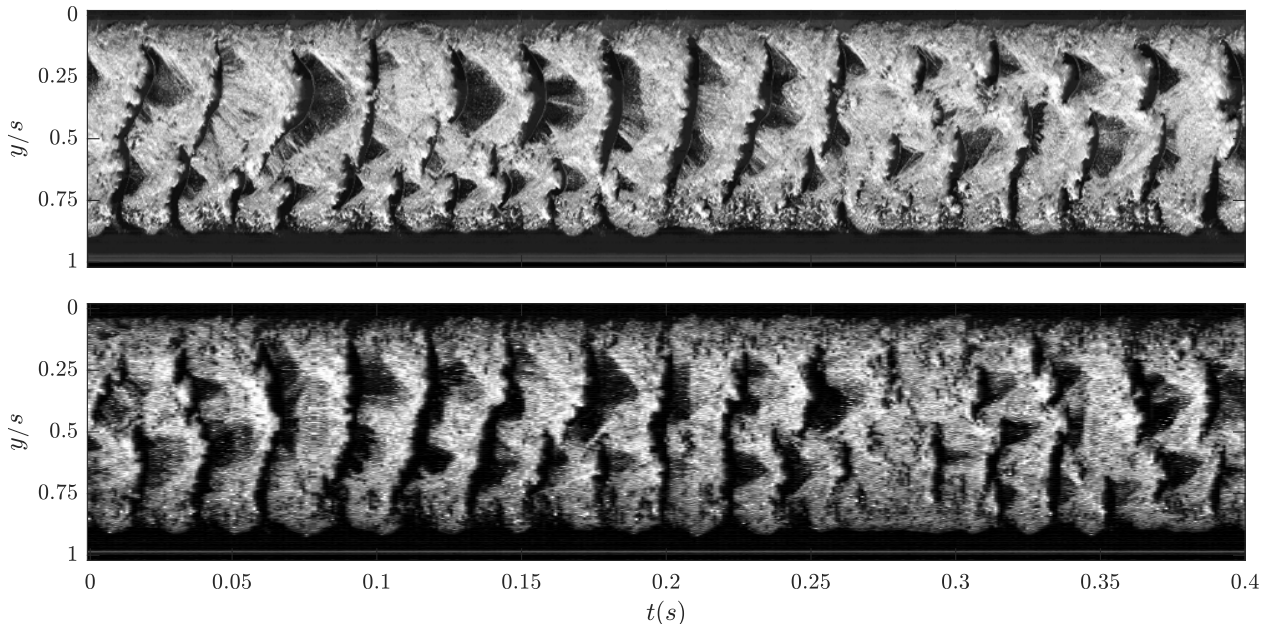

Figure 7. Span-wise space-time plots from high speed images 10 mm upstream of the mid-chord for the rigid (top) and flexible hydrofoil (bottom) at $\sigma = 0.8$, $Re_c = 0.7 \times 10^6$ and $\alpha = 6°$. The flow direction is left to right.

results in cavitation number gradient along the span as well as buoyancy effects on the cavities.

A level of consistency is seen in the periodicity of shedding, but the shedding behaviour of each event varies with clear re-entrant jet observed in some, but not in others. Analysis of the rigid hydrofoil reveals the existence of two shedding modes along the span at frequencies of approximately 37 Hz and 50 Hz for the upper and lower parts of the hydrofoil, respectively, calculated from space-time plots. The flexible hydrofoil also shows signs of two shedding modes, 37 Hz and 42 Hz, with two crescent cut-outs along the span-wise length of the cavity observed, similar to the rigid hydrofoil. Non-dimensionalizing these frequencies using a cavity length based Strouhal number, $St = fL_c/U_\infty$, where L_c is the maxi-

mum cavity length, the rigid frequencies equate to 0.33 and 0.37 for the upper and lower parts, respectively, compared to 0.33 and 0.32 for the flexible hydrofoil.

Comparing the span-wise space-time plots, the flexible hydrofoils secondary shedding mode at the bottom doesn't appear to have as strong a periodicity as the rigid hydrofoil. This could be due to the force induced tip displacement imposed by the larger shedding cavity from the top interfering with the lower shedding physics. These observations coincide with frequencies present in the X force spectrum (figure 3) supporting the strong correlation between cavity dynamics and forces.

4. CONCLUSIONS

Preliminary results are presented for the effect of FSI on cloud cavitation about a hydrofoil. The normal force, tip bending displacement and cavitation behaviour were compared for a nominally rigid stainless steel and flexible composite NACA0009 hydrofoil at $Re_c = 0.7 \times 10^6$, $\sigma = 0.8$ and $\alpha = 6°$.

The bending deformations of the flexible hydrofoil were seen to dampen some of the higher frequency fluctuations in the normal force measurements while showing a strong correlation between tip displacement and normal force.

A re-entrant jet was identified as the primary shedding mechanism showing changes in growth and jet speed at various stages in the shedding cycle. Due to the thin cavity, surface perturbations were seen to have significant interaction, sometimes resulting in small-scale vapour pockets being shed instead of large-scale cloud cavitation.

The cavitation behaviour is observed to be highly complex due to the 3D nature of the flow leading to significant span-wise flow disparity. Both hydrofoils exhibited fairly consistent periodic shedding but varying behaviour between each event. Two shedding modes appeared to form along the span with either hydrofoil showing two curved regions in the cavity trailing edge typical of a re-entrant jet. This results in two shedding frequencies for either hydrofoil with both having a primary frequency of 37 Hz and secondary frequencies of 50 Hz and 42 Hz for the rigid and flexible hydrofoil, respectively. These differences are attributed to force induced tip bending displacements affecting the cavity dynamics due to changes in the flow field. This is supported by the fact that the observed shedding frequencies matched those present in the X force spectrum.

The fluid-structure interaction phenomena observed for a flexible 3D hydrofoil experiencing cavitation is highly complex. This complicated behaviour makes it difficult to predict the performance of real world applications such as composite propellers. Further investigation into the phenomena in a wider range of conditions will allow more detailed and accurate predictions, permitting improved designs of control surfaces and marine propulsors.

ACKNOWLEDGEMENTS

This project was supported by the University of Tasmania, the Defence Science and Technology Group, US Office of Naval Research (Dr.Ki-Han Kim, Program Officer) and ONR Global (Dr.Woei-Min Lin) through NICOP S&T Grant no. N62909-11-1-7013. The authors would like to acknowledge the assistance of Mr Steven Kent and Mr Robert Wrigley from the Australian Maritime College for their essential help with setting up and carrying out the experiments.

REFERENCES

[1] Y. L. Young. Fluid–structure interaction analysis of flexible composite marine propellers. *Journal of Fluids and Structures*, 24(6):799–818, 2008.

[2] M. R. Motley, Z. Liu, and Y. L. Young. Utilizing fluid–structure interactions to improve energy efficiency of composite marine propellers in spatially varying wake. *Composite Structures*, 90(3):304–313, 2009.

[3] S. R. Turnock and A. M. Wright. Directly coupled fluid structural model of a ship rudder behind a propeller. *Marine Structures*, 13(1):53–72, 2000.

[4] Y. L. Young. Time-dependent hydroelastic analysis of cavitating propulsors. *Journal of Fluids and Structures*, 23(2):269–295, 2007.

[5] D. T. Akcabay and Y. L. Young. Influence of cavitation on the hydroelastic stability of hydrofoils. *Journal of Fluids and Structures*, 49:170–185, 2014.

[6] D. T. Akcabay, E. J. Chae, Y. L. Young, A. Ducoin, and J. A. Astolfi. Cavity induced vibration of flexible hydrofoils. *Journal of Fluids and Structures*, 49(Supplement C):463–484, 2014.

[7] D. T. Akcabay and Y. L. Young. Parametric excitations and lock-in of flexible hydrofoils in two-phase flows. *Journal of Fluids and Structures*, 57:344–356, 2015.

[8] P. Ausoni, M. Farhat, X. Escaler, E. Egusquiza, and F. Avellan. Cavitation influence on von kármán vortex shedding and induced hydrofoil vibrations. *Journal of Fluids Engineering*, 129(8):966–973, 2007.

[9] Q. Wu, B. Huang, G. Wang, and Y. Gao. Experimental and numerical investigation of hydroelastic response of a flexible hydrofoil in cavitating flow. *International Journal of Multiphase Flow*, 74:19–33, 2015.

[10] A. Ducoin, J. A. Astolfi, and J. Sigrist. An experimental analysis of fluid structure interaction on a flexible hydrofoil in various flow regimes including cavitating flow. *European Journal of Mechanics-B/Fluids*, 36:63–74, 2012.

[11] B. W. Pearce, P. A. Brandner, N. Garg, Y. L. Young, A. W. Phillips, and D. B. Clarke. The influence of bend-twist coupling on the dynamic response of cavitating composite hydrofoils. In *5th International Symposium on Marine Propulsors (SMP'17)*, pages 803–813.

[12] R. T. Knapp. Recent investigations of the mechanics of cavitation and cavitation damage. *Transactions of the ASME*, 77:1045–1054, 1955.

[13] C. E. Brennen. The dynamic balances of dissolved air and heat in natural cavity flows. *Journal of Fluid Mechanics*, 37(1):115–127, 1969.

[14] F. Avellan, P. Dupont, and I. L. Ryhming. Generation mechanism and dynamics of cavitation vortices downstream of a fixed leading edge cavity. In *17th Symposium on Naval Hydrodynamics*, pages 1–13, 1988.

[15] S.P. Furness and S. P. Hutton. Experimental and theoretical studies of two-dimensional fixed-type cavities. *Journal of Fluids Engineering*, page 515, 1975.

[16] Q. Le, J. Franc, and J. Michel. Partial cavities: Global behaviour and mean pressure distribution. *Journal of Fluids Engineering*, 115:243–243, 1993.

[17] Y. Kawanami, H. Kato, H. Yamaguchi, M. Tanimura, and Y. Tagaya. Mechanism and control of cloud cavitation. *Journal of Fluids Engineering*, 119(4):788–794, 1997.

[18] B. Stutz and J. L. Reboud. Experiments on unsteady cavitation. *Experiments in Fluids*, 22(3):191–198, 1997.

[19] M. Callenaere, J. Franc, J. Michel, and M. Riondet. The cavitation instability induced by the development of a re-entrant jet. *Journal of Fluid Mechanics*, 444:223–256, 2001.

[20] K. R. Laberteaux and S. L. Ceccio. Partial cavity flows. part 1. cavities forming on models without spanwise variation. *Journal of Fluid Mechanics*, 431:1–41, 2001.

[21] J. K. Jakobsen. On the mechanism of head breakdown in cavitating inducers. *Journal of Basic Engineering*, 86(2):291–305, 1964.

[22] G. E. Reisman, Y. C. Wang, and C. E. Brennen. Observations of shock waves in cloud cavitation. *Journal of Fluid Mechanics*, 355:255–283, 1998.

[23] H. Ganesh, S. A. Mäkiharju, and S. L. Ceccio. Bubbly shock propagation as a mechanism for sheet-to-cloud transition of partial cavities. *Journal of Fluid Mechanics*, 802:37–78, 2016.

[24] KL De Graaf, PA Brandner, and BW Pearce. Spectral content of cloud cavitation about a sphere. *Journal of Fluid Mechanics*, 812, 2017.

[25] E. J. Foeth, C. W. H. Van Doorne, T. Van Terwisga, and B. Wieneke. Time resolved piv and flow visualization of 3d sheet cavitation. *Experiments in Fluids*, 40(4):503–513, 2006.

[26] Y. Kawanami, H. Kato, and H. Yamaguchi. Three-dimensional characteristics of the cavities formed on a two-dimensional hydrofoil. In *Third International Symposium on Cavitation*, volume 1, pages 191–196. Laboratoire des Ecoulements Géophysiques et Industriels, Grenoble, France, 1998.

[27] G. A. Zarruk, P. A. Brandner, B. W. Pearce, and A. W. Phillips. Experimental study of the steady fluid-structure interaction of flexible hydrofoils. *Journal of Fluids and Structures*, 51:326–343, 2014.

[28] P. A. Brandner, Y. Lecoffre, and G. J. Walker. Design considerations in the development of a modern cavitation tunnel. In *16th Australasian Fluid Mechanics Conference*, pages 630–637, 2007.

[29] Y. L. Young, N. Garg, P. A. Brandner, B. W. Pearce, D. Butler, D. Clarke, and A. W. Phillips. Load-dependent bend-twist coupling effects on the steady-state hydroelastic response of composite hydrofoils. *Composite Structures*, 2017.

[30] P. F. Pelz, T. Keil, and T. F. Groß. The transition from sheet to cloud cavitation. *Journal of Fluid Mechanics*, 817:439–454, 2017.

Appendix C has been removed for copyright or proprietary reasons.

It has been published as:

Smith, S. M., Venning, J. A., Giosio, D. R., Brandner, P. A, Pearce, B. W. and Young, Y.L. (2019). Cloud cavitation behaviour on a hydrofoil due to fluid-structure interaction. ASME J. Fluids Eng. 141 (4), 041105. DOI: http://dx.doi.org/10.1115/1.4042067

Appendix D

The influence of fluid-structure interaction on cloud cavitation about a hydrofoil

This paper was presented at the (peer-reviewed) *10th International Symposium on Cavitation (CAV2018)*, Baltimore, Maryland, US, 14-16 May, 2018.

The citation for the conference paper is:

Smith, S. M., Venning, J. A., Brandner, P. A, Pearce, B. W., Giosio, D. R. and Young, Y. L. (2018). The influence of fluid-structure interaction on cloud cavitation about a hydrofoil. In *10th International Symposium on Cavitation (CAV2018)*.

The influence of fluid-structure interaction on cloud cavitation about a hydrofoil

[1]Samuel M Smith*; [1]James A Venning; [1]Paul A Brandner; [1]Bryce W Pearce; [1]Dean R Giosio; [2]Yin Lu Young

[1]*Cavitation Research Laboratory, Australian Maritime College, Launceston, Tasmania, Australia*

[2]*Department of Naval Architecture and Marine Engineering, University of Michigan, Ann Arbour, MI, USA*

Abstract

The dynamics of cloud cavitation about rigid and flexible 3D hydrofoils is investigated in a cavitation tunnel. The two hydrofoils have identical undeformed geometry of tapered planform, NACA-0009 section and cantilevered setup at the hydrofoil root. The rigid model is made of stainless steel and the flexible model of carbon and glass-fibre reinforced epoxy resin with an effectively quasi-isotropic lay-up without material bend-twist coupling. Tests were conducted at a fixed incidence of 6°, a chord-based Reynolds number of 0.7×10^6 and a cavitation number ranging from 1.0 to 0.2. Unsteady force measurements were made simultaneously with high-speed imaging to enable correlation of forces and with cavity dynamics. High-resolution force spectra at discrete cavitation numbers and separate pressure sweeps were taken to acquire spectrograms of frequency response as a function of cavitation number. Three shedding modes, designated as types 1, 2 and 3, are apparent for both rigid and flexible hydrofoils although significant differences in peak amplitudes were observed. Types 2 and 3 shedding occur at high cavitation numbers where frequency varied with cavitation number and high-speed imaging showed the dominant shedding mechanism to be due to re-entrant jet formation. The type 1 shedding that developed with reduction in cavitation number, once cavity lengths grew to about full-chord, occurred at a nominally constant frequency. In this case, the imaging showed the dominant mechanism to be shockwave formation. This behaviour has been reported upon extensively in literature although there are some new features apparent from the data. The flexibility of the composite hydrofoil was found to increase the magnitude of the force fluctuations for the low frequency type 1 mode compared to the rigid hydrofoil. However, hydrofoil flexibility was seen to dampen the fluctuating magnitude of the high-frequency type 2 and 3 modes, despite being close to the hydrofoil's natural frequency.

Keywords: Fluid-structure interaction; Cloud cavitation; Hydrofoil

Introduction

The adverse effects of cavitation on hydrofoils, such as unsteady loading and induced vibration due to the shedding of cloud cavitation, can be delayed and mitigated through utilizing passive control of the 3-D morphology. Recent research on these self-adaptive properties of lifting surfaces has been carried out on composite propellers [1,2] and active control surfaces [3]. Geometric aspects of hydrofoils, such as skew and pitch, can be passively tailored allowing for the suppression or delay of cavitation on propellers operating in unsteady inflows [4].

The effects of unsteady cloud cavitation on the hydroelastic response of hydrofoils has previously been investigated [5] with Akcabay et al. [6] showing that greater spanwise flexibility of isotropic hydrofoils with the centre of pressure upstream of the shear centre causes increased cavity length, reduced shedding frequency and broadening of the induced vibration frequencies. Depending on the flow conditions, several possible mechanisms have been identified as the primary instability causing periodic shedding. These include re-entrant jet formation [7-10], shockwave propagation [9-14] and growth of interfacial instabilities such as Kelvin-Helmholtz waves [15]. In a recent study on cloud cavitation about a sphere, all three mechanisms have been observed occurring either under varying flow conditions or as a complex coupled mechanism [13]. Each of these instabilities have certain flow conditions in which they become the critical driver of shedding in cloud cavitation, resulting in the formation of two distinct modes [16]. The low-frequency (type 1) mode, typically defined as transitional cavity oscillation, occurs at relatively low cavitation number to incidence ratios ($\sigma/2\alpha$) where the long cavity is periodically shed due to shockwave propagation generated from the collapse of a previously shed cavity. The shedding frequency of the type 1 mode is typically independent of $\sigma/2\alpha$, occurring at chord-based Strouhal numbers, St, between 0.15-0.3. The type 2 mode, typically defined as partial cavity instability, occurs at higher $\sigma/2\alpha$, where a re-entrant jet is the cause of periodic shedding with its frequency changing with σ due to cavity length dependence on σ.

Fluid-structure interaction (FSI) between cloud cavitation and hydrofoils is an intricate phenomenon due to complex interactions between turbulent flow structures, phase-change dynamics, and the structural response of

*Corresponding Author, Samuel Smith: ssmith18@utas.edu.au

the hydrofoil (Figure 1). To investigate this phenomena, we present force measurements with synchronised high-speed photography, providing insight into the spectral content of unsteady force oscillations. The data obtained also sheds light on the disparity in some previous findings as discussed in [17]. The aim of this study is to further the understanding of cloud cavitation about a 3D hydrofoil and how FSI can influence its behaviour by assessing the correlation between the cavity dynamics and forces.

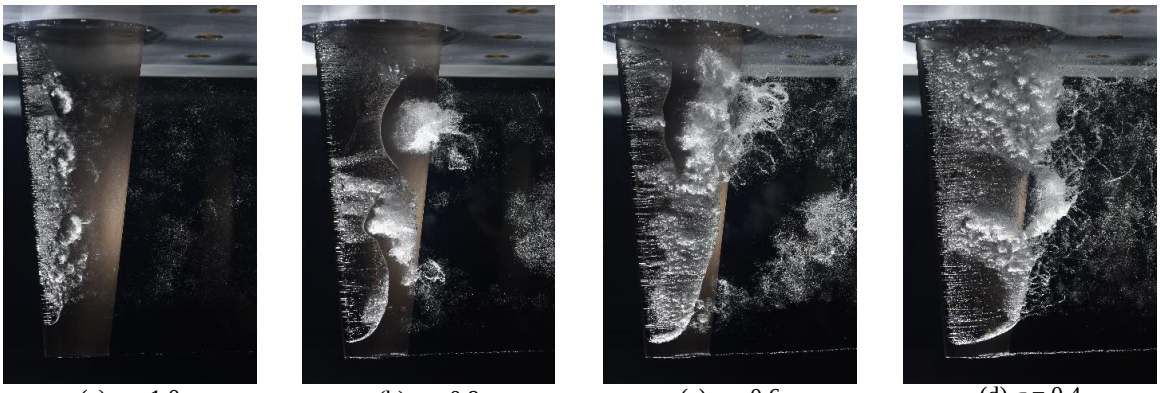

(a) $\sigma = 1.0$ (b) $\sigma = 0.8$ (c) $\sigma = 0.6$ (d) $\sigma = 0.4$

Figure 1 Photographs of the cloud cavitation about a stainless steel NACA-0009 hydrofoil with variations in σ at $\alpha = 6°$ and $Re = 0.7 \times 10^6$.

Experimental overview

The geometry and the mechanical properties of the hydrofoil models were selected based on modelling the static and dynamic fluid-structure interaction representative of propellers and control surfaces. Measurements were conducted using a flexible composite hydrofoil and a nominally rigid steel hydrofoil. The chosen geometry was a symmetric trapezoidal planform of 300 mm span (s) with a chord of 60 mm at the tip and 120 mm at the root, providing a geometric aspect ratio of 3.33 without considering the double body effect provided by the fixed well at the root. The chord length was chosen to be compatible with the mounting to the water tunnel test section and to achieve a chord-based Reynolds number, $Re_c = U_\infty c/\nu = 0.7 \times 10^6$ with $c = 90$ mm as the mean chord, which is representative of full scale applications. The geometry, in conjunction with a span-wise alignment of the fibre orientation, was intentionally chosen to principally consider bending deformation only of the flexible hydrofoil. A modified NACA-0009 section profile with a thicker trailing edge was selected for improved manufacture of the flexible composite model (see [18] for further details). Deflection measurements [18] showed that the maximum tip bending deflection of the flexible hydrofoil was 15% of the mean chord and negligible twist deformation, while the stainless steel hydrofoil was nominally rigid. The force data for the stainless steel model was found to be nominally invariant with Reynolds number for $\alpha \leq 6°$.

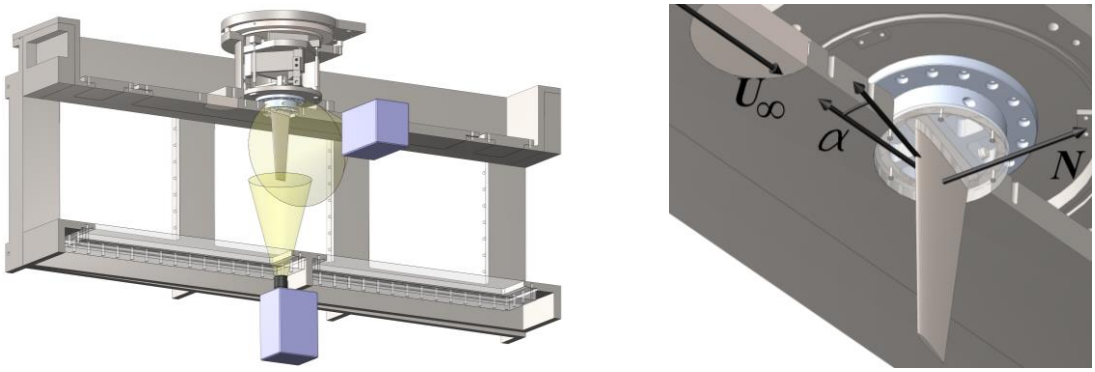

Figure 2 (Left) Section view of the experimental setup where the model hydrofoils are mounted via a 6-component force balance while the cavitation behaviour and tip deflection are imaged using two high-speed cameras. Tip deflection data is presented in [8]. (Right) A close-up of the hydrofoil showing the coordinate system used.

The flexible (composite) model was manufactured as a carbon/glass-epoxy hybrid structure with the lay-up sequence that yield quasi-isotropic response. The construction procedure is detailed in [18]. The nominally rigid (stainless steel) model was machined from a 316 grade stainless steel billet. First mode natural frequencies were obtained in air at 96 Hz and 112 Hz, and in water at 54 and 40 Hz for the stainless steel (rigid) and composite (flexible) models, respectively, determined from impact tests and hydrofoil loading spectra [18].

*Corresponding Author, Samuel Smith: ssmith18@utas.edu.au

Measurements were carried out in the Cavitation Research Laboratory water tunnel at the Australian Maritime College. The tunnel test section is 0.6 m square by 2.6 m long, in which the operating velocity and pressure ranges are 2 to 12 m/s and 4 to 400 kPa absolute, respectively. The tunnel volume is 365 m^3 of demineralised water. A detailed description of the facility is given in [19]. Two profiled plates were used to clamp the model within a housing that was attached to a 6-component force balance (Figure 2) with estimated precision of less than 0.1% on all components. Further description of the mounting arrangement may be found in [8]. Data was obtained for cavitation numbers from 1.0 to 0.2 and at a Reynolds number of 0.7×10^6 and an incidence of 6°. The hydrofoil tip cavitation number is defined as $\sigma = 2(p_\infty - p_v)/\rho U^2_\infty$, where p_∞ is the static pressure at the test section centreline, p_v is the vapour pressure, ρ is the water density and U_∞ is the test section velocity.

The cavitation behaviour was recorded using high-speed photography with a HighSpeedStar8 (LaVision, Germany) camera set up as shown in Figure 2. A Nikkor f/1.4 50 mm lens was used resulting in a magnification factor of 3.28 px/mm. High-speed images were recorded with a spatial resolution of 1024×1024 for 1 s at 7,000 Hz for the rigid hydrofoil while the flexible hydrofoil was recorded for 5 s at 1,000 Hz (due to synchronisation compatibility of the two cameras) to allow tip deflection measurements for data presented in [8]. The high-speed photography was synchronized with the force measurement acquisition by simultaneous triggering. Force and tunnel flow data were sampled at 7,000 Hz and 1,000 Hz, respectively.

Results and Discussion

High-resolution spectra of the hydrofoil normal force (perpendicular to the planform as shown in Figure 2) are presented in Figure 3 for all σ. Spectra were obtained using the Power Spectral Density (PSD) derived with the Welch estimate of the PSD [20] utilizing a window size of 4096 samples (4.1 s) and overlap of 256 samples (0.26 s). At each σ, both the rigid and flexible hydrofoils exhibited similar peak frequencies. As σ decreases, the frequency at which these peaks occur reduces due to the increasing cavity length requiring greater time for the cavity to grow and detach. It was also observed that there is an increase in the peak frequency amplitude by approximately one order of magnitude for every 0.2 reduction in σ (note the changing vertical scale in Figure 3).

Comparing the force spectra from both models, it is evident that the amplitude of the rigid hydrofoil is approximately double that of the flexible at σ = 0.8 and 0.6 for the peak frequencies. However, at σ = 0.4, the amplitude of the flexible is more than 3 times that of the rigid. The small differences at σ = 1.0, noting the scale of the PSD, is negligible. The horizontal axis is the cavity shedding frequency (*f)* Strouhal number defined using the mean chord, $St = fc/U_\infty$. Inconsistencies between rigid and flexible hydrofoil *St* is attributed to varying flow velocity between runs to maintain a constant Re_c at different temperatures. The 135 Hz (*St* = 1.43) peaks are associated with the structural response of the force balance based on previous experiments [21] and is evident in that the peaks occur at the same frequency for all σ.

At σ = 0.8, the common 37 Hz (*St* = 0.39) peak is linked to the periodic shedding of cloud cavitation from the upper half of the hydrofoil as seen in Figure 1(b). The secondary peaks at 42 and 49 Hz (*St* = 0.44 and 0.52) for the flexible and rigid hydrofoil, respectively, are attributable to the presence of another shedding event on the lower half of the span evident in the power distribution maps (Figure 5) discussed below.

Through measuring the normal force on the hydrofoils while the pressure is gradually increased, a joint time-frequency analysis (JTFA) can be conducted to investigate spectral characteristics at fine σ increments. The JTFA spectrograms shown in Figure 4 are obtained from 256 individual PSD spectra based on time series with 2048 samples (2 s) each and overlap of 1024 (1 s). Overlaying the high-resolution PSDs from Figure 3, good correspondence between the pressure sweep and steady state condition tests is observed showing the transient nature of the JTFA does not influence the resulting spectra. The pressure sweep was conducted both by increasing and decreasing σ and revealed no evidence of hysteresis.

Three trends are evident in the spectrograms corresponding to differing cloud cavitation shedding mechanisms discussed in the introduction. A shockwave-driven (type 1) mode occurs at $St \approx 0.1$ and within a range of σ from 0.3 – 0.55 for both hydrofoils. A slight dependence on σ is observed in both cases with the frequency increasing slightly with σ. A similar trait observed in [17] attributing it to low dissolved oxygen levels (≈ 7 ppm) where current results are for a constant dissolved oxygen level of about 3 ppm. Comparing the hydrofoils, the flexible model exhibits significantly greater amplitude than the rigid for virtually the entire type 1 mode region. As σ increases from 0.2, the flexible hydrofoil reaches its maximum at $\sigma \approx 0.38$, compared to $\sigma \approx 0.45$ for the rigid. As

*Corresponding Author, Samuel Smith: ssmith18@utas.edu.au

σ increases to approximately 0.5, the cavity becomes smaller, closing further upstream from the hydrofoil trailing edge. This reduction in cavity size causes a change in the pressure distribution and the resulting unsteady forces acting on the hydrofoil. With the cavity closing on the hydrofoil, a re-entrant flow may form (evident in Figure 1), becoming the primary shedding instability mechanism as σ increases.

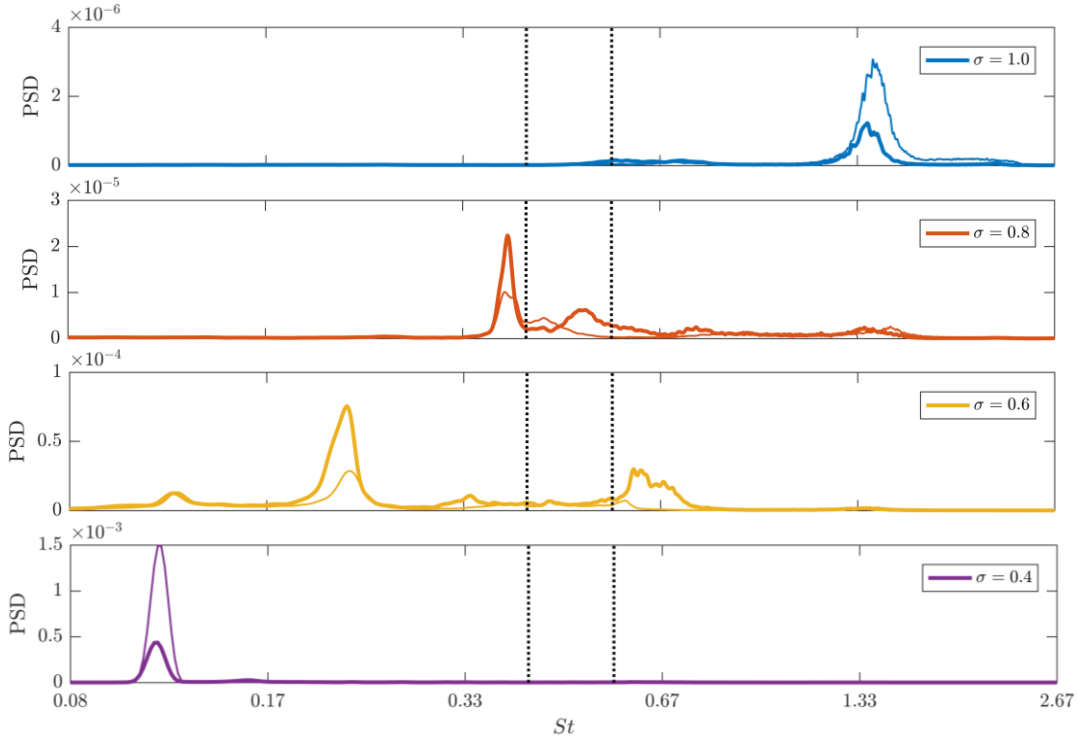

Figure 3 High-resolution non-dimensional normal-force spectra for the rigid (thick line) and flexible (thin line) hydrofoils for various σ. The vertical dashed lines show the flexible and rigid hydrofoils wetted natural frequencies. Note the ordinate axis limits change for each σ.

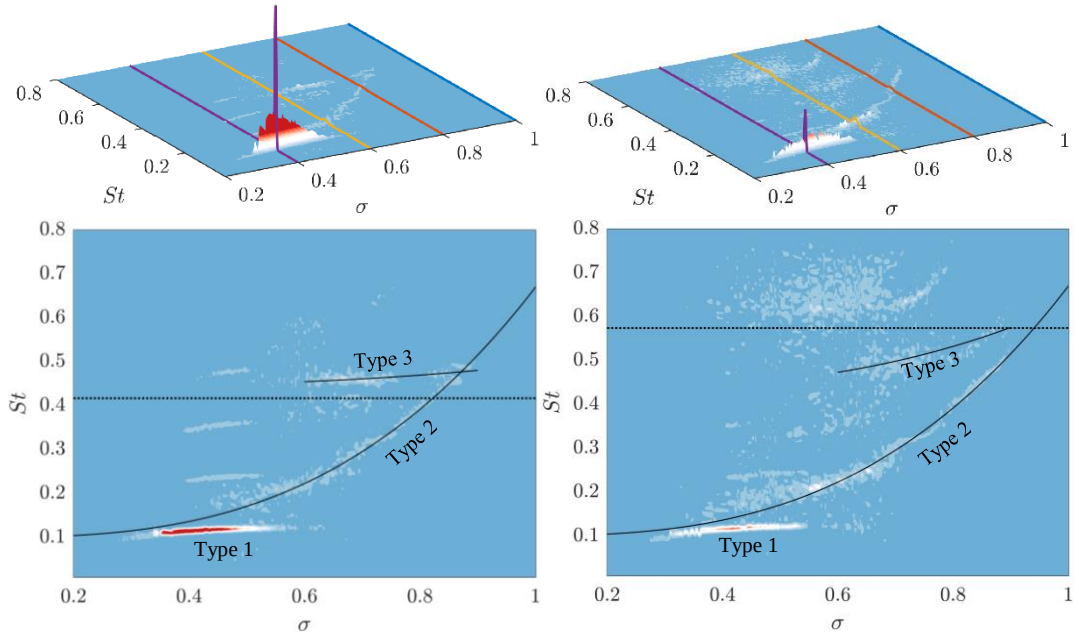

Figure 4 (Top) Isometric overlay of high-resolution spectra and low resolution spectrograms. (Bottom) Top view of the spectrograms with identified shedding modes and hydrofoil wetted natural frequency (dotted line). The left and right columns are data for the flexible and rigid hydrofoils, respectively. The results show convergence of type 2 into type 3 shedding modes with decreasing σ. Type 2 and 3 mode shedding frequencies varies as a power law with σ where $St_2 \approx 0.57\sigma^3 + St_1$, $St_{3F} \approx 0.05\sigma^3 + 0.44$ and $St_{3R} \approx 0.2\sigma^3 + 0.43$, where the subscripts are the shedding modes.

The type 2 mode, driven by re-entrant flow, follows an almost identical trend for both hydrofoils, showing strong dependence on σ and diminishing by $\sigma \approx 0.9$. Figure 4 shows the type 2 mode varies with σ as a power law with an exponent of 3 where $St_2 \approx 0.57\sigma^3 + St_1$, where the subscripts are the shedding modes. From approximately σ =

*Corresponding Author, Samuel Smith: ssmith18@utas.edu.au

0.5 to 0.6, types 1 and 2 modes co-exist, indicating that shedding-induced unsteady forces may be due to either re-entrant flow, shockwave induced cavity collapse or both in this region. This is reinforced by the high-resolution PSD in Figure 3 where at σ = 0.6, the spectra exhibit peaks at both 11.7 Hz (St = 0.12, shockwave-driven) and 21.5 Hz (St = 0.23, re-entrant jet-driven) with visual evidence observed in high-speed imaging for both hydrofoils.

The third mode (type 3) is evident in the spectrograms at $0.6 < \sigma < 0.9$, co-existing with type 2 for both hydrofoils. The type 3 mode is also seen to vary with σ as a power lower with an exponent of 3 but the trend differs between hydrofoils where $St_{3F} \approx 0.05\sigma^3+0.44$ and $St_{3R} \approx 0.2\sigma^3+0.43$ for the flexible and rigid, respectively. Identification of the tertiary mode is made evident in the power distribution maps below.

To gain spatial insight into the shedding behaviour, power distribution maps of identified shedding modes are shown in Figure 5. The maps are obtained by performing a FFT on the time series of each pixel and extracting the frequency specific power, then plotting the values to form a plot of distribution of power through the image. At σ = 0.8, both hydrofoils exhibit two shedding modes (type 2 and 3) of which the type 2 shedding occurs at similar frequencies of 37.7 and 37.4 Hz (St = 0.392 and 0.397, also shown in Figure 3) for the flexible and rigid hydrofoils, respectively. Power distributions reveal that this fundamental frequency is driven by shedding between s/6 and s/2 from the root for both hydrofoils.

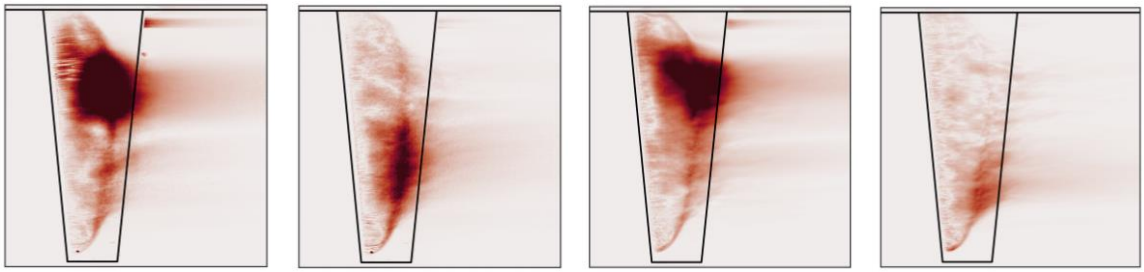

(a) Flexible: 37.7 Hz, St = 0.392 (b) Flexible: 44.4 Hz, St = 0.462 (c) Rigid: 37.4 Hz, St = 0.397 (d) Rigid: 49.9 Hz, St = 0.53

Figure 5 Power distribution of shedding events for the (a & b) flexible and (c & d) rigid hydrofoil with type 2 mode shown in (a) and (c) while a type 3 mode is shown in (b) and (d). All data is for σ = 0.8.

The tertiary mode (type 3) of each hydrofoil occurs at different frequencies coinciding with those observed in the normal force PSD (Figure 3) at 44.4 Hz (St = 0.462) and 49.9 Hz (St = 0.53) for the flexible and rigid hydrofoil, respectively. The power concentration of the tertiary mode is localized to the lower half of the span in contrast to the type 2 mode in the top half. Due to the principle spanwise bending deformations of the flexible hydrofoil, the type 3 mode power distribution extends further along the span than that of the rigid hydrofoil. High-speed imaging show that both the type 2 and 3 shedding modes are re-entrant jet driven.

With both hydrofoils exhibiting two shedding modes and power distributions showing they cover separate regions of the planform indicates the formation of two shedding events on the hydrofoil for a particular σ. The occurrence of the differing shedding events along the span is supported by the span-wise space-time plots in [8] and high-speed imaging. The formation of multiple span-wise shedding events is not observed at σ other than 0.8 as the cavity length, both stream-wise and span-wise, are incompatible with the hydrofoil span and, instead, result in an irregular break-off mechanism [22]. In the present study additional variations in spanwise geometry, hydrostatic pressure and hydroelastic response may also attribute to this behaviour.

Conclusions

Fluid-structure interaction is seen to have an effect on the cavity dynamics and induced normal force fluctuations experienced by a hydrofoil operating under cloud cavitation conditions. JTFA identified three shedding modes, type 1, 2 and 3, where the type 2 and 3 modes are seen to vary as a power law with σ. Power in the peak frequencies is seen to drop by approximately one order of magnitude with every 0.2 reduction in σ. Furthermore, it is shown that the rigid hydrofoil exhibits double the power of the flexible hydrofoil at the fundamental peak frequencies for σ between 0.6 and 0.8. However, the flexibility of the composite hydrofoil resulted in 3 times the power of that of the rigid at σ equal to 0.4, where the shedding mode has transitioned from type 2 to 1. The fundamental peak frequencies at each σ were not seen to vary significantly between hydrofoils, suggesting flexibility has more effect on the severity of cloud cavitation than its shedding frequency. Power distribution maps show the existence of two shedding modes (type 2 and 3) along the span of the hydrofoils that match those in the PSDs. The common

*Corresponding Author, Samuel Smith: ssmith18@utas.edu.au

type 2 mode frequency (37 Hz, St = 0.39) is seen to be due to shedding cavities on the upper half of the hydrofoil. The flexibility of the composite hydrofoil is seen to drop the type 3 mode frequency from 49 Hz (St = 0.52) to 42 Hz (St = 0.44) as well as change the spatial distribution of the secondary shedding across the bottom half of the span. The complex behaviour found under cavitation conditions indicates that any simple design assumptions applied to flexible hydrofoils may be not sufficient and a detailed analysis of these structures is required.

Acknowledgements

This project was supported by the University of Tasmania, the Defence Science and Technology Group, US Office of Naval Research (Dr. Ki-Han Kim, Program Officer) and ONR Global (Dr. Woei-Min Lin) through NICOP S&T Grant no. N62909-11-1-7013. The authors would like to acknowledge the assistance of Mr Steven Kent and Mr Robert Wrigley from the Australian Maritime College for their essential help with setting up and carrying out the experiments.

References

[1] Young, Y. L. (2008). *Fluid–structure interaction analysis of flexible composite marine propeller*s. Journal of Fluids and Structures. 24(6):799–818.
[2] Motley, M., Liu, Z., & Young, Y. (2009). *Utilizing fluid–structure interactions to improve energy efficiency of composite marine propellers in spatially varying wake.* Composite Structures. 90(3), 304-313.
[3] Turnock, S., Wright, A. (2000). *Directly coupled fluid structural model of a ship rudder behind a propeller.* Marine Structures. 13(1), 53-72.
[4] Young, Y. L. (2007). *Time-dependent hydroelastic analysis of cavitating propulsors*. Journal of Fluids and Structures, 23(2), 269-295.
[5] Akcabay, D. T., Chae, E. J., Young, Y. L., Ducoin, A., & Astolfi, J. A. (2014). *Cavity induced vibration of flexible hydrofoils.* Journal of Fluids and Structures, 49 (Supplement C), 463-484
[6] Akcabay, D. T., & Young, Y. L. (2014). *Influence of cavitation on the hydroelastic stability of hydrofoils.* Journal of Fluids and Structures, 49, 170-185.
[7] Callenaere, M., Franc, J.-P., Michel, J.-M., & Riondet, M. (2001). *The cavitation instability induced by the development of a re-entrant jet.* Journal of Fluid Mechanics, 444, 223-256.
[8] Smith, S., Venning, J., Brandner, P., Pearce, B., Giosio, D., & Young, Y. L. (2017). *Cloud cavitation behaviour on a hydrofoil due to fluid-structure interaction*. 17th International Symposium on Transport Phenomena and Dynamics of Rotating Machinery, Maui, Hawaii.
[9] Ganesh, H., Wu, J., & Ceccio, S. (2016). *Investigation of cavity shedding dynamics on a NACA0015 hydrofoil using time resolved x-ray densitometry*. 31st Symposium on Naval Hydrodynamics, ONR.
[10] Ganesh, H., Mäkiharju, S. A., & Ceccio, S. L. (2016). *Bubbly shock propagation as a mechanism for sheet-to-cloud transition of partial cavities.* Journal of Fluid Mechanics, 802, 37-78.
[11] Reisman, G., Wang, Y.-C., & Brennen, C. E. (1998). *Observations of shock waves in cloud cavitation.* Journal of Fluid Mechanics, 355, 255-283.
[12] Venning, J., Giosio, D., Smith, S., Pearce, B. & Brandner, P. (2018). *The influence of nucleation on the spectral content of cloud cavitation about a hydrofoil.* The 10th International Symposium on Cavitation, Baltimore, Maryland, accepted paper.
[13] De Graaf, K. L., Brandner, P. A., & Pearce, B. W. (2017). *Spectral content of cloud cavitation about a sphere*. Journal of Fluid Mechanics, 812, R1.
[14] Venning, J., Smith, S., Brandner, P., Giosio, D., & Pearce, B. (2017). *The influence of nuclei content on cloud cavitation about a hydrofoil*. 17th International Symposium on Transport Phenomena and Dynamics of Rotating Machinery, Maui, Hawaii.
[15] Avellan, F., Dupont, P., & Ryhming, I. L. (1988). *Generation mechanism and dynamics of cavitation vortices downstream of a fixed leading edge cavity.* 17th Symposium on Naval Hydrodynamics, Berkeley, California.
[16] Kjeldsen, M., Arndt, R. E., & Effertz, M. (2000). *Spectral characteristics of sheet/cloud cavitation.* Journal of Fluids Engineering, 122(3), 481-487.
[17] Kawakami, D. T., Fuji, A., Tsujimoto, Y., & Arndt, R. (2008). *An assessment of the influence of environmental factors on cavitation instabilities*. Journal of Fluids Engineering, 130(3).
[18] Zarruk, G. A., Brandner, P. A., Pearce, B. W., & Phillips, A. W. (2014). *Experimental study of the steady fluid–structure interaction of flexible hydrofoils.* Journal of Fluids and Structures, 51, 326-343.
[19] Brandner, P., Lecoffre, Y., & Walker, G. (2007). *Design considerations in the development of a modern cavitation tunnel*. 16th Australasian Fluid Mechanics Conference, Gold Coast, Australia.
[20] Welch, P. (1967). *The use of fast Fourier transform for the estimation of power spectra: a method based on time averaging over short, modified periodograms*. IEEE Transactions on audio and electroacoustics, 15(2), 70-73.
[21] Smith, S., Pearce, B., Brandner, P., Clarke, D., Moreau, D., & Xue, Y. (2016). *Steady and unsteady loads acting on a hydrofoil immersed in a turbulent boundary layer.* 20th Australasian Fluid Mechanics Conference, Perth, Australia.
[22] Kawanami, Y., Kato, H., & Yamaguchi, H. (1998). *Three-dimensional characteristics of the cavities formed on a two-dimensional hydrofoil.* Third International Symposium on Cavitation. Grenoble, France.

*Corresponding Author, Samuel Smith: ssmith18@utas.edu.au